School of Science
Department of Imaging & Applied Physics

Ocean Colour Remote Sensing of the Great Barrier Reef Waters

Matthew M. Slivkoff

This thesis is presented for the Degree of
Doctor of Philosophy
of
Curtin University

November 2014

Declaration

To the best of my knowledge and belief this thesis contains no material previously published by any other person except where due acknowledgment has been made.
This thesis contains no material which has been accepted for the award of any other degree or diploma in any university.

Signature:

Date: 27^{th} of November, 2014

Contents

0.1 Abstract

The Great Barrier Reef (GBR) region is the most spatially extensive, ecologically significant and least disturbed large coral reef ecosystem in the world. The reef was placed on the World Heritage List in 1981 due to its significance to humanity. The adjacent land mass, the Australian State of Queensland, has had increases in deforestation, agriculture, urbanisation, and the associated eutrophication of coastal waters. Whilst these human activities are important for the Australian economy, since heritage listing we also have an international obligation to preserve the reef. This, combined with fishing and the emergence of the now-billion dollar tourist industry places a high importance to reef conservation.

With increased land use in the region, there is an need to monitor the GBR and its catchment on an ongoing basis to ensure sustainable practices are employed to prolong the benefits of having relatively unspoilt and unique coastal environments. Extending over 1500 km in length and approximately 15° latitude, the GBR is the largest contiguous coral reef ecosystem in the world, and presents a challenge for ecosystem health monitoring. Although initially intended for optically simple oceanic applications, satellite-based ocean colour measurements such as those from MODIS-Aqua can provide a synoptic and near-daily coverage of the GBR region. Ocean colour satellites exhibit enormous potential to quantify coastal water quality parameters, but before potential end-users can trust the measurements derived from satellites, relationships must be determined which accurately convert the satellite measured signals (i.e reflectance, R_{rs}) into these familiar units of water quality measurement. This relationship or process is referred to as an "algorithm".

The research undertaken herein has developed relationships between the concentrations and types of substances found in GBR water and their respective inherent optical properties (Chapter 2). Based on this knowledge, a physics-based spectral deconvolution routine was established in Chapter 3 and evaluated in Chapter 4. The deconvolution routine was able to successfully and simultaneously retrieve the concentrations of optically-significant substances (phytoplank-

ton, Colour Dissolved Organic Matter (CDOM), and particulates) from passive ocean colour observations.

The principal remote sensor developed for, and used in this study (described in Chapter 3) is known as the Dynamic Above water Radiance and Irradiance Collector (DALEC). Combined with flow-though measurements of water quality parameters, the DALEC proved to be an incredibly useful tool for rapid data collection for algorithm development studies, passive water quality monitoring, and satellite algorithm validation.

Based on this dataset, the DALEC-based water quality parameter retrievals yielded Root-Mean-Squared Errors (RMSE) of 26.6%, 17.2% and 10% for Total Chlorophyll-a (TChl), Total Suspended Solids (TSS) and Dissolved Organic Carbon (DOC), respectively.

The DALEC was used to test the accuracy of a variety of MODIS atmospheric correction approaches suitable for turbid and glint-effected coastal waters. The spectral inversion methodology developed on the DALEC measurements was also applied in Chapter 5 to a GBR flood plume scene from the MODIS satellite sensor, where it successfully retrieved TChl, TSS from the images with of 26.9% and 11.8% respectively. A MODIS-based DOC product was also presented.

0.2 Acknowledgments

First, I would like to thank my family for all of their support and guidance to get me into this position in the first place. There was a time in the early 2000 where having a BSc (Hons) in physics with no industry experience meant absolutely nothing for a potential employer in sunny pre-boom Perth. Mum and Dad had the perfect solution for kids like me; by putting me to work in the glue corner at their furniture manufacturing operation. For about one year I inhaled volatile solvents dreaming that one day I could use what I had learned at university for some real world application other than what I could do in the confines of being the lowest-ranked labourer at the factory. I am thankful to Merv Lynch because after I had reached my limit of working in the glue corner, Merv pointed to me Eastward in the direction of Miles Furnas. I thank Mum and Dad (and that factory) for flying me across from Perth to Townsville in order to meet with Miles and discuss the potential for a PhD project based in Townsville.

Moving to Townsville was an amazing learning experience from me. It wasn't long before Miles had me out on a rubber duckie, retrieving transmissometers in the Wet Tropics. He also showed me how to perform my first ever CTD cast, grab my first Niskin sample, and filter my first sample on a GF/F. Monumental. I considered it an absolute privilege to learn and work at the Australian Institute of Marine Science. I would like to thank Michelle Skuza, Margaret Wright and Irena Zagorskis for expert laboratory analyses used in this study. Between these three people, the majority of the crucial water quality parameters used in this study were analysed. I would also like to thank Miles Furnas, David McKinnon, Tim Cooper, Katharina Fabricius, Sven Uthicke and Craig Humphrey for sharing their ship time with me. I'd like to thank Britta Schaffelke and David McKinnon for kindness and encouraging words. Thanks to Mike Mahoney putting up with me asking countless questions about Unix and why Fritz was on the Fritz. Thanks also to Craig Steinberg for providing some crucial work experience working in batch-processing SeaWiFS imagery, and Stuart Kinninmonth for providing some GIS layers used in this study. I would also like to thank the AIMS engineering workshop, especially Eric Gill and Gary Brinkman for bringing me closer

to realising my dream. I am also thankful for the help of the crew on the RV's Lady Basten, Cape Ferguson and James Kirby between 2004 - 2006. A special mention also goes out to Lachlan McKinna and Kadija Oubelkheir for providing some additional IOP data used in this study.

I'd like to thank Leon Majewski and Wojciech Klonowski for teaching me to have healthy skepticism, for providing me with a wealth of programming tips and for always humouring my silly ideas whilst keeping me on the ground. Also a special mention should be made to Wojciech Klonowski for assisting in the DALEC calibration measurements.

Finally, I would again like to thank my Supervisors Merv Lynch and Miles Furnas for being patient with me, letting me find my own path and providing such great feedback through this process.

Chapter 1

An introduction to the Great Barrier Reef

The Great Barrier Reef (GBR) lies on the North Eastern coast of the Australian continent (see Figure 1.1), in the Australian State of Queensland (QLD). The GBR is the world's largest coral reef system which spans between approximately 9 °S in the Torres Straight near the coast of Papua New Guinea and 24 °S, near Bundaberg, QLD. Its seaward margin essentially defines the continental shelf which lies 21 km offshore in the north, and approximately 150 km offshore near the Swain Reefs offshore from Rockhampton in the south (see Fig. 1.3). Locally, the term GBR "lagoon" is used to describe the semi-enclosed body of water on the shelf inside the outer barrier structure. Although not a strictly a contiguous barrier as the name might suggest, the GBR is a series of several thousand individual reefs and sandy cays. The general structure of the reef can clearly be seen from space, running nearly parallel with the coast as shown by the composite MODIS-Aqua satellite image in Figure 1.2.

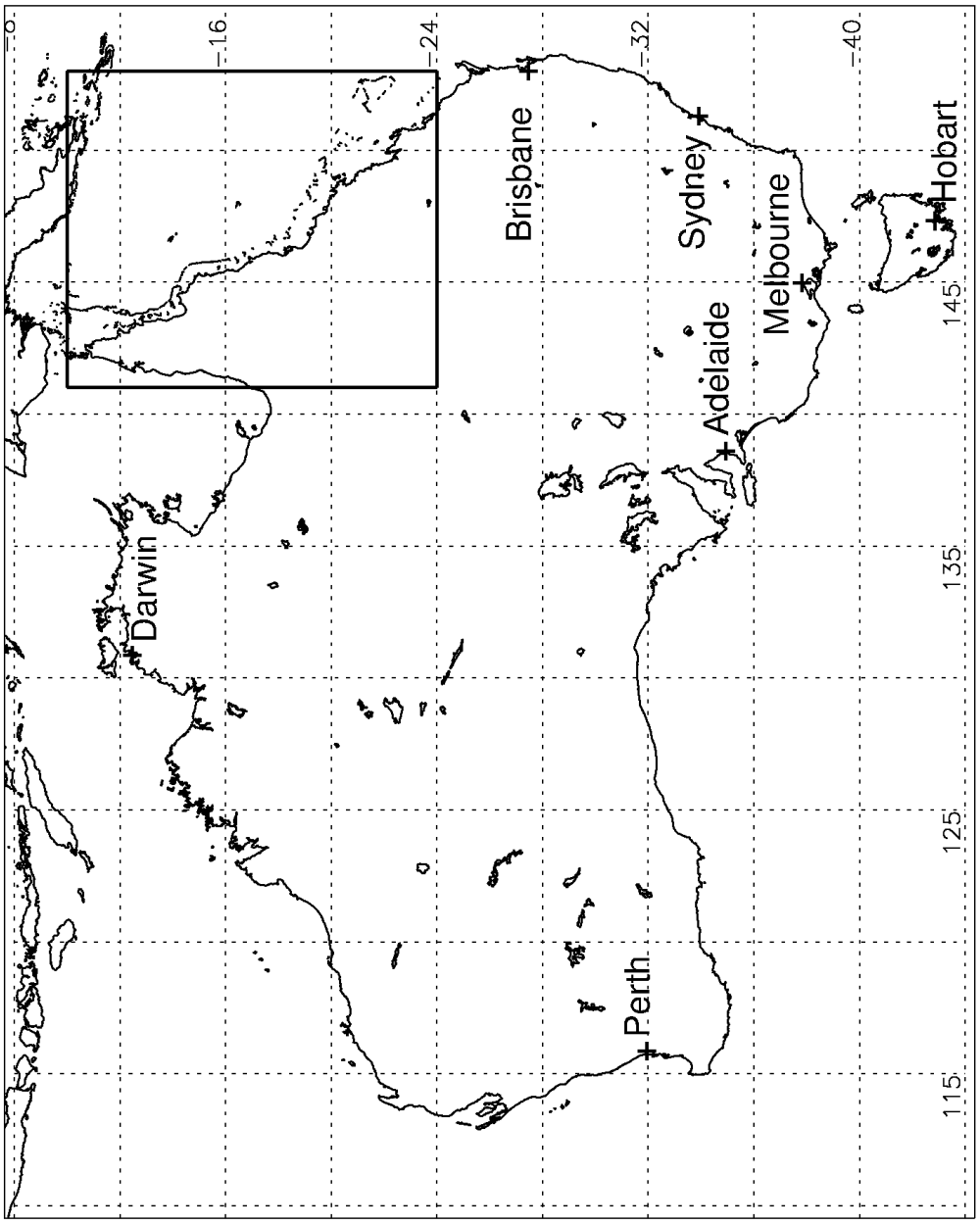

Figure 1.1: Map of Australia featuring major city centres and the showing the Northern Queensland coastline where the GBR is located.

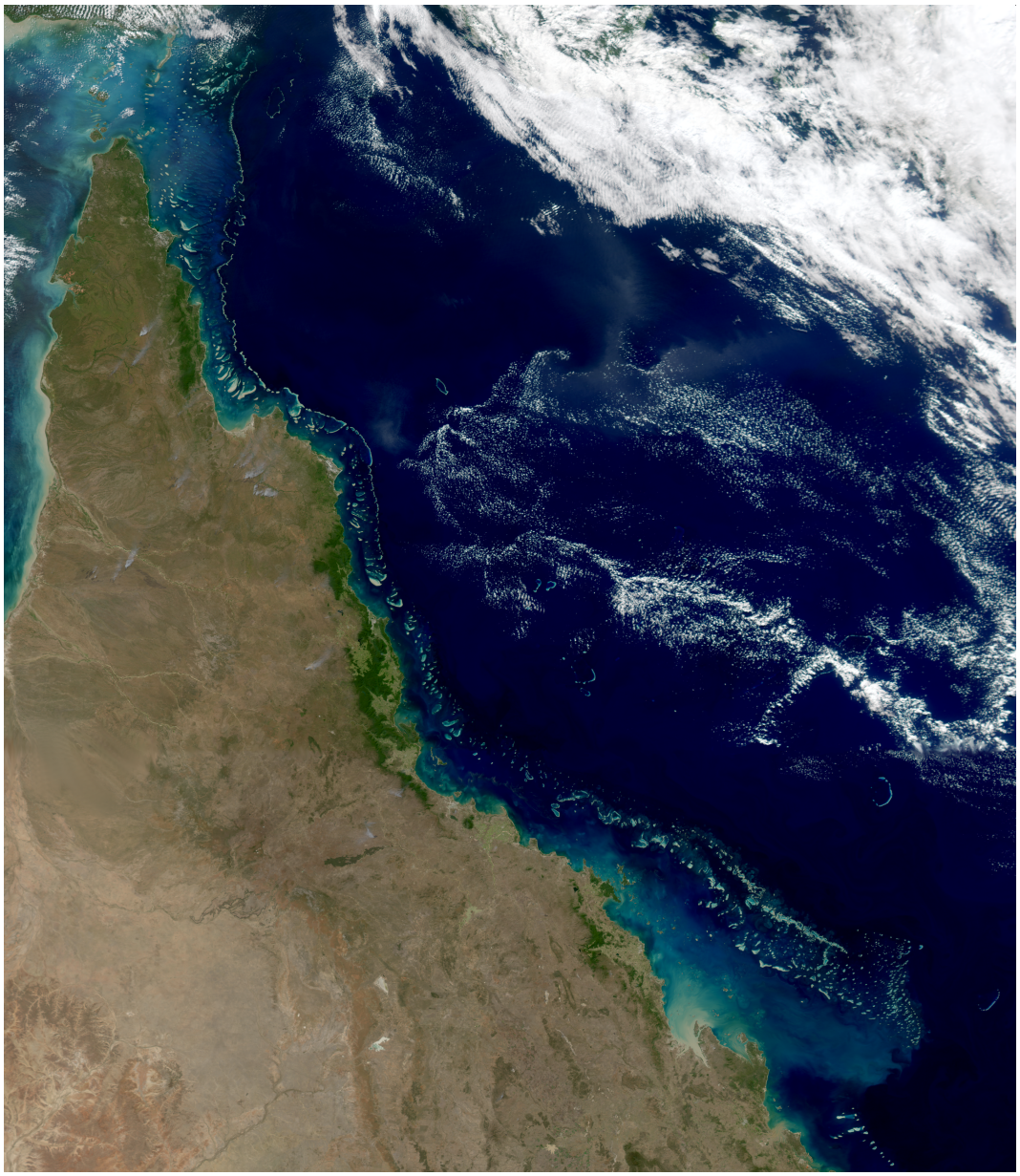

Figure 1.2: MODIS-Aqua true colour composite image of the northern queensland coast and the majority of the Great Barrier Reef. The top half of the image was captured on the 22^{nd} May 2009 and the bottom half of the image was captured on the 31^{st} July 2008.

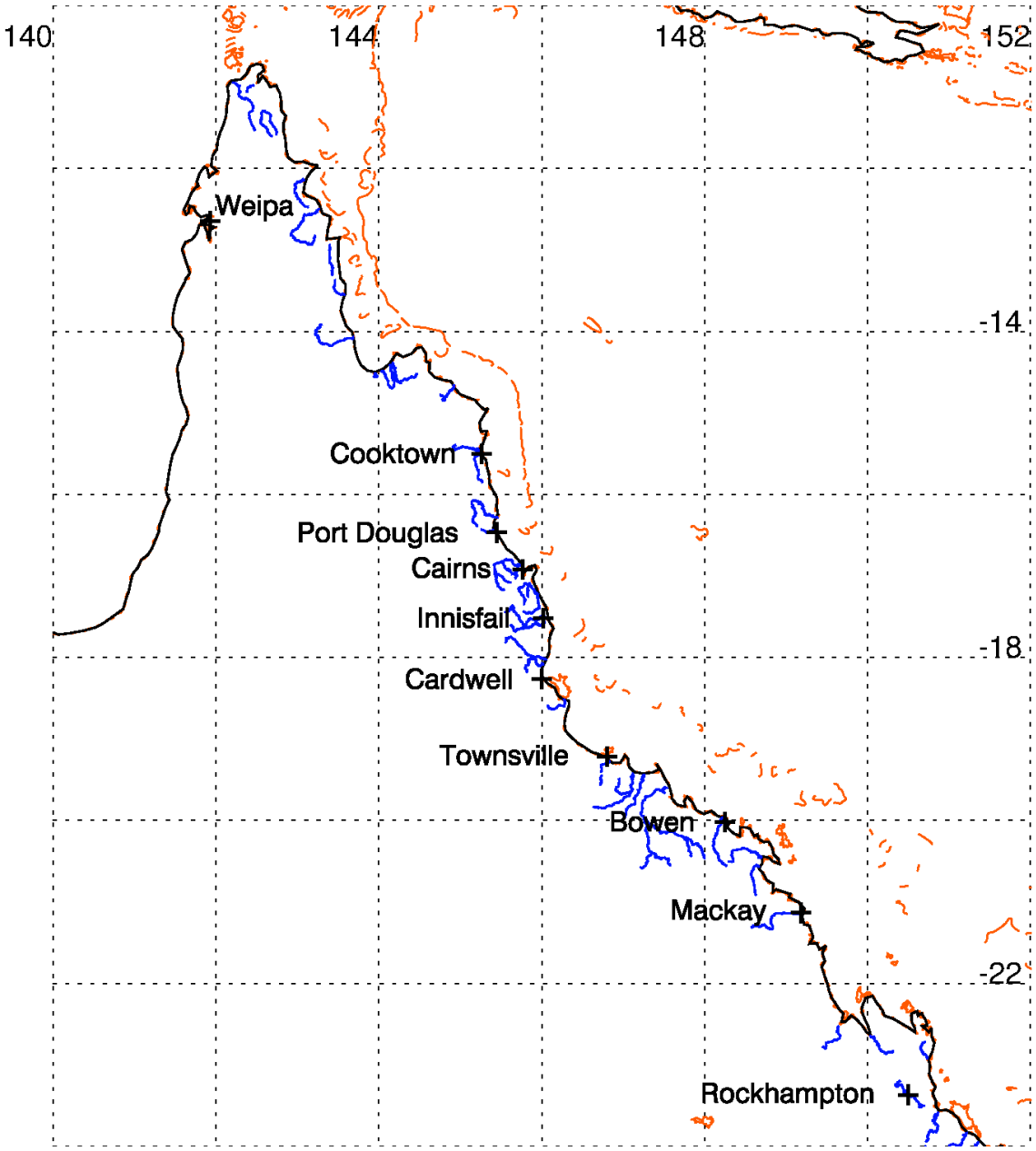

Figure 1.3: The GBR region, showing prominent regional centers and selected eastward-flowing coastal watercourses (in blue) derived from Geoscience Australia's TOPO 2.5M 1998 hydrography theme (GA 1998). Partial barrier reef outlines and islands are shown in orange.

The north-eastern Queensland coast has a generally warm and humid climate, with daily mean maximum temperatures varying from approximately 31° C in summer (Dec. - Feb.) to 26° C in winter (Jun. - Aug.). The daily mean minimum temperatures varying from approximately 23° C in summer to 17° C in winter (see Fig. 1.4).

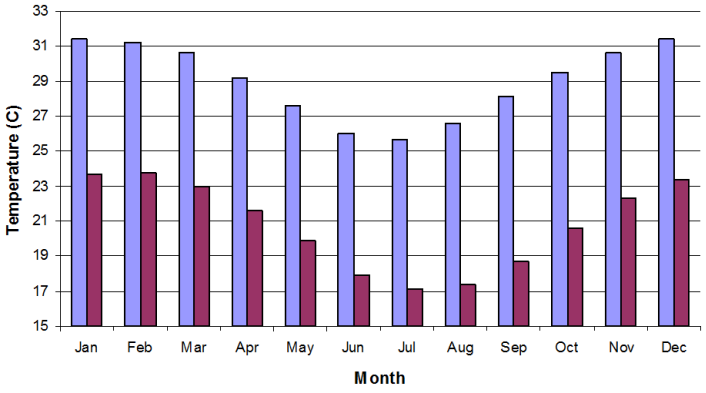

Figure 1.4: Monthly mean maximum and minimum temperatures recorded at Cairns Airport, based on data collected from 1942-2011 (BOM 2012*b*).

From approximately May to November, SE trade winds blow from the Pacific Ocean up towards the equatorial trough (Wolanski et al. 1981). This period is known as the dry season. Towards the summer months, warm and moist air moves towards Queensland from the northwest. This is referred to as the Indo-Australian monsoon, and lasts from approximately December to March, although the timing and duration are known to vary (Robertson et al. 2006). During the monsoon season, tropical depressions and cyclones bring increased rainfall to North Queensland. This season is also referred to as the 'wet' season.

The monsoon months bring the majority of the annual rainfall for the area. Figure 1.5 shows the seasonal rainfall distribution near the prominent tourist town, Cairns (see Fig. 1.3 for location). This seasonality is representative of other coastal northern Queensland coastal towns, although total rainfall varies significantly across the 14 degrees of latitude, as shown in Fig. 1.7.

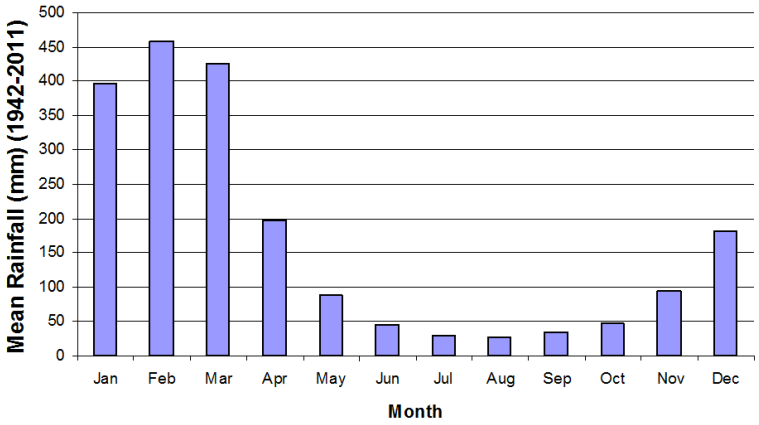

Figure 1.5: Monthly mean rainfall recorded at Cairns Airport, based on data collected from 1942-2011. The annual mean total is 2020.4 mm (BOM 2012*b*).

In addition to the yearly monsoon period and the trade winds-dominated dry season, the El Niño - Southern Oscillation (ENSO) also affects the Queensland climate. ENSO is influenced by multiple-year cycles of heating and cooling of the sea-surface temperature (SST) in the central and eastern tropical Pacific Ocean (Whifield et al. 2010). El Niño events are associated with above average SST, and generally bring below-average dry season rainfall. La Niña events are associated with below-average SST, and generally bring above average dry season rainfall. The link between ENSO and Australian rainfall is not always prominent, as the ENSO process itself is said to modulated by more complicated processes such as the Interdecadal Pacific Oscillation (IPO) (Arblaster et al. 2002, Power et al. 2006). The result is that between ENSO/IPO and monsoonal lows and cyclone events, Northern Queensland is subject to a significant degree of interannual vari-

ability in rainfall (see Fig. 1.6).

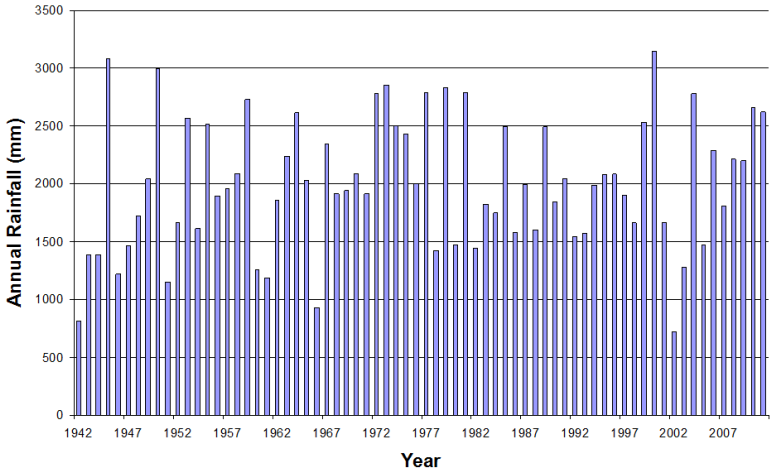

Figure 1.6: Yearly rainfall recorded at Cairns Airport, based on data collected from 1942-2011. (BOM 2012*b*).

In Figures 1.7 and 1.8, it can be seen that the seaward (eastern) sides of the Great Dividing range typically experience much higher annual rainfall. This geographical selectivity in rainfall is also demonstrated by the green vegetation in Fig 1.2. The area between Cooktown and Cardwell experiences in excess of approximately 2500 mm per year and is referred to as the 'Wet Tropics'.

The Wet Tropics consists of undeveloped rainforest-clad mountains, giving way to extensive areas of cleared forest in the coastal lowlands. Forested areas were cleared for timber, and now largely accommodates cattle pastures and sugar-cane plantations. Cleared land in the Wet Tropics typically surrounds watercourses and is identifiable in satellite imagery such as Fig. 1.2. Outside the Wet Tropics, sugar cane and cattle grazing is still the most common use of land, alongside horticulture, cotton and minor urban development (Brodie et al. 2003).

As shown in the preceding Figures (1.5, 1.7), the monsoonal months can bring

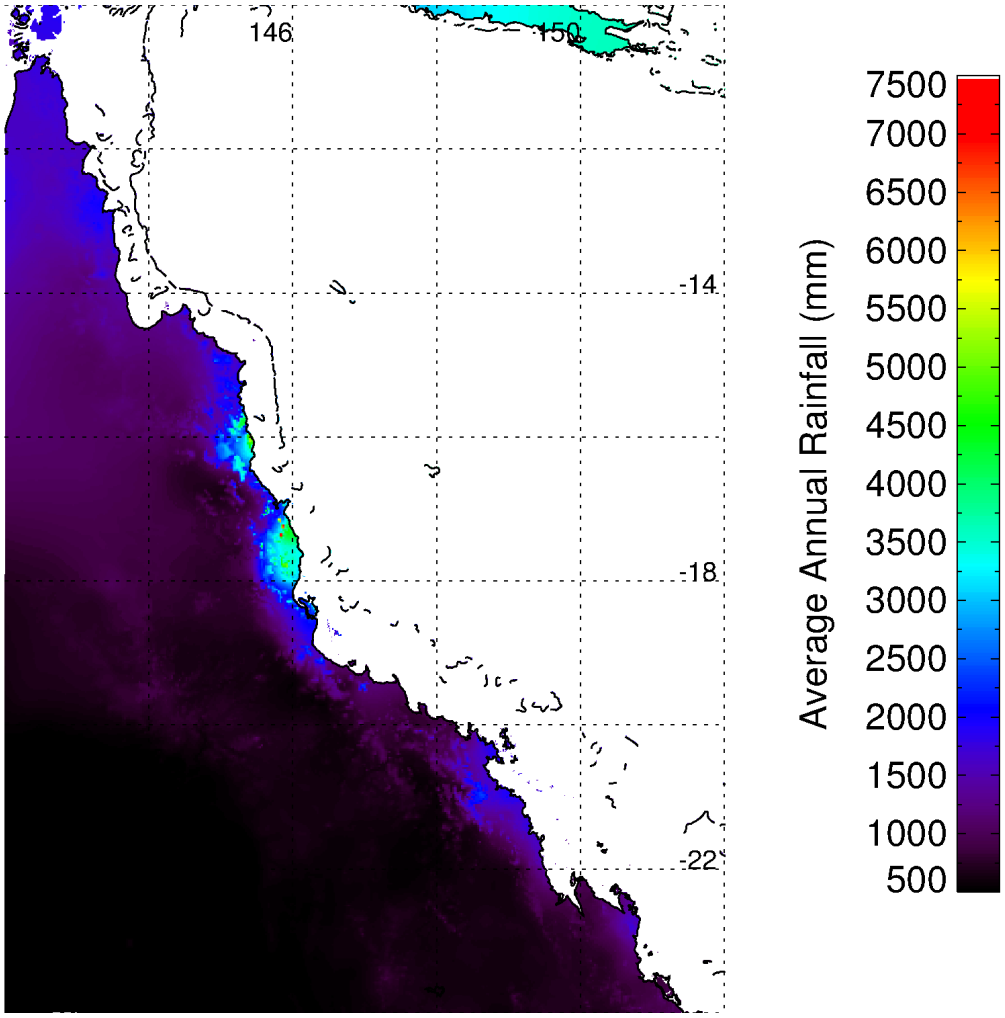

Figure 1.7: Gridded average annual rainfall product for Northern Queensland (1961-1990) (BOM 2009). No data presented over the ocean.

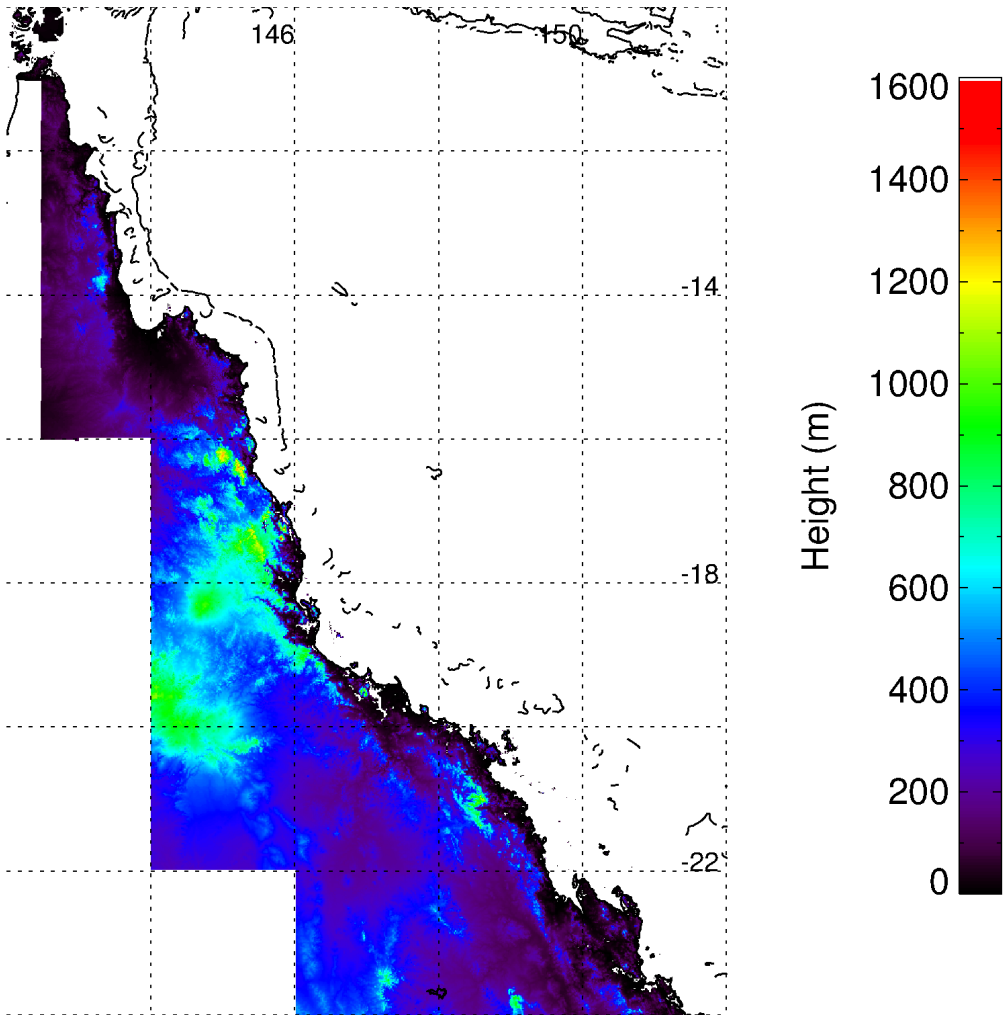

Figure 1.8: Digital Elevation Map showing the Great Dividing Range and the low-lying areas which lead to the GBR (Lewis 2001). No data presented over the ocean. See later in Fig. 2.1 for GBR bathymetry.

very high rainfall to the GBR catchment. It is estimated that an average of 380 km^3 per annum of rain falls on the GBR catchment; 18% of which runs into the GBR lagoon (Furnas 2003), bringing with it terrestrial sediments and pollutants including pesticides. This episodic flooding into Great Barrier Reef waters can be clearly resolved by the MODIS satellite sensor (see Fig. 1.9 and 1.10).

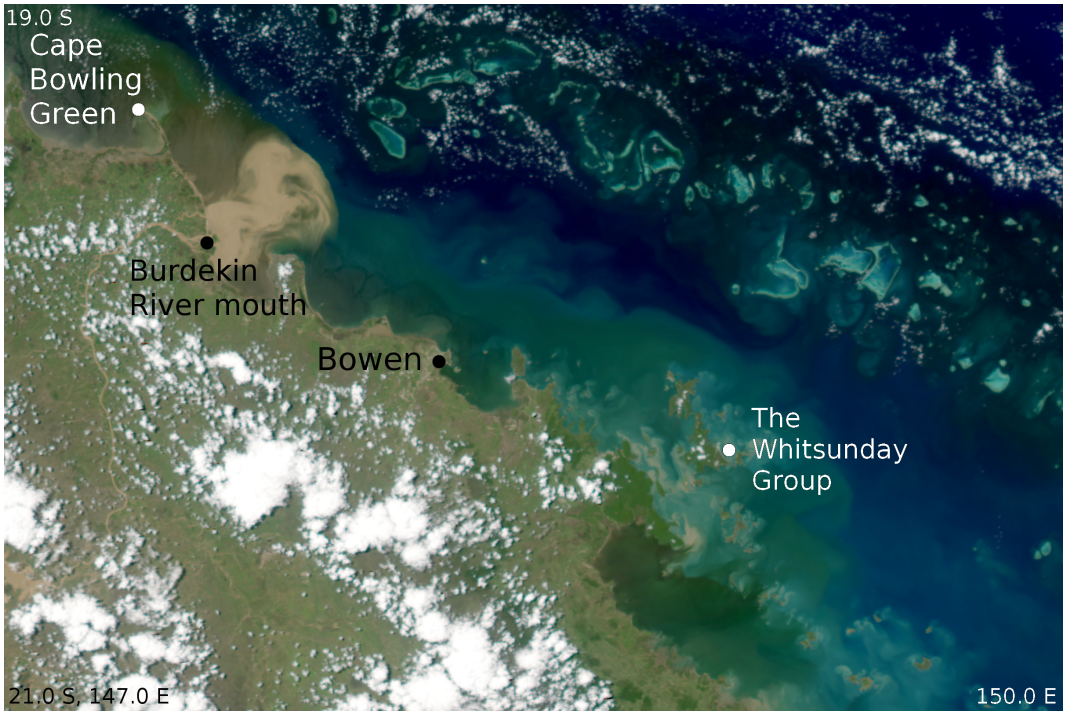

Figure 1.9: MODIS pseudo true colour image of the central GBR coast after a monsoon flood (Feb, 2008). The bright coloured flood water north-west of Bowen is sourced from the Burdekin river catchment whereas the southernmost flood near the Whitsunday Group is sourced from the wetter, forested Proserpine and O'Connell river catchments. Here, nutrient-rich flood waters appear to be rapidly converted to phytoplankton biomass. Note plumes of tidal or wind re-suspended sediments in the Whitsunday Group.

It is almost certain that clearing the forests in the low-lying areas of the GBR catchment and using the land as pasture has led to increased erosion and sediment discharge into the GBR (McCulloch et al. 2003). As flood waters are a significant contributor of nutrients to the GBR lagoon (Furnas et al. 1997), it is very important to monitor terrestrial discharge and the effect of increased nutrient influx to the reef. In addition to sediment and nutrients, intensive sugar cane farming and other horticulture uses pesticides which have been identified as

a threat to the GBR (Lewis et al. 2009).

The GBR and part of its adjacent coastline was recognised by the United Nations Educational, Scientific and Cultural Organisation (UNESCO) as a World Heritage Site. With UNESCO Heritage listing comes the obligation of the Australian Government to preserve the site for all humanity. Superimposed on this international obligation is the need for the ever-increasing utilisation of this resource-rich area so that Australia may compete in the expanding global economy.

The combination of the GBR, rainforest-clad mountains and tropical climate makes North Queensland a very important tourist destination. Between tourism, commercial fishing and recreational activities, it was estimated that the Great Barrier Reef Marine Park Catchment Area (GBRCA) contributed $3.7 billion to the Australian economy in the 2005-2006 period (GBRMPA 2007). As the tourism industry increases global public awareness of the GBR and surrounds, there is increased pressure on those engaged in agriculture to operate in ways that will not jeopardise the tourism industry or the World Heritage status of the GBR and catchment. There is also a need to monitor the effects of improving agricultural practices and changing land use in the area.

Remote sensing offers a unique view of the entire GBR. With near-daily coverage spanning over a decade, the polar-orbiting satellite MODerate resolution Imaging Spectroradiometer (MODIS) sensors provide a long record over which to measure changes in the GBR ecosystem. Ocean colour satellites exhibit enormous potential to quantify coastal water quality parameters, but before potential end-users can trust the measurements and algorithms based on satellite radiometry in this region, a number of key issues need to be addressed. This thesis attempts to answer the following broad questions in order to establish ocean colour satellite imagery as a quantitative tool for monitoring the Great Barrier Reef region:

1) How do the optical (spectral) characteristics of tropical Australian coastal waters relate to traditionally-measured water quality parameters?

Figure 1.10: MODIS pseudo true colour image of the Wet Tropics after a monsoon flood (Feb, 2007). Flood waters escape the reef past Arlington Reef, and sediment is ejected east from Hinchinbrook Passage.

2) How does a complex mixture of these coloured constituents affect the apparent colour of the coastal ocean?

3) How well can ocean colour be analysed to retrieve the concentration of coloured substances in coastal waters?

In answering these questions, this study represents significant research because, for the first time in the GBR region, ocean colour algorithms are developed from an extensive *in situ* data set and are documented with the necessary detail to assist the global community in evaluating the merits of the algorithms and facilitating their improvement. The results could have applicability to other tropical shallow water systems, or at least the instrumentation and methodology described herein could be applied to obtain an accurate parameterisation of other waters of interest. The *in situ* dataset collected for this research project can also contribute to international efforts to produce a generalised physics-based ocean colour retrieval algorithm.

In terms of novel methodology, the research required combining continuous flow-through water quality measurements with simultaneous transecting above-water remote sensing reflectance measurements for the purposes of algorithm development and validation. This thesis initiated the development of the Dynamic Above-water L_u (radiance) and E_d (irradiance) Collector (DALEC) spectroradiometer, which represents a significant and lasting contribution to the remote sensing algorithm development and validation process in Australia, and hopefully abroad. The unique methodology employed in this project collected large volumes of data which can rapidly speed up the ocean colour algorithm development process, and generally improve on our understanding of optical oceanography by significantly reducing spatial mismatches which could otherwise lead to poor conclusions about the true optical variability in coastal waters.

The research undertaken has developed and evaluated quantitative approaches to the spatio-temporal monitoring of GBR water quality and demonstrated that a

high level of accuracy can be achieved from remote sensing.

Chapter 2

Water Quality and Inherent Optical Properties

2.1 Introduction

2.1.1 GBR Water Quality and Oceanography

The GBR region is often spatially classified into three broad depth ranges (Maxwell 1968, Larcombe & Carter 2004, Devlin & Brodie 2005); for example, 0-20 m, 20-40 m and waters deeper than 40 m. The shallowest range identifies inshore lagoon waters that are subject to wind driven re-suspension and terrestrial influence. Waters from 20-40 m is generally described as 'middle shelf' GBR lagoon waters, and waters deeper than 40 m are described as 'off-shelf'. Figure 2.1 shows these broad bathymetric contours from 0-20 m, 20-40 m and 40-100 m, applied to the GBR Digital Elevation Model (Lewis 2001).

Ocean circulation in the GBR is driven by the North Caledonia Jet and the North Vanuatu Jet, which brings oceanic Coral Sea water into the GBR. The westward moving Jet currents meet the eastern side of the GBR and bifurcate to form the northward-flowing North Queensland Current (NQC), and the southward-flowing East Australian Current (EAC) (Choukroun et al. 2009). A portion of this bifurcated current enters the GBR lagoon. The position of the bifurcation shifts between 14° S during the monsoon and 20° S in the dry season (Church 1987).

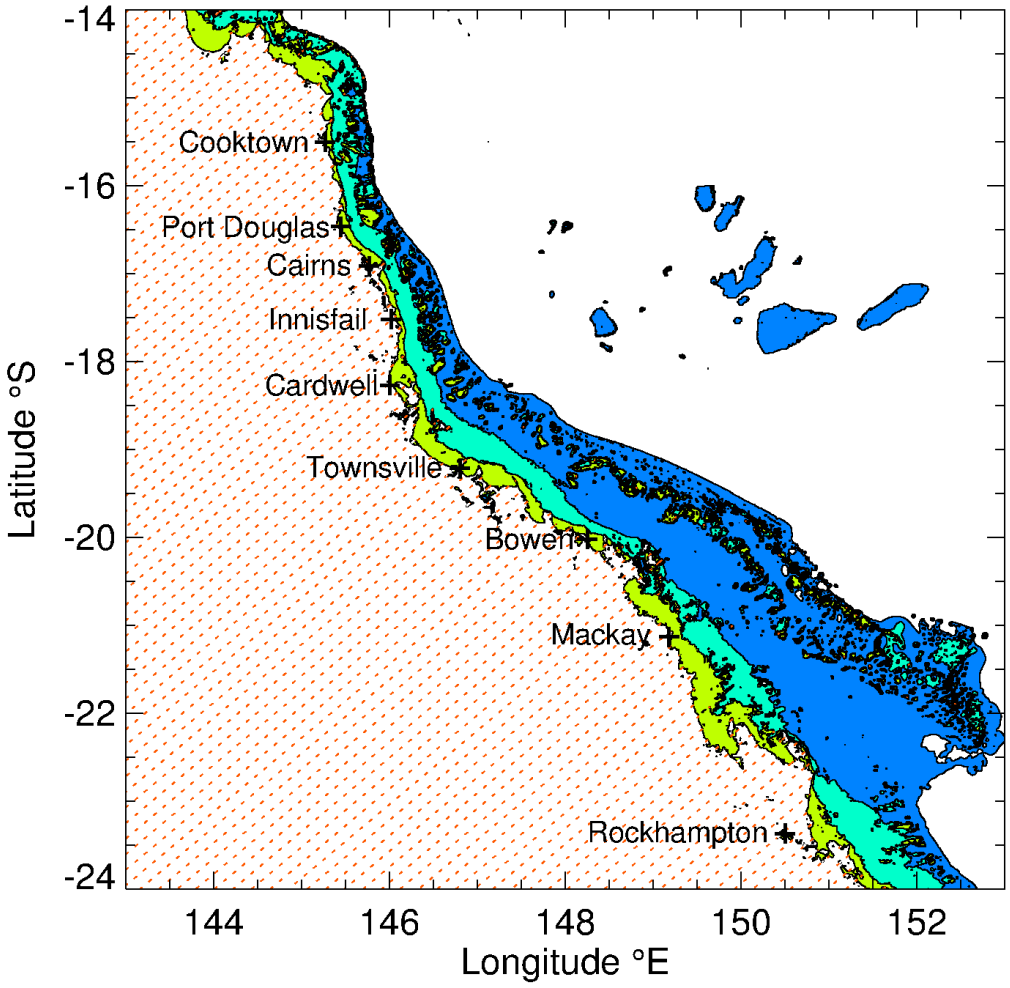

Figure 2.1: Bathymetric contours of the GBR lagoon. 0-20 m shown in yellow, 20-40 m shown in cyan and 40-100 m shown in blue. Waters deeper than 100 m are uncoloured. Original bathymetry data source: GBRDEM (Lewis 2001)

The latitudinal position of the bifurcation governs how much Coral Sea water flows through the outer reef and into the GBR lagoon, because certain areas of the outer GBR 'barrier' are less dense and so provide less resistance to inflow (Choukroun et al. 2009).

Seawater contains a vast diversity of constituents including phytoplankton, detritus, viruses, bacteria, chromophoric dissolved organic matter (CDOM), suspended minerals and gas bubbles. These constituents vary in concentration and size (0.1 nm - 100 μm) (Mobley 1994, Stramski et al. 2004). The concentrations of these constituents define water quality and also influence the overall optical

properties of the seawater. Coastal waters in particular, can contain higher concentrations of suspended minerals, phytoplankton and CDOM.

Water quality is a complex and subjective term defining the suitability of water for a particular purpose. For environmental studies in the GBR, water quality could refer to an assessment of its ability to sustain indigenous marine life. In the GBR region, turbidity and nutrients have been identified as two principal influences on water quality (Haynes et al. 2001), coral biodiversity and macroalgae (De'ath & Fabricius 2010). Marine turbidity and nutrients can be quantified by *in situ* sampling and standardized laboratory measurements including Total Suspended Solids (TSS), Chlorophyll-a (Chl-a) and Dissolved Organic Carbon (DOC). These parameters are also potentially measurable from an orbiting ocean colour sensor i.e.Garver et al. (1994), which would allow the synoptic spatial quantification of these three parameters across the GBR region.

Chlorophyll is the photosynthetic pigment ubiquitous to all phytoplankton (Bissett et al. 1997) so its concentration has long been used as a proxy for algal biomass (Yentsch & Menzel 1963). In the typically high-light tropical GBR region (21 $MJ.m^{-2}$ annually (BOM 2012*a*)), available nutrients are rapidly converted into phytoplankton biomass (Furnas et al. 2005), so chlorophyll-a concentration is an indicator for increased nutrient input in the region (Steven et al. 1998, Wooldridge et al. 2006).

Upwelling processes along the seaward margin of the GBR shelf typically occurs a number of times during the summer months when calm or northerly wind conditions prevail (Furnas et al. 1990). These upwelling events bring colder, more saline, and nutrient-enriched waters onto the outer shelf where light can penetrate and create suitable conditions for species of phytoplankton to bloom (Furnas & Mitchell 1986). Generally, prochlorophytes (*Prochlorococcus*) dominate the standing oceanic stock in oligotrophic regions (Crosbie & Furnas 2001), but during periods of upwelling, diatoms, and picocyanophytes (*Synechococcus*) can form blooms. Crosbie & Furnas (2001) documented a cross-shelf gradient

in nanoplankton, where the ratio of *Synechococcus* to *Prochlorococcus* increased towards the coast. *Prochlorococcus* was confined to mid-shelf and outer shelf waters. *Synechococcus* was more abundant at most inshore and mid-shelf sites in the central GBR. For a diagrammatical view of plankton distribution in the GBR region, the findings of Revelante et al. (1982), Furnas & Mitchell (1986), Furnas et al. (1990) and Crosbie & Furnas (2001) are condensed into a cross-sectional diagram adapted from Moss et al. (2005).

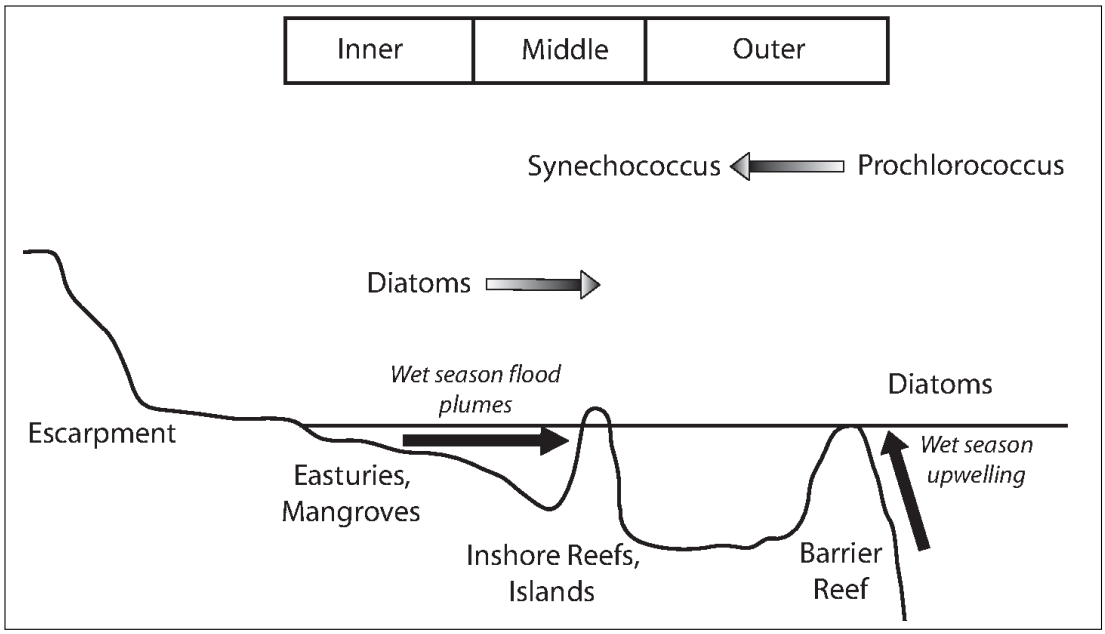

Figure 2.2: Cross section of GBR bathymetric features and generalized phytoplankton distribution. Adapted from Moss et al. (2005).

In addition to living Chl-a, degradation products of the Chl-a molecule also fluoresce and absorb light. These degradation products are operationally classified as phaeopigments, consisting mainly of phaeophytin-a and phaeophorbide-a. These phaeopigments are "produced" by a number of phytoplankton consuming mechanisms; herbivorous zooplankton grazing (Lorenzen & Downs 1986), bacterial and viral infection, periods of prolonged darkness, and nutrient deficiency. Phaeopigments are degraded in the water column by photo-oxidation (Herbland 1988). From the standpoint of ocean colour remote sensors, phaeopigments have similar visible light absorption properties to chlorophyll-a (Roesler et al. 1989), but do not contribute to phytoplankton primary production. Due to the spec-

tral similarities, optical remote sensing researchers often combine chlorophyll-a and phaeopigment concentrations are refer to this quantity as Total Chlorophyll (TChl) (Babin, Stramski, Ferrari, Claustre, Bricaud, Obolensky & Hoepnffner 2003). Both Chl-a and TChl are used throughout this study.

Total Suspended Solid (TSS) is the dried mass concentration of particulate matter suspended in seawater. It is derived from (previously) living phytoplankton, minerals, detritus (previously non-living particulate organic matter) and other particles retained on a filter. In waters of the GBR region, wind-driven resuspension (Larcombe et al. 2001) of sediments and terrestrially-sourced river plumes increase TSS concentration (Devlin et al. 2001). TSS is significant for at least two key reasons; the first is that in turbid coastal waters, TSS strongly influences the light attenuation coefficient of Photosynthetically Available Radiation (PAR) and secchi disk visibility depths (Wolanski et al. 1981, Udy et al. 2005, Cooper et al. 2007). Light is rapidly attenuated in waters with a high sediment load. This is a significant variable that impacts photosynthetic benthic organisms including algae, corals and seagrass which derive their energy from light. Sediment re-suspension events can also be indicative of nutrients reaching surface waters, where the abundance of light and nutrients can support phytoplankton growth (Walker 1981).

The GBR experiences a monsoonal weather pattern with a wet season from December to March, generally bringing north-west winds, higher rainfall and episodic river flood events which deposit terrigenous sediments into coastal waters. During the rest of the year, from May to November, the dry season south-east trade winds predominate (Wolanski et al. 1981). These winds establish northerly along-shore currents and waves which are primarily responsible for re-suspension of fine terrigenous sediments in shallow areas (denoted in green in figure 2.1) and their subsequent northerly transport (Orpin et al. 1999, Larcombe et al. 2001). Wind events are more important than tidal currents for the re-suspension of sediment in inner-shelf regions (Larcombe et al. 2001). The re-suspension of sediment can bring the re-suspension of nutrients and detritus which may have settled out of the water column in between river discharge or

re-suspension events (Devlin & Brodie 2005). In the non-flood conditions of the dry season, rivers become tidal estuaries where the sea water penetrates upstream, and is then mixed back towards the ocean. This mechanism also creates re-suspension and a potential for eutrophication of coastal waters, although wind-wave driven re-suspension dominates tidal re-suspension in this region (Larcombe et al. 2001).

In flood conditions during the tropical wet season, there is an increase in nutrient-rich, turbid and less saline water draining off the land into the coastal region. This fresher, more buoyant and turbid riverine water is usually easily visible with the naked eye amidst the background of less turbid, more saline 'background' coastal waters (Orpin et al. 1999). On the edges of these plumes is a region of diffusion were the fresh water mixes with ocean water, particles settle out of the water column and terrestrially-sourced dissolved materials interact with the saline waters to enhance flocculation and the subsequent removal of sub-micron 'dissolved' particles from the water column. UV light can also break down organic carbon molecules into smaller constituent fragments (Twardowski & Donaghay 2002). Despite flocculation and degradation processes, dissolved nutrients have been found to disperse much further than particulate material during tropical Queensland riverine discharges (Devlin & Brodie 2005). In these coastal regions of the GBR, riverine nutrient inputs can support the growth of larger phytoplankton including diatoms and dinoflagellates (Revelante et al. 1982).

The third water quality component of interest to remote sensors is Dissolved Organic Carbon (DOC). DOC is a heterogeneous mixture of organic compounds (Del-Castillo 2005) which are the degradation products of marine phytoplankton (fulvic) or terrestrial organic matter (humic) (Carder et al. 1989, Mueller & Ayukai 1998, Yacobi et al. 2003). Terrestrial runoff is considered to be a significant contributor to DOC levels in some coastal areas (Bricaud et al. 1981, Boss et al. 2001). The visible light absorbing component of the DOC pool is referred to as Chromophoric (or Coloured) Dissolved Organic Matter (CDOM). Studies in the open ocean indicate CDOM is also produced by zooplankton, *Trichodesmium*

(Steinberg et al. 2004), phytoplankton, bacteria and virii (Siegel et al. 2002). A number of studies have been performed to optically characterise and distinguish between the fulvic and humic CDOM components in coastal areas where a combination is likely to exist (Carder et al. 1989, Twardowski & Donaghay 2001). However, CDOM can be photo-oxidised which makes terrigenous humic acids exhibit optical properties similar to marine-sourced fulvic acids. (Obernosterer & Benner 2004, Twardowski & Donaghay 2002).

Quantitative measurements of TSS, CHL and DOC largely rely on discrete volume water sampling where particles are either concentrated onto (CHL, TSS and Phaeopgiments) or removed by filters (DOC). Inherent in this reductionist approach is the operational distinction between particulate and dissolved components based on the effective pore size of the filter being used. In bio-optical studies, the *dissolved* fraction is usually defined as matter smaller than 0.2 μm (Mitchell et al. 2000, 2003). However, laboratories analysing water samples from the GBR typically use 0.4 μm filters for their DOC measurements due to excessive turbidity increasing the filtering time for samples collected in turbid waters (Boto et al. 1989). In their DOC studies, Boto et al. (1989) found that their choice of the 0.4 μm filters removed 70% of the bacteria from their samples, thus their DOC measurements would be slightly higher than if using the 0.2 μm standard filter size.

The *particulate* fraction is usually defined as particles greater than 0.2 μm although commonly an operational distinction is made by the nominal 0.7 μm effective pore size of a Whatman glass-fibre filter (GF/F) matrix for CHL measurements (Steven et al. 1998). Chavez et al. (1995) determined for a large oligotrophic tropical and sub-tropical latitude range in the Pacific, that photosynthetic pigment concentrations retained on 0.7 μm GF/F filters were consistent with the pigment retention of 0.2 μm membrane filters. Cooper et al. (2007) specifies the retention of a Whatman GF/F to be 0.2 μm. Other researchers claim the effective pore size is between 0.5 and 0.7 μm (Loisel et al. 2009). However, it is likely that the effective pore size is a function of the particle loading on the

filter and possibly also the vacuum pressure (Mitchell et al. 2003). A polycarbonate 0.4 μm (i.e. Nuclepore® or Poretics®) pore size is typically used for TSS measurements in the GBR (Devlin et al. 2001), which should closely match the effective retention properties of GF/F filters. Poretics filters are also recommended for use in the Joint Global Ocean Flux Study (JGOFS) protocols (Knap. et al. 1994). In summary, the dissolved and particulate fractions are operationally defined, and so there may be subtle differences in the results of different researchers using different filter types.

2.1.2 Inherent Optical Properties

2.1.2.1 Radiometric Fundamentals

Light exists as photons which are massless and chargeless 'packets' of energy. The energy of a photon is related to its frequency (ν), according to Eq. 2.1:

$$E = h\nu = \frac{hc}{\lambda}, \tag{2.1}$$

where E is the photon energy (J), h is Planck's constant ($m^2.kg.s^{-1}$), ν is the photon frequency (s^{-1}), λ is the wavelength of the photon in a vacuum (m) and c is the speed of light in a vacuum ($m.s^{-1}$).

When dealing with light measurements and optical properties, it is useful to define some fundamental radiometric and geometric units. These are summarised in Table 2.1. The radiant flux (Φ) is also referred to as optical power, for it is the unit for describing the amount of radiant energy per unit time. A steradian (Ω) is a measure of the proportion of a sphere that is visible by an infinitesimal point at the center of a sphere. It can be determined by $\Omega = \frac{dA}{r^2}$, where dA is the elemental surface area normal to the center of the sphere, and r is the distance from the center of the sphere to the surface. Figure 2.3 shows a hemisphere and an example of the calculation of the solid angle subtended by the elemental surface area dA. Radiance is typically measured with a photodetector which accepts light from a restricted angular field of view (for example, a telescope). Irradiance is typically measured with a photodetector adjacent to a diffuser which serves to

accept light from a full hemisphere. The terms radiance and irradiance do not provide information about the wavelength of the photons in question, however if not specified, usually describes monochromatic light. The terms *spectral* radiance and irradiance describe the spectral nature of the aforementioned quantities.

Quantity	Symbol	SI Unit	Abbreviation
radiant energy	Q	joule	J
radiant flux	Φ	watt	W
steradian	Ω	steradian	sr
radiance	L	watt per square meter per steradian	$W.m^{-2}.sr^{-1}$
irradiance	E	watt per square meter	$W.m^{-2}$

Table 2.1: Fundamental radiometric quantities. (Mobley 1994)

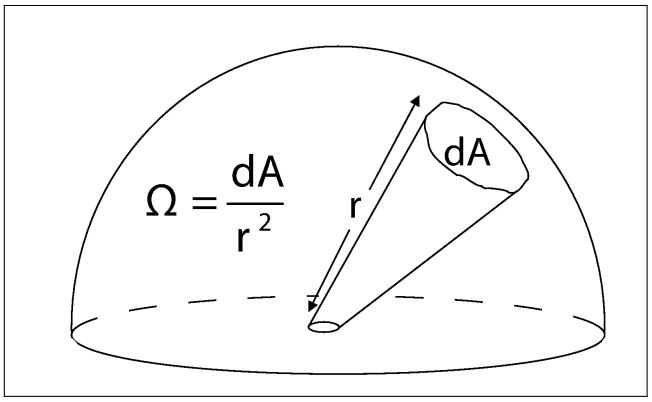

Figure 2.3: The geometry and calculation of the solid angle subtended by the surface area dA, at radius r.

2.1.2.2 Radiative Transfer

Figure 2.4, from Kirk (1983) illustrates the concept of transfer of photon energy (or flux or radiance), through an optically significant medium (the shaded rectangle). Inside the medium, light can be absorbed (removed from the beam) or scattered outside the beam. Scattered light may also re-join the beam to emerge out of the other side of the medium.

Similarly, light photons coming downward from the sun and scattered by the atmosphere can interact with the ocean and its constituents in the same two ways. One interaction is absorption, whereby the photon's energy is converted into another form of energy within the absorbing substance and thus ceases to

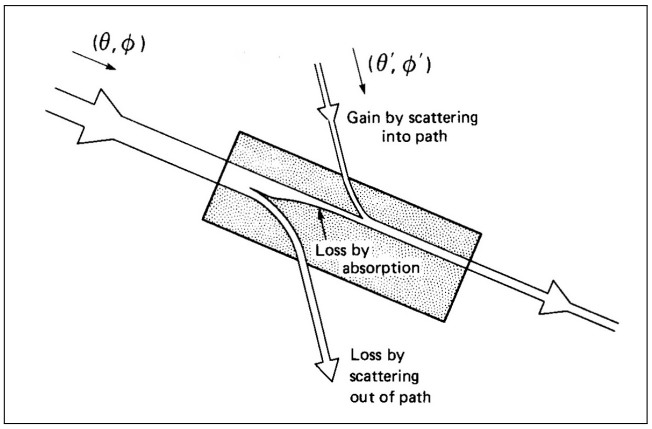

Figure 2.4: Conceptual radiative transfer from the incident photon energy from left to right. Photon energy is removed out of the light path by absorption and scattering (Kirk 1983).

exist as light. The other main interaction is scattering, whereby the direction of the photon's initial trajectory is altered by the medium.

To assist studying these two different optical processes in isolation, Preisendorfer (1976) established the concept of Inherent Optical Properties (IOP); the absorption coefficient (a), the total scattering coefficient (b), the backscattering coefficient (b_b) and the volume scattering function (β). By definition, the IOPs are only influenced by the optically significant substances in the medium and not with the surrounding illumination conditions of that medium. Apparent Optical Properties (AOPs), i.e. satellite-observed ocean colour or diffuse attenuation coefficient (the vertical rate of solar and atmospheric light reduction) are functions of both the IOPs of the substances in the medium and the geometry and structure of the ambient light field (Mobley 1994).

IOPs are generally additive [1], so the total absorption or scattering coefficients of coastal ocean waters can be can be attributed to the sum of the optically or operationally distinct fractions present in the mixture. As an example, the following equations describe the total spectral absorption ($a(\lambda)$) and total spectral backscatter ($b_b(\lambda)$) (scattering in the backwards direction from the initial photon trajectory) of ocean waters as a sum of its broadly-defined optically unique

[1]Provided particles are separated by at least 3X their radii for scattering, and assuming no packaging effect for absorption.

constituents:

$$a(\lambda) = a_w(\lambda) + a_\phi(\lambda) + a_{NAP}(\lambda) + a_{CDOM}(\lambda) + \ldots \tag{2.2}$$

$$b_b(\lambda) = b_{bw} + b_{b\phi}(\lambda) + b_{bNAP}(\lambda) + \ldots \tag{2.3}$$

where the subscripts denote example contributions from water (w), phytoplankton (ϕ), Non-Algal Particulates (NAP) and Chromophoric (Coloured) Dissolved Organic Matter ($CDOM$).

IOPs are wavelength-specific (denoted by (λ) in Eq. 2.2 and 2.3), so spectral observations of the total IOPs may theoretically be decomposed into their separate constituent IOPs if each expected constituent's spectral shape was known *a priori*. This Chapter discusses attempts to measure the spectral shapes of the operationally-defined in-water constituents and their relationship with the water quality parameters namely, TSS, Chl-a (or TChl) and DOC. The significance of this initial Chapter will become apparent in Chapter 3.1 when it is demonstrated that passive multi or hyper-spectral measurements of the AOP remote sensing reflectance (R_{rs}) may be used to determine the water's surface IOPs. This then allows TSS, Chl-a and DOC concentrations to be estimated optically from a remote location.

2.1.2.3 Absorption

When a photon passes within close proximity to a molecule, the molecule may absorb this light energy and retain the energy in another form. Each molecule is able to possess energy in a number of ways. The molecule can be energised to *rotate* about its inertial reference frame, the bonds between atoms in the molecule can be stretched and restored; exhibiting *vibrational* energy, and *electrons* within the molecule can be promoted to higher energy states. Thus an absorbed photon can add rotational, vibrational or electronic energy to a molecule. Quantum mechanics predicts that each of these types of energy expressions may only exist

in discrete or quantised states. So for example, a molecule may only exhibit four different energy rotational states, three different energy vibrational states and six different energy electronic states. These permissible energy levels are dependent on the general structure of the molecule, the types of atoms that exist in the molecule and their arrangement, so each molecule has unique set of energy-level features. If a photon possesses the required energy to excite any of these states from their initial energy levels to a higher permissible energy level, then the photon can be absorbed. The number of possible transitions *within* and *between* rotational, vibrational and electronic[2] modes of a molecule typically results in a broad selection of light energies being absorbed. However, the underlying discrete nature of molecule-specific energy levels can permit the identification of the molecule by just observing the spectral (energetic) nature of light absorption within the medium.

Phytoplankton contain chlorophyll and accessory pigments that exhibit strong absorption around 440 nm and 676 nm. This leads to the absorption of blue and red light, leaving green light to be scattered back to the observer. This absorption and scattering gives rise to the apparent green colour of the ocean during phytoplankton blooms. Due to the complex rotational, vibrational and electronic excitation energy structure of organic molecules, these spectral features are much broader than spectral absorption properties of simpler substances like the metallic atoms inside the chlorophyll molecule.

Fluorescence can sometimes be observed after the process of absorption. Fluorescence refers to the emission of a lower-energy photon of light from the particle, after being illuminated by photons of a higher energy. Fluorescence occurs in substances whose discrete electronic energy levels are spaced sufficiently close so that when electrons make a transition from a high energy state to a low energy state, visible light is emitted. The photosynthetic pigment chlorophyll-a is a fluorescent pigment that absorbs blue light and emits deep-red fluoresced light. Chlorophyll-a fluorescence can be used to quantify chlorophyll-a concentration. The angular

[2]not mentioning other quantum intricacies such as electron spin, nuclear magnetic moments and other interactions outside the scope of this thesis...

distribution of fluoresced light is isotropic. Fluorescence is also sometimes referred to as inelastic scattering, because the original source of the energy is from an incident photon which is absorbed in the process.

2.1.2.4 Scattering

Elastic scattering refers to the re-direction of light from its original path due to inhomogeneities in the medium the light travels through. Scattering interactions are categorised under different names, however they all stem from the same inhomogeneity (Bohren & Huffman 1983).

Consider a stream of photons (light) impinging on a single particle, suspended in water. A portion of the photons will interact with the particle boundary, to be reflected backwards from the original direction of motion. Secondly, a portion of the incident photons will actually enter the particle, and will refract (change direction) when passing though the particle. The angular deflection is described by Snell's Law. Thirdly, a portion of the incident photons will travel very close to the particle edge, and their trajectory will bend or diffract around the edge. The relative probabilities of these interactions depends on the particle size and the relative refractive index between the particle and the medium (i.e. water).
In ocean optics, relative refractive indices of hydrosols are close to unity (Fournier & Forand 1994). This allows Rayleigh-Gans scattering approximation theory to describe and predict scattering for small particles present in the ocean. Fortunately, the scattering of larger spherical particles can be predicted by anomalous diffraction theory based on Huygen's Principle and geometrical optics (van de Hulst 1981).

The most comprehensive scattering parameter is the Volume Scattering Function (VSF), formally defined as the scattered radiant intensity, I (in $W.sr^{-1}$) measured at angle θ from the incident ray, emanating from an elemental volume dV (in m^3) which is being irradiated by irradiance E (in $W.m^{-2}$). The units for VSF

are inverse steradians (sr^{-1}) (Kirk 1983),

$$\beta(\theta) = \frac{dI(\theta)}{EdV}. \tag{2.4}$$

By integration of the VSF, one may determine the two other commonly used scattering parameters; total scattering (b) and backscattering (b_b) respectively,

$$b = 2\pi \int_0^{\pi} \beta(\theta) \sin(\theta) d\theta, \tag{2.5}$$

$$b_b = 2\pi \int_{\frac{\pi}{2}}^{\pi} \beta(\theta) \sin(\theta) d\theta. \tag{2.6}$$

Total scattering refers to light scattered in any direction with reference to the original beam's direction. Backscattering refers to the fraction of light incident on the medium which is scattered in the backward direction, i.e. from 90 degrees ($\frac{\pi}{2}$ radian) to 180 degrees (π radian) away from the original photon direction. The ratio of the backward to total scattering is referred to as the backscattering ratio (unitless),

$$B = \frac{b_b}{b}. \tag{2.7}$$

Another commonly used term is the phase function ($\widetilde{\beta}(\theta)$), which is the VSF normalised by the total scattering. The phase function is expressed in units of sr^{-1}:

$$\widetilde{\beta(\theta)} = \frac{\beta(\theta)}{b}. \tag{2.8}$$

For ocean colour remote sensing applications, backscattering is the most relevant parameter for it is the backscattering process that returns photons from the ocean upward to the satellite (Mobley et al. 2002). As expressed by Gordon et al. (1988) and Lee et al. (1999), the remote sensing reflectance (R_{rs}), is a function of the backscattering coefficient (b_b),

$$R_{rs} \sim f \frac{b_b}{a + b_b}, \tag{2.9}$$

where a is the absorption coefficient and f is considered a constant for the pur-

poses of this section (Chapter 3 deals with determining f and studying any functional dependence). R_{rs} is expressed in units of sr^{-1}.

A number of studies (Oishi 1990, Maffione & Dana 1997, Boss & Pegau 2001, Sullivan & Twardowski 2009, Sullivan et al. 2013) show that due to the consistency of the shape of oceanic VSFs in the backward direction, measuring the VSF at one angle may be sufficient to reliably estimate the backscattering coefficient. Considering the relatively straightforward engineering required to measure scattered light at only one angle, a number of commercially available single-angle backscattering devices exist e.g. the ECO (WET Labs 2005), Hydroscat (HOBI-Labs 2008) and the OBS-3 (D&A 2006).

In situ multiple angle detectors resolving portions of the VSF include the commercially available LISST-100X (0.05 - 14°) (SEQUIOA Scientific 2008) and ECO-VSF (100, 120, and 150°) (WET Labs 2004) instruments. However, these do not cover the entire range of scattering angles from 0 to π radian. Higher angular coverage instruments currently providing the largest angular range *in situ* VSF measurements include the Multi-spectral Volume Scattering Meter (MVSM) (0.6 - 177.3°) (Lee & Lewis 2003) and the Multiple-Angle SCattering Optical Tool (MASCOT) (10 - 170°), (Twardowski et al. 2012), although these instruments are still under development and are not yet commercially available.

2.1.2.5 Practical IOP Measurements

Quantitative optical transmission measurements are perhaps the most conceptually straightforward measurement. Consider a collimated beam of radiant flux (Js^{-1}) incident on a rectangular slab of a particular medium of thickness (dl) as pictured in Figure 2.5. Of the light Φ_0 that impinges on the slab, a fraction Φ_l will be transmitted to the other side of the medium; thus the incident light is attenuated by the medium.

Provided that scattered light is removed from the original beam, and that scattered light does not re-join the original light path, then the attenuation coeffi-

cient c of incident flux described above is expressed mathematically by the Beer-Lambert relationship,

$$\Phi_l = \Phi_0 e^{-cl}, \tag{2.10}$$

where Φ_0 is the incident flux, Φ_l is the transmitted flux, l is the path length of the medium and c (in m^{-1}) is the (beam) attenuation coefficient. Re-arranging Eq. 2.10 determines the beam attenuation coefficient,

$$c = -\frac{\ln(\frac{\Phi_l}{\Phi_0})}{l}, \tag{2.11}$$

where the beam attenuation coefficient consists of the sum of absorption a and total scattering b, namely,

$$c = a + b. \tag{2.12}$$

The Beer-Lambert relationship (Eq. 2.10) is the basis behind spectrophotometery, were radiant flux through a sample is measured by light detectors as either a potential difference in volt or a digitised detector count. In reality, the transmitted radiant flux is difficult to measure directly, requiring an instrument with a stable power supply, lamp of known spectral emission, clean detector optics and regular lamp re-calibration or replacement. To minimise these problems, most spectrophotometers measure radiant flux V_s of the sample of interest relative to a sample blank measurement V_b (usually pure water in the ocean optics field).

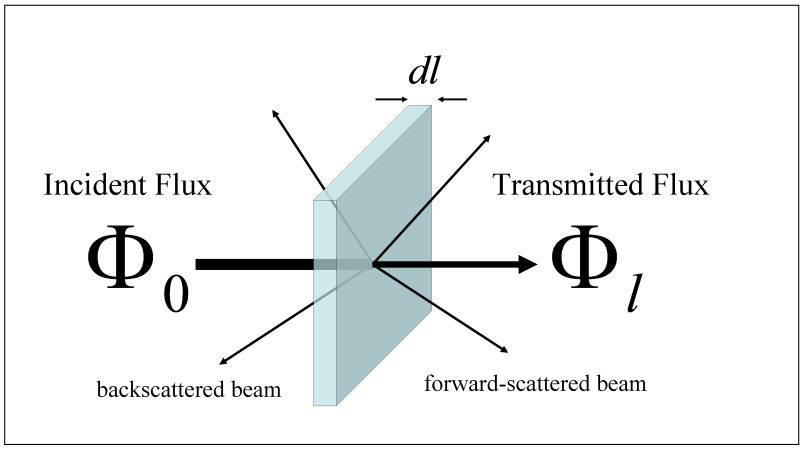

Figure 2.5: Transmission of radiant flux through a slab of known thickness, dl

Dual-beam spectrophotometers perform the blank and the sample measurement simultaneously with two different optical paths and detectors. This requires the use of a pair of matched cuvettes which are optically identical, and a baseline measurement where the two different combined detector responses (V_{0s}, V_{0b}) are measured with both the sample and reference cuvettes filled with the same substance (usually pure water). These four measurements are used to determine c_{pg},

$$c_{pg} = -\frac{\ln(\frac{V_s V_{0b}}{V_b V_{0s}})}{l}, \tag{2.13}$$

where c_{pg} is a commonly used designation in ocean optics to denote attenuation due to particles and gelbstoffe (CDOM), without the pure water contribution, V_s is the voltage measured by the detector for the sample, V_b is the voltage measured by the detector for the blank, V_{0s} is the voltage measured during the baseline scan of the sample path, V_{0b} is the voltage measured during the baseline scan of the reference path, and l is the optical path length.

It should be noted that the dual beam reference spectrophotometer technique measures attenuation above that of the instrument blank (in this case pure water, c_w). Determining the total attenuation c from c_{pg} requires the addition of the attenuation of pure water, which is documented by Pope & Fry (1997) and Mitchell et al. (2003).

The transmission configuration is also used to determine the absorption of a medium. As the photodetector needs a finite collection area to receive photons in any instrument setup, these instruments will always collects a fraction of the near forward scattered light. For measuring absorption, the photodetector geometry is optimized to capture as much of the scattered light as possible, with the goal of reducing b in Eq. 2.12, and/or accurately estimating it. This procedure involves some or all of the following steps: 1) placing the sample as close to the detector as possible (Mitchell et al. 2000), 2) using a diffuser in front of the detector to capture scattered light (Yentsch & Phinney 1989), and / or 3) using a reflective cuvette to re-direct scattered light towards the detector (Zaneveld et al.

1994). Once these efforts have been implemented, then various assumptions can be applied to remove the residual scattering from the measurement to yield an absorption coefficient. These assumptions are discussed in Zaneveld et al. (1994), McKee et al. (2008) and are addressed later in the dissertation, specific to my methodology.

To detect scattering, instead of placing a detector in-line with the incident beam as in the transmission configuration, off-axis radiance detectors are placed relative to the incident beam in order to capture scattered light emanating from the sample volume. If the incident irradiance (E) and scattering sample volume (dV) are known, then by using Eq. 2.4, a measurement of the scattered radiant intensity dI can yield a scattering measurement $\beta(\theta)$. Typically, the geometry of off-axis scattering detectors and divergent light sources makes the product (EdV) difficult to determine analytically. However, instrument manufacturers empirically calibrate their instruments in order to determine a scaling factor which relates detector counts directly to $\beta(\theta)$ (Sullivan et al. 2013).

2.2 Materials and Methods

2.2.1 Sampling Summary

Collecting data for developing an algorithm suitable for applying to satellite images of the whole GBR region across different seasons is a challenging task. In an attempt to represent the water quality and optical conditions experienced across the GBR over seasons, effort was made to sample as widely as possible and as frequently as possible. Field trips were conducted on research vessels across a large section of the Queensland coastline on alternate dry/wet season regimes, (see Figure 2.6 and Table 2.2).

2.2.2 Water Quality

At each station, a series of Niskin water sampler bottles were used to collect water from multiple depths. Surface waters $<2\ m$ were always sampled and samples were usually also taken from mid-water column depth in coastal waters (varying from 6 to 15 m depth). Water was immediately drawn from the Niskin bottles to prepare sub-samples for analysis.

For chlorophyll-a measurement, duplicate water samples were drawn from Niskin bottles into sample-rinsed 250 ml measuring cylinders. These samples were filtered through pre-combusted 25 mm Whatman GF/F filters at low vacuum. Filters were then folded in half (towards the particle-laden side), wrapped in pre-combusted aluminium foil, labeled and stored at -20 $°C$. Chlorophyll a and phaeopigment concentrations were determined by fluorometry with a Turner 10AU fluorometer after a dark extraction in 90% acetone and acidification with 0.1 M HCl (Parsons et al. 1984). Filter pads were ground to assist the extraction process. Fluorescent standards were analysed by spectrophotometry using the equations of Jeffrey & Humphrey (1975). The sum of the chlorophyll-a plus phaeopigment will be referred to herein as TChl (Babin, Stramski, Ferrari, Claustre, Bricaud, Obolensky & Hoepnffner 2003).

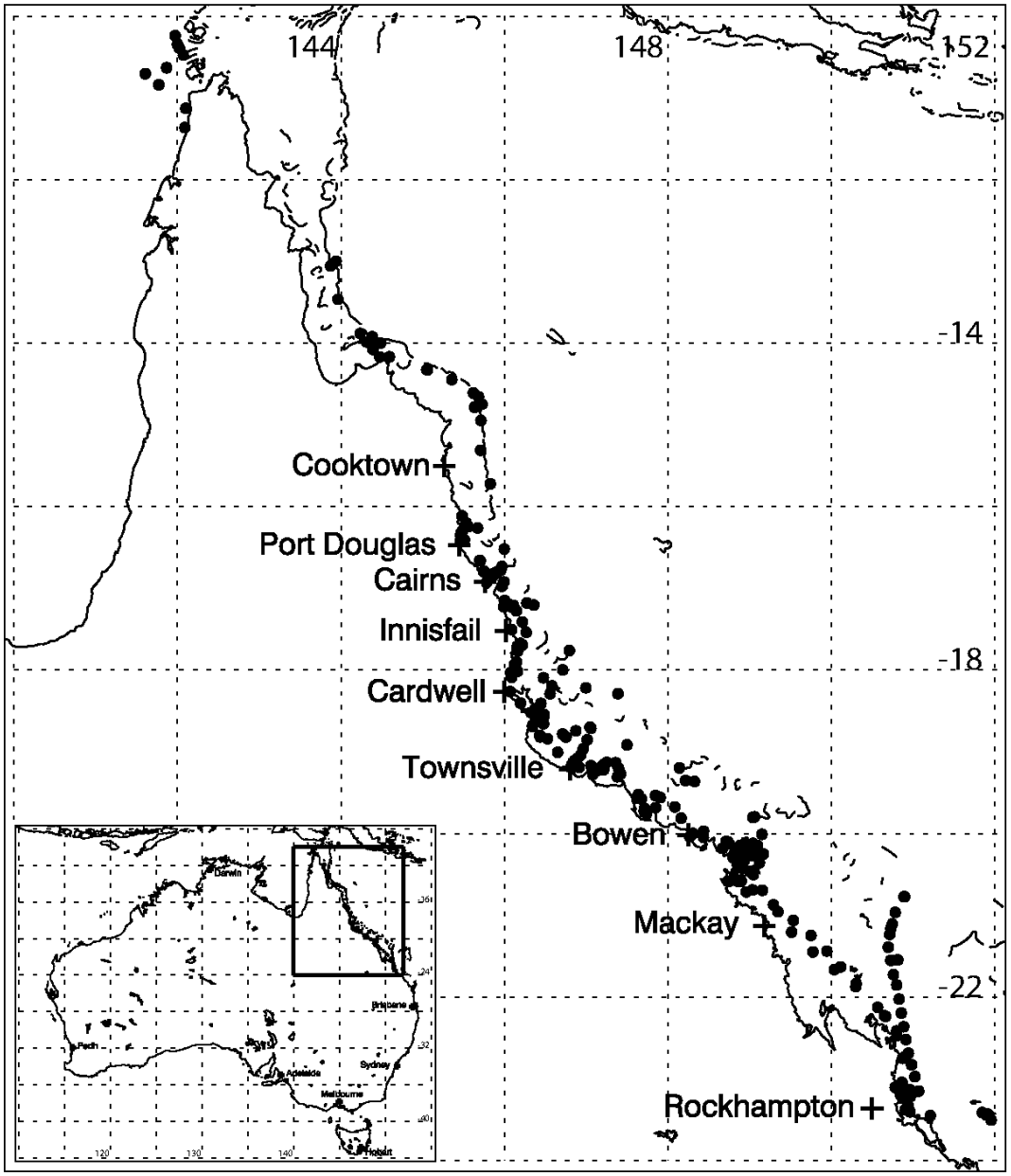

Figure 2.6: Region of interest and the 339 sampling sites shown with black circles. Not all parameters of interest were able to be measured at all sampling sites.

Trip	Year	Month	Season	Rainfall	# Stations	a_{phi}	a_{CDOM}	a_{NAP}	b_b	TChl	TSS	DOC	SAL	TEMP
SAT*	2002	Oct	Dry	none	16	-	-	-	yes	yes	yes	yes	yes	yes
POM	2004	Aug	Dry	none	37	-	yes	-	-	yes	yes	yes	yes	yes
INN	2005	Jan	Dry	none	8	yes	yes	yes	-	yes	yes	-	yes	yes
CNS	2005	Jan	Dry	minimal	9	yes	yes	yes	-	yes	yes	-	yes	yes
KBY	2005	Feb	Wet	none	24	yes	yes	yes	-	yes	yes	-	yes	yes
WQNa	2005	Aug	Dry	none	29	yes	yes	yes	yes	yes	yes	yes	yes	yes
WQSa	2005	Aug	Dry	minimal	19	yes	yes	yes	yes	yes	yes	yes	yes	yes
FNQ**	2005	Nov	Dry	none	9	yes	-	yes	-	yes	yes	-	yes	yes
WQNb	2006	Jan	Wet	minimal	47	yes	yes	yes	yes	yes	yes	yes	yes	yes
WQSb	2006	Jan	Dry	minimal	58	yes	yes	yes	yes	yes	yes	yes	yes	yes
WQMa***	2008	Feb	Wet	floods	36	-	yes	-	-	-	-	yes	yes	yes
UWF***	2008	Feb	Wet	floods	22	-	yes	-	-	-	-	yes	yes	yes
WQMb***	2009	Feb	Wet	floods	25	-	yes	-	-	-	-	yes	yes	yes

Table 2.2: Field trip data collection showing trip identifiers, time of year, season, recent rainfall, number of stations sampled and when IOP, water quality, salinity (SAL) and temperature (TEMP) measurements were made. * Denotes where optical data was provided by Kadija Oubelkheir (CSIRO). ** Denotes where optical data was provided by Leon Majewski (Curtin). *** Denotes trips where optical data was provided by (McKinna 2008) (AIMS/JCU).

For TSS measurement, 0.4 μm pure polycarbonate (Poretics®) membrane filters were prepared prior to fieldwork by drying them overnight at 60 °C, and then pre-weighing them on a 0.01 mg precision balance. During fieldwork, duplicate water samples were drawn from Niskin bottles into volume-marked 1 litre High Density Polyethylene (HDPE) bottles which were pre-rinsed with sample water. These bottles were inverted directly over the filtering funnel containing the pre-weighed filter. This allowed any heavier particles to end up on the filter, rather than being stuck on the side of the sample bottle, and also protected the sample from airborne particle contamination. The filters were not rinsed to remove salts; however, filtered seawater blanks were prepared to quantify the small mass of salt in the water retained on the membrane filters. The particle-laden filters were folded in half and stored in clean, pre-combusted glass scintillation vials. Upon returning to the laboratory, filters were dried overnight at 60 °C, and then post-weighed on the same 0.01 mg precision balance.

DOC samples were drawn from Niskin bottles into a sample-rinsed HDPE syringe and 10 ml samples filtered via a 0.45 μm Sartorius Minisart cartridge into sample-rinsed 12 ml plastic tubes. Samples were acidified with 100 μl of AR grade 12N HCl and refrigerated for no longer than three weeks before analysis with a SHIMADZU TOC-5000A Analyser.

Whilst at station, Secchi disk measurements were made. A solid white disk of 30 cm diameter was lowered vertically into the water column with a rope. The depth at which the Secchi disk was no longer visible by the observer was recorded. Multiple observers were used for this data set.

2.2.3 Conductivity, Temperature and Depth (CTD) Package

The combination of simultaneously acquired conductivity, temperature and depth (CTD) measurements is extremely valuable for identifying different water masses. The conductivity and temperature measurements are combined to determine the

salinity of the water mass which is useful for identifying the presence of riverine inputs. The CTD instruments used in this study were equipped with optical instruments including a pumped WET Labs chlorophyll fluorometer, beam transmissometer (see attenuation section 2.1.2.5) and a Biospherical Photosynthetically Active Radiation (PAR) scalar irradiance sensor. At nearly all stations visited, a CTD cast was initially performed to classify the physical conditions for that station. Upon station arrival, the CTD package was lowered into the water just below the surface where it was allowed to equilibrate for approximately 1 minute. After this time, the CTD was lowered into the ocean at 1 ms^{-1}. The CTD was preset to average eight individual CTD measurements and store the result to the internal data file at 4 Hz. The deepest depth sampled depended on the site. In shallow coastal waters the CTD was lowered to within a few meters of the bottom. In deep oceanic waters, CTD profiles were limited to approximately 300 m.

All CTD data was post-processed to remove near-surface data taken during the equilibration period after immersion. Wherever a discrete water sample was taken, all CTD data within $\pm$ 0.5 m of the bottle depth was extracted, averaged and stored for comparison with water quality measurements. For surface water sampling, all CTD data between approximately 0.5 m and 1.5 m deep was extracted for comparison with laboratory analysis of the discrete water sample from the surface Niskin bottle.

2.2.3.1 CTD Optical Instrument Calibration

The performance of *in situ* optical instrumentation, including the beam transmissometer, chlorophyll fluorometer and optical backscatter sensor can be affected by ambient temperature and pressure, descent or flow rate, bio-fouling and the accumulation of grime when not in use. Changes in sensor sensitivity or performance may also change in time due to optical alignment or semiconductor detector sensitivity degradation. To counter these potential issues, CTD optical data was post-calibrated when possible with *in situ* field samples on a per-trip basis. All of the optical instruments used on the CTD profilers produce an analog

voltage in response to various water quality parameters, which is recorded by the data-logger in the CTD. These voltages are converted to engineering units (i.e. chlorophyll concentration, Nephelometric Turbidity Units (NTU) etc.) via two coefficients, a linear slope (sometimes referred to as a gain or multiplier) and an offset (or dark current) coefficient.

The Wet Labs Wetstar fluorometer uses Equation 2.14;

$$Engineering\,Units = (Voltage - Offset) \times Slope. \tag{2.14}$$

The NTU sensors and transmissometers use Equation 2.15:

$$Engineering\,Units = (Slope \times Voltage) + Offset. \tag{2.15}$$

For the benefit of potential users of these optical instruments and to monitor instrument stability over time, slopes and offsets were determined from raw voltages and expressed in the relevant formats used in 2.14 and 2.15 so these newly derived coefficients can be added to the respective CTD package configuration files for automatic processing by the CTD software. Table 2.3 shows the older calibration information for the sensors.

Package	Instrument	Slope	Offset	Units	Date
SBE25	OBS SN1046	200	0	NTU	18/6/1997
SBE25	Wetstar WS3S-163	0.332	0.057	μg^{-l}	27/6/1996
SBE25	Trans 105/2894/045	26.9370	-0.2690	%	3/7/1996
SBE19+	OBS SN2169	400	0	NTU	4/9/2003
SBE19+	Wetstar WS3S-948P	15	0.065	μg^{-l}	17/3/2003
SBE19+	C-Star CST-653PR	20.0338	-1.1019	%	14/3/2003

Table 2.3: Pre-existing CTD Factory calibration information.

In the case of the transmissometer used on the SBE25 CTD profiler, the manufacturer-provided calibration values gave transmissions in excess of 110 % in some of the lagoon and reef matrix waters sampled - a physical impossibility. The original factory transmissometer calibration was intended to read somewhere between 90.2 and 91.3 percent for a 0.25 m path-length 660 nm transmissometer (SBE 2003) in

water, because the transmission is referenced to air. Non-physical transmissions in excess of 110%, roughly 20% greater than the theoretical maximum transmissions recorded was cause to re-evaluate the calibration of the transmissometer.

In order to calibrate the beam transmissometers, ideally they would be cleaned and then their detector voltages would be recorded whilst immersed in pure water. Additionally, the "dark" voltage should be measured; the response of the detector with the detector lens occulted from any light source. If the electrical engineering is decent, the dark current voltages should not fluctuate appreciably from the factory defaults. During the field campaign, pure water immersion is impractical. However, there were regions in the GBR where the deep water around 200 m should be clear enough to approximate the pure water response of the transmissometer. For each transmissometer, the maximum recorded voltages were used as the pure water reference, so transmission is determined by Eq. 2.16:

$$T = \frac{V_m - V_d}{V_{clean} - V_d}, \tag{2.16}$$

where T is the transmission, V_m is the measured voltage, V_d is the factory measured dark voltage and V_{clean} is the highest measured voltage in clear waters.

The newly derived calibration values for the beam transmissometer are shown in Table 2.4, however potential users should be aware that these values are now referenced to very clear sea water, not air, thus beam attenuation coefficients derived from the new transmission coefficients will be slightly underestimated and will only be due to particles and dissolved substances, c_{pg}. Additionally, c_{pg} measurements are dependent on the acceptance angle of the transmissometer being used (Boss et al. 2009). The beam attenuation coefficient of water at 660 nm, approximately 0.364 m^{-1} (Pope & Fry 1997, Pegau et al. 2002), can be added if total beam attenuation is required. The magnitude of the underestimation of c_{pg} may be roughly estimated by observing the y-intercept between a plot of c_{pg} and TSS [3]. Figure 2.7a and b shows the beam attenuation coefficient of particles and dissolved substances versus TSS for all non-surface samples at all locations. Sur-

[3]Although CDOM and particle composition will subtly influence the y-intercept

face bins of CTD data were highly variable, presumably due to surface bubbles and so were left out of this scatter-plot and regression. Additionally, data from the KBY stations was left out due to noticeably dirty optical windows.

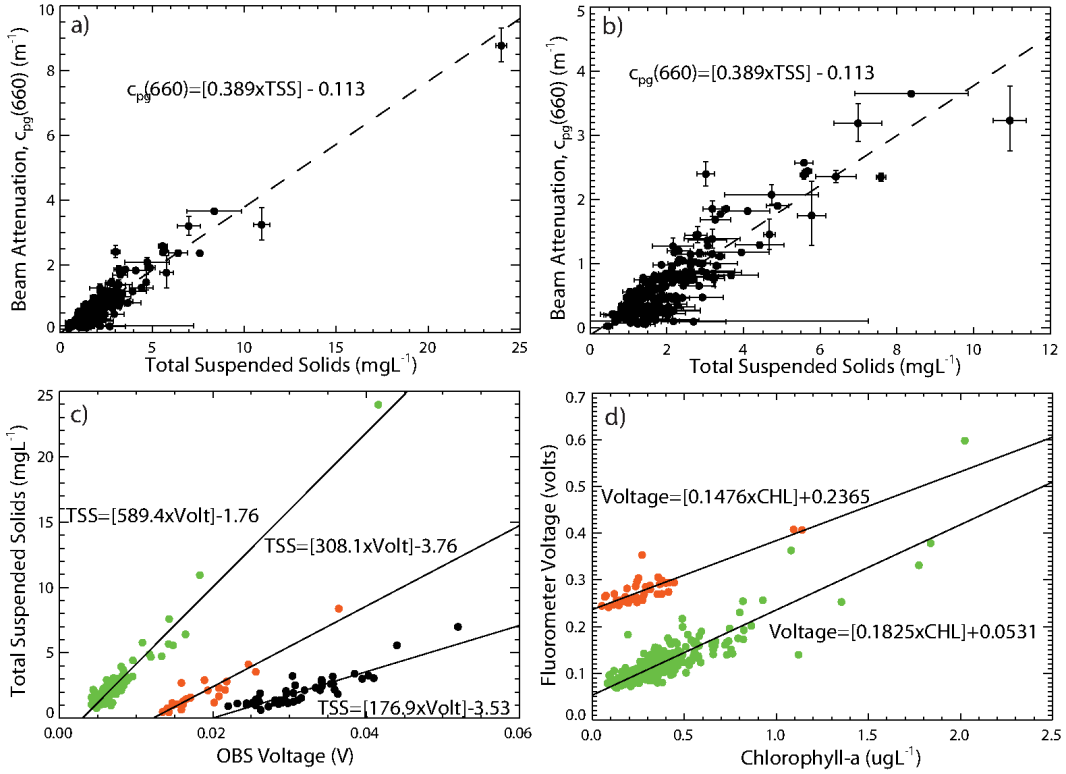

Figure 2.7: a) Beam attenuation coefficient at 660 nm versus TSS. b) Data as in a), but re-scaled. c) Total Suspended Solids versus OBS sensor voltage responses, (from left to right) SBE19+, SBE25 in 2002 only, SBE25 from 2004-2006. d) Wet-star Chlorophyll Fluorometer voltage versus discrete chlorophyll analysis (SBE25 in 2002 upper, SBE19+ 2004-2006 lower

The integer OBS sensor calibration slopes in Table 2.3 (200 and 400, respectively) imply no calibration is performed on individual sensors unless electronic calibration is done by the manufacturer, and the zero offset implies that the dark current of the semiconductor light detector used in the OBS sensor is non-existent. Additionally, the engineering units for this 'calibration' are NTU, which should strictly apply only to measurements made at right-angles from the incident beam. This is probably not the case, so the NTU calibration is considered suspect and is instead calibrated in terms of total suspended solids concentrations measured *in situ*.

Figure 2.7c shows three distinct populations of TSS versus OBS voltage relationships. From what information is available, the two rightmost relationships come from the same instrument (SN1046) on the same sensor package, but were collected over different years. This highlights the importance of maintaining CTD documentation to end users or performing regular in-house calibration exercises to monitor changes to the responsivities over time. Fortunately, in this case, we see clearly defined differences which allow suitable calibration equations to be developed for particular time periods. These are given in Table 2.4

The chlorophyll fluorescence response as a function of chlorophyll concentration is highly variable, both within regions and within species under different light regimes. It is desirable that the fluorescence response is calibrated with field samples of the water where the chlorophyll fluorometer is used. Figure 2.7d shows the *in situ* data set used for calibrating the chlorophyll fluorometers.
The chlorophyll fluorometer on the SBE25 profiler did not show any significant correlation with discrete chlorophyll measurements in 2006, and so this data was discarded from the calibration data set.

Package	Instrument	Slope	Offset	Units	Date
SBE25	OBS SN1046	308.119	-3.75861	mg^{-l}	2002 only
SBE25	OBS SN1046	176.910	-3.52525	mg^{-l}	2004-2006
SBE25	Wetstar WS3S-163	0.147556	0.236532	μg^{-l}	2002 only
SBE25	Trans 105/2894/045	24.1820	-0.0412963	percent	2002-2006
SBE19+	OBS SN2169	589.415	-1.75550	mg^{-l}	2004-2006
SBE19+	Wetstar WS3S-948P	0.182506	0.0531380	μg^{-l}	2004-2006
SBE19+	C-Star CST-653PR	21.9573	-0.250496	percent	2004-2006

Table 2.4: New CTD Calibration information - note transmissometers are now referenced to read 100 percent in pure water, not air

2.2.4 IOPS

2.2.4.1 Dissolved Absorption

CDOM absorption measurements were made with either a benchtop spectrophotometer or a submersible mutli-wavelength absorption and attenuation meter (WET labs ac-9) with a 0.2 μm pre-filter. For benchtop measurements, 200

ml sea water samples were taken for CDOM absorption measurement, drawn from a Niskin bottle into a sample-rinsed syringe and then filtered via a 0.45 μm Minisart® cartridge into HCl-washed and sample-rinsed Teflon bottles. For physical consistency, the 0.45 μm pore size was chosen to match the filter used for the the Dissolved Organic Carbon (DOC) sample (Schaffelke et al. 2011). Additionally, this 0.45 μm nominal particle size cutoff complements the GF/F particulate measurements, which retain particles larger than 0.5 - 0.7 μm (discussed previously).

To avoid issues with sample degradation, samples were either stored at room temperature for no longer than two hours before measurement, or stored in refrigeration overnight and then allowed to equilibrate in room temperature for up to 2 hours. All samples were drawn in subdued lighting and stored in the dark until measurement with the spectrophotometer. Matched 10 cm path-length quartz cuvettes were used in a 2 nm bandwidth dual beam Shimadzu UV-Vis 1601 spectrophotometer or a 1 nm bandwidth Shimadzu Pharmaspec 1700 spectrophotometer. The optical density of the sample was measured from at least 400 nm to 800 nm, recording in 1 nm steps. Reference water was fresh Milli-Q created on demand at ambient laboratory temperature from a Nanopure system with reverse osmosis source water and filled directly into the Milli-Q rinsed cuvettes. A spectrophotometer baseline correction spectrum was collected with two pure water references for every new measurement session. For most CDOM measuring sessions, a spectrum 'blank' was acquired immediately after the baseline correction spectrum was collected to ensure the accuracy of the baseline measurement. These initial 'blank' spectra were recorded to monitor the magnitude of the instrumental noise. To monitor any instrumental drift or to identify effects of possible reference contamination during the initial baseline scan, an additional 'blank' reference scan was often performed towards at the end of measuring sessions. When available, this final 'blank' spectrum was subtracted from the measurements for that recording session.

A small subset of CDOM absorption measurements were performed with a WET Labs ac-9 submersible spectrophotometer with a 0.2 μm Pall® pre filter. With

the ship stationary, the ac-9 was initially submerged at 3 m to purge bubbles from the flow tubes and optical pathlength. The system was then raised to approximately one meter below the surface and allowed to equilibrate with the water for one to two minutes. Vertical profiles were made with a slow decent rate of approximately half a meter per second. Upcast data was discarded, and cast data was binned to provide averaged data at nominal depths co-incident with Niskin bottle DOC samples. The median of ac-9 data within each bin was used for further analysis.

For CDOM measurements, the raw optical densities measured by the dual beam spectrophotometer were converted into absorption coefficients by:

$$a'_{CDOM}(\lambda) = \frac{2.303}{l}\, OD_s(\lambda), \tag{2.17}$$

where $a'_{CDOM}(\lambda)$ is the raw CDOM absorption (m^{-1}), l is the cuvette length in meters and $OD_s(\lambda)$ is the optical density of the sample as measured from a dual beam spectrophotometer (negative log base 10 of the transmission).

The ac-9 is calibrated in Napierian (absorption (m^{-1})) coefficients, and so ac-9 data did not need to be converted prior to the null point correction.

Despite the fact that CDOM samples are filtered with a 0.45 μm filter, and are considered to be wholly comprised of dissolved material, scattering errors may still be present in 'dissolved' absorption measurements. This error is introduced when a fraction of light incident on the spectrophotometer sample is not detected by the spectrophotometer, and is attributed erroneously to sample absorption. This effect is usually corrected by subtracting a spectrally constant null-point value from each measurement. Due to the widely-observed exponential spectral shape of CDOM absorption in the visible, a Near Infra-Red (NIR) null point wavelength is recommended (Mitchell et al. 2003), where sample absorption is assumed to be zero. This widely used scattering correction assumes that the optical density at the chosen null point is due entirely to scattering in the medium, and that the scattering of light is wavelength independent. This is known not to be the

case for scattering from particles with a size similar to the wavelength of light (van de Hulst 1981); however the actual light lost is usually small relative to the magnitude of the desired absorption signal in the visible and NIR regions, so this simple correction is routinely applied. Due to the different concentrations and variable nature of CDOM in coastal waters, the exact wavelength of the null-point correction is left to the researcher's discretion (Mitchell et al. 2003), and thus can introduce some methodological variability in the reported absorption coefficients and downstream derived products. In addition, spectrophotometric absorption measurements in the NIR region are extremely susceptible to sample-reference temperature and salinity difference-related variability during measurement. This variability would increase the uncertainty of the overall determined absorption coefficients if the NIR region is not chosen carefully (Mitchell et al. 2000). Fortunately, studies have been performed to document the temperature-specific absorption coefficients (Langford et al. 2001) and salinity-specific absorption coefficients of water (Sullivan et al. 2006, Pegau et al. 1997), which would allow for a better null-point wavelength decision to be made.

In this study, the null point was calculated from the average raw CDOM absorption (a'_{CDOM}) measured at 715, 725 and 770nm. Using these three data points in determining the null point value minimizes the influence of instrumental noise on the result, and these wavelengths were selected for minimal temperature and salinity effects based on the aforementioned studies. The null point corrected CDOM absorption spectrum was determined by:

$$a_{CDOM}(\lambda) = a'_{CDOM}(\lambda) - \left(\frac{a'_{CDOM}(715) + a'_{CDOM}(725) + a'_{CDOM}(770)}{3} \right). \tag{2.18}$$

Figure 2.8a shows a number of spectrophotometer scans performed with Milli-Q reference water sample in the cuvette, made over time throughout a normal spectrophotometric measurement cycle, in between baselines. To estimate the spectrophotometer uncertainty, these scans were averaged to determine a mean and a standard deviation spectrum. The mean spectrum represents the average spectral bias exhibited during the measurement process due to consistent base-

line drift, and the standard deviation spectrum shows the spectral nature of the uncertainty which could be likened to the detection limit. Figure 2.8b shows the near-zero average spectral bias and the baseline uncertainty spectrum. To determine the overall uncertainty of a CDOM measurement for use in proceeding plots and calculations, the baseline uncertainty (Figure 2.8b) is added to standard deviation of the 3 different wavelengths (715,725,770) used for each scan's null point correction. The order of magnitude is comparable to the detection limits of other researchers (Bricaud et al. 1981, Carder et al. 1989, Warnock et al. 1999).

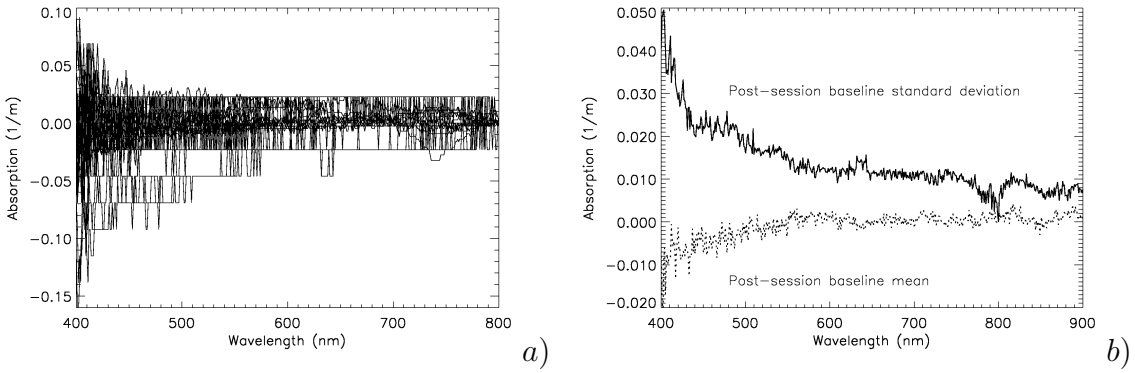

Figure 2.8: a) CDOM blank set spectra b) Post-session CDOM blank average (spectral bias) and standard deviation (detection limit).

2.2.4.2 Particulate Absorption

To determine the absorption of suspended particulates, particulate matter in sea water was concentrated onto GF/F filters and then measured using the quantitative filter technique (QFT) (Mitchell et al. 2000, 2003) with the Shimadzu 1601 bench-top spectrophotometer. Depending on the particle load, between 250 ml and 2000 ml of sample was filtered under vacuum pressures less than approximately 25 kPa to minimize cell rupture. Filter funnels were rinsed with approximately 20 ml of 0.45 μm filtered seawater to include particles adhering to the sides of the apparatus. Sample filter pads were either stored flat on clean and dry plastic petri-dishes in a dark refrigerator for no longer than 4 hours prior to measuring, or stored in 1 cm diameter cryogenic vials which were immediately placed in liquid nitrogen and stored for less than one month.

A specially designed filter holder was inserted into the Shimadzu UV-Vis 1601 dual beam spectrophotometer's optical path to position the filter pads as close as possible to the detectors (see Figure 2.9). The filters sat on very thin glass cover slips so that the particle-laden side was facing the detector.

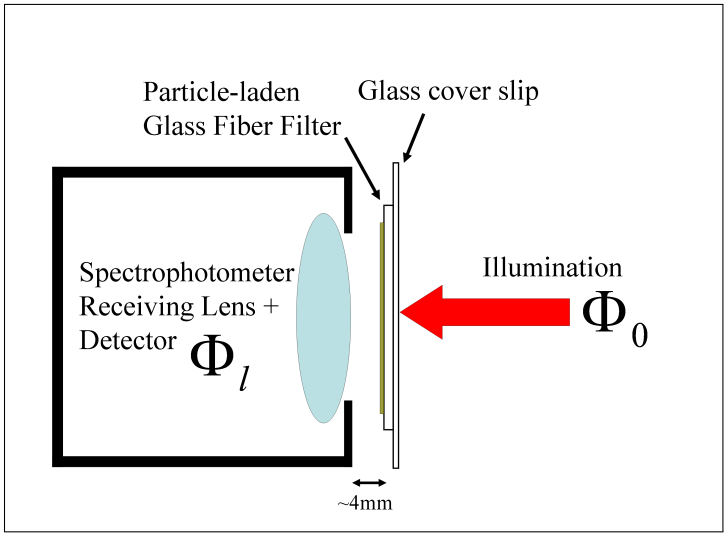

Figure 2.9: Filter pad position with respect to the spectrophotometer window

Before every measurement, the filter/glass interface was inspected for excess moisture, and was corrected if necessary by removing the filter and delicately blotting absorbent, lint-free tissue on the glass mounting surface. A set of blank refer-

ence filter pads were soaked in 0.45 μm Filtered Sea Water (FSW) for 4 hours in the dark, and spectrophotometric baseline correction spectra were acquired with two pre-soaked blank filter pads. After the baseline was collected, reference filter blanks were measured as samples to determine the baseline flatness. By observing repeat spectrophotometric measurements of the same filter pad after successive removal and re-mounting, it was visually determined that optical density measurements performed at wavelengths greater than 920 nm were non-zero and inconsistent. The cause of the inconsistency was possibly due to the large absorption coefficient of water in this spectral region (Langford et al. 2001), combined with the subtly varying thickness of the moist filter pad medium after successive re-mounting. Each sample was scanned from 400 nm to 900 nm, and the absorbance was recorded at 1 nm intervals.

To differentiate between the total particulate absorption due to the phytoplankton and other detrital or mineral particles on the sample filter, the particulate sample was removed and bleached of algal pigments, and then re-measured as the non-algal fraction of the initial sample (referred to herein as Non-Algal Particulate (NAP)). A variety of solvents were initially tested to remove the phytoplankton pigments from the filter pads including methanol, acetone, ethanol and sodium hypochlorite (bleach) solution. Each solvent was evaluated based on their ability to remove the signature phytoplankton chlorophyll absorption peak at 676 nm and *Trichodesmium* pigments after a 30 minute soaking period followed by rinsing with 30 ml of 0.45 μm filtered sea-water. The sodium hypochlorite solution is inexpensive and removed the absorption effects of both regular phytoplankton and *Trichodesmium* rapidly. Repeat trials showed that a double 5 minute soaking treatment of 5 ml 10% NaClO solution was effective in removing the optical effects of phytoplankton photosynthetic pigments, as other researchers reported (Tassan & Ferrari 1995). This treatment became the routine pigment removal method for this study, and blank filters were prepared with the same bleaching and rinsing regimen to compensate for residual NaClO on the filters.

Each scan (total particulate (p) and Non-Algal Particulate (NAP)) was converted

from optical density into absorption coefficients as described in Mitchell et al. (2003). i.e.

$$a_p = \frac{2.303 A_f}{\beta_f V_f}[OD_{fp} - OD_{null}], \tag{2.19}$$

$$a_{NAP} = \frac{2.303 A_f}{\beta_f V_f}[OD_{fp} - OD_{null}], \tag{2.20}$$

where A_f is the filter pad collection area (based on vernier caliper diameter measurements), V_f is the volume of seawater passed through the filter, OD_{fp} is the optical density of the sample filter pad (relative to a FSW moistened filter pad), OD_{null} is the estimated scattering error of the sample, and β_f is the pathlength amplification factor of the filter matrix; initially set to $\beta_f = 2$ (Roesler 1998).

The phytoplankton absorption $a_\phi(\lambda)$ can be estimated from the additive nature of IOPs:

$$a_\phi(\lambda) = a_p(\lambda) - a_{NAP}(\lambda). \tag{2.21}$$

In addition to the routine Transmission QFT particulate measurement described above and in Mitchell et al. (2000, 2003), a variation was performed to investigate the implications of conclusions made by Tassan & Ferrari (1995) for particles from turbid coastal waters of the GBR. They assert that sample backscattering from "high" concentrations of suspended inorganic particles leads to spurious absorption in standard transmission QFT measurements. To determine whether inorganic sample backscattering or increased path length affected the standard transmission measurement-derived phytoplankton absorption (the result of Eq. 2.21), a simple Dual Filter measurement protocol was established. This protocol attempted to match the sample and reference inorganic sediment content to provide phytoplankton absorbance data. Duplicate filter pad samples were collected, filtered and stored as described previously. The modified QFT measurements consisted of scanning both particulate sample filters (P1 and P2) with a FSW moistened filter blank as reference, bleaching and measuring the first bleached filter (NAP1) with a FSW moistened filter blank, and then measuring the unbleached sample (P2) with the bleached sample as the reference. The unbleached sample was then bleached and measured relative to a FSW moistened filter blank. To correct for differences between the duplicate filter samples non-algal loading,

the second bleached filter was measured relative to the first bleached filter. The measurements performed per station are outlined in Table 2.5:

Scan	Sample	Reference
1	P1	blank
2	P2	blank
3	NAP1	blank
4	P2	NAP1
5	NAP2	blank
6	NAP2	NAP1

Table 2.5: Dual Filter measurement procedure.

Considering the dual-beam spectrophotometer's reference was chosen to be a FSW-moistened filter pad which should closely match the particle laden filter pad, any signal measured by the spectrophotometer should be due to the sample alone. In the standard QFT or dual-sample methods based on spectrophotometry (i.e. Eq. 2.19), it was necessary to estimate the magnitude of the spectrophotometric scattering error for each sample ($OD_{null}(\lambda)$). The scattering error may be estimated from the $OD_{fp}(\lambda)$ measurement by relying on two assumptions. The first is that there is negligible non-algal particle / mineral absorption in the NIR (Babin & Stramski 2002, 2004), so in this region $OD_{fp}(NIR)$ consists entirely of scattering error (i.e. $OD_{fp}(NIR) \approx OD_{null}(NIR)$). The second assumption is that the spectral properties of scattered light in the visible and NIR regions follow a power-law function (as theoretically determined for a Junge-type seawater constituent population) (Forand & Fournier 1999, Twardowski et al. 2001, Doxaran et al. 2007). By fitting a power law function (parameters A and K in Eq. 2.22) to the measured $OD_{fp}(\lambda)$ spectrophotometric optical density measurements from 750 nm to 920 nm, a full-spectrum scattering error estimate can be made by extrapolation:

$$OD_{null}(\lambda) \approx A\lambda^{-\gamma_b} + K, \tag{2.22}$$

where λ is the wavelength, γ_b is the hyperbolic slope of the particulate scattering spectrum ($b_p(\lambda)$), A is the amplitude proportional to the pathlength amplification factor and the magnitude of scattering, and K is a linear offset proportional to

spectrally-independent differences between the baseline and the sample OD. A and K are model fit parameters based on $OD_{fp}(NIR)$ measurements.

A similar NIR-to-visible extrapolation was performed by Dall'Olmo & Gitelson (2006), however they used a linear spectral dependency which does not have a theoretical basis unlike the power-law function.

It is important to note that $a_\phi(\lambda)$ as determined with this de-pigmentation methodology does not discriminate between living and detrital algal pigments (phaeopigments). Distinction between these two pigment sets is necessary if more precision is required in using remote sensing to estimate primary production. Thus,

$$a_\phi(\lambda) = a_{\phi_{living}}(\lambda) + a_{\phi_{detrital}}(\lambda) \tag{2.23}$$

Similarly, the NAP measurements can be thought of as a combination of absorption contributions from minerals, living phytoplankton cell walls and detrital cell walls. The term NAP is inappropriate, for the measurement contains information about both previously living and detrital algal cell walls (a_{cell}). For example the contributions may be written as,

$$a_{NAP}(\lambda) = a_{min}(\lambda) + a_{cell_{living}}(\lambda) + a_{cell_{detrital}}(\lambda). \tag{2.24}$$

2.2.4.3 Particulate Scattering

A 25 cm pathlength beam transmissometer was mounted on the CTD profiler and was used to measure the beam attenuation coefficient at 660 nm, $c_{pg}(660)$. Considering $c = a + b$, and the transmissometer is calibrated with pure water, then the particulate scattering b_p can be found by subtracting the CDOM, NAP and phytoplankton absorption coefficients at 660 nm, namely

$$b_p(660) = c_{pg} - a_\phi - a_{NAP} - a_{CDOM}, \tag{2.25}$$

where the wavelengths on the right hand side terms were omitted for brevity.

The spectral nature of the particulate scattering can be inferred by observing the spectral slope γ_b calculated as a byproduct of the scattering correction of the phytoplankton from Eq 2.22. The full b_p can then be approximated by a commonly-used (Forand & Fournier 1999, Mobley 1994, Doxaran et al. 2007) hyperbolic spectral function:

$$b_p(\lambda) = b_p(660)\left(\frac{\lambda}{660}\right)^{-\gamma_b}. \tag{2.26}$$

2.2.4.4 Particulate Backscattering

A Hobilabs Hydroscat-6 backscattering sensor was used to measure backscattering of GBR particles. A flow-through system was created whereby ship hull-intake water was pumped with a diaphragm pump through a coarse-meshed (2 mm square) filter and then up to a 9 l de-bubbling column, approximately 2 m above the deck. The Hydroscat-6 instrument was mounted in a matt black inverted 20 litre container which allowed water to be gravity-fed from the de-bubbling column. The container had slightly tapered sides, and was cut at the appropriate height to produce an opening that matched the diameter of the Hydroscat so it could be slid inside the bin. The outflow of the bin was positioned at the lowest point, to assist in the constant flow of particulates from the top to the bottom of the Hydroscat sampling volume (see Fig. 2.10). The Hydroscat instrument frame was positioned in between 2 plastic containers to support the weight of the device, but allow space for the flow-through chamber to reside (see Fig. 2.11). The outflow had a tap on the end to apply back-pressure to the chamber for the purposes of priming the chamber to remove bubbles from the optical windows of the Hydroscat. Prior to deployment, this apparatus was tested in the laboratory with Reverse Osmosis (RO) purified water to ensure that data from the Hydroscat was not affected by reflections off the inner walls of the chamber. The scattering measurements of RO water were close to published coefficients of pure seawater (Buiteveld et al. 1994), so no correction for tank reflection was made.

The Hydroscat has a path length of approximately 15 cm, and so its measurements may suffer from artifacts due to the loss of scattered light through the process

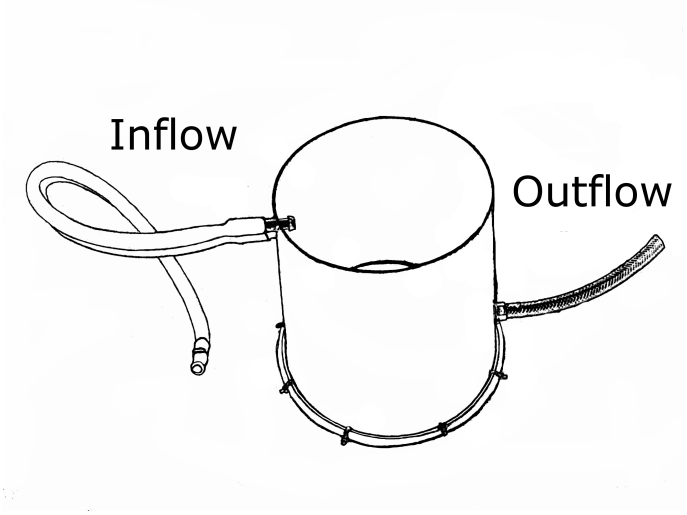

Figure 2.10: Close-up of the custom-built flow-through chamber for the Hydroscat. The inlet is at the top of the chamber (on the left) and the outlet is on the right.

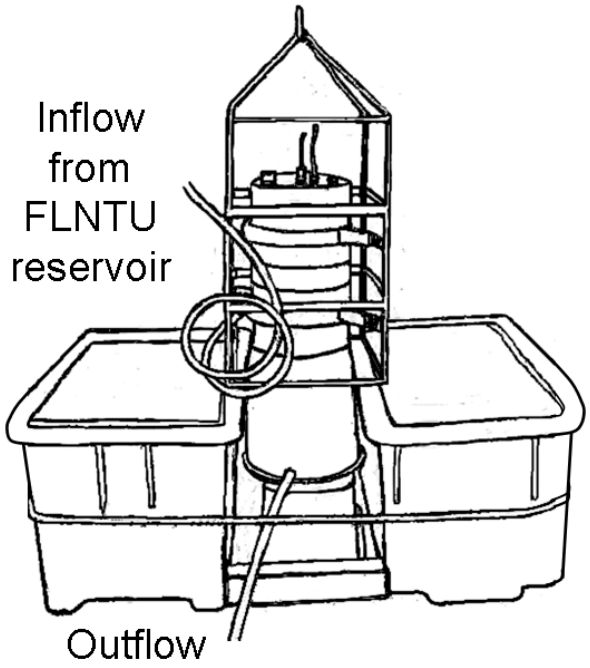

Figure 2.11: The Hydroscat flow-through system. Note this picture is depicted during the setup stage of the experiment. Data was never collected with a double-loop in the inflow tube. All plumbing distances were minimised to reduce flow-through lag time.

of attenuation of scattered light. To correct the measurements made by the Hydroscat, the manufacturer recommends applying a multiplier σ to data from all wavelengths (*Hydrosoft 2.5 Software for HOBI Labs Optical Oceanographic Instruments: User's Manual* 2002):

$$\beta_t(140) = \sigma\beta_u(140), \tag{2.27}$$

where $\beta_u(140)$ is the calibrated, uncorrected scattering measurement made at 140°, and

$$\sigma = k_0 + k_1 K_{bb} + k_2 K_{bb}^2, \tag{2.28}$$

where k_0, k_1 and k_2 are wavelength dependent coefficients that are characteristic of the specific instrument and stored in the instrument's calibration file, and

$$K_{bb} = a_{pg} + 0.4b_p, \tag{2.29}$$

where a_{pg} is the absorption coefficient (m^{-1}) and b_p is the scattering coefficient (m^{-1}).

The absorption coefficient used to correct the Hydroscat data was determined from field measurements where available, or modelled with a 2 component phytoplankton absorption model based on measurements of chlorophyll concentration (see Results section). The scattering coefficient was modelled in terms of TSS based on the tabulated mean TSS and b_p measurements provided by Blondeau-Patissier et al. (2009). The equation determined is $b_p(555) = 0.56[TSS]$, where $R^2 = 0.9691$. Once $\beta(140)$ has been attenuation-corrected, then pure seawater scattering at 140° must be subtracted from the measurement for the best accuracy in clear waters (Boss & Pegau 2001). The particulate backscatter is then calculated as:

$$b_{bp} = \chi_p(140)[\beta_t(140) - \beta_{sw}(140)], \tag{2.30}$$

where $\beta_{sw}(140)$ is the pure seawater scattering at 140° as determined by the approach of Zhang et al. (2009), and $\chi_p(140)$ is the backscattering conversion factor

for a 140° viewing sensor, determined by Sullivan & Twardowski (2009).

The Sullivan & Twardowski (2009) average value of $\chi_p(140)$=1.167 (σ=0.049) was determined with the 658 nm MASCOT instrument. However, they compared their value with other researchers (Berthon et al. 2007, Boss & Pegau 2001) who determined $\chi_p(140)$ from different wavelengths, and agreement was within the standard error of the MASCOT measurements.

2.2.4.5 Scattering Phase Function

No measurements of phase function were made in the aforementioned IOP data collection; however, lab-based phase function measurements have been made by O'Bree (2007) from samples collected in the GBR region. The phase functions of small particles vary due to the refractive index and size of the particles (van de Hulst 1957), and there is recent evidence to suggest phase functions also depend on wavelength (McKee & Cunningham 2005, Chami et al. 2006). The shape of the phase function at mid scattering angles can influence the light field and thus $R_{rs}(\theta, \phi, \lambda)$ (Mobley et al. 2002).

In this study, phytoplankon phase functions were modelled with Mie theory (Bohren & Huffman 1983) from estimates of particle size and cellular material refractive indices (Stramski et al. 2001). A *Prochlorococcus* phase function was modelled by performing Mie calculations for a Gaussian size distribution of particles, centered on 0.65 μm and having a standard deviation (σ) of 0.1 μm to match the average *Prochlorococcus* size distributions shown in Morel et al. (1993). The real and imaginary parts of the refractive index (relative to seawater) used to model *Prochlorococcus* were averages of the three strains tabulated by Stramski et al. (2001). The averaged, wavelength dependent imaginary refractive indices from Stramski et al. (2001) were then linearly interpolated to suit the required calculation wavelength.

Mie-based modelling to determine a representative GBR 'Diatom' phase func-

tion is much more questionable than modelling the relatively simple, spherical *Procholorococcus*. Firstly, the (assumed) 'Diatom' endmember determined by identifying the most packaged $a_\phi(\lambda)$ measurement could also consist of contributions of dinoflagellates and other larger eukaryotic phytoplankton. Secondly these larger phytoplankton are more complex in structure compared to the spherical *Prochlorococcus*, so the results of Mie theory will be dubious.

Revelante et al. (1982) listed the names of some more commonly-found diatoms and dinoflagellates in their studies in the GBR region, and a select group of these are listed in Table 2.6, along with estimates of their dimensions in two different axes (r_1 and r_2, where available).

Name	r_1	unc.	r_2	unc.	Reference
Nitzschia longissima	2.77	1.61	-	-	Marken (2005)
Chaetoceros compressus	15	5	6.5	1.5	Tabassum & Saifullah (2010)
Nitzschia bicapitata	18.7	8.3	4.8	1	Scott & Marchant (2005)
Bacteriastrum comosum	100	5	5	5	Teanpisut & Patarajinda (2007)*
Gymnodinium fusus	25	5	10	2.5	Gomez (2007)**

Table 2.6: Some commonly-found GBR phytoplankton described by Revelante et al. (1982) and estimated axial and longitudinal (where applicable) radii (r_1, r_2) from various references. Radius data and uncertainties are in μm. **Bacteriastrum comosum* dimensions estimated from a image in Teanpisut & Patarajinda (2007). ***Gymnodinium fusus* dimensions estimated from a image in Gomez (2007).

By observing the prevalence of different (axial, longitudinal) dimensions in commonly-occuring, non-spherical GBR Diatoms, a series of spherical Mie calculations can be made for different dimensional sizes and averaged to approximate a size population. To estimate a representative Diatom size population, a series of Gaussians were fitted; centered on each radius for each dimension in Table 2.6. The standard deviation (σ) of each Gaussian was estimated by the uncertainty of each radius and each dimension. The real and imaginary parts of the the refractive index (relative to seawater) were unavaliable, so data from the two diatom and one dinoflagellate planktonic components from Stramski et al. (2001) (their labels PSEU, CURV and MICA) were averaged and used to model the higher order populations. The population particle size distributions are shown in Fig. 2.12.

The particle size distribution of suspended minerals was assumed to be hyperbolic (Junge) in shape, and thus adequately modelled by the Fournier-Forand Phase Function (Forand & Fournier 1999). This equation creates a phase function at angle ψ for a bulk refractive index n and Junge PSD slope μ. The phase function is described below (modified from Mobley et al. (2002)).

$$\widetilde{\beta_{min}(\psi)} = \frac{1}{4\pi Z^2 \delta^\nu}\left[\nu Z - (1-\delta^\nu) + [\delta(1-\delta^\nu) - \nu Z]\sin^{-2}\left(\frac{\psi}{2}\right)\right] + Y, \quad (2.31)$$

where

$$Y = \frac{1-\delta_{180}^\nu}{16\pi(\delta_{180}-1)\delta_{180}^\nu}(3\cos^2\psi - 1), \quad (2.32)$$

$$Z = (1-\delta), \quad (2.33)$$

$$\delta = \frac{4}{3(n-1)^2\sin^2}\left(\frac{\psi}{2}\right), and \quad (2.34)$$

$$\nu = \frac{3-\mu}{2}. \quad (2.35)$$

The Junge PSD slope μ can be estimated from the spectral slope of the scattering (Forand & Fournier 1999) or attenuation spectrum (Twardowski et al. 2001) γ using the following relationship:

$$\mu = \gamma + 3. \quad (2.36)$$

Based on the cumulative probability distribution equations shown in Forand & Fournier (1999), Mobley et al. (2002) published the analytical expression for the backscattering ratio:

$$B_p = 1 - \frac{1-\delta_{90}^{\nu+1} - 0.5(1-\delta_{90}^\nu)}{(1-\delta_{90})\delta_{90}^\nu}. \quad (2.37)$$

This equation allows the parameterization of the Fournier-Forand Phase Function with either n and μ or with B_p and μ through numerical means. In the GBR region, if the assumption of a Junge PSD is valid for mineral particles, then measured backscattering ratios and scattering spectral slopes can be input into Eq. 2.31 and 2.37 in order to numerically determine the refractive index n and generate a phase function. As the phytoplankton-based phase functions have

been calculated with Mie theory, the use of the Fournier Forand phase function in this work is concerned primarily with modelling the mineral particle assemblage, where refractive indicies of 1.18 ± 0.06 are expected (the average and σ of the tabulated data used in Twardowski et al. (2001)).

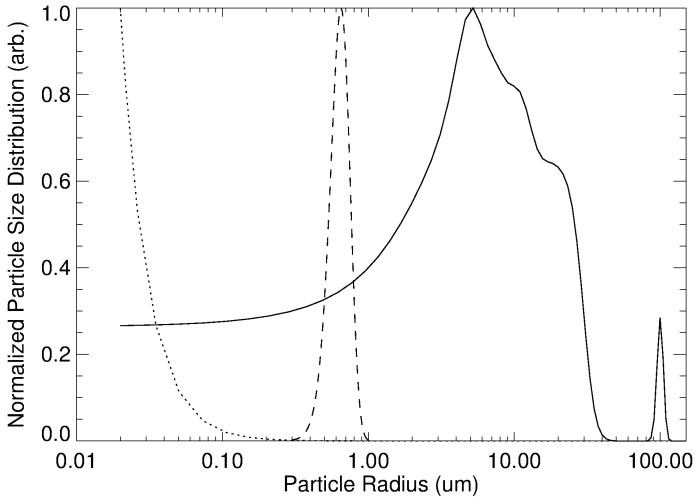

Figure 2.12: Normalized Particle Size Distribution for a Prochlorococcus monoculture (dashed line), a mixture of higher-order phytoplankton (solid line) described in Table 2.6, and an example Junge distribution ($\mu = 2.35$) for use with the Fournier Forand phase function in Eq. 2.31 (dotted line).

2.3 Results

2.3.1 Water Quality

Table 2.7 provides an initial reduction of the primary water quality parameters (Chl-a, TSS, DOC and Secchi) from the dataset acquired for this study (also see 2.2). Each water quality parameter is separated into inner, middle and outer (I,M,O) shelf regions as denoted by the "loc." column. These regions correspond to the bathymetric regions shown in Fig. 2.1. The reproducibility (rep. - see Table 2.7) of the water quality measurements are estimated by the average replicate standard deviation for each sample made within that particular region. Table 2.7 and Fig. 2.13 demonstrate that generally, higher concentrations of Chl-a, TSS, DOC were found inshore with progressive reductions towards offshore. This trend supports the notion that a significant portion of nutrients and sediment are terrestrially-sourced. Secchi depth has an inverse proportionality to particle concentration and also follows the trend. The standard deviations of the inner and middle shelf TSS measurements is high (approximately 90% of their respective means), indicating that both these regions experience large variations in sediment concentrations. In contrast, outer shelf areas only varied by approximately 30% of their means; a value close to the replicability of TSS measurements made using our methodology. This is evidence that the outer shelf samples were not influenced by terrigeneous sediment deposition events. Inner, middle and outer shelf chlorophyll-a measurements are also variable, with their standard deviations varying by approximately 70% of the respective means. This fluctuation is much larger than the replicability of Chl-a measurements made using our methodology. It indicates that phytoplankton blooms occurred in inner, middle and outer shelf regions during the sampling campaign. DOC measurements were larger and more variable in inshore regions, and decreasingly variable towards the outer shelf regions. Higher DOC levels and variability towards the coast also suggest terrigenous sources of DOC in these regions. Inshore water have at least twice the number of samples collected, however these are the regions where existing satellite algorithms fail (Qin et al. 2007), so the preference is convenient. Density and frequency histograms of the data are shown in Fig. 2.13. The highest ever CHL

measurement was recorded in Hinchinbrook Passage. The highest TSS concentration measurement was made at Cape Bowling Green (19°19′46″S, 147°21′38″E), and the highest concentration DOC measurement was made at the Burdekin River mouth (19°38′23″S, 147°38′44″E). These places of distinction are marked in Figures 1.9 and 1.10. The lowest TSS and CHL measurements were made at Myrmidon Reef (18°16′15″S, 147°22′30″E), and the lowest DOC measurement was made near Cheviot Is (22°05′30″S, 150°40′18″E).

type	units	loc.	rep.	mean	median	σ	N	min	max
Chl-a	μgl^{-1}	I	0.04	0.52	0.41	0.37	298	0.11	2.25
Chl-a	μgl^{-1}	M	0.04	0.39	0.34	0.26	148	0.08	2.02
Chl-a	μgl^{-1}	O	0.05	0.44	0.34	0.32	115	0.05	1.77
TSS	mgl^{-1}	I	0.26	2.91	2.31	2.74	296	0.74	23.98
TSS	mgl^{-1}	M	0.28	1.68	1.44	1.49	148	0.63	16.90
TSS	mgl^{-1}	O	0.20	1.16	1.12	0.34	114	0.46	2.41
DOC	mgl^{-1}	I	0.03	0.79	0.72	0.34	247	0.46	4.16
DOC	mgl^{-1}	M	0.03	0.75	0.71	0.19	125	0.51	2.17
DOC	mgl^{-1}	O	0.03	0.67	0.67	0.10	46	0.50	0.91
Secchi	m	I	1.00	6.70	6.00	3.30	105	1.50	17.00
Secchi	m	M	1.00	12.54	12.00	5.33	36	5.50	28.00
Secchi	m	O	1.00	20.43	20.00	5.73	23	13.00	33.00

Table 2.7: Field data collection summary. The location identifiers are I (inner), M (middle) and O (outer) shelf waters. σ is the standard deviation, N is the number of samples.

Fig. 2.14 shows scatter plots between the water quality parameters measured. Being particulate in nature, phytoplankton biomass (as indicated by chlorophyll-a) will contribute to TSS measurements made. In outer-shelf waters, a trend between the TSS minimum and chlorophyll-a can be seen. This relationship is important and will be re-visited in latter sections.

In general relationships between the parameters are poor, however the inverse Secchi disk depth versus TSS shown in Fig. 2.14c appears to have a linear correlation. Here it can be inferred that in inner shelf waters, suspended particulate mass concentration significantly influences Secchi depth measurements. This is consistent with the well known inverse proportionality between Secchi disk depth and sum of the beam attenuation coefficient c and the diffuse attenuation coefficient K (Zaneveld & Pegau 2003), which themselves are linearly correlated to TSS. It is

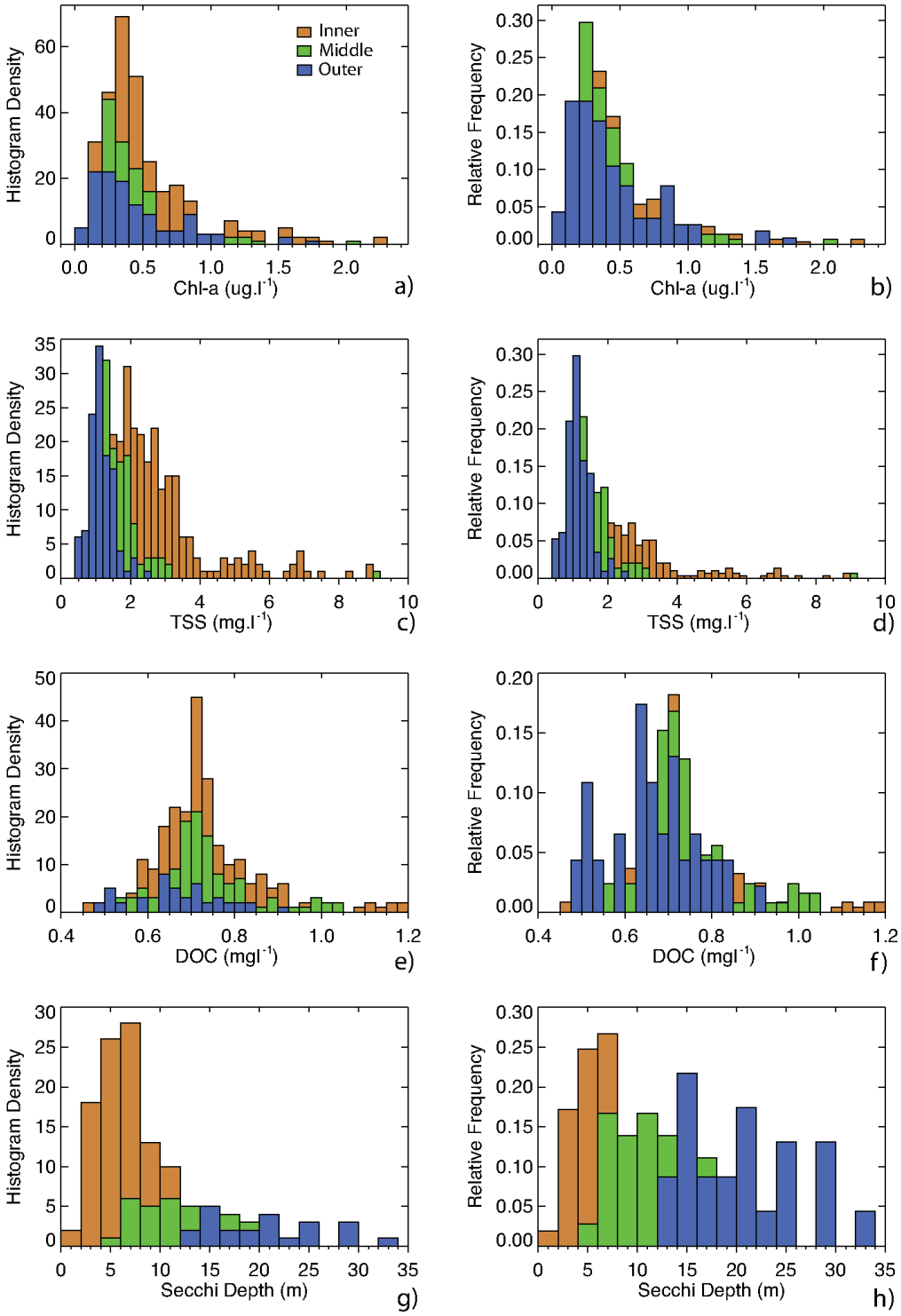

Figure 2.13: a-h) Histogram density and frequency of measured Water Quality concentration samples performed on inner, middle and outer sites following the definition of Devlin & Brodie (2005) (coloured in orange, green and blue, respectively)

unclear from Figs. 2.14c, 2.14d or 2.14e which water quality parameter controls inverse Secchi depth in outer shelf waters. Marine snow (Wolanski et al. 2003) may be a significant factor contributing to Secchi disk readings; however, marine snow will not be quantified adequately in either TSS or TChl measurements. The spectral nature of Secchi disk measurements is defined by the human eye's spectral response, which should be peaked in the yellowish-green wavelengths. As Secchi disk measurements are essentially measuring $c + K$ in green wavelengths, they are less sensitive to substances which attenuate outside the green region of the spectrum. This means phytoplankton (Chl-a) will be less influential to Secchi depths compared to substances which absorb and scatter green wavelengths more readily. This is probably why the correlation in Fig. 2.14d is worse than that of 2.14c. The spectral nature of water constituents will be investigated further in this thesis.

There is a relationship between phaeopigment concentration and chlorophyll-a concentration, which supports the idea that the production of phaeopigments is tied to the abundance of living phytoplankton in the water. Departures from this trend may contain information about unique pheopigment photooxidation or grazing rates, highlight regions where detrital phytoplankton dominates living phytoplankton, or indicate sample degradation from the time of sampling to analysis. Additionally, fluorometrically-determined phaeopigment concentrations may contain artifacts due to other fluorescent phytoplankton pigments including chlorophyll-b (Herbland 1988). Without additional HPLC pigment information, the extent of the contamination is unknown.

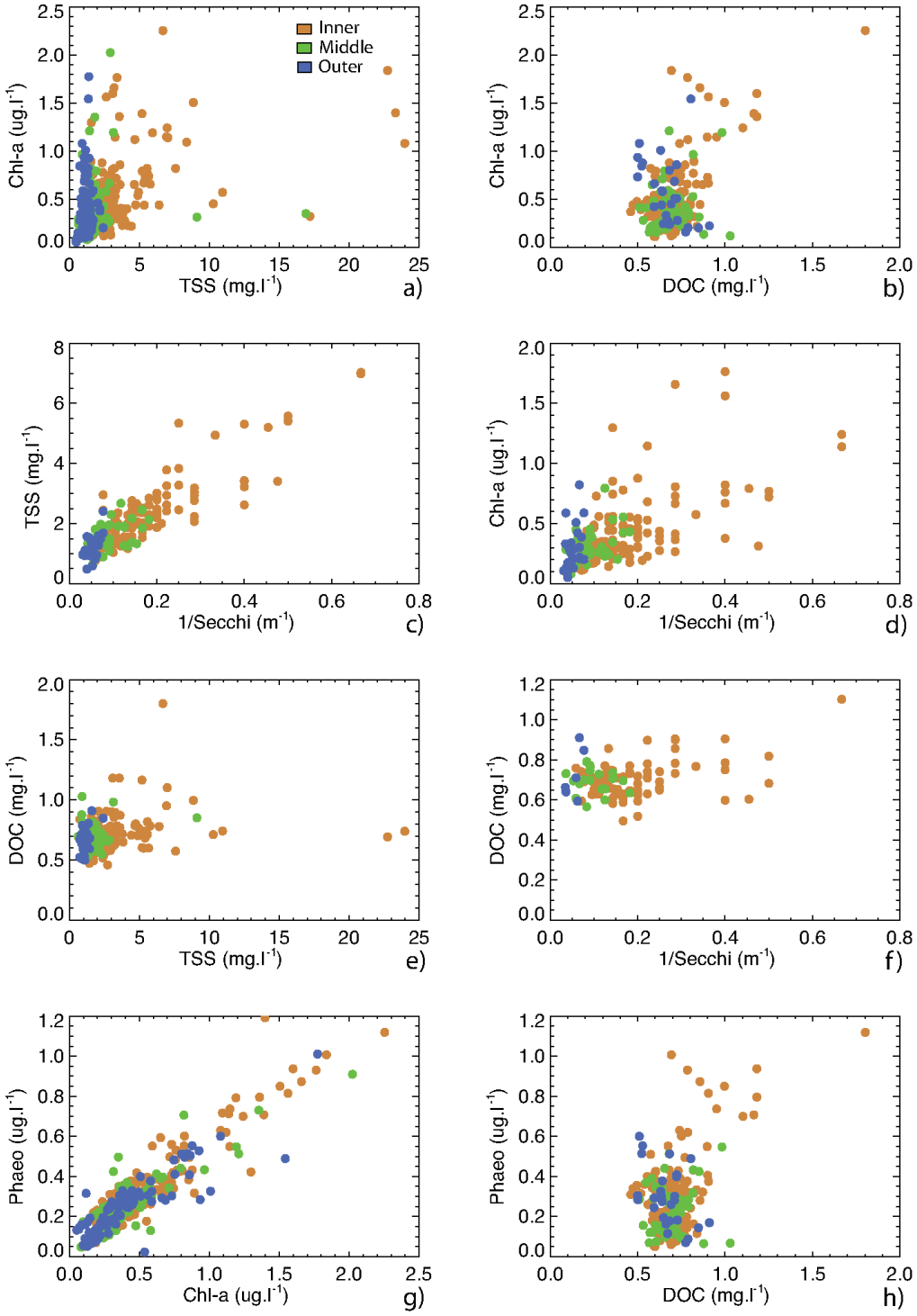

Figure 2.14: a-h) Scatter plots of the Water Quality concentration samples performed on inner, middle and outer sites following the definition of Devlin & Brodie (2005) (coloured in orange, green and blue, respectively).

2.3.2 Conductivity, Temperature and Depth (CTD) Measurements

CTD measurements were used to identify different water masses during the field sampling from 2002 to 2009. Figure 2.15a shows 4 different temperature versus salinity (TS) plots for all GBR waters sampled. Surface water in summer (wet season) months is generally above 27°C, which is consistent with periods of higher insolation (downwelling irradiance). Water in summer tends be of lower salinity than in winter, indicating that fresh water input is often a stronger influence in GBR waters than increases of salinity due to enhanced evaporation during periods of elevated sea temperature. Wet season river plume flood TS data can be seen as a filament on Figures 2.15 a-d towards the top left, and in contrast, there are a few measurements which exhibit high salinity and high temperature in the summer months which suggest that these casts were outside the influence of recent riverine input. The dry season population also exhibits features consistent with surface evaporation, where the warmest waters have the highest salinity.

With knowledge of the TS properties, the types of water which supported phytoplankton blooms can be identified. A Chl-a colour-scaled TS plot (Fig. 2.15c) shows elevated chlorophyll-a concentrations indicative of phytoplankton blooms over a range of salinities in the wet season, which in part supports the hypothesis that riverine waters were providing nutrients required for phytoplankton blooms. The phytoplankton signatures found in waters with salinity higher than 35.5 PSU in the wet season are probably not influenced by recent terrestrial sources of nutrient, but could be due to the nitrogen fixing organism *Trichodesmium*.

Discrete TSS data was used to colour code the TS diagram shown in Fig. 2.15b. In this figure, the cooler, higher salinity dry season water is often turbid, which indicates this water parcel is re-suspended from deeper waters.

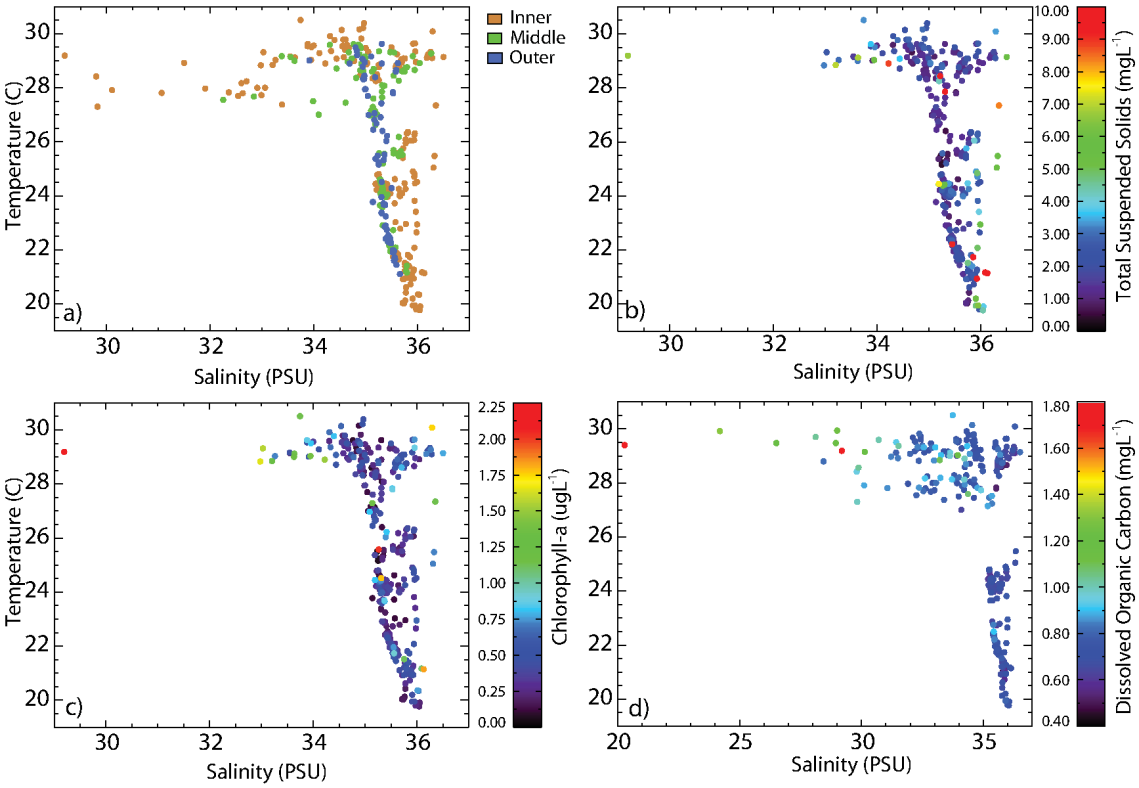

Figure 2.15: Temperature vs Salinity for all waters where discrete samples were taken. Plot symbols are colour coded to represent a) Inner, Middle or Outer samples, b) TSS concentration, c) Chlorophyll-a concentration, and d) DOC concentration.

2.3.3 IOPS

2.3.3.1 Dissolved

Table 2.2 previously showed the trip codes, numbers of stations and the dates when CDOM absorption spectra were measured for inclusion in this study. Figure 2.16 shows the entire CDOM absorption spectral data set in a) linear b) logarithmic ordinate representations. Figure 2.16b shows the estimated detection limit of the spectrophotometer.

Of the 417 CDOM spectra measured, 100 were in the very low absorption range (0-0.025 m^{-1}) in the same order of magnitude of the detection limit of around 0.017 m^{-1} at 443 nm. When looking at individual spectra at low CDOM concentrations, the combined effect of the spectrophotometer detection limit, and imperfect temperature and salinity corrections makes some absorption spectra

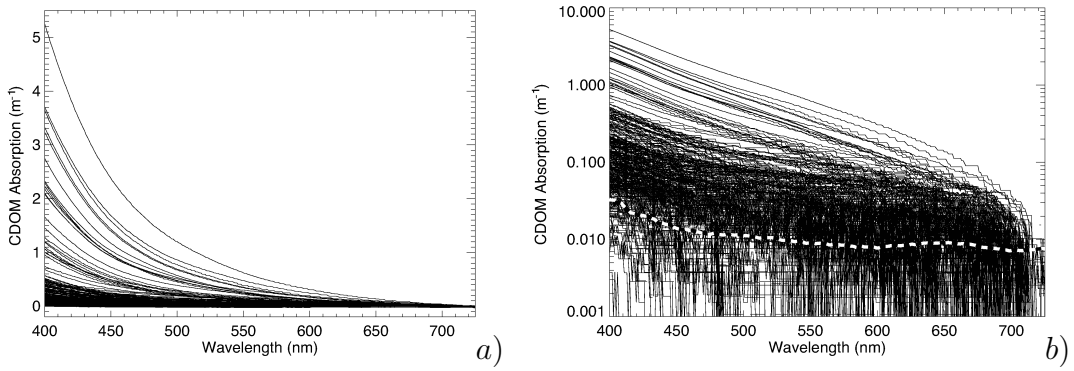

Figure 2.16: Entire CDOM absorption spectra, linear (a) and logarithmic axes (b). b) shows the empirically estimated detection limit of the spectrophotometer.

appear anomalous, not exhibiting the typical and widely reported exponential shape (Prieur & Sathyendranath 1981). Due to the shape and magnitude of some of these spectral scans, contamination either from the CDOM sample storage bottle or cuvette contamination is suspected. Anomalous scans could also be due to 0.45 μm filter membrane rupture, which could potentially allow phytoplankton and non-algal particulates into the solution. Phytoplankton contamination would be most prominent around 676 nm, where there is a local maximum of chlorophyll absorption, but a relatively small absorption due to CDOM itself. No such rupture artifacts were located in the data. These low magnitude CDOM absorption spectra were not discarded however, because subsequent regression analysis weighted each data point with the spectral detection uncertainty (shown in Figure 2.17c), so data with large fractional uncertainties are suppressed.

The CDOM absorption spectrum is usually described and modelled as a decaying exponential with negligible absorption in the NIR wavelengths (Prieur & Sathyendranath 1981, Bricaud et al. 1981). This simplistic modelling approach seeks to parameterize the entire CDOM absorption spectrum with two terms; the concentration A at a reference wavelength (λ_0) and spectral slope parameter S. For example:

$$a_{CDOM}(\lambda) = A(\lambda_0)e^{-S(\lambda-\lambda_0)}. \tag{2.38}$$

The exponential slope (S in Eq. 2.38) of the CDOM absorption spectrum has been shown to vary from approximately 0.007 to 0.023 nm^{-1} and is dependent on

the spectral range being fit since spectra typically do not follow an exponential model exactly (Twardowski et al. 2004). Carder et al. (1989) recognised that the spectral shapes of CDOM absorption spectra could provide information about the molecular weights of the dissolved organic materials, by confirming differences in exponential slope parameter between isolated fulvic and humic acid samples collected from the Mississippi River plume and the Gulf Loop Current intrusion. Their slope coefficients for fulvic acids were approximately 0.019 nm^{-1} whereas their humic acid slope was 0.0110 nm^{-1}. Twardowski & Donaghay (2002) studied the UV degradation of humic substances and observed increasing spectral slopes as a function of time exposed to sunlight. Although the functional form of the exponential equation shown in Eq. 2.38 is generally consistent among researchers [4], spectrophotometer precision, spectral baseline drifts and parameter fitting methodologies used to determine A and S are not. Unfortunately, this adds variability to the S slope parameters found in literature, so caution must be exercised when comparing the results of different researchers (Twardowski et al. 2004).

The exponential slope parameter S and magnitude A were calculated for each CDOM spectral measurement, using wavelengths from 400 to 600 nm to perform the spectral fit. A scatter plot of A vs S is shown in Figure 2.17a, and salinity vs S is shown in Figure 2.17b. A dotted line on Figure 2.17b assists in estimating the spectral slope of high-CDOM waters. This line was fitted to data with salinities less than 30 PSU, and results in an extrapolated slope of approximately 0.017 nm^{-1} for fresh water. Figure 2.17c suggests higher CDOM absorption coefficients are typically sourced from lower-salinity GBR flood plumes. At $a_{CDOM}(412)$ coefficients less than 0.1 m^{-1}, there is a larger deviation in slopes, which is attributed to increases in spectrophotometer noise relative to the CDOM absorption signal. This is despite the inclusion of all wavelengths from 400 to 600 nm in the spectral fit which serves to reduce the sensitivity of S to spectrophotometric noise. Error bar extents shown on Figure 2.17a and b are determined from spectral fits of each measured CDOM spectrum $\pm$ the spectral baseline uncertainty. Even

[4] although Twardowski et al. (2004) recommends using a power law.

after considering the errors in S, there is an apparent increase in spectral slope in Fig. 2.17a with decreasing CDOM absorption. These results are consistent with the concept that either larger terrigenous humic (lower slopes) molecules are either being mixed with more fulvic, marine waters or that processes such as photobleaching are occurring, converting humic molecules thus increasing the measured slope parameter (Twardowski & Donaghay 2002). Despite this, there is no solid relationship between the full range of salinity encountered on the GBR and the spectral slope of CDOM. This may demonstrate that there is an occasional source of the highest-slope CDOM absorption spectra that occurs in saline waters. The relative uncertainty of the low absorption coefficient waters is high, so more accurate data is required to determine whether this feature is real or an artifact.

The relationship between DOC and CDOM absorption at 412 nm is shown in Figure 2.17e. The regression was determined from the entire dataset including lower salinity flood plume waters. The full-dataset regression exhibits a negative y-intercept, indicating that there is a consistent background concentration of the DOC that is non-coloured. This finding is consistent with other researchers (Del-Castillo & Miller 2008). By performing the regression for all wavelengths, a spectral DOC-specific end member can be identified, along with the offset which corrects the derived DOC for the invisible DOC fraction, using the form:

$$a_{CDOM}(\lambda) = a^*_{CDOM}(\lambda)[DOC - DOC_{inv}], \tag{2.39}$$

where a^*_{CDOM} is the DOC-specific absorption spectrum (shown in Figure 2.17g), and DOC_{inv} is the invisible DOC 'background' (approximately 0.65 mgl^{-1}).

Using the model described in Eq 2.38, the CDOM absorption dataset may be inverted to test the applicability of the model. Figure 2.17f shows the comparison between the inverted DOC and the measured DOC, where the correlation coefficient $R^2 = 0.93$ and the RMS error is approximately 9%. Figure 2.17d shows the relationship between DOC and salinity for the region. The DOC concentration is reduced as the salinity increases, supporting the concept that terrestrial DOC

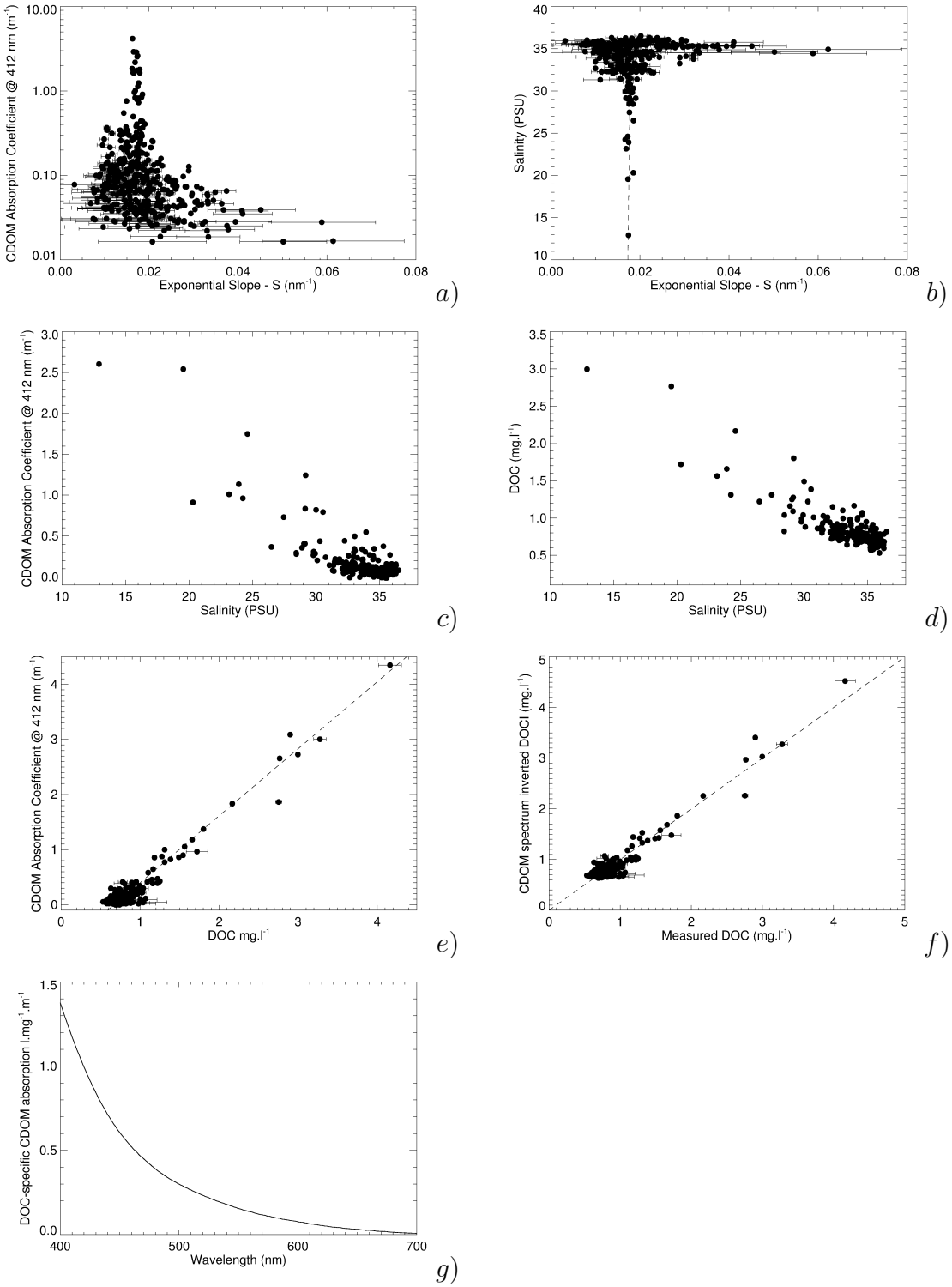

Figure 2.17: a) CDOM absorption coefficient at 412 nm versus the spectral slope S. b) Salinity (PSU) versus the spectral slope S. c) CDOM absorption coefficient at 412 nm versus Salinity (PSU). d) Dissolved Organic Carbon (mgl^{-1}) versus Salinity (PSU). e) CDOM absorption coefficient at 412 nm versus DOC concentration (mgl^{-1}). f) CDOM absorption-inverted DOC versus measured DOC (mgl^{-1}). $R^2 = 0.93$ and $RMSE = 0.09$. g) Regression-determined DOC-specific CDOM aborption spectrum.

is diluted with lower-DOC coastal waters.

2.3.3.2 Particulates

2.3.3.2.1 Phytoplankon Pigment Absorption

Table 2.2 previously showed the trip codes, numbers of stations and the dates when phytoplankton pigment absorption spectra were measured for inclusion in this study. The entire set of phytoplankton pigment absorption spectra is shown in Figures 2.18a and 2.18b. In the visible domain (Fig. 2.18b), two prominent peaks exist in the phytoplankton absorption spectra; the first at approximately 440 nm and another at 676 nm. These peaks are associated with chlorophyll-a, the dominant photosynthetic pigment of marine phytoplankton. At 440 nm, the phytoplankton absorption coefficients varied from approximately 0.01 to 0.1 m^{-1}; the same order of magnitude as those measured by Bricaud et al. (1995) for Case 1 waters. Filter pad absorption replicability was tested for approximately 60 duplicate filter pad preparations from the same Niskin bottle sample, and was typically better than 0.005 m^{-1}, and provides an estimate of the precision of the spectrophotometric technique used in this study. For clarity, error bars are not shown on Figures 2.18a-f. The exact relationship between phytoplankton spectral absorption and the chlorophyll-a concentration varies somewhat depending on phytoplankton species composition (Nair et al. 2008) due to i) the presence of different accessory pigmentation which overlaps the absorption bands of chlorophyll-a (Faust & Norris 1985, Hoepnffner & Sathyendranath 1991), ii) particle size (Stramski et al. 2001) and iii) light history. All attempts to quantify chlorophyll-a concentration from remotely-sensed phytoplankton absorption properties will be constrained by this variability. This variability is demonstrated by the low correlation ($R^2 = 0.46$) of the 440 nm absorption data with TChl ($TChl$=Chl-a + Phaeopigments), as shown in Figures 2.18c. In comparison, the data at 676 nm, where pigment packaging is reduced or negligible (Bissett et al. 1997), has a markedly better correlation ($R^2 = 0.70$) with TChl. This suggests that the combination of optical density, volumetric and diameter measurement uncertainties inherent in the filter pad method (Mitchell et al. 2000, 2003) are dominated by natural pigment variability or pigment packaging variability of the

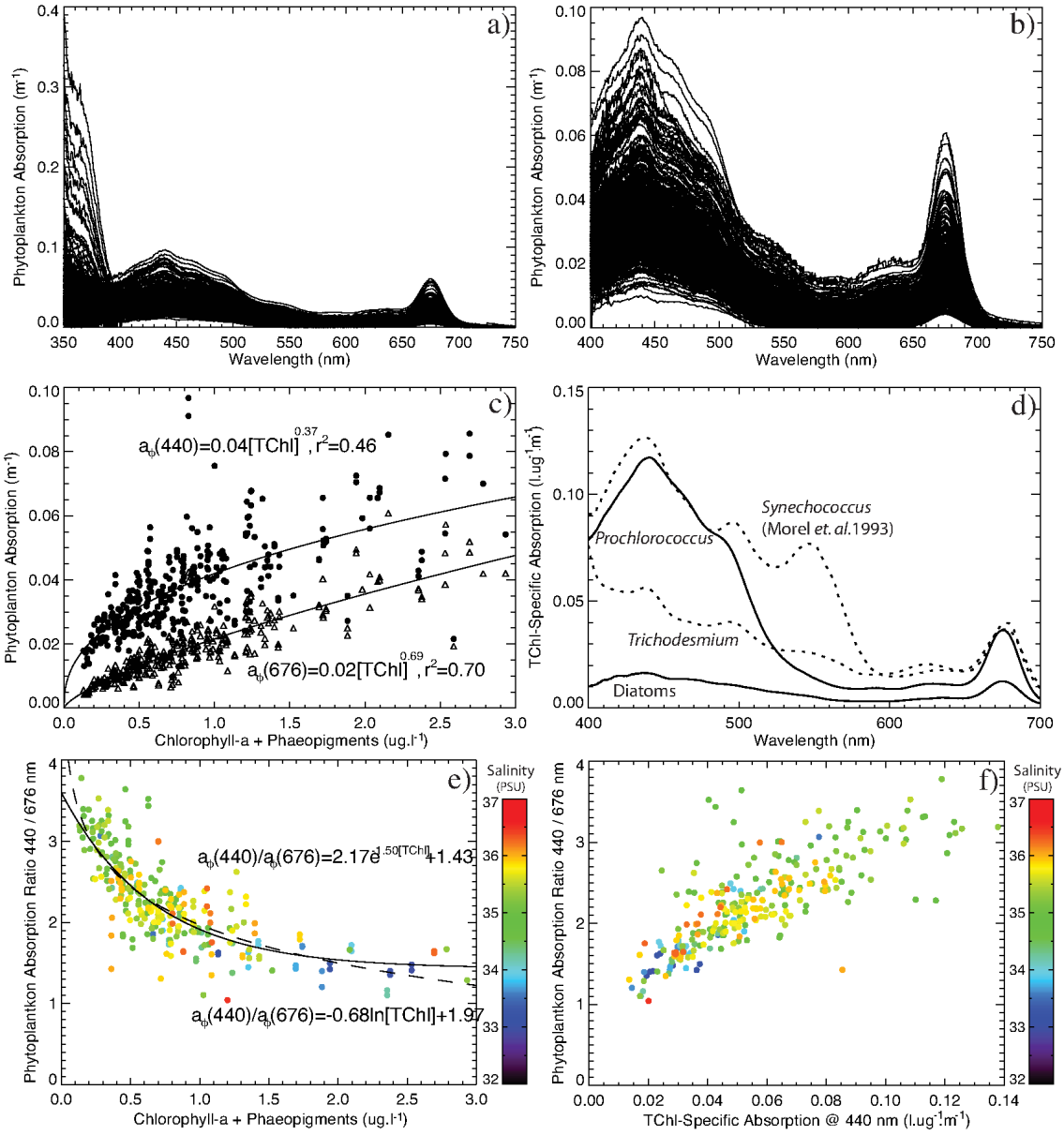

Figure 2.18: a) Full phytoplankton absorption data set measured in this study. b) as for (a), but excludes UV region. c) Phytoplankton absorption at 440 and 676 nm (shown as dots and triangles, respectively) versus TChl concentration, showing regression coefficients for a commonly-used model (Bricaud et al. 1995). d) Four TChl-specific basis vectors. From highest to lowest specific absorption; *Synnechococcus* (Morel et al. 1993), and *Prochlorococcus*, *Trichodesmium* and Diatoms (this study). e) The 440:676 phytoplankton absorption ratio versus TChl concentration for the entire data set. Plot symbol colours denote sample salinity, and two non-linear models are shown on the plot. f) The 440:676 phytoplankton absorption ratio versus TChl-specific absorption, showing the increase in absorption efficiency when packaging is reduced.

samples themselves (Bricaud et al. 2004).

To demonstrate the spectral (and TChl-specific) diversity of GBR phytoplankton types, 3 hand-picked absorption end members are shown in Fig. 2.18d. Based on the spectral shape and amplitude, these end members have been assigned to represent *Prochlorococcus*, *Trichodesmium* and Diatom dominated waters (from high specific absorption to low at 440 nm). The *Synechococcus* TChl-specifc absorption spectrum from Morel et al. (1993) was also included for comparison, as the spectral features present in this end-member is also expected to contribute to the total phytoplankton absorption of GBR waters.

Despite the variability and intricacies in the absorption properties of GBR phytoplankton, broad generalizations must be made which relate the spectral phytoplankton absorption with the chlorophyll-a concentration, even though there is probably no unique chlorophyll-a concentration for a given absorption coefficient. The correlation coefficients from Fig. 2.18c indicate it is more accurate to use the phytoplankton absorption at 676 nm than at 440 nm as a predictor for chlorophyll concentration. However ultimately, remote sensing-derived absorption coefficients are dominated by pure water absorption itself at 676 nm, and so $a_\phi(676)$ retrievals may suffer from a poor signal-to-noise ratio, leading to erroneous TChl retrievals. In terms of maximising signal-to-noise, it is far better to utilize the blue end of the spectrum were absorption due to pure water is lower, and absorption due to phytoplankton is relatively higher. With this in mind, the following phytoplankton absorption modelling approaches strive to relate the entire spectrum to TChl concentration.

A widely-cited non-linear parameterization between phytoplankton absorption at a given wavelength and the combined chlorophyll-a + phaeopigments concentration (TChl) was published by Bricaud et al. (1995). This type of combined chlorophyll-a and phaeopigment parameterization leads to a more robust relationship with phytoplankton absorption than just chlorophyll-a alone (Babin, Stramski, Ferrari, Claustre, Bricaud, Obolensky & Hoepnffner 2003). However,

such a combined parameterization assumes that the spectral characteristics of phaeopigments are either identical or very similar to that of chlorophyll-a or that the chlorophyll-a to phaeopigment ratio does not change appreciably. Whether these assumptions hold in GBR reef waters needs to be tested. The *in vivo* chlorophyll-a and phaeophytin absorption spectra were known to differ (Roesler et al. 1989). The Bricaud et al. (1995) model was only developed using data from Case-1 stations where the phaeopigment concentration was less than a few percent of the total pigment concentration, whereas phaeopigments measured in the GBR water sampled in this study typically contribute 35% (σ=5.3) of TChl (see Fig. 2.14g), so phaeopigments may generally have a greater importance in GBR waters. Unfortunately, it is still not clear with the sampling methods used if the phaeopigment measurements made in the GBR are spectrally contaminated by Chl-b and Chl-c. Without HPLC or chlorophyll speciation data to provide further insight, Bricaud et al. (1995) is followed in using TChl to parameterise phytoplankton absorption, with the caveat that the overall magnitude of living, photosynthesizing chlorophyll may be slightly overestimated. The Bricaud et al. (1995) regression approach was used on our dataset, and these model coefficients are shown in Figs. 2.18c for absorption at 440 nm and 676 nm, and spectrally shown in Fig. 2.19. The Bricaud et al. (1995) model approach (subsequently referred to as 'B95') is shown below:

$$a_{\phi}(\lambda) = A(\lambda)[TChl]^{B(\lambda)}, \tag{2.40}$$

where $A(\lambda)$ and $B(\lambda)$ are the regression-determined model coefficients (see Fig. 2.19 column 1, row 1).

As can be seen from Fig. 2.18e, the 440:676 nm phytoplankton absorption ratio generally decreases with overall TChl magnitude in the GBR dataset. This effect is known as pigment 'packaging', where the phytoplankton spectrum becomes 'flatter' as the chlorophyll concentration increases. This is explained by pigment-containing chromophores shading each other as the phytoplankton cell size increases and / or the density of chromophores increases (Duysens 1956,

Morel & Bricaud 1981). By observing the salinity-based colour scale in Fig. 2.18e, it is evident that the higher TChl (more packaged phytoplankton) often occurred as salinity decreased. This effect is indicative of eutrophic coastal water conditions in the presence of riverine input and a subsequent growth of a larger-cell (i.e. Diatom dominated) phytoplankton population. Considering that these lower salinity flood waters are a key area of interest in the GBR, and that the transition between these waters and more oligotrophic waters is evident in the dataset, attention must given to pigment packaging effects.

The fractional package effect Q_a^* for spherical particles can be estimated theoretically from the efficiency factor for absorption given by Eq. 2.41 (Morel 1991) and the normalisation shown in Eq. 2.42 (Nelson et al. 1993),

$$Q_{a(\lambda)} = 1 + \frac{2e^{-\rho'(\lambda)}}{\rho'(\lambda)} + 2\frac{e^{-\rho'(\lambda)} - 1}{\rho'(\lambda)^2}, \tag{2.41}$$

$$Q_a^* = \frac{3}{2}\frac{Q_{a(\lambda)}}{\rho'(\lambda)}, \tag{2.42}$$

where $\rho'(\lambda) = a_{cm}d$, the dimensionless product of the absorption coefficient of the cellular pigmented material a_{cm}, and the spherical cell diameter d.

Eq. 2.41 and 2.42 provide a mathematical framework for estimating the packaging effect, however $\rho'(\lambda) = a_{cm}d$ is typically not known *a priori*, and natural assemblages contain a number of different phytoplankton size classes. Understanding this product may help explain the scatter of plots such as Fig. 2.18c. Interpreting Figs. 2.18c and d and the above equations, one may hypothesize that if the TChl concentration in the water increases, then $\rho'(\lambda) = a_{cm}d$ will also increase (i.e. TChl is a proxy for ρ'). To test this hypothesis, computational methods were used to minimize the difference between the measured absorption at a given wavelength and a linear function of TChl, thus determining forward model coefficients to estimate a phytoplankton absorption spectrum as a function of TChl. This technique is referred to as 'PACK' herein. A Levenberg-Marquardt

technique minimized the following function,

$$a_\phi(\lambda) = C[TChl]Q^*, \tag{2.43}$$

where Q^* was calculated via Equations 2.41 and 2.42 with $\rho^{'} = D[TChl]$. Physically, the regression-determined spectral coefficient C describes the generalised model-extrapolated TChl-specific shape of unpackaged GBR phytoplankton, and D represents the residual TChl-specific absorption properties of a more packaged GBR phytoplankton assemblage. The coefficients C and D are plotted in Figure 2.19, column 1, row 2 and appear to support the hypothesis that TChl can be used as a proxy for ρ'.

Considering that waters dominated by different phytoplankton may be physically mixed or that a mixture of optically different phytoplankton may co-exist, Ciotti et al. (2002) introduced the notion of a mixture of two different spectrally distinct phytoplankton types. Their work suggested that a 'background' of *Prochlorococcus* is mixed with larger-size phytoplankton in increasing abundance with eutrophication. This notion is generally supported in the GBR by the work of Furnas & Mitchell (1986), Furnas et al. (1990) and Revelante et al. (1982). Indeed, two of the high and low packaged end members of the GBR absorption dataset (see Fig. 2.18d) appear spectrally similar to those identified by methods of Ciotti et al. (2002), although the *Prochlorococcus* end member selected from the GBR dataset has a TChl specific absorption of nearly 0.12 $l.\mu g^{-1}m^{-1}$ at 440 nm whereas the Ciotti et al. (2002) value for picoplankton approached 0.08 $l.\mu g^{-1}m^{-1}$ (both normalised to TChl). The increased chlorophyll specific absorption can be attributed to a combination of higher light levels present in this study, and also uncertainties in the pathlength amplification factor.
Expressing this basis vector approach mathematically, the phytoplankton absorption spectrum of a natural GBR assemblage can be approximately composed of the sum of *Prochlorococcus*, and set of larger, highly packaged terrestrially-influenced coastal phytoplankton (i.e. Diatoms and Dinoflagellates), for example:

$$a_\phi(\lambda) = a^*_{\phi_{Pro}}(\lambda)[TChl_{Pro}] + a^*_{\phi_{Diat}}(\lambda)[TChl_{Diat}], \tag{2.44}$$

where $a^*_{\phi_{Pro}}(\lambda)$ is the TChl-specific absorption spectrum for *Prochlorococcus*, $a^*_{\phi_{Diat}}(\lambda)$ is the TChl-specific absorption spectrum for large cell sized phytoplankton (i.e. Diatoms) and $TChl_{Pro}$, $TChl_{Dia}$ are respectively the TChl concentrations due to each plankton component.

This approach may be extended to include a third component, namely the prevalent GBR cyanobacteria *Trichodesmium* or *Synechococcus*, where

$$a_\phi(\lambda) = a^*_{\phi_{Pro}}(\lambda)[TChl_{Pro}] + a^*_{\phi_{Tricho}}(\lambda)[TChl_{Tricho}] + a^*_{\phi_{Diat}}(\lambda)[TChl_{Diat}] \quad (2.45)$$

or:

$$a_\phi(\lambda) = a^*_{\phi_{Pro}}(\lambda)[TChl_{Pro}] + a^*_{\phi_{Syn}}(\lambda)[TChl_{Syn}] + a^*_{\phi_{Diat}}(\lambda)[TChl_{Diat}], \quad (2.46)$$

where $a^*_{\phi_{Tricho}}(\lambda)$ is the TChl-specific absorption spectrum for *Trichodesmium*, $a^*_{\phi_{Syn}}(\lambda)$ is the TChl-specific absorption spectrum for *Synechococcus* and $TChl_{Pro}$, $TChl_{Dia}$, $TChl_{Tricho}$, $TChl_{Syn}$ are respectively, the TChl concentrations due to each plankton component.

There is no cell size information for the GBR dataset; however, by observing the extremities of the 440:676 nm phytoplankton absorption ratio plot (Figure 2.18e), examples of high and low packaging can be identified in the dataset. By using these two extremities and their corresponding TChl concentrations as end-members representative of the two dominant phytoplankton types in the GBR, a TChl estimate may be made for a given phytoplankton absorption measurement. Hand-picked spectral absorption end-members for *Prochlorococcus* and large cell sized phytoplankton (i.e. Diatoms) were chosen from the GBR dataset and formed the basis of the spectral mixing models as described by Eq. 2.44-2.46. The *Trichodesmium* basis vector spectrum used in Eq. 2.45 was determined from the average of two separate measurements of 'puff' and 'raft' *Trichodesmium* colonies, and then normalized by an arbitrary number in order to match the chlorophyll-a-specific *Trichodesmium* absorption at 440 nm, as published in Subramaniam et al. (1999). The *Synechococcus* basis vector spectrum used in Eq.

2.46 was digitized from a published chlorophyll-a specific absorption spectrum by Morel et al. (1993), which was a high-light grown culture (ROS04). These basis vectors are shown in Fig 2.18d).

Figure 2.19, row 1 shows the spectral model coefficients developed for a_ϕ and example model outputs of the Bricaud et al. (1995) method, along with the PACK (Figure 2.19, rows 2), and three variants of the spectral mixing model approach (Pro + Diat, Pro + Diat + Tricho, Pro + Diat + Syn) are featured in Figure 2.19 (rows 3 to 5, respectively). The B95 and PACK models embed any accessory pigment information into the model when they correlate with TChl concentration. This embedding should also reflect the shifting phytoplankton size assemblage from inshore to offshore waters. The spectral mixing model approach reflects the shifting phytoplankton assemblage by altering the relative magnitudes of the different components.

The validity of these five different modelling approaches was tested by quantifying their ability to determine the field measured chlorophyll-a concentration based on the the field measured phytoplankton absorption spectrum from 400 to 700 nm. For each model, Levenberg-Marquardt optimization code was used to vary the TChl concentration to obtain the 'best fit' spectrum. For B95 and PACK, this was just one parameter (TChl), but for the spectral mixing models, the relative contribution of the different phytoplankton components (either 2 or 3) was altered to obtain the best spectral match. The total chlorophyll was then determined from the sum of the phytoplankton components. The results of these inversions are shown in column C of Fig. 2.19, and presented in Table 2.8.

Model	Slope	Offset	R^2	RMS
B95	1.04	0.02	0.51	0.40
PACK	1.11	-0.03	0.53	0.37
2 MIX	1.14	-0.03	0.83	0.26
3 MIX Trich.	0.92	0.03	0.80	0.23
3 Mix Syn.	1.07	-0.01	0.82	0.24

Table 2.8: TChl Inversion results

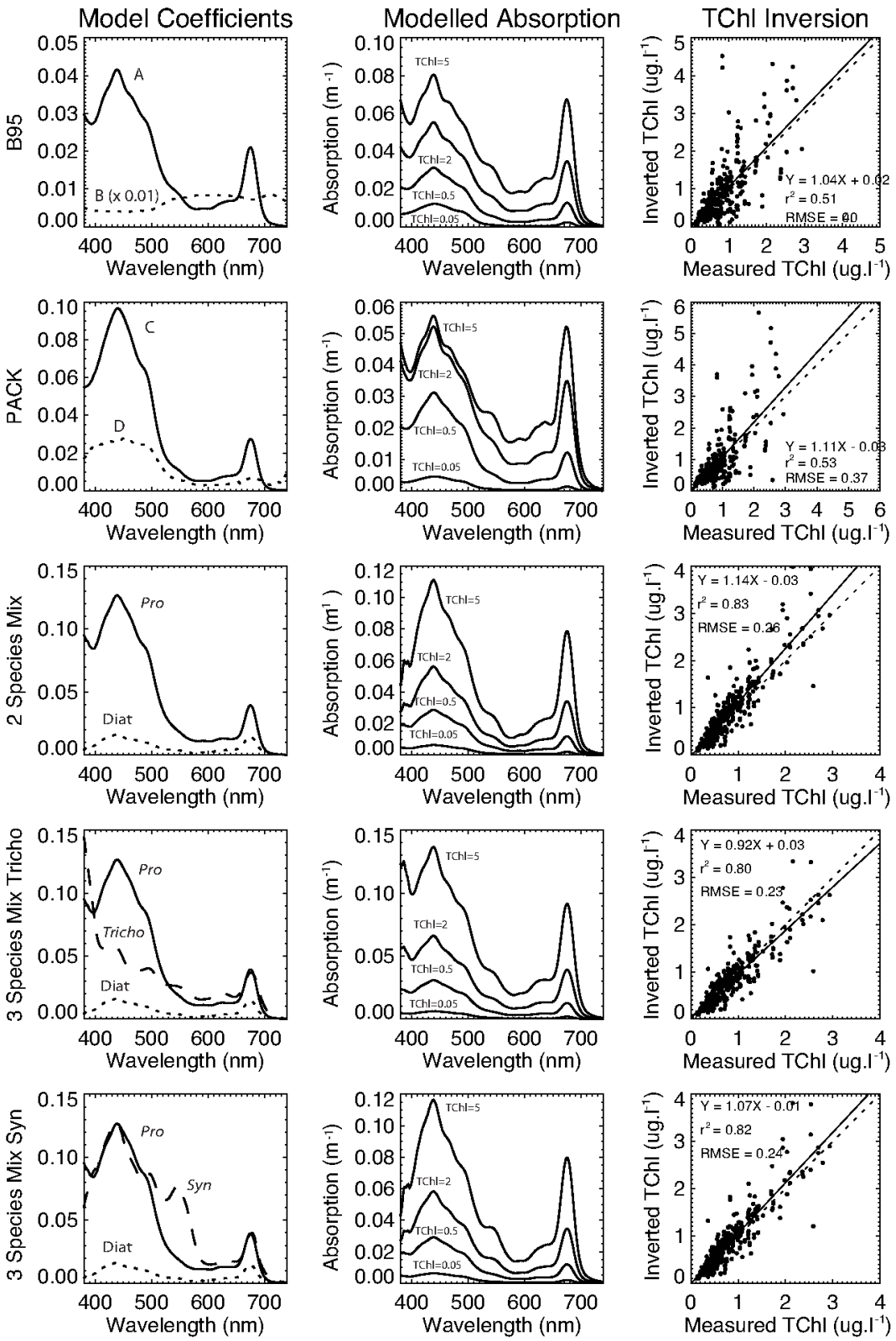

Figure 2.19: Column 1) Spectral model coefficients. Column 2) Example generated absorption spectra for TChl values 0.05, 0.5, 2 and 5 μgl^{-1}. Column 3) TChl inversion results for each phytoplankton model (shown in rows). The annotations A and B in row 1 refer to Eq. 2.40. The annotations C and D in row 2 refer to Eq. 2.43. Rows 3-5, respectively refer to Equations. 2.44 to 2.46.

In considering the best performing model, the slope, correlation coefficient and the RMS error are all important factors. Significant scatter around the dashed 1:1 line for the B95 and PACK models (see Fig. 2.19 column 3, rows 1 and 2) is most likely a result of the packaging variability and changes in phytoplankton pigmentation. This variability is expressed as poor R^2 and RMSE coefficients when compared to the MIX methods. The PACK model produces anomalous outputs for the highest modelled TChl concentration, as it appears to rapidly approach a highly-packaged state for TChl concentrations approaching 2 μgl^{-1} (see Fig. 2.19 column 2, row 2). The highest concentration of TChl experienced during field sampling was approximately 3.4 μgl^{-1}, so this extrapolation artifact highlights the importance of collecting more data for highly-packaged phytoplankton species using the PACK approach in flood waters. Considering the majority of the chlorophyll-a concentrations in the GBR were found to be less than 0.5 μgl^{-1} (see Fig. 2.13), the PACK approach may still have merit.

Overall, the two and three-component models yielded the best R^2 and RMS parameters, with the three-component *Synechococcus* model yielding the best combination of slope and offset, combined with high regression coefficients and lowest RMS error. Based on the fractional decomposition of this best-performing 3-component model (*Synechococcus*), and its inherent assumptions (i.e. just three components can represent all TChl), the fractional component of the *Prochlorococcus* TChl contribution can be calculated:

$$S_{Pro} = \frac{TChl_{Pro}}{TChl_{Pro} + TChl_{Diat} + TChl_{Syn}}. \tag{2.47}$$

Equation 2.47 was used to calculate S_{Pro} and is shown in relation to the total TChl in Fig. 2.20. There is an inverse trend apparent in Fig. 2.20, which supports the idea that the fractional contribution *Prochlorococcus* is reduced as TChl increases. This relationship was functionalised manually through the use of linear fits to inversed $TChl$ values, in the form of Eq. 2.48,

$$S_{Pro} = \frac{M}{8.94TChl} + 0.0214M - 0.1125, \tag{2.48}$$

where values for M govern the slope of the relationship and are manually chosen.

The curves on Fig. 2.20 were generated with $M = 0.75$, 1.5 and 3 (lower dashed, middle solid and upper dashed lines, respectively). Approximately 95% of the data falls between $M = 0.75$ and $M = 3$, so even though the coefficients were manually-determined, Eq. 2.48 is a useful descriptor of the subtle shift in GBR phytoplankton assemblage when the overall TChl concentration increases. It should be noted that S_{pro} should never be allowed to be greater than 1 or less than 0. In identifying this, it is acknowledged that there is probably a better functional fit to the data shown in Fig. 2.20. However, Equation 2.48 is considered adequate for this study, provided the physical limits are obeyed when using Eq. 2.48. Modelling the shift in S_{Pro} will be important later in Section 3.2.2, where it is necessary to synthesize the spectral absorption properties of GBR phytoplankton populations.

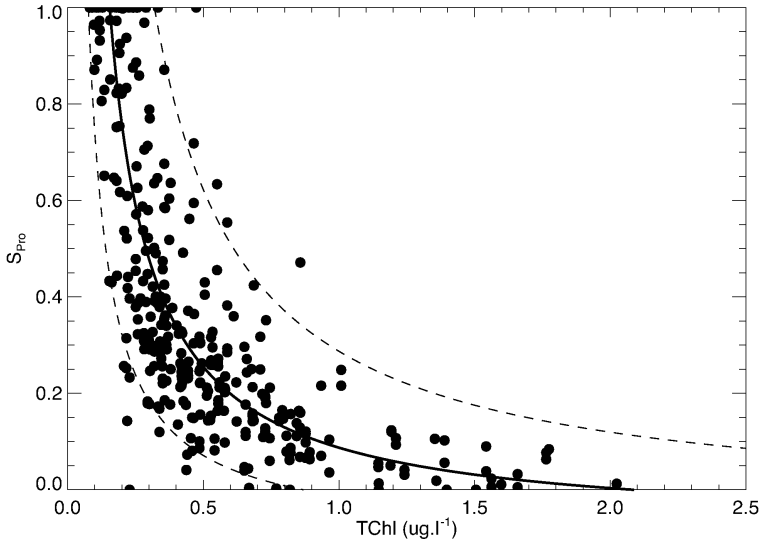

Figure 2.20: The relationship between measurement-reduced S_{Pro} (Eq. 2.47) and TChl sampled in the GBR. The curves are generated with Eq. 2.48 for coefficients $M = 0.75$, 1.5 and 3 (lower dashed, middle solid and upper dashed lines, respectively).

2.3.3.2.2 Non-pigmented Particle Absorption

Table 2.2 previously showed the trip codes, numbers of stations and the dates when Non-Algal Particulate (NAP) absorption spectra were measured for inclusion in this study. The non-pigmented particle absorption coefficients measured in the GBR varied from near zero, up to 0.4 m^{-1} at 440 nm. This corresponds to approximately four times the range of phytoplankton pigment absorption (see Fig. 2.18a).

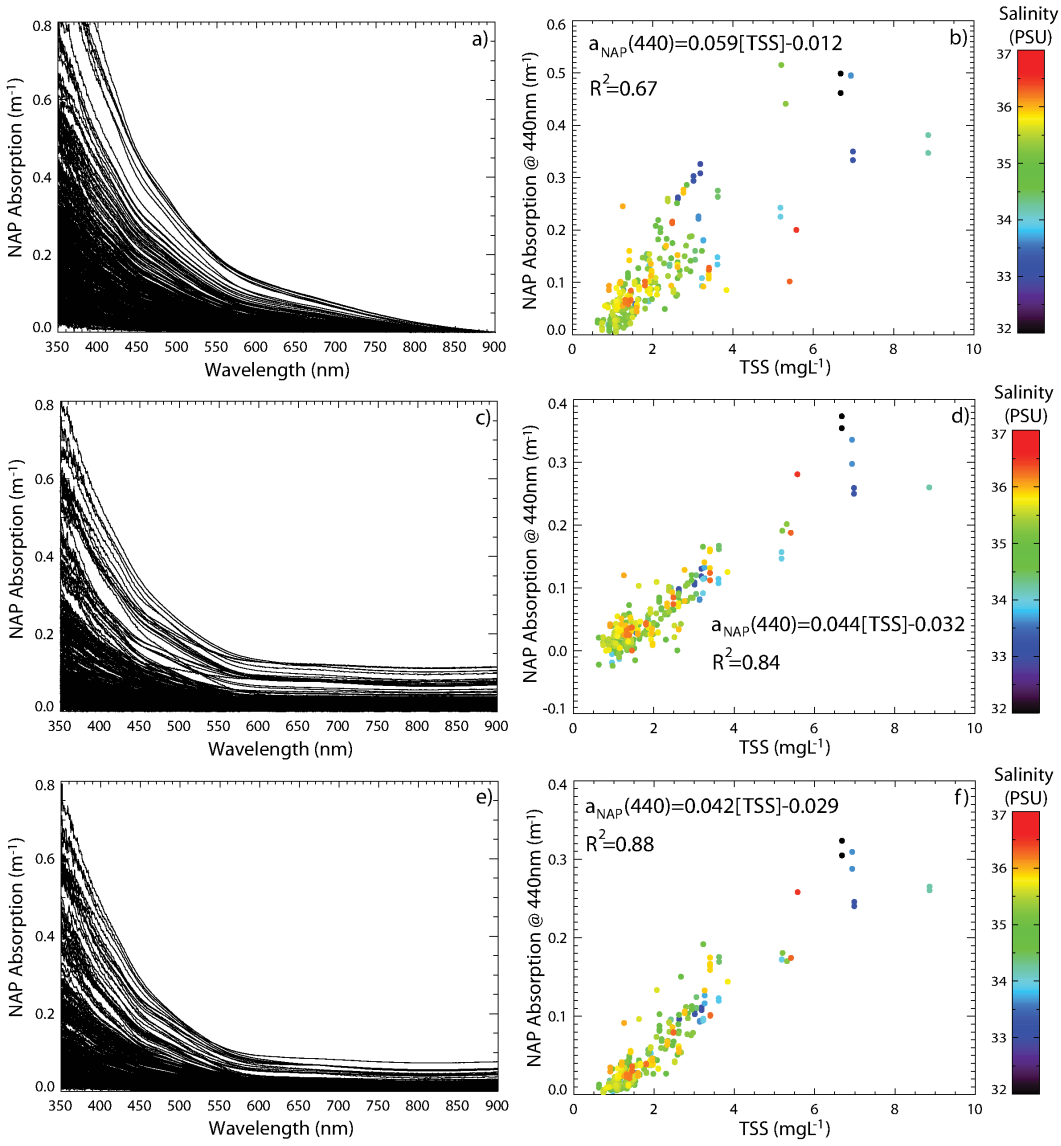

Figure 2.21: Full NAP particle absorption dataset and NAP particle absorption at 440 nm vs TSS for 1) The standard, wavelength independent "Null Offset" at 900 nm scattering correction (a and b). 2) The extrapolative spectral scattering method without baseline offset correction (c and d). 3) The extrapolative spectral scattering method with baseline offset correction (e and f).

Figure 2.21 shows results of the non-pigmented particulate absorption spectra dataset for 3 different scattering correction methods. Figures 2.21a and b show data where OD_{null} in Eq. 2.20 is set to the measured OD value at 900 nm. This is the standard scattering correction approach, except that 900 nm was used instead of the more common 715 or 750 nm value (Zaneveld et al. 1994, Mitchell et al. 2000). It is clear that in this dataset (especially Fig. 2.21c and e) that there is evidence of non-zero spectrophotometer signal in the NIR (700 - 900 nm) region which may be attributable to either scattering or absorption or both.

The second NAP dataset (Fig. 2.21c and d) was scattering-corrected using $OD_{null} = A\lambda^{-\gamma_b}$, where the slight curvature in the uncorrected NIR portion of the NAP absorption was attributed to scattering, and was subtracted from the signal. In this set, spectrally-independent differences between the baseline and the sample OD were not corrected for, thus there are still some random wavelength independent deviations on the resultant absorption data which introduces spread in the data shown in Fig. 2.21d. By studying the general relationship between the scattering-corrected NIR absorption using this method and TSS, and assuming particulate scattering has been adequately removed from the measurement using $OD_{null} = A\lambda^{-\gamma_b}$, then the non-zero NIR absorption coefficient can be estimated from a TSS measurement.

The third NAP dataset (Fig. 2.21e and f) was scattering-corrected using $OD_{null} = A\lambda^{-\gamma_b} + K - B[TSS]$, yielding the final processed dataset. By observing the general relationship between the offset parameter K (Eq. 2.22) and the TSS of the field samples, one may estimate the magnitude of the absorption removed from the spectrum by using K from Eq. 2.22, whilst still correcting for the baseline differences which cause scatter around the true relationship. In this way, the only assumption applied to the a_{NAP} dataset is that, in the NIR, absorption is spectrally flat, and the only source of spectral structure between 730 and 920 nm is due to scattered light loss from the spectrophotometer.

Comparing Figs. 2.21b, d and f, it is clear that progressive processing improve-

ments enhances the correlation coefficient of the non-pigmented particle absorption at 440 nm versus TSS scatter plots ($R^2 = 0.67$, $R^2 = 0.84$ and $R^2 = 0.88$, respectively). However, in observing Fig. 2.21f, there is evidence of a positive TSS-axis intercept which suggests that a TSS of approximately 0.5 mgl^{-1} leads to nil absorption in the blue region. This positive TSS-axis intercept suggests methodological issues which require further discussion. Firstly, the filters used to determine absorption (glass fibre) are physically different from those that are used to measure TSS (polycarbonate). If their retention properties are as reported (and cited previously in the Methods section), the inclusion of the extra sample population of particles from 0.45 to $\approx$ 0.7 μm would increase the TSS measurement slightly, however this cannot explain the $\sim$0.5 mgl^{-1} magnitude of the TSS-axis intercept. Secondly, the TSS filters in this dataset were not rinsed for salts. Instead, the average mass of a salt 'blank' was estimated from a previous fieldwork value and was subtracted, instead of using an offset determined from the salinity of the water. This introduction of a salinity-dependent bias is also far below the magnitude of the TSS x-intercept shown in Fig. 2.4f. Thirdly, it may be possible that a fraction of the non-pigmented particles contributing to TSS are 'invisible', as in the case for DOC (Del-Castillo & Miller 2008). However, to my knowledge there is nothing documented in the literature about this artifact in relation to TSS.

Figure 2.21f presents an approximately linear relationship between non-pigmented particle absorption and TSS concentration, and by observing the salinity-based colour scale, it can be seen that river plume sediment generally exhibits a similar mass specific absorption at 440 nm as does the re-suspended coastal material at higher-salinity. This scatter plot does not, however, reveal if any spectral differences are present. However, it is likely that most of the re-suspended material is similar in composition to the terrestrially-discharged material. Considering the sampling locations were chosen to cover a wide variety of natural particle assemblages, and that there is a clear difference in source mineral content between outer reef lagoon waters and river discharge waters, a mixture of at least two dominant NAP particle types is realistic. In outer reef areas, it is most likely that

terrigeneous coastal particles contribute negligibly to TSS and measured a_{NAP}, while detrital material and/or calcareous material predominates. To study these outer-reef optical properties, spectral linear regression analysis between $a_{NAP}(\lambda)$ and TSS was performed on the 66 outer reef samples to determine TSS specific absorption spectra. To determine the mass-specific absorption properties of the terrestrially-sourced minerals, the entire data set was used. These 2 distinct mass specific absorption spectra are shown in Fig. 2.22a.

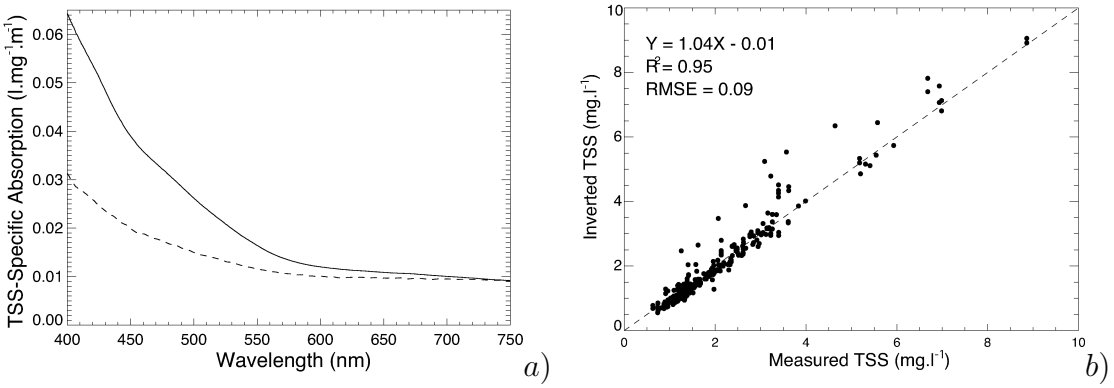

Figure 2.22: a) Regression-derived mass-specific non-pigmented particle absorption spectra of terrestrial (solid) and oceanic (dashed) particles. b) Non-pigmented particle absorption-based TSS versus measured TSS (mgl^{-1}) $R^2 = 0.95$ and $RMSE = 0.09$.

The double basis vector inversion approach (analogous to that outlined for phytoplankton in Eq. 2.44) yielded TSS retrievals with 9% RMS error (see Fig. 2.22b). The spectral shapes of the two different basis vectors in Fig. 2.22a are different, with the oceanic spectral basis vector appearing slightly less than half as efficient at absorbing than the terrestrial basis spectrum. It is assumed that the detritus associated with bleached, living phytoplankton ($a_{cell_{living}}(\lambda)$) and truly detrital particles ($a_{cell_{detrital}}(\lambda)$) in the samples would have a similar spectral shapes to the oceanic basis vector. Based on the data collected, there is at present no way to quantify the relative abundance of these two different fractions.

The terrestrial NAP absorption spectrum contains features consistent with the work of Bowers & Binding (2006) and Babin & Stramski (2002), possibly at-

tributable to iron content (Babin & Stramski 2004). In contrast, the data presented by Blondeau-Patissier et al. (2009) for the same geographic region as reported here shows no spectral structure in the NAP absorption. Although unclear from their methodology, this lack of spectral content may stem from their choice to use a simple exponential function to represent NAP absorption in their figures instead of the actual measurements made. The terrestrial NAP absorption spectrum is assumed to contribute $a_{min}(\lambda)$ to Eq. 2.24.

A ternary plot is shown in Fig. 2.23, indicating the relative contributions of phytoplankton, non-pigmented particles and CDOM absorption at 440 nm for station measurements where all three parameters were measured. The most absorbing waters occurred when a_ϕ contributed approximately 10% of the total absorption, whereas the a_{CDOM} coefficient contributed 65%. The ternary plot highlights that for 440 nm at least, there are no co-varying absorbing constituents. This plot is similar to that of Blondeau-Patissier et al. (2009), where the majority of the absorption budget is usually attributed to either CDOM or NAP.

2.3.3.2.3 Particulate Scattering

The transmissometer measurements of total non-water attenuation coefficients (c_{pg}) collected during fieldwork varied from approximately 0.10 to 3.5 m^{-1} at 660 nm. Figure 2.24a shows the relationship between $c_{pg}(660)$ and TChl. For comparison, a Case 1 relationship $c_p(660) = 0.407[TChl]^{0.795}$ from Loisel & Morel (1998) is shown, which approximately marks out the lower bound of the data points measured in the GBR. The significant spread in data between c_{pg} and TChl demonstrates that non-algal particulates and/or CDOM influences attenuation in the GBR waters sampled.

The suspended mineral scattering at 660 nm (b_{min}) shown in Fig. 2.24b was calculated by correcting measured $c_p(660)$ values by subtracting coincident station absorption measurements of NAP (a_{NAP}), CDOM (a_{CDOM}), phytoplankton absorption (a_ϕ) and estimates of phytoplankton scattering (b_ϕ):

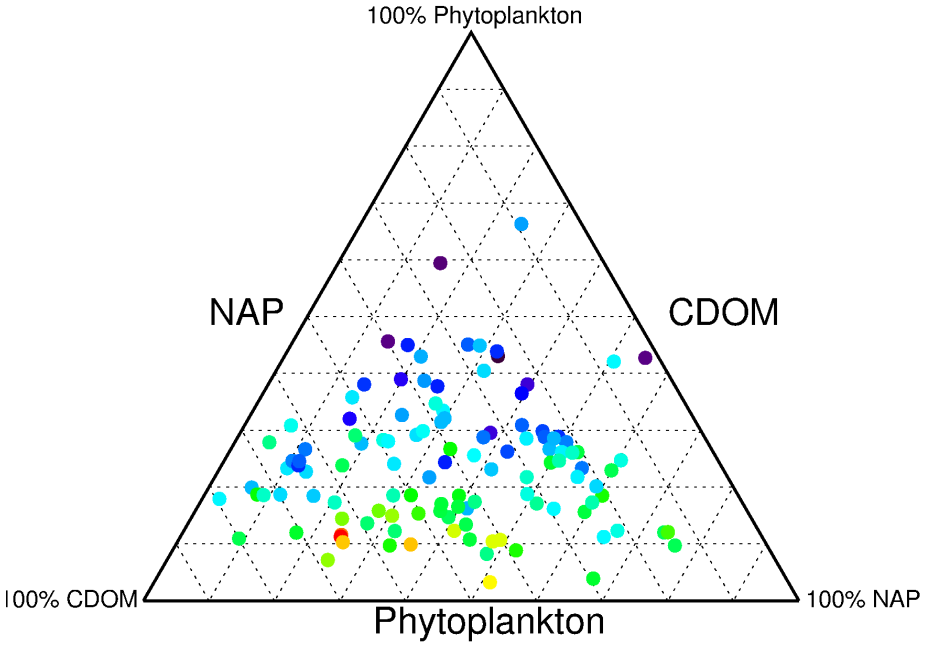

Figure 2.23: Ternary plot showing the relative absorption at 440 nm of the three distinct optical components; CDOM, phytoplankton and non-pigmented particles (NAP). The dotted lines indicate 10% intervals in consituent concentration. Plot symbols are colour coded with total non-water absorption (red being the highest at 1.32 m^{-1}, and violet being the lowest at 0.04 m^{-1})

$$b_{min}(660) = c_{pg}(660) - a_{NAP}(660) - a_{CDOM}(660) - a_{\phi}(660) - b_{\phi}(660), \quad (2.49)$$

where, according to the models published by Loisel & Morel (1998):

$$b_{\phi}(660) = 0.407[TChl]^{0.795} - 0.014[TChl]^{0.817}. \quad (2.50)$$

Based on the regression in Fig. 2.24b, and assuming the small intercept is a byproduct of methodological uncertainties, the relationship between TSS and $b_{min}(660)$ can be described as:

$$b_{min}(660) = b^{*}_{min}(660)[TSS], \quad (2.51)$$

where $b^{*}_{min}(660) = 0.339$ (determined from the slope of Fig. 2.24b).

The slope of 0.339 is very close to the mineral mass-specific coefficients of Bowers & Binding (2006), and also very close to the simulated inorganic mass specific scattering coefficients shown in Table 6 of Babin, Morel, Fournier-Sicre, Fell & Stramski (2003). The relationship between the total scattering coefficient, b and TSS will be useful later in Chapter 3, however later the backscattering coefficient (b_b) will be of prime importance when dealing with the interpretation of ocean colour remote sensing data.

2.3.3.2.4 Particulate Backscatter

Backscattering coefficients (b_{bp}) varied from near-zero to approximately 0.37 m^{-1} at 442 nm. Figure 2.25a shows the entire particulate backscatter (b_{bp}) dataset, with hyperbolic model fits overplotted to assist visualising the backscattering spectrum.

The hyperbolic model is in the form:

$$b_{bp}(\lambda) = b_{bp}(555)\left(\frac{\lambda}{555}\right)^{-\gamma_{bb}}, \quad (2.52)$$

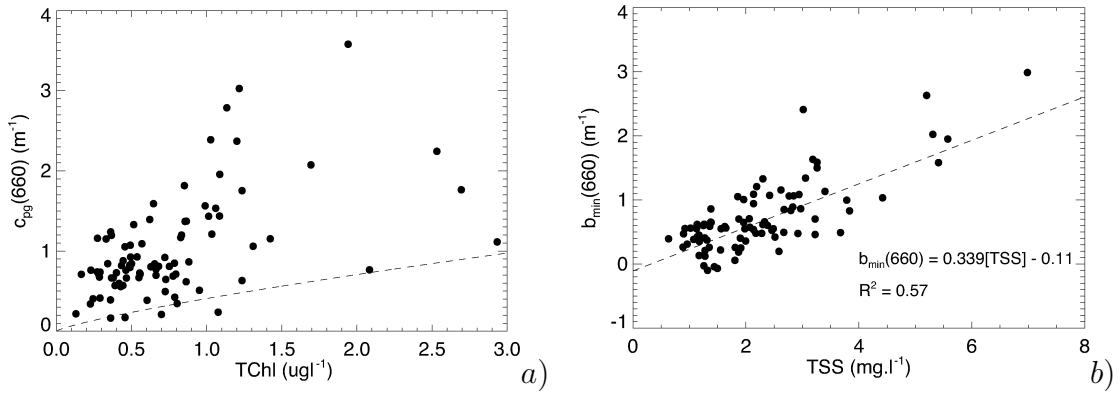

Figure 2.24: a) Total non-water attenuation (c_{pg}) at 660 nm versus TChl for the GBR dataset. The non-linear Case-1 relationship of Loisel & Morel (1998) is shown for comparison (dashed line). b) The estimated non-algal particulate scattering at 660 nm versus TSS for the GBR dataset. The dashed line is the linear fit to $b_{min}(660)$ vs TSS data.

where γ_{bb} is the spectral slope of the backscattering spectrum, and 555 nm is chosen arbitrarily to normalise the spectra. 555 nm is a widely-used wavelength in ocean optics is also a wavelength where phytoplankton absorption is minimal, so the possibility of measurement artifacts are reduced.

The backscattering coefficient at 555 nm ($b_{bp}(555)$) varied approximately linearly with TSS concentration ($R^2 = 0.85$), as shown in Figure 2.25b, and described by:

$$b_{bp}(555) = 0.00986[TSS] - 0.00555. \tag{2.53}$$

Due to the apparent or expected simplicity of the backscattering spectrum, or lack of hyperspectral backscattering information, remote sensing inversion algorithms often rely on the use of Eq. 2.52 (Lee et al. 1999). Depending on the approach, some inversion techniques would benefit from characterising the γ_{bb} slope parameter for a particular region. The γ_{bb} slope parameter is plotted versus $b_{bp}(555)$ in Figure 2.25c. The slope parameter varies from a value near 5 in clear waters, down to approximately 1.5 in the most turbid waters sampled. Slopes greater than 4 are considered too high for marine hydrosols, so two data points in Figure 2.25c are questionable. By plotting γ_{bb} versus $1/b_{bp}(555)$ in Fig. 2.25d, an approximately linear relationship is seen. From this data, the slope parameter

γ_{bb} in Eq. 2.52 can be modelled with the inverse relationship shown below:

$$\gamma_{bb} = \frac{0.00380}{b_{bp}(555)} + 1.454, \tag{2.54}$$

where 0.00380 is the slope and 1.454 is the intercept of the line in Figure 2.25d.

The equations 2.52 and 2.54 have the potential for modelling the spectral shift of the backscattering spectrum in GBR waters from only one parameter - $b_{bp}(555)$ (or TSS assuming the quasi-linear trend shown in the logarithmic axis in Figure 2.25b). Figure 2.25e shows a histogram of the errors in modelling γ_{bb} using Eq. 2.54. It should be noted that there is some spread in the histogram population (σ=0.28). The $\pm 1\sigma$ and $\pm 2\sigma$ confidence limits are shown in Figures 2.25c and d. The potential impact of the uncertainty in the modelled γ is propagated into Eq. 2.52, and shown in Fig. 2.25f. These results indicate the Eq. 2.54 model will produce b_{bp} with errors less than approximately 10% in approximately 68.3% of the data and errors less than approximately 20% in approximately 95% of the data in the visible range from 400 to 700 nm.

As mentioned previously for non-pigmented particle absorption, it is expected that there is a shift from terrestrial to oceanic sourced particulates from coastal to outer shelf waters. An oceanic (detrital / phytoplankton) mass-specific backscattering end-member was determined from the 23 coincident TSS and b_{bp} measurements performed on the outer shelf region, and the terrestrial mass-specific backscattering was determined from the entire dataset. These two basis vectors are shown in Fig. 2.26a. The TSS-specific basis vectors can be represented using Eq. 2.52, with $b^*_{bp(min)}(555) = 0.01114$, $\gamma_{bb} = 1.227$ for terrestrial particles, and $b^*_{bp(det)}(555) = 0.00302$, $\gamma_{bb} = 3.347$ for the outer shelf particles. These coefficients were determined ignoring the data from 676 nm channel of the Hydroscat due to possible fluorescence artifacts which could bias the basis vectors (McKee & Cunningham 2005). These basis vectors may be used to retrieve the TSS concentrations based on a measured $b_{bp}(\lambda)$ alone, by a spectral optimisation blending approach analogous to Eq. 2.44, where the concentrations TSS_{det} and TSS_{min} are varied until the reconstructed $b_{bp}(\lambda)$ matches the measured $b_{bp}(\lambda)$. The spectral

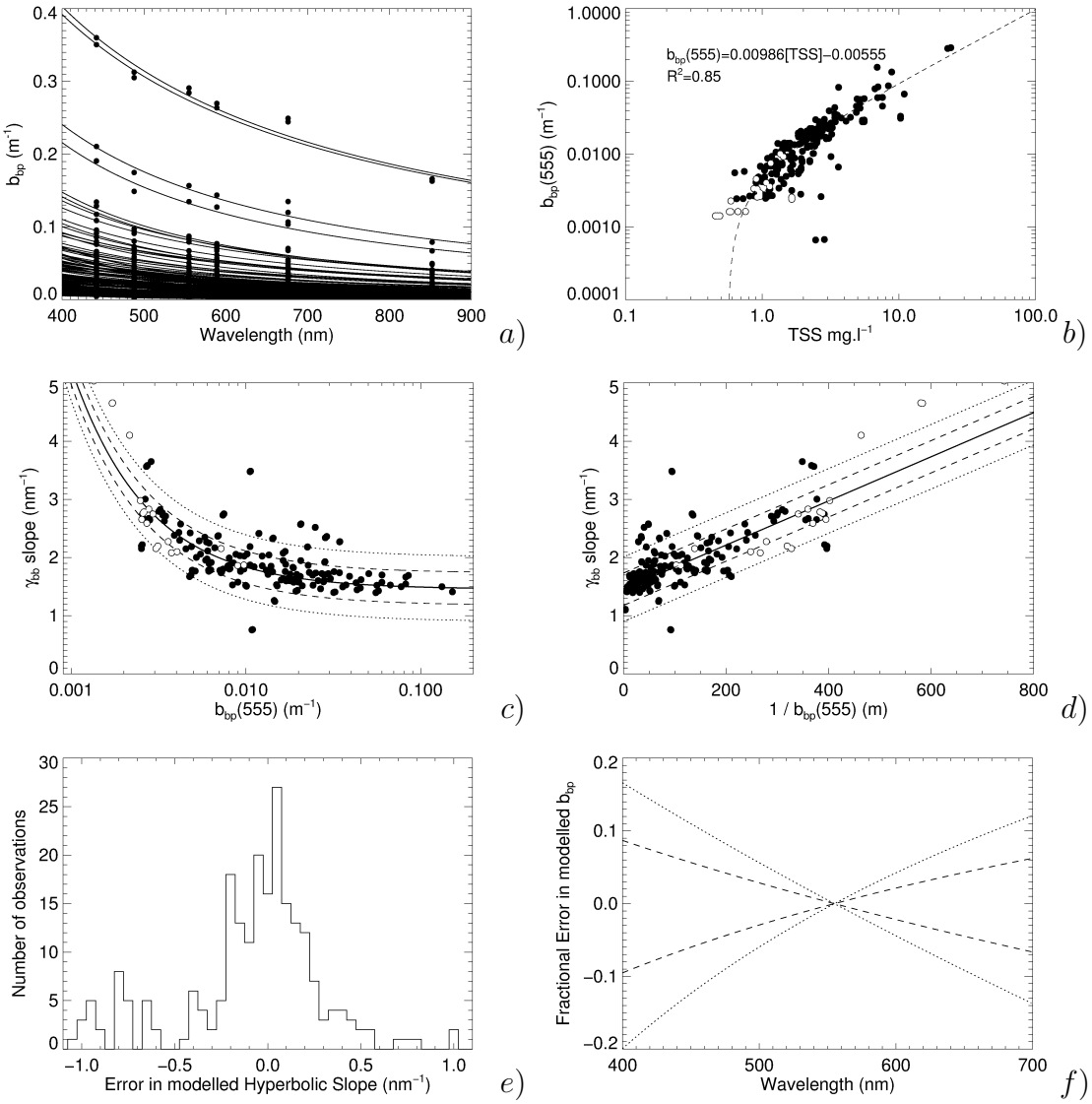

Figure 2.25: a) The full particulate backscattering dataset (black plot symbols), with hyperbolic model spectral match (solid, continuous line). b) Particulate backscatter at 555 nm ($b_{bp}(555)$) versus Total Suspended Solids (TSS). Note: unfilled plot symbols denote the outer-shelf data points, both axes are logarithmic and the dashed line is the line of best fit. c) Hyperbolic model spectral slope (γ) versus particulate backscatter at 555 nm ($b_{bp}(555)$). The solid line is plotted from Eq. 2.54. The dashed lines show the $\pm 1\sigma$ interval, and the dotted lines show $\pm 2\sigma$ interval, generated with Eq. 2.54. d) Hyperoblic model spectral slope (γ) versus inversed particulate backscatter at 555 nm ($1/b_{bp}(555)$), showing the same Eq. 2.54 model fits and confidence intervals as c. e) Histogram of the error in γ_{bb}, as modelled from b_{bp} using Eq. 2.54. f) Fractional errors in modelling $b_{bp}(\lambda)$ based on the propagation of the confidence interval uncertainties of Eq. 2.54. As in c and d, the dashed line is $\pm 1\sigma$ and the dotted line is $\pm 2\sigma$.

reconstruction equation is expressed as:

$$b_{bp}(\lambda) = TSS_{min}\left[b^*_{bp(min)}(555)\left(\frac{\lambda}{555}\right)^{-\gamma_{min}}\right] + TSS_{det}\left[b^*_{bp(min)}(555)\left(\frac{\lambda}{555}\right)^{-\gamma_{det}}\right], \tag{2.55}$$

where TSS_{det} is the estimated TSS concentration due to detrial / calcareous particles and TSS_{min} is the estimated TSS concentration due to terrestrially-sourced particles. The total TSS is the sum of these values. $b^*_{bp(min)}(555) = 0.01081$, $\gamma_{det} = 1.228$ for terrestrial particles, and $b^*_{bp(det)}(555) = 0.00302$, $\gamma_{det} = 3.347$ for the outer shelf particles (see Figure 2.26a).

To test the suitability of the two different model approaches to reproduce the measured dataset, the measured $b_{bp}(\lambda)$ dataset was spectrally inverted using Levenberg-Marquardt spectral optimization of both the double basis vector (Equation 2.55) and spectral slope (Equations 2.52-2.54) inversion approached. Both approaches worked satisfactorily, with RMS errors of 0.34 and 0.23, respectively. By comparing Figs 2.26b and c, it can be seen that the spectral slope inversion produces a tighter distribution (correlation coefficients $R^2 = 0.84$ v.s. $R^2 = 0.78$), resulting in higher precision retrievals.

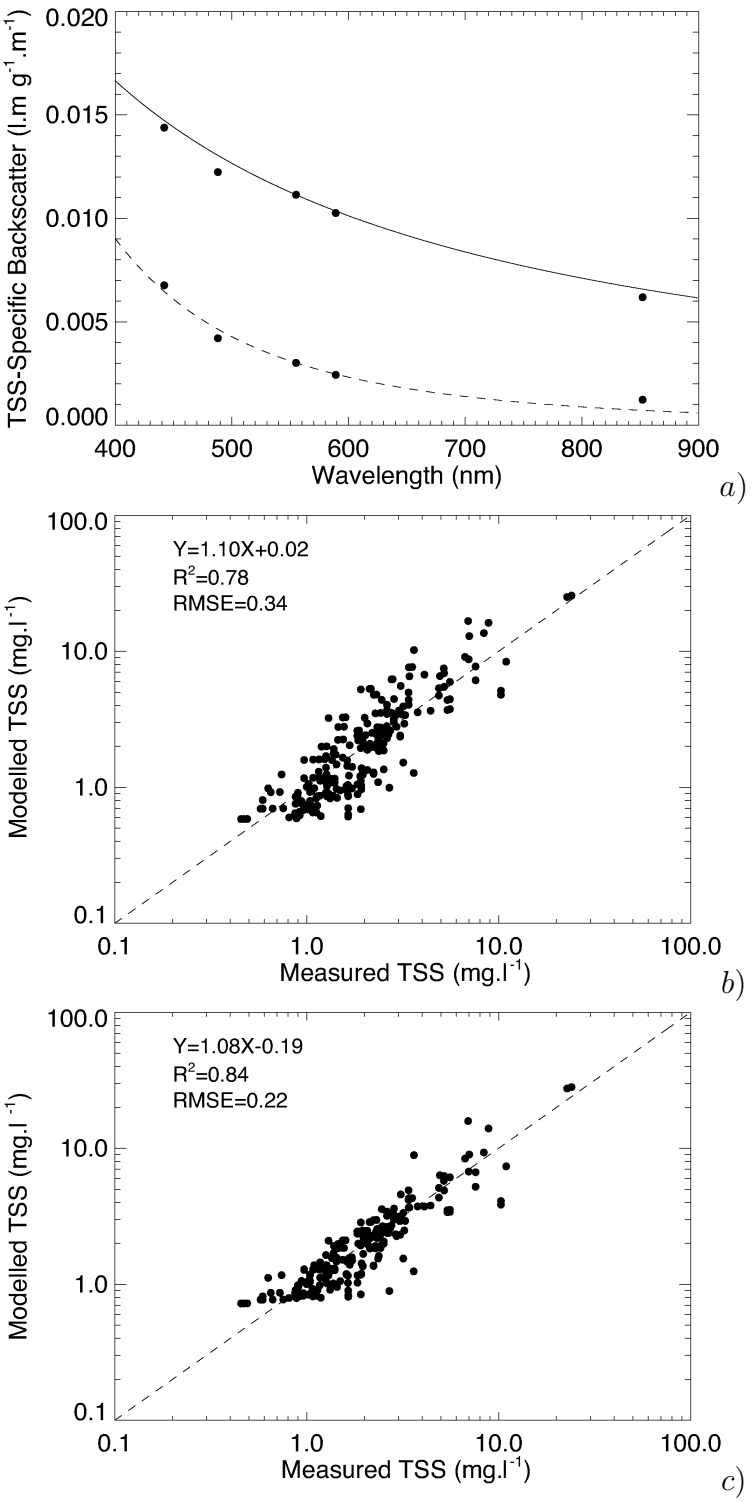

Figure 2.26: a) The TSS-specific $b_{bp}(\lambda)$ end-members. The TSS-specific basis vectors can be represented using Eq. 2.52, with $b^*_{bp}(555) = 0.01081$, $\gamma_{bb} = 1.228$ for terrestrial particles (solid line), and $b^*_{bp}(555) = 0.00302$, $\gamma_{bb} = 3.347$ for the outer shelf particles (dashed line). b) The TSS inversion using the double-basis blend vector b_{bp} model to approximate measured b_{bp}. c) The TSS inversion results using Eq. 2.52-2.54 to approximate measured b_{bp}.

2.3.3.2.5 Phase Function

As shown in Fig. 2.27a, the Mie modelled scattering phase function calculations of the *Prochlorococcus* population at 400 nm contains a spectral feature at approximately 25° and 40°. Similar features were also apparent in the VSF measurements of O'Bree (2007) for samples collected in the tropical GBR waters, however the angular locations of these features differed. This may be due to the presence of *Synnechococcus* in the field samples measured and/or that the O'Bree (2007) VSF measurements were performed at 633 nm (both of these shift the minima to larger angles). Figure 2.27b shows Mie model outputs for the *Prochlorococcus* population, evaluated over a range of wavelengths to demonstrate the wavelength dependency exhibited in the spectral feature. The backscattering ratio ($B_p = b_{bp}/b_p$) of the simulated Diatom and *Prochlorococcus* phase functions were calculated as 0.0342 and 0.0017 respectively, which is very close to the upper range measured by Boss et al. (2004). However, these *Prochlorococcus* backscattering ratio is approximately a factor of 2 lower than the minimum backscattering ratio presented in Boss et al. (2004). This is perhaps not surprising considering the field measurements of Boss et al. (2004) would contain contributions from detrius and minerals in addition to *Prochlorococcus*.

The Fournier-Forand phase function (generated by Eq. 2.31) requires the input of either the refractive index n and the hyperbolic slope of the Junge size distribution μ (see Eq. 2.36) or μ and the backscattering ratio B_{min}. For calculations used in this study, μ was determined using the average spectral slope of $\gamma_b = 0.65$, determined as a byproduct of the NIR Quantitative Filter Technique-based scattering correction process (Eq. 2.22). This γ_b was used to estimate μ (i.e. $\mu = \gamma_b + 3$ as in Eq. 2.36).

The spectral backscattering ratio ($B_{min}(\lambda)$) was estimated by combining the mass specific backscattering and total scattering spectral models, i.e.

$$B_{min}(\lambda) = \frac{b^*_{b_{min}}(\lambda)}{b^*_{min}(\lambda)}, \tag{2.56}$$

where:

$$b^*_{b_{min}}(\lambda) = 0.0087 \left(\frac{\lambda}{660} \right)^{-1.228} \tag{2.57}$$

is derived from Eq. 2.52 using the coastal end-member coefficients shown in Fig. 2.26a ($b^*_{bp}(555) = 0.01081$ and $\gamma_{bb} = 1.228$), and

$$b^*_{min}(\lambda) = 0.339 \left(\frac{\lambda}{660} \right)^{-0.65} \tag{2.58}$$

is derived from combining Eq. 2.26 ($\gamma_b = 0.65$) with Eq. 2.51.

The resultant estimated mineral particulate backscattering ratio (B_{min}):

$$B_{min}(\lambda) = 0.0257 \left(\frac{\lambda}{660} \right)^{-0.578} \tag{2.59}$$

The modelled *Prochlorococcus* phase function is determined on a realistic, nearly monodisperse particle size distribution, so it exhibits wavelength dependence (see Fig. 2.27b). Once a wide variety of different sized phytoplankton particles are considered, however, (as in the simulation of the Diatom population), this wavelength dependence is significantly reduced (see Fig. 2.27c). The Fournier-Forand phase function is inherently determined for hyperbolic particle size distributions, but is parameterised by the backscattering ratio model which was found to be wavelength dependent (Eq. 3.38). The Fournier-Forand phase functions for different wavelengths are shown in Fig. 2.27d, and only exhibit subtle wavelength dependence. The phase function modelling shown here provides an important input into software-based radiative transfer modelling, which will become important in the next chapter. Although the wavelength dependence is small, ultimately, the overall wavelength dependence depends on the relative abundance of the different scatterers. This wavelength dependence is maintained through subsequent simulation chapters.

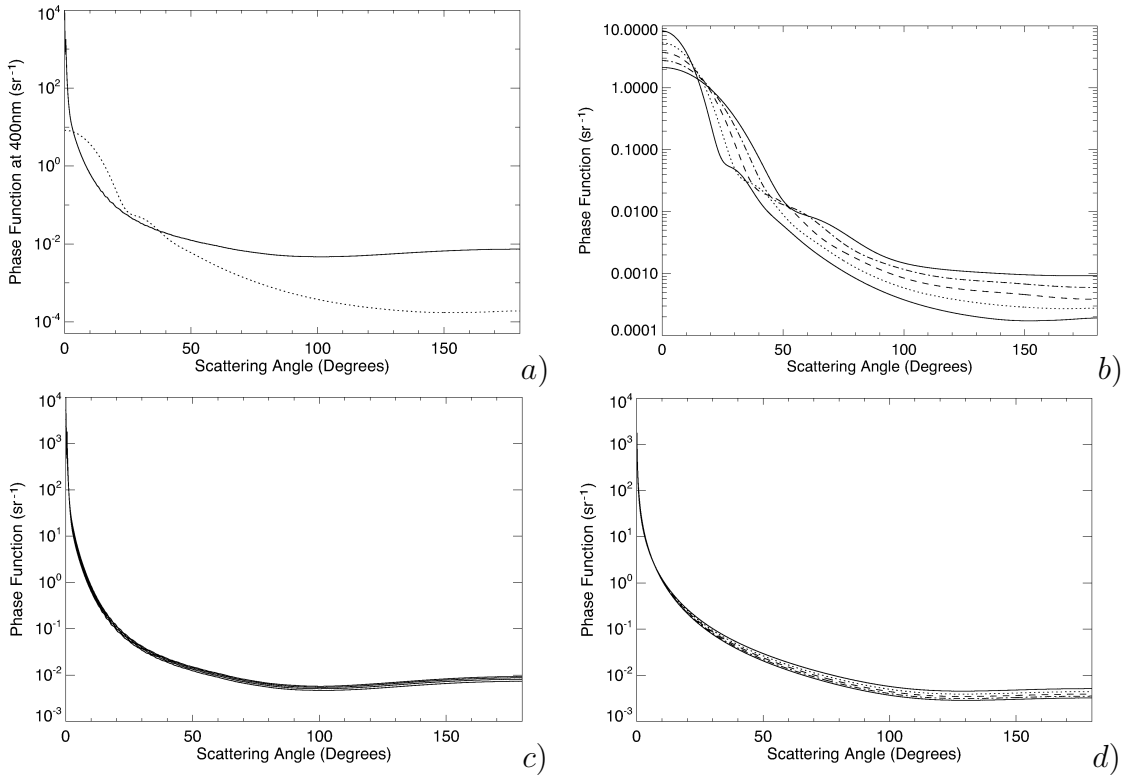

Figure 2.27: a) Mie scattering-determined phase functions for *Prochlorococcus* (dotted line), simulated Diatom assemblage (solid line). b) Mie-based *Prochlorococcus* phase functions at $400, 500, 600, 700$ and 800 nm (solid, dotted, dashed, dot-dash and triple-dot-dash lines, respectively). c) Mie-based Diatom phase functions at $400, 500, 600, 700$ and 800 nm. d) Fournier-Forand mineral phase functions generated by Eqs. 3.38, 2.36 and Eq. 2.31 at $400, 500, 600, 700$ and 800 nm.

2.4 Summary

- IOPs (namely a_ϕ, a_{NAP}, a_{CDOM} and b_{bp}) were measured in GBR waters alongside water quality parameters of interest (namely TSS, TChl, and DOC).

- A series of candidate functional relationships (or end-members) were derived to predict the spectral IOPs of GBR waters for a given water quality concentration. These spectral relationships were then used to invert measured IOP spectra in order to retrieve the corresponding optically-based water quality parameters. The retrieval accuracy of each functional relationship was estimated based on the comparison with *in situ* measured water quality parameters.

- GBR specific phytoplankton phase functions were estimated using Mie theory, with literature-based refractive index inputs and estimated size populations. GBR-specific mineral phase functions were estimated using Fournier-Forand using a mass-specific backscattering ratio estimated from GBR measurements and an average Junge size distribution hyperbolic slope, based on the NIR spectral scattering errors from the GBR QFT absorption measurements.

Figure 2.28 collects together the absorption end-members determined from the data measured in the GBR region in this study. Both DOC-specific CDOM absorption and TSS-specific detrital or mineral absorption spectra are similar in shape, exhibiting a decaying exponential form, although the exponential slope of the CDOM absorption end-member is greater than that of either mineral or oceanic/detrital absorption. The similarity of the spectral shapes may present difficulty for distinguishing the different constituents from total absorption information alone. However, fortunately, backscattering is also correlated strongly with TSS and not with CDOM, so including backscatter in a simultaneous TSS and DOC retrieval scheme should be effective. This will be evaluated later. It should be noted that the spectra

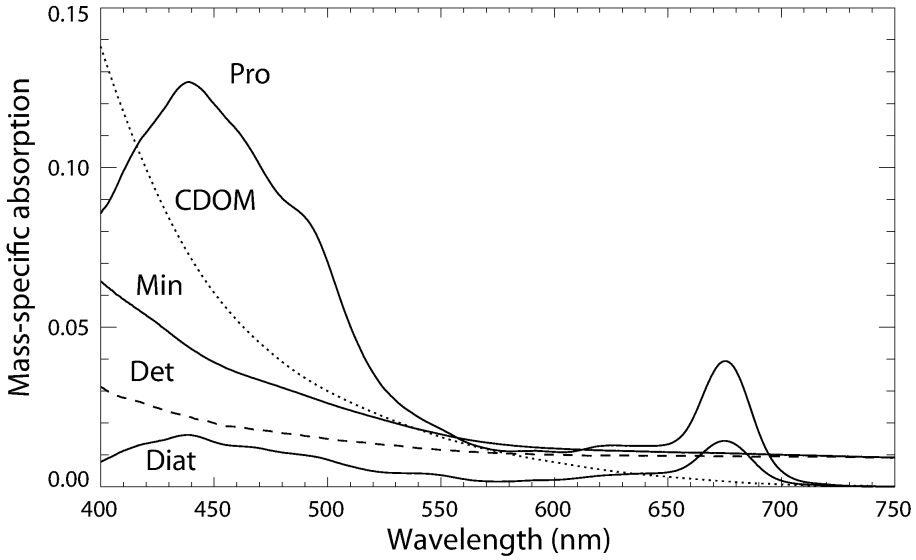

Figure 2.28: Mass-specific absorption end-members determined from the GBR dataset. Pro is *Prochlorococcus* and Diat is Diatom TChl-specific absorption ($l.\mu g^{-1}m^{-1}$). CDOM is the scaled DOC-specific CDOM absorption ($l.cg^{-1}m^{-1}$). Min is the (terrestrial) mineral and Det is the (oceanic) detrital TSS-specific absorption ($l.mg^{-1}m^{-1}$).

Chapter 3

Remote Sensing Reflectance and Inherent Optical Properties

3.1 Introduction

The apparent colour of the ocean is governed by the spectral Inherent Optical Properties (IOPs) (namely, a, b_b or $\beta(\theta)$) of water and its constituents and the geometry of the incident light field. Significant research efforts over the last 30 years have sought to functionalise the relationship between the remotely-sensed signal and the in-water inherent optical properties (Gordon et al. 1975, Morel & Prieur 1977, Carder et al. 1986, Gordon et al. 1988, Lee et al. 1998, 1999, 2002). The common goal of this research lineage was to be able to use large-scale spatial and temporal reflectance measurements such as those provided from polar-orbiting satellites to obtain biogeochemical information about the world's oceans.

Ocean colour remote sensing imagers are typically designed[1] to measure the radiance $L_w(\lambda)$ emanating from the water (denoted by subscript w), for it contains the information about the constituents of the water column. These polar orbiting satellites take images during different seasons with differing viewing geometries, so it is commonplace to normalize $L_w(\lambda)$ by the downwelling irradiance ($E_d(\lambda)$)

[1]The total radiance recorded by satellites is referred to as L_t or L_{TOA} (Top Of Atmosphere), for this measurement is subject to atmospheric contributions, sun-glint and surface reflected skylight. The subtraction of these other confounding terms to deduce L_w is outside the scope of this thesis, however remains an active region of research - especially in coastal waters.

incident on the ocean surface in order to produce a more spatially and temporally consistent dataset which highlights changes due to in-water constituents rather than illumination conditions. This normalized product is referred to as the remote sensing reflectance as defined by (Sathyendranath 2000):

$$R_{rs}(\theta_v, \theta_s, \phi_{az}, \lambda) = \frac{L_w(\theta_v, \theta_s, \phi_{az}, \lambda)}{E_d(\theta_s, \lambda)}, \tag{3.1}$$

where θ_v is the view nadir angle, θ_s is the solar zenith angle, ϕ_{az} is the sun-relative azimuth angle, λ is the wavelength, L_w is the water-leaving radiance and E_d is the downwelling irradiance.

In order to interpret observed multi or hyper-spectral $R_{rs}(\theta, \phi, \lambda)$ measurements to spatially quantify in-water substances that have an optical signature, the following expression based on the assumption of elastic scattering is commonly used (Gordon et al. 1988, Lee et al. 1998):

$$R_{rs}(\theta_v, \theta_s, \phi_{az}, \lambda) = \frac{f(\theta_s, \lambda)}{Q(\theta_v, \theta_s, \lambda, \phi_{az})} \left(\frac{b_b(\lambda)}{a(\lambda) + b_b(\lambda)} \right), \tag{3.2}$$

where $a(\lambda)$ is the total absorption spectrum (m^{-1}), $b_b(\lambda)$ is the total backscattering spectrum (m^{-1}) and $\frac{f}{Q}$ partly depends on solar and sensor geometry (θ_v,θ_s,ϕ_{az}), but also on the phase function of the scattering particles present and the sea surface state (related to wind speed).

The total absorption and backscattering coefficients can be attributed to the sum of the optically or operationally distinct fractions present in the water column:

$$a(\lambda) = a_w(\lambda) + a_\phi(\lambda) + a_{NAP}(\lambda) + a_{CDOM}(\lambda) + \ldots \tag{3.3}$$

$$b_b(\lambda) = b_{bw} + b_{b\phi}(\lambda) + b_{bNAP}(\lambda) + \ldots \tag{3.4}$$

where the subscripts denote contributions from water (w), phytoplankton (ϕ), non-algal particulates (NAP) and chromophoric (coloured) dissolved organic matter ($CDOM$).

Chapter 2 demonstrated the link between the IOPs of GBR waters and their corresponding water quality parameters, so that the inputs to Eqs. 3.3 and 3.4 may be functionalised with TSS, TChl and DOC parameters. This Chapter is concerned with first measuring R_{rs} accurately, and then establishing the validity of Eq. 3.2 for GBR waters, and more specifically, the nature of $\frac{f}{Q}$, so that field-measured R_{rs} spectra can be converted into information about the IOPs (and hence water quality) of the GBR waters.

3.2 Methods

3.2.1 Measuring R_{rs} with the DALEC Spectroradiometer

The DALEC (Dynamic Above-water radiance (L_u) and irradiance (E_d) Collector), the primary sensor used in this research, is comprised of three radiometrically-calibrated spectroradiometers designed to measure the sky radiance (L_{sky}), the upwelling radiance (L_t) and the downwelling irradiance (E_d) in near-simultaneous fashion. The instrument was designed specifically to operate from a moving vessel, whilst continually recording a large number of measurements across previously unattainable spatial scales. The spectrometer integration times (analogous with the concept of 'exposure time' in a camera) are designed to be dynamically optimised throughout the course of the transect to ensure optimum signals are measured. In this way, the often rapidly-changing spectral signatures of coastal waters could be sampled with higher quality. Another benefit of the DALEC approach is that sampling can be performed rapidly across spatial scales more relevant to comparing with large remote sensing satellite image pixels which are in the order of 250 m up to 1 km^2.

The data from the three separate calibrated above-water radiometers is generally combined in an equation described by Mobley (1999) to determine the remote sensing reflectance (R_{rs}):

$$R_{rs} = \frac{L_t - \rho L_{sky}}{E_d}, \tag{3.5}$$

where ρ is the fraction of skylight which is reflected from the ocean surface into the sea-viewing sensor, L_{sky} is the sky radiance measured at the complementary angle of the sea-viewing radiance (L_t) sensor.

The radiance (L_{sky}, L_t) sensors were designed to be view angle adjustable, however were set to 40° from zenith and nadir respectively, to provide complementary L_{sky} are L_t measurements applicable to Eq. 3.5 when the DALEC is level. The DALEC housing design incorporates a friction-damped dual-axis gymbal mount to help maintain consistent optical view geometry despite vessel motion often encountered during transit.

3.2.1.1 DALEC Geometry

The DALEC has an in-built Global Positioning Satellite (GPS) receiver, so each spectrum has an associated GPS position, date and UTC time. This GPS information can be used to calculate solar zenith angle and solar azimuth (Reda & Andreas 2008, NOAA 1997). When in transit, successive GPS positions allow the calculation of an estimate ship heading. The DALEC's boom azimuth relative to the ship heading was manually set and recorded in a log book. To avoid ship shadow and sun glint, the DALEC boom azimuth angle was manually adjusted to achieve an approximate $\phi_{rel} = 135°$ separation between the DALEC azimuth and the solar azimuth (see Fig. 3.3). Collection of this data during transect allows the DALEC sun-relative azimuth angle to be estimated at any time. This information, useful for quality control purposes, may assist the skylight reflection correction process and is also useful for determining the appropriate conversion factor between R_{rs} and $\frac{b_b}{a+b_b}$ which will be discussed later in the chapter.

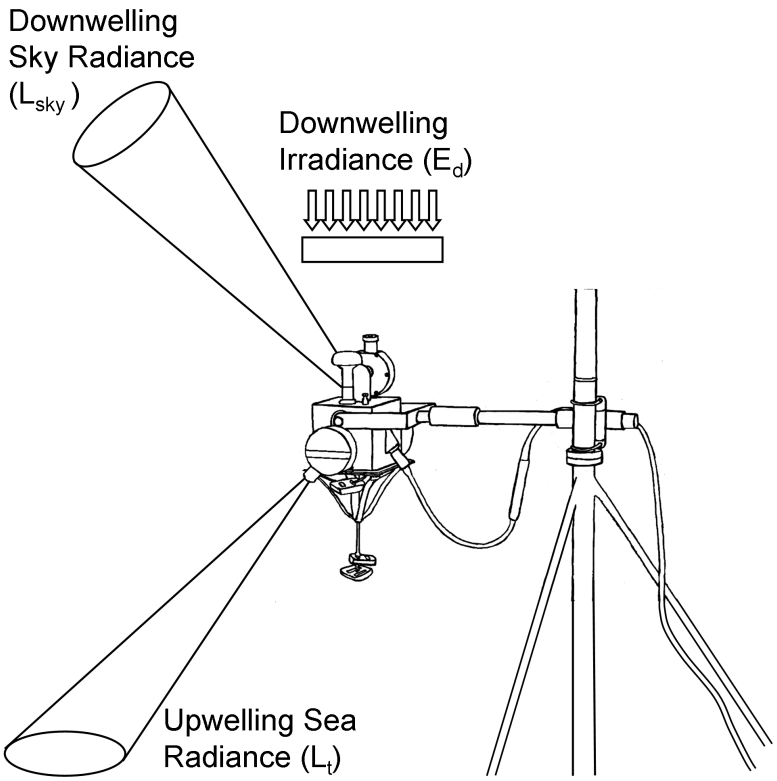

Figure 3.1: The DALEC spectroradiometer, showing its principal radiometric measurements of L_t, E_d and L_{sky}. The sky-viewing radiance sensor is located on the other side of the DALEC, so is not shown. It looks identical to the L_t sensor, but is pointing skyward.

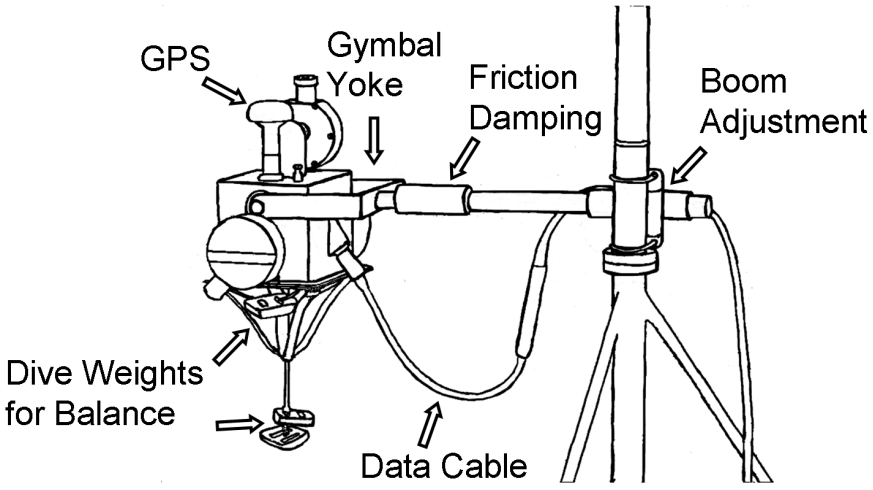

Figure 3.2: More details of the DALEC spectroradiometer and mounting.

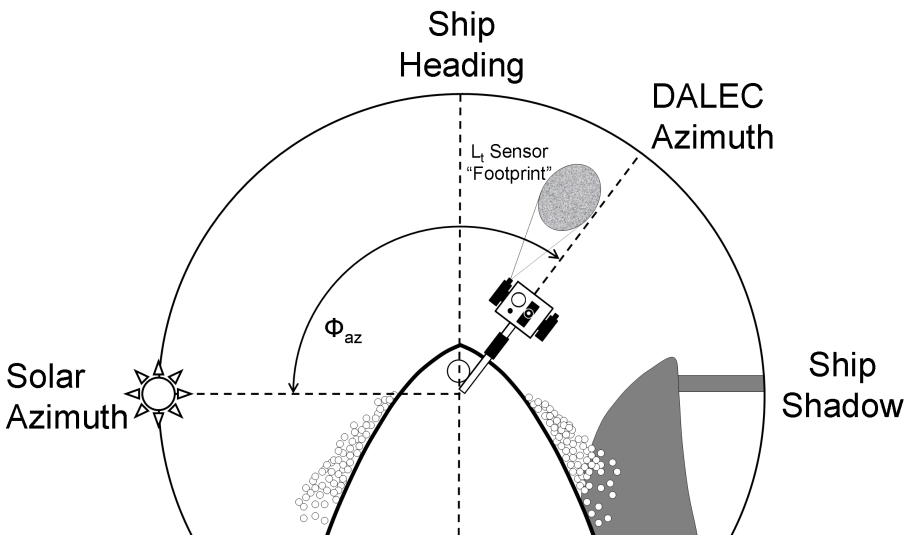

Figure 3.3: Overhead (nadir) view diagram of the ideal DALEC azimuthal geometry during deployment.

3.2.1.2 Calibration and characterisation

The accuracy of water quality inversions depends partly on the accuracy of the input spectroradiometric measurements which are used to form the R_{rs} sample. For L_u and E_d measurements, Zeiss MMS-1 UV-VIS NIR enhanced spectrometers were used. The Zeiss MMS-1 spectrometer modules have been in use in scientific radiometric studies for over a decade (Kutser et al. 2003). These spectrometers are described by the manufacturer as being 'monolithic' because the light-receiving fibre optic bundle is glued directly to the entrance slit of a spectrometer. This manufacturing design feature is intended to improve the radiometric stability of the device. To further improve radiometric stability, the MMS-1 modules are installed in the DALEC so that the input fibre bundles are never bent past their specified bend radius and once in place inside the DALEC housing, cannot move.

For the L_{sky} measurement, a compact but less mature Ocean Optics' USB2000 spectrometer was used. This spectrometer featured a threaded entrance port which was connected directly to the rigid collimating optics.

In order to have accurate R_{rs} data, the digital 'count' outputs of the three spectroradiometers from the DALEC were compared with the spectral calibration of a

1000 W NIST-traceable lamp (Optronic Laboratories, OL-83A) powered at 8 A, 120 V with a 0.01% stable current power supply. The direct lamp and reflectance plaque methods of Meuller & Austin (2003) were used for irradiance and radiance respectively. The particular lamp (SN F-793, Optronic Laboratories) was within the 50 hour, 1 year calibration transfer period.

The spectral irradiance (E) emitted by the NIST-calibrated FEL lamp, measured at a distance (r) from the filament was determined by the following equation:

$$E_r(\lambda) = E_{50}(\lambda) \left[\frac{50 + \Delta f}{r + \Delta f} \right]^2, \tag{3.6}$$

where Δf is typically $\approx 3\ mm$ (the distance from the front face of the lamp alignment jig and the front face of the filament), E_{50} is the spectral irradiance calibration data of the lamp measured at the standard 50 cm, and $r = 50.50 \pm 0.15\ cm$. The irradiance responsivity factors F_E were then determined by:

$$F_E(\lambda) = \frac{E_r(\lambda)}{V_r(\lambda) - V_{amb}(\lambda)}, \tag{3.7}$$

where $V_r(\lambda)$ are the detector counts during illumination and $V_{amb}(\lambda)$ are the counts when the filament is occluded (the ambient signal). The calibrations were then applied to field measurement using the following formula:

$$E(\lambda) = F_E(\lambda)[V(\lambda) - V_{dark}(\lambda)], \tag{3.8}$$

where $V_{dark}(\lambda)$ is the 'dark count'; the count when no light is incident on the spectrometer input.

For radiance calibration, a Labsphere SRT-99-100 Spectralon plaque was used to reflect light from the aforementioned NIST lamp at distance $r = 201.10 \pm 0.25\ cm$ from the plaque. The radiance responsivity factors (F_L) were then determined using:

$$F_L(\lambda) = \frac{\rho(\lambda, 45°) E_r(\lambda)}{\pi(V_r(\lambda) - V_{amb}(\lambda))}, \tag{3.9}$$

where $\rho(\lambda, 45°)$ is the spectral reflectivity of the Spectralon plaque viewed at $45°$[2].

The calibrations were then applied to field measurement using the following formula:

$$L(\lambda) = F_L(\lambda)[V(\lambda) - V_{dark}(\lambda)]. \tag{3.10}$$

3.2.1.2.1 Detector Linearity

Solid state spectrometers utilize an electronic circuit known as an 'integrator', where charge due to photon and thermal excitation of the detector is accumulated on capacitive electronic components over a user-defined time *integration time* (t) in milliseconds. The Zeiss spectrometer detector 'charge' (or voltage) signals are digitised with 15-bit analog-to-digital converters (ADCs), so for any given integration time, the maximum resolvable charge 'count' ($V(\lambda)$) is $2^{15} = 32,768$. The USB2000 spectrometer has a 12-bit ADC, resolving $2^{12} = 4,096$ counts. In order to make accurate spectrometer measurements, it is then important to know the integration time associated with a given $V(\lambda)$ measurement. Due to the limited dynamic range of the spectrometers (i.e. 15 or 12 bit), and the natural variability in ocean and sky radiance and solar irradiance, it is often necessary to vary the spectrometer integration time in order to maximise the number of counts being measured. In this work, the term 'linearity' refers to the ability of the spectrometer to accumulate counts from a constant source of radiant flux at a constant rate (counts per second), regardless of the total accumulated count in the integrating capacitor. Although it is likely that there are significant differences in the spectral radiant flux densities between the calibration lamp during calibration and the ocean/atmosphere during deployment, it is assumed that the spectrometers are equally sensitive to the dynamic range of illumination sources encountered. Thus, the linearity corrections derived from the calibration lamp measurements are applicable to field measurements.

Prior to using radiometric counts (V_r, V_{amb} and V) in the aforementioned cali-

[2]The Spectralon plaque manufacturer provides $\rho(\lambda, 8°)$ only, however the Spectralon is assumed to be a perfect Lambertian (isotropic) reflector, so $\rho(\lambda, 8°) = \rho(\lambda, 45°)$.

bration equations, it was critical to consider the spectrometer's detector linearity. One way of investigating deviations from linearity is to take measurements of a known light source across a large range of counts (ideally from $\approx V_{dark}$ counts up to 2^{15}). Ideally, a light source would either be able to generate (or be attenuated to produce) a range of known, NIST-traceable $E_r(\lambda)$ values, so that for each possible spectrometer integration time, a series of $V(\lambda)$ measurements could be made across the entire dynamic range of each sensor pixel. Then, successive plots of $E_r(\lambda)$ vs. $V_r(\lambda)$ for a given integration time would reveal any non linearity and could be modelled with mathematical equation. This type of measurement would be time consuming and was not possible to achieve accurately with the equipment available.

Instead, the net effect of detector flux linearity and integration time was investigated with the data collected during the radiometric calibration process (discussed in the next section). This approach is similar to that described by instrument manufacturer, Ocean Optics (2011*a*). Briefly; the lamp $E_r(\lambda)$ was observed at a variety of spectrometer integration times in order to collect counts across a large portion of the dynamic range of the detectors[3]. For a perfect linear performance, the count rate of a spectrometer should be constant regardless of how many counts are recorded. Count rates for the different spectrometers used in the DALEC were calculated by Eq 3.11, and were assessed for linearity:

$$P = \frac{V_r(\lambda) - V_{dark}(\lambda)}{t}, \tag{3.11}$$

where P is the count rate.

If there are deviations from linearity in the detector, then P will be seen to vary under different measurement conditions. Figures 3.4a, c and e shows example count rates for one pixel from each of the E_d, L_u and L_{sky} detectors as a function of detector count. There are clearly differences in the count rate as a function of accumulated count evident in Figures 3.4a, c and e which need to be corrected.

[3]The detectors were never allowed to saturate, in case the CCD charge from the saturated pixels 'bloomed' into other pixels.

In the low count range (measured with very small integration times, but large uncertainties), there is a drop-off feature in count rate, possibly associated with a linear offset in the overall effective integration time calibration for each individual spectrometer. For the Zeiss spectrometers, maximum count rates are observed at an accumulated count (well depth) of approximately 2000 counts, and then gradually drops off as the accumulated count increases.

Determining the exact source(s) of the nonlinearity is outside the scope of this thesis. The goal of the subsequent analysis is to ensure that a constant count rate is achieved at any accumulated count value. This non-linearity compensation procedure was implemented in two stages. First, a spectrometer-dependent Δt integration time-offset was introduced into Eq. 3.11 to linearize the count rate of each spectrometer when counts are low:

$$Q(\lambda) = \frac{V_r(\lambda) - V_{dark}(\lambda)}{t + \Delta t}. \tag{3.12}$$

where $Q(\lambda)$ is the modified count rate, and the integration time offset Δt was manually determined as $\Delta t = -1.3, -0.95, -2.5ms$ for E_d, L_u and L_{sky} respectively.

The negative sign of these integration time offsets indicates that there is a portion of the integration time which is ineffective in collecting photons. The value of 550 nm was chosen in Figs. 3.4a, c and e because this is near the maximum spectral count range achievable without saturation. Unfortunately, not all pixels were observed across the majority of their dynamic range. These pixels are still part of the same CCD array, so it is assumed they require the same non-linearity correction. To test the assumption that pixels from the same CCD array will require the same non-linearity correction, the corrected count rates $Q(\lambda)$ for different pixels were compared. In order to do this, the $Q(\lambda)$ values needed to be normalised to remove differences in measured count rates due to the non-uniform spectral output (flux density) of the lamp. The dimensionless normalised count rate is calculated by:

$$Q_{norm} = \frac{Q(\lambda)}{Q_{ref}(\lambda)}, \tag{3.13}$$

where $Q_{ref}(\lambda)$ is the interpolated $Q(\lambda)$ value at a reference accumulated count value (fixed at 10,000 for L_u and E_d spectrometers, and 500 for L_{sky}).

The normalised count rate Q_{norm} data from all relevant pixels for each spectrometer is shown in Figs. 3.4b, d and f. For E_d and L_{sky}, the pixel variability is typically less than the error bars of Q_{norm}, which supports the assumption that nonlinearity is pixel-independent. The L_{sky} spectrometer exhibited higher Q_{norm} variability during the measurements indicating either an instrumental or experimental artifact, however the inter-pixel variability is still small relative to the overall non-linearity experienced by the instrument as a whole.

For the Zeiss spectrometers, a 5^{th} order polynomial approach was used to model the non-linearity shown in Fig. 3.4b and d:

$$Q_{norm} = B_0 + B_1 N + B_2 N^2 + B_3 N^3 + B_4 N^4 + B_5 N^5 \tag{3.14}$$

where N is the photon-induced count ($V - V_{dark}$), and B_x coefficients are listed in Table 3.1.

The 5^{th} order polynomial is plotted with a white dashed line on Fig. 3.4b and d. Fortunately, the 5^{th} order polynomial appears to extrapolate to count ranges which were not measured during the detector linearity experiments. The overall intercept (B_0) of the non-linearity correction (Eq. 3.14) is not important, as spectrometer counts get corrected prior to the determination of the radiometric calibration coefficients. For simplicity, the lowest order terms of these polynomials are shifted so that the normalised count-rate intercept is exactly 1; thus the lowest count measurements require no linearity correction (other than the Δt correction). The shifted polynomial coefficients are shown below in Table 3.1. These polynomials generate the correction factor, by which the measured photon-induced counts (C) are divided in order to yield the corrected counts (C_{corr}):

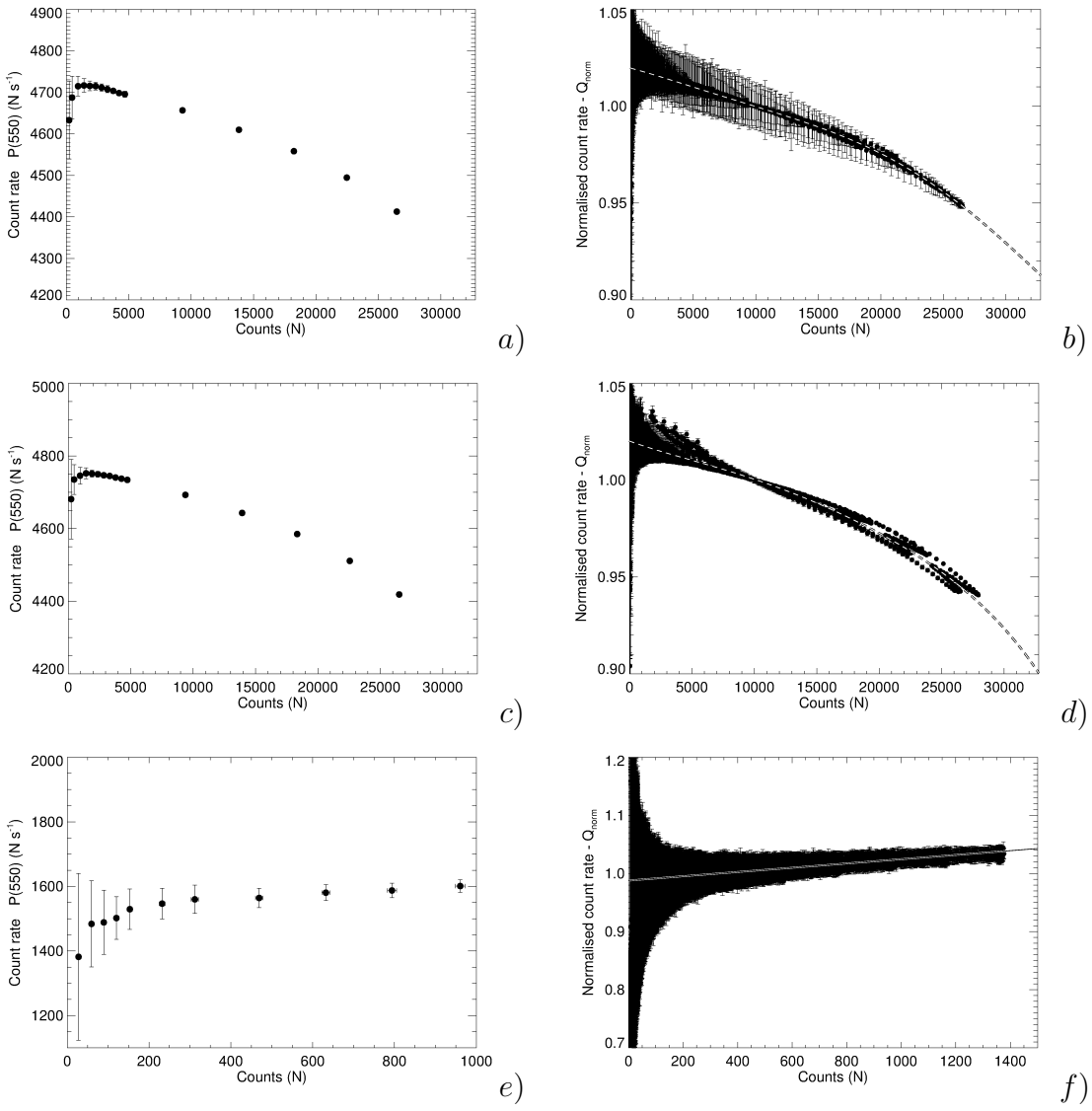

Figure 3.4: a) Count rate versus counts for the 550 nm E_d pixel. b) Corrected, normalised count rate versus counts for all wavelengths. The 5^{th} order polynomial is overplotted with a white dashed line and the extrapolated parabolic line is shown with a black dashed line. c) Count rate versus counts for the 550 nm L_u pixel. d) Corrected, normalised count rate versus counts for all wavelengths. The 5^{th} order polynomial is overplotted with a white dashed line and the extrapolated parabolic line is shown with a black dashed line. e) Count rate versus counts for the 550 nm L_{sky} pixel. f) Corrected, normalised count rate versus counts for all wavelengths. The linear function is overplotted with a white solid line and the extrapolated line is shown with a black solid line. For all plots, each 'count' is an average of 100 V_r and V_{dark} measurements, and the count rate error bar magnitudes are calculated with Eq. 3.11, with the standard deviations $\pm(\sigma_{V_r} + \sigma_{V_{dark}})$ propagated into the numerator.

$$C_{corr} = \frac{C}{Q_{norm}}. \tag{3.15}$$

Coefficient	E_d	L_u
B_0	1.00	1.00
B_1	-2.8859394e-006	-2.3443405e-006
B_2	1.1065396e-010	1.2537352e-010
B_3	-5.3532978e-015	-1.2443476e-014
B_4	8.7211449e-020	4.2848903e-019
B_5	-1.4329147e-024	-6.1826742e-024

Table 3.1: Polynomial coefficients for the linearity compensation of each Zeiss spectrometer pixel to be used in Eq. 3.14.

The USB2000 spectrometer behaved differently to the Zeiss spectrometers. As the photon count increased, the photon rate actually increased in a near linear fashion (see Fig. 3.4e and f). Unfortunately, the full dynamic range of the USB2000 was not calibrated, so non-linearities were not observed, other than those corrected with the Δt correction. It is assumed herein that the linear region extends throughout the 2^{12} count range for the USB2000. Whilst this is unlikely, no data were collected to confirm otherwise. The linear fit was modelled with $Q_{norm} = 1 + B_0 N$, where $B_0 = 3.6683368e-005$, and N is the recorded photon-induced $(V - V_{dark})$ counts.

The non-linearity correction is important for overall R_{rs} accuracy because it is evident there is an approximate 10% variation of count rate throughout the spectrometer's dynamic range for both E_d and L_u. This is evident in the range of normalised count rates shown in Figures 3.4b and d.

3.2.1.2.2 Calibration Coefficients

For each of the aforementioned irradiance and radiance calibration configurations (see Section 3.2.1.2), measurements were made across a variety of integration times. After detector linearity corrections which get applied to both $V_r(\lambda)$ and $V_{amb}(\lambda)$ independently, a number of $F_E(\lambda)$ and $F_L(\lambda)$ calibration coefficients were determined for the range of integration times. Figures 3.5a, c and e show the inverse linear relationship between the F_E and F_L coefficients at 550 nm and

the integration time for the three different spectrometers. Characterising the relationship between the calibration coefficients (F_E, F_L) and integration time is useful because the DALEC's integration time may then be adjusted to suit any illumination condition to achieve optimum signal-to-noise, and appropriate calibration coefficients can always be determined. Fortunately, after detector linearity corrections were made, the calibration coefficients were nearly perfectly *inversely* proportional to the integration time (t), so:

$$F_{E,L}(\lambda) = \frac{M(\lambda)}{t + \Delta t}, \tag{3.16}$$

where $F_{E,L}$ refers to the irradiance or radiance responsivity coefficients respectively, t is the spectrometer integration time in ms, Δt is the aforementioned spectrometer-dependent integration time offset in ms, and $M(\lambda)$ is the spectral calibration constant for each channel, shown in Figs. 3.5b, d and f.

It is useful to estimate the reliability of the calibration coefficients determined by Eq. 3.16. First, a qualitative assessment was made. The calibration lamp measurements made at different integration times were calibrated using Eq. 3.16, and were overplotted in Figs. 3.6a, c and e, along with the equivalent NIST characterisation (shown in white). The spectral Route Mean Square Error (RMSE) was determined for lamp observations for all tested integration times for each spectrometer. For the Zeiss spectrometers, the RMSE was typically under 1% for the 400 to 950 nm spectral region. The spectral RMSE for each spectrometer is shown in Figs. 3.6b, d and f.

The calibration measurements for the L_{sky} were less effective, for they failed to characterize the instrument across the full dynamic range of the device. The maximum count measured during calibration was approximately 1440, out of an approximate $2^{12} = 4096$, so the USB2000 calibration measurements exhibited a lower signal-to-noise ratio than the Zeiss spectrometer calibration measurements. As a consequence, the lamp reproduction RMSE were slightly higher for the USB2000 L_{sky} radiometer, typically under 5% for the 400 to 950 nm spectral region. The calibration coefficients $M(\lambda)$ for the L_{sky} sensor are reasonably

smooth (see Fig. 3.5f), so it is likely that the linear regression used to determine $M(\lambda)$ reduced the effect of detector noise at low integration times. Even if the accuracy of the L_{sky} measurements were of lower accuracy, these only contribute marginally to the overall calculation of R_{rs} by Eq. 3.5, where $\rho \approx 3\%$.

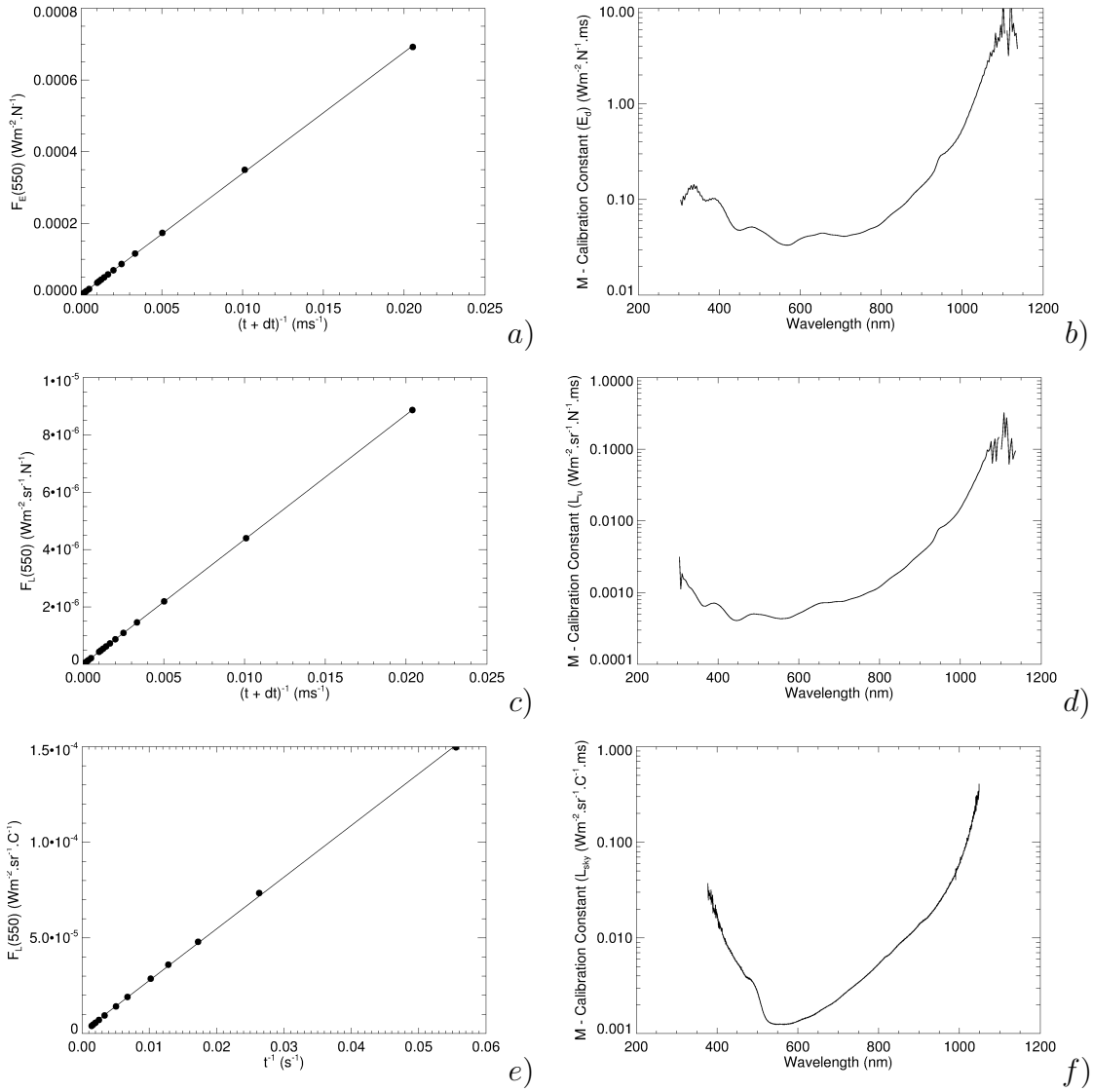

Figure 3.5: a) Calibration coefficients (F_E) for 550 nm versus the inverse of the offset-corrected integration time for the E_d sensor. b) The spectral calibration coefficients, $M(\lambda)$, of the E_d sensor. c) Calibration coefficients (F_L) for 550 nm versus the inverse of the offset-corrected integration time for the L_u sensor. d) The spectral calibration coefficients, $M(\lambda)$, of the L_u sensor. e) Calibration coefficients (F_L) for 550 nm pixel versus the inverse of the offset-corrected integration time for the L_{sky} sensor. f) The spectral calibration coefficients, $M(\lambda)$, of the L_{sky} sensor.

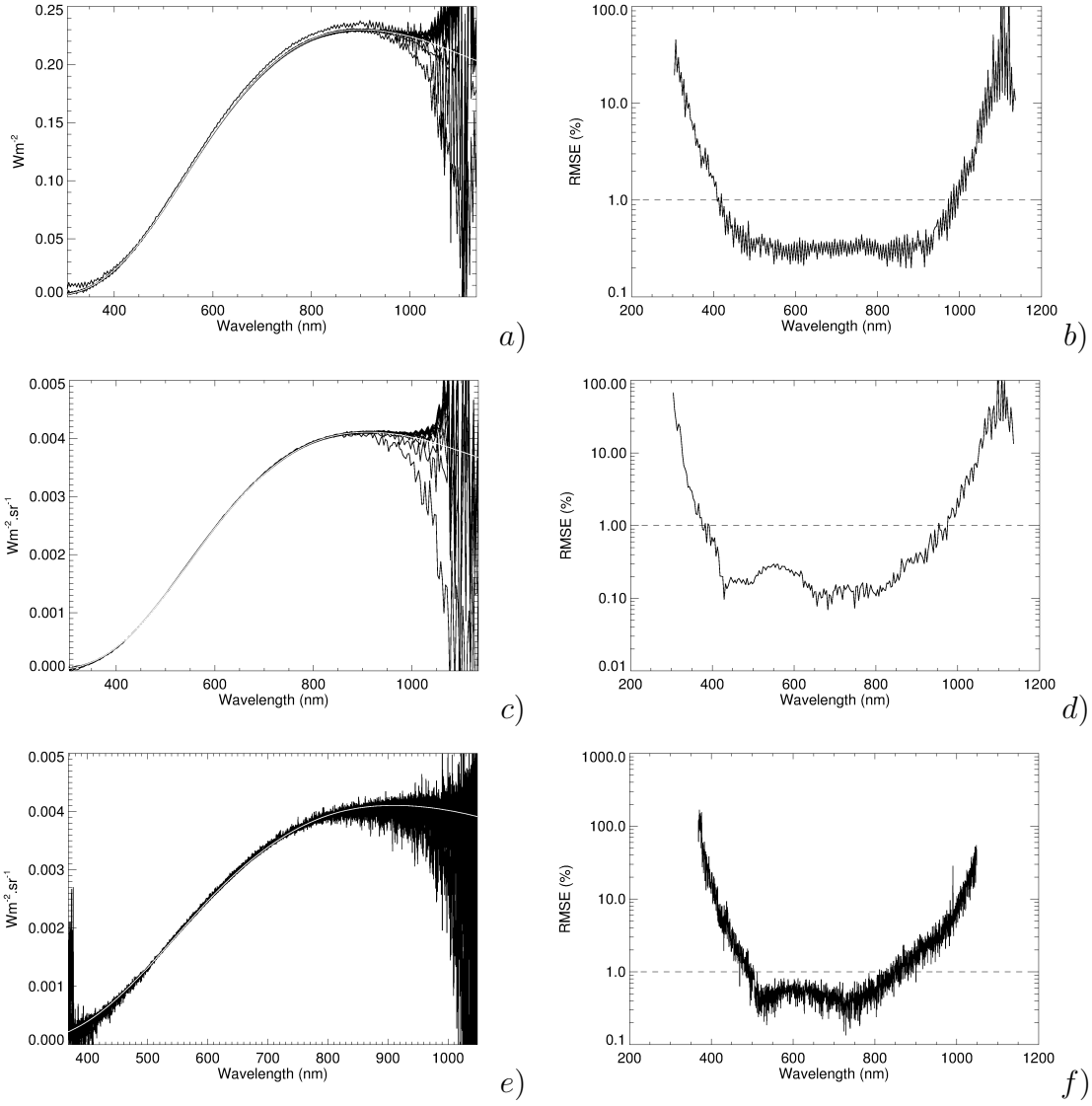

Figure 3.6: a) Calibrated measurements of the NIST lamp E_d spectrometer measurements performed at all integration times (overplotted), with the NIST-sourced lamp spectral calibration overplotted in white. b) The spectral RMSE of the lamp spectral irradiance measurements determined from data recorded at all measured integration times. The 1% level is shown with a dashed line. c) The reproduction of the spectralon plaque radiance by the calibrated L_u spectrometer measurements. All integration times are overplotted. The calibration irradiance spectrum as reflected by the spectralon plaque is overplotted in white (see Eq. 3.9). d) The spectral RMSE of the lamp reproduction, determined from calibrated spectra collected at all measured integration times. The 1% level is shown with a dashed line. e) The reproduction of the spectralon plaque radiance by the calibrated L_{sky} spectrometer measurements. All integration times are overplotted. The calibration irradiance spectrum as reflected by the spectralon plaque is overplotted in white (see Eq. 3.9). f) The spectral RMSE of the lamp reproduction, determined from calibrated spectra collected at all measured integration times. The 1% level is shown with a dashed line.

3.2.1.2.3 Dark Count Characterisation

All three spectrometers in the DALEC record counts even when no light enters the spectrometer. These counts are due to thermal excitation of the semiconductor detector and other sources of electronic noise, and must be removed from the signal prior to the application of the calibration coefficients. V_{dark} measurements were performed routinely throughout field campaigns in order to characterise any spectral shape in the 'dark' spectrometer outputs (i.e. due to hot pixels etc.). The magnitude of V_{dark} fluctuates with temperature[4], so it is desirable to know the actual magnitude of the dark count simultaneously with each measurement throughout the course of the day. With the exception of a few outlying hot pixels, the spectral shape of the dark count was essentially flat for all spectrometers.

The first 24 pixels of the USB2000 spectrometer array were blocked or filtered out by the manufacturer. The average value of these 24 pixels provides an estimate of the overall dark count of the L_{sky} detector for any given spectrum. For the E_d and L_u sensors, less information is known. For each spectrometer, the general relationship between dark count and integration time was investigated in a series of tests throughout the DALEC deployment period. The relationship between dark count and integration time was not consistent (see Fig. 3.7). The data measured during midday tended to have lower dark counts for a given integration time (data not shown). The most extreme outlying curve in Fig. 3.7b was performed after sundown, and the two other curved outliers were performed just before sundown and proceeded into the evening. This structure is most likely due to fluctuations in spectrometer temperatures, however in the absence of any other data, these general relationships based on Eq. 3.17 can provide estimates of dark current shape and magnitude based on the selected integration time. The linear relationships based on the linear regression of the data overplotted in Fig. 3.7 were determined for each spectrometer:

$$V_{dark}(\lambda) = Y(\lambda) + O(\lambda)(t + \Delta t), \tag{3.17}$$

[4]Both the semiconductor detector temperature and the read-out electronics, which heat up with increased charge throughput (higher counts).

where $O(\lambda)$ is the integration-time dependent portion of the dark count and $Y(\lambda)$ is the mean invariant dark count contribution.

For L_{sky}, once this dark count shape is determined for a given corrected integration time, it is scaled so that it exactly matches the magnitude of the first 24 filtered pixels. For the E_d sensor, the dark count spectral model described by Eq. 3.17 is used without further modification, acknowledging that errors of up to approximately 300 counts may be introduced (based on observing the data spread in Fig. 3.7a). For the L_u sensor, the average of the three lowest L_u values are used to scale the modelled L_u dark spectrum. This assumes that for every spectrum, there is a portion of the L_u with negligible photon-induced count. This is likely in the NIR region, provided there is no floating algae such as *Trichodesmium* in the scene under observation. Data where floating algae is likely is flagged and not used for further analysis. This is discussed later.

It is acknowledged that the lack of continuous dark count monitoring is a shortcoming of the DALEC's design. An improved DALEC could incorporate automated internal temperature sensors, optical shutters or filtered portions of the spectrum on the L_u and E_d channels. All of these would provide information about the appropriate dark current levels throughout deployment.

3.2.1.3 Spectral Convolution

The two Zeiss spectrometers (E_d and L_u) in the DALEC have a spectral resolution of approximately 10 nm (Zeiss 1999), whereas the USB2000 has a much higher spectral resolution of approximately 1.5 nm (Ocean Optics 2011*b*). To calculate R_{rs}, the data from all three spectrometers needed to be combined in an equation similar to Eq. 3.5, so it is preferable if the spectral resolution of all three spectrometers are identical. Additionally, the wavelength calibrations of the Zeiss spectrometers are wavelength dependent, with deviations from approximately 0.5 nm in the blue to 1.5 nm in the NIR. This difference also needed to be accounted for due to the sharp spectral absorption features in the E_d spectrum; otherwise spectral artifacts may be introduced in the final R_{rs} product.

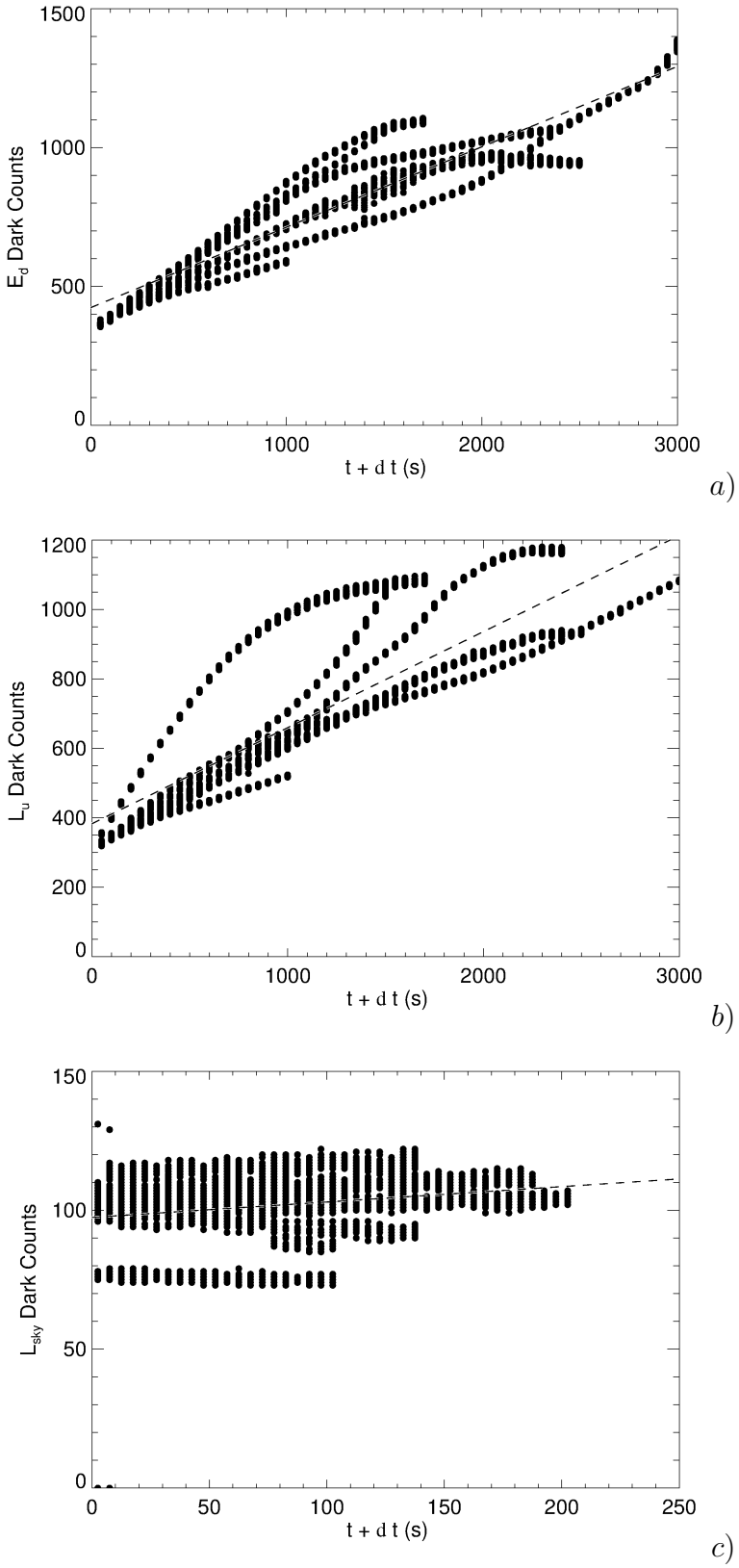

Figure 3.7: Dark Counts at 550 nm versus corrected integration time (see Eq. 3.12) for a) E_d, N=7504, b) L_u, N=7504 and c) L_{sky}, N=4551. All data acquired on 11 different days during fieldwork (morning, noon and afternoon) are overplotted to show the variability introduced with changes in temperature.

To achieve an accurate wavelength alignment and compatible spectral resolution, all field-measured spectrometer data was convolved with a 10 nm FWHM gaussian kernel, centered on each of the L_u wavelengths. Figures 3.8a-c shows examples of calibrated spectrometer signals, with the corresponding convolved spectra overplotted in white. The most noticeable spectral change after convolution is seen in the L_{sky} spectrum. Here, the convolution is removing spectral information related to molecular absorption in the atmosphere.

3.2.1.4 Surface reflection correction

At any particular DALEC instrument azimuth geometry, a certain fraction (K) of the sky radiance is reflected from the ocean surface into the L_u sensor:

$$L_t(\lambda, \theta_v) = L_u(\lambda, \theta_v) + K L_{sky}(\lambda, \theta_v^{'}), \tag{3.18}$$

where θ_v is the view angle of the sea-viewing radiance spectrometer (from nadir) and $\theta_v^{'}$ denotes the complement of this angle, from zenith.

Depending on the sea state, at any particular time, this contaminating sky radiance comes from a variety of regions in the sky. For a perfect DALEC alignment (relative to the horizon), and a flat ocean surface, much of the contaminating sky radiance would come from the complementary view angle (40° from zenith), and this radiance is measured by the L_{sky} sensor. Theoretical studies by Mobley (1999) for a perfectly aligned above-water sensor introduced the ρ parameter in Eq. 3.5, which can be used to correct for skylight contamination, and is a function of solar zenith angle, wind speed, relative solar azimuth, instrument's field of view and wavelength.

Mobley (1999) suggests an optimal sun-viewing azimuth angle (ϕ_{az}) of approximately 135° to minimise ρ (see Fig. 3.3). The DALEC's gymbal mount is attached to a boom whose view azimuth angle is set to point near this optimal azimuth angle, however the fixed DALEC boom design and the ship's variable heading

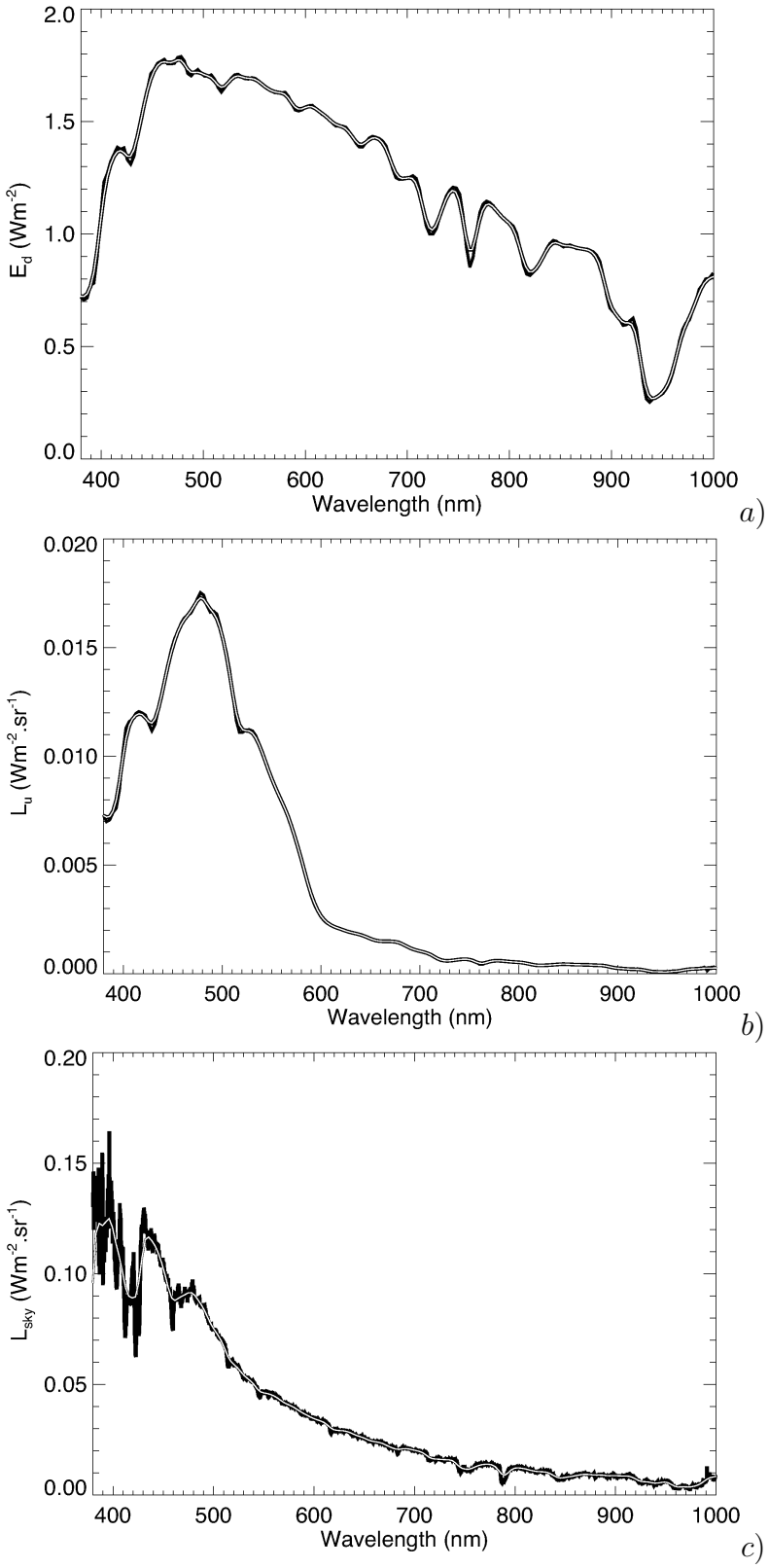

Figure 3.8: a),b),c) Examples of calibrated E_d, L_u and L_{sky} spectra (respectively). The 10 nm Gaussian-convolved equivalent spectrum is overplotted in white. Note in particular, the reduction of fine structure in the L_{sky} spectrum.

throughout the sampling days lead to variations in the sun-viewing azimuth angle of the DALEC. It was then important to record the sun-viewing azimuth angle and implement a skylight correction strategy based on this information.

3.2.1.4.1 Hydrolight-based look-up table correction

Hydrolight® (Sequioa Scientific, USA) is a commercially available and widely-used radiative transfer software package which can simulate the propagation of light from a modelled sun and atmosphere, through a wind-roughened air-ocean interface (Mobley 1989), up towards a sensor such as the DALEC's L_u spectrometer.

A series of Hydrolight modelling runs were made to calculate $\rho(\lambda)$ for a range of wind speeds (U), solar zenith angles (θ_s), sun-viewing azimuth angles (ϕ_{az}) and view angles (θ_v). From these simulations, a look-up table (LUT) was generated in order to retrieve $\rho(\lambda)$ given the instrument's view angle, sun relative azimuth angle, wind speed and solar zenith angle. Assuming perfect instrument viewing angle (i.e. $\theta_v = 40$), the look-up table was used to retrieve ρ to produce the corrected R_{rs} spectrum (Mobley 1999):

$$R_{rs} = \frac{L_w}{E_d} = \frac{L_t - \rho(\lambda, \phi_{az}, U, \theta_z) L_{sky}}{E_d}, \tag{3.19}$$

where L_t is the measured sea-viewing radiance, L_{sky} is the sky-viewing radiance, E_d is the downwelling irradiance, L_w is the water leaving radiance. ρ is determined from the Hydrolight-generated LUT which is applicable to time-averaged measurements (Mobley 1999).

3.2.1.4.2 Residual glint subtraction

The measured L_{sky} spectrum is not always representative of the spectrum of light that is contaminating instantaneous L_t measurements. Although the Hydrolight-based skylight correction approach considers the broadening of the solid angle of

skylight reflections and resultant shifts in the spectrum, the time-averaged nature of Hydrolight does not deal with the instantaneous spectral effects of sun-glint, caused when the direct sunlight is reflected into the L_t sensor; often for only fractions of a second. To compensate for the instantaneous sun-glint effect, an additional term in Eq. 3.18 was required (Lee et al. 1997).

Building on Eq. 3.18 to include a sun-glint factor (ϵ), Eq. 3.18 becomes:

$$L_t(\lambda, \theta_v) = L_u(\lambda, \theta_v) + KL_{sky}(\lambda, \theta_v^{'}) + \epsilon E_d, \tag{3.20}$$

and Eq. 3.19 becomes:

$$R_{rs} = \frac{L_w}{E_d} = \frac{L_t - \rho(\lambda, \phi_{az}, U, \theta_z)L_{sky}}{E_d} - \epsilon. \tag{3.21}$$

Often, ϵ is approximated to be the uncorrected R_{rs} in the NIR region (say, at 750 nm) (Lee et al. 1997). Hence, the assumption is that there is no R_{rs} signal at 750 nm. This is not always the case for coastal waters, where high NIR b_b values may occur; contributing to a $R_{rs}(NIR)$ signal.

Ruddick et al. (2006) observed that there is a normalised reflectance spectral signature ('similarity spectrum') in the deep red to NIR region which is invariant with sediment concentration because water absorption in these regions is so large. In other words, in the absence of floating algae and fluorescence, the spectral shape of R_{rs} is invariant in the NIR spectral region, but non-zero. This spectral shape was provided in a Table from Ruddick et al. (2006), and is represented as $S(\lambda)$ in Eq. 3.24. $S(\lambda)$ was spectrally convoluted as described in Section 3.2.1.3. This spectral shape was based on 27 quality-controlled measurements made in the North Sea. Unfortunately these measurements are themselves potentially subject to residual above water skylight correction artifacts. Additionally, the water temperature in the North Sea is expected to vary greatly compared to that of the tropical Great Barrier Reef, and $S(\lambda)$ is dependent on water temperature and salinity. Since the work of Ruddick et al. (2006), temperature and salinity specific NIR absorption data have been made available to the remote sensing community

(Rottgers et al. 2013). By using these new coefficients, a 'similarity spectrum' was generated for this study using a theoretical approach. The resultant spectrum will not contain residual skylight artifacts, and the temperature and salinity of GBR waters can be represented. Assuming negligible CDOM and particulate absorption in the NIR, the spectral shape of u (and R_{rs}) is influenced only by particulate backscatter and water absorption:

$$u_{NIR} \approx \frac{b_{bw} + b_{bp}}{a_w + b_{bw} + b_{bp}}, \tag{3.22}$$

where the wavelength dependency has been omitted for brevity, and a_w was modelled for a salinity of 35 PSU and a temperature of 29° C using the coefficients of Rottgers et al. (2013). This u modelled spectrum was then at normalised at 780 nm, consistent with Ruddick et al. (2006):

$$S_{new} = \frac{u_{NIR}}{u_{NIR}(780)}. \tag{3.23}$$

To demonstrate the sensitivity of $S_{new}(\lambda)$ to likely variations in b_{bp} in the GBR region, equations 2.52 and 2.54 were used to generate a series of $S_{new}(\lambda)$ spectra for $b_{bp}(555)$ values between 0 and 0.3 m^{-1}. These different spectra are overplotted with faint dotted lines in Fig. 3.9a. The average value is shown as a solid line with a white outline. The Ruddick et al. (2006) similarity spectrum is plotted with a dashed line. In comparing the normalised theoretical $S_{new}(\lambda)$ with the approach of Ruddick et al. (2006), it is assumed that any spectral differences between R_{rs} and u are negligible in the NIR. From this comparison, it is evident that the spectral feature around 800 nm is shifted approximately 20 nm between the two approaches. Also, the theoretical approach does not contain the small feature evident in the Ruddick et al. (2006) at approximately 760 nm. This feature may be due to the presence of residual reflected skylight in the measurements or Raman fluorescence.

Whilst the theoretically-based similarity spectrum $S_{new}(\lambda)$ deals with absorption and elastic scattering, the remote sensing signal will also contain fluorescence $F(\lambda)$ and spectral influence from floating *Trichodesmium* $T(\lambda)$. These contribu-

tions should be considered in addition to the similarity spectrum. An optimisation inversion model was formulated to determine appropriate glint (ϵ), floating algae (κ), fluorescence (A_0 and A_1) correction factors and the theoretically-based similarity spectrum scaling factor (J):

$$\frac{L_t - \rho(\lambda, \phi_{az}, U, \theta_z) L_{sky}}{E_d} - \epsilon = JS_{new}(\lambda) + \kappa T(\lambda) + F(\lambda), \tag{3.24}$$

where fluroescence $F(\lambda)$ is modelled with the double-Gaussian parameters of Zarco-Tejada et al. (2000):

$$F(\lambda) = A_0 e^{\frac{-(\lambda-688.3)^2}{313.29}} + A_1 e^{\frac{-(\lambda-746.1)^2}{1007.43}}. \tag{3.25}$$

A Levenberg-Marquardt (MPFIT) (Markwardt 2009) routine was employed to vary the five parameters - $[\epsilon, J, \kappa, A_0, A_1]$ to minimize the difference between the left hand side and right hand side of Eq. 3.24 from 650 to 900 nm where $S_{new}(\lambda)$ is from Eq. 3.23. For the inversion, ϵ was initialised to $\left(\frac{L_t(900)}{E_d(900)}\right)$, J was initialised to $\left(\frac{L_t(780)}{E_d(780)}\right)$ and κ, A_0 and A_1 were all initialised to 0.

The *Trichodesmium* basis vector, $T(\lambda)$ was extracted from a DALEC transect and was left uncorrected for glint or skylight correction. Due to the slick density and surface expression, no glint could be seen by eye; nor any skylight reflection. This spectral signature looked similar to the those measured by McKinna (2010).

There are several benefits of this skylight correction approach. First and foremost, this method allows skylight and glint correction in turbid coastal waters where $R_{rs}(750) > 0$, providing more accurate R_{rs} measurements in GBR waters. Secondly, the commonly encountered floating *Trichodesmium* may be detected and is quantified by (κ) using this approach. This quantity can be used as a quality control flag, or the effects of the *Trichodesmium* can be removed so that standard radiative-transfer based R_{rs} inversions, which assume submerged particles, can still be performed on the data. Thirdly, the retrieval of the fluorescence peak (especially the dominant A_0 magnitude) can be used to estimate surface wa-

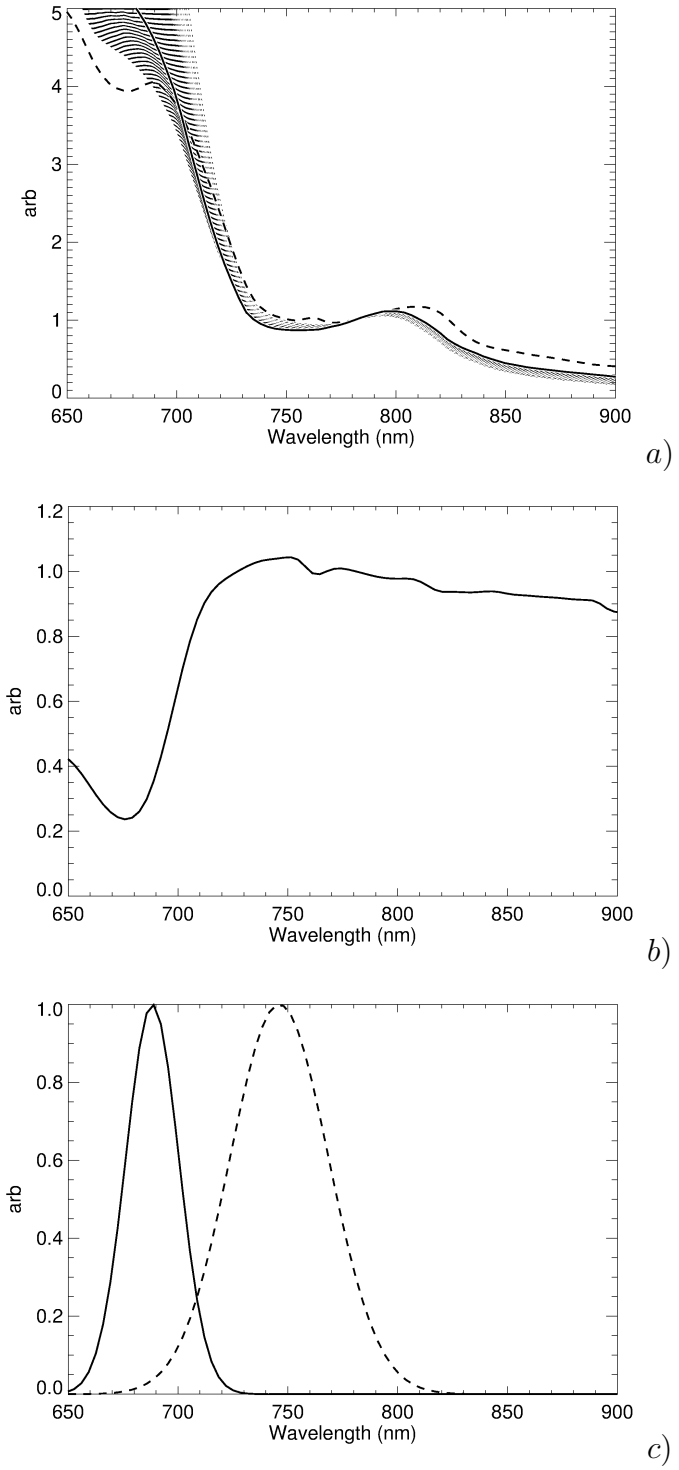

Figure 3.9: a) The 'similarity spectrum' approaches. The Ruddick et al. (2006) spectrum is shown with a dashed line. The thin, dotted lines show variations in the theoretical similarity spectrum due to variations in b_{bp}. The solid line with a white outline is an average theoretical similarity spectrum.. b) The floating *Trichodesmium* basis vector, $T(\lambda)$, obtained from a DALEC measurement directly over a thick, red *Trichodesmium* mat, normalised at 780 nm. c) The separate Gaussian chlorophyll fluorescence emission spectra as generated with Eq. 3.25 (Zarco-Tejada et al. 2000).

ter chlorophyll-a concentrations from DALEC measurements. This fluorescence signal can then be subtracted from R_{rs} prior to the standard radiative-transfer based R_{rs} inversion which usually assumes elastic scattering and absorption only (Lee et al. 1998).

Ultimately, the validity of this skylight correction approach should be assessed by comparing with above water R_{rs} extrapolated from subsurface L_u and E_d measurements. Unfortunately, these validation measurements were not made. Instead, the overall DALEC post-processing and inversion methodology will be validated in their entirety later.

3.2.1.5 DALEC Data Quality Control

To quality control DALEC measurements, a number of quality control flags were created, and are summarised in Table 3.2. The most important requirement is that DALEC pixels are not saturated. The next important requirement is that the GPS has a valid positional fix, and that the DALEC's viewing azimuth angle (ϕ_{az}) (see Fig. 3.3) is known (either by measuring the compass heading or calculating the heading of the ship based on successive GPS positions whilst in motion). The DALEC viewing azimuth angle is used to filter the data to remove regions with a high probability of sun-glint (i.e. for $\phi_{az} < 40°$) and regions where ship shadow is probable ($\phi_{az} > 160°$). In addition to these fundamental flags, there are the skylight and glint correction-derived flags. When a large amount of sun-glint is present and is subtracted from the R_{rs} measurement in Eq. 3.24, its value is recorded in the ϵ parameter. When this is too large, even corrected R_{rs} start to look anomalous (i.e. the presence of atmospheric absorption lines in the NIR region). All data over a certain glint threshold are ignored.

The κ coefficient is employed as a higher level quality control parameter, equal to the magnitude of the *Trichodesmium* R_{rs} contribution at 780 nm. This contribution is not subtracted from the reflectance spectrum, however it could be. This QC parameter is of vital importance because *Trichodesmium* present on the ocean surface covers the underlying water column and invalidates the assumptions

of the fundamental radiative transfer-based equation $R_{rs} \approx f\left(\frac{b_b}{a+b_b}\right)$ (McKinna 2010).

QC Flag	Condition
SATURATED	L_u, E_d counts $> 32,000$ and L_{sky} counts $> 4,000$.
NO GPS	GPS FIX $= 0$
GOOD GEOMETRY	$40° < \phi_{az} < 160°$
GLINT	$\epsilon > 0.01$
TRICHO	$\kappa > 0.00001$

Table 3.2: DALEC Quality Control flag conditions.

3.2.2 Hydrolight Synthetic R_{rs} Dataset Creation

Hydrolight (described previously) can be used to simulate the above-water $R_{rs}(\theta, \phi, \lambda)$ for a given set of water column spectral IOPs. By using Hydrolight to simulate the $R_{rs}(\theta_v, \theta_s, \phi_{az}, \lambda)$ of known IOPS and concentrations found in the GBR region (based on the findings of Chapter 2), a dataset can be generated to investigate the validity of equations such as Eq. 3.2, and in particular $f(\theta_v, \theta_s, \phi_{az}, \lambda)$, specifically for GBR waters.

The Hydrolight 'ABCASE2' 4-component (water, phytoplankton, CDOM and non-algal particles) IOP model was used to perform model runs. For every constituent the concentration-specific absorption, total scattering and phase functions are required as input into Hydrolight (with the exception of CDOM, which is assumed to contribute negligibly to scattering). The values used in the creation of this dataset are shown in Table 3.3, and were combined in a FOR loop so that Hydrolight runs were made for each unique combination of the TChl, TSS and DOC concentrations.

The synthetic dataset was created for chlorophyll concentrations listed in Table 3.3, ranging from zero up to 5 μgl^{-1} in order to encompass and slightly extend the range of chlorophyll concentrations encountered during fieldwork. The synthetic dataset was created for mineral TSS concentrations listed in Table 3.3, ranging from near-zero up to approximately 100 μgl^{-1}. This concentration range encompasses the range of TSS concentrations encountered during the fieldwork, and should also represent the TSS values found during highly-turbid flood plumes or dredging plumes which are known to occur in the region of interest (Islam et al. 2007). DOC concentration in the modelling exercise of this section was varied from 0.65 to 5.65 mgl^{-1}. The highest field-measured DOC was approximately 4 mgl^{-1}.

All water quality concentrations chosen in Table 3.3 cover, and extend past the ranges measured in the GBR. This is to assist in simulating the ocean colour for both 'normal' and what is considered to be extreme conditions in the area.

Discrete concentrations were chosen instead of random sampling from the measured cumulative water quality probability functions to ensure that these extreme conditions were present in the simulations.

TChl (μgl^{-1})	TSS (mgl^{-1})	DOC (mgl^{-1})
0	$0+TSS_\phi$	0.65
0.25	$0.5+TSS_\phi$	1.15
0.5	$2+TSS_\phi$	2.65
2	$5+TSS_\phi$	5.65
5	$10+TSS_\phi$	-
-	$100+TSS_\phi$	-

Table 3.3: Water quality concentrations of each optically active constituent used for the synthetic dataset creation. $TSS_\phi = 0.85\sqrt{TChl}$, which is the assumed contribution of TSS due to living organic matter correlated with TChl (see Section 3.2.2.2).

Details of the different optical models used for the Hydrolight simulations are provided in Sections 3.2.2.1 to 3.2.2.4.

3.2.2.1 Phytoplankton

Hydrolight allows only one user-provided chlorophyll-specific absorption spectrum as standard. However, as discovered in Chapter 2, a two phytoplankton component (*Procholorococcus* and Diatom) model fits the observed variations in pigment packaging and was shown to be useful for retrieving TChl concentrations based on a_ϕ spectra.

The contribution of the Diatom spectrum (relative to *Prochlorococcus*) was often seen to increase as TChl increased (see Fig. 2.20), and in Chapter 2, this trend was modelled with Eq. 2.48. In order to model a realistic phytoplankton assemblage for the GBR to be input into Hydrolight, chlorophyll-specific absorption spectra needed to be determined for these different relative abundances of *Procholorococcus* and Diatoms. From Chapter 2:

$$S_{Pro} = \frac{M}{8.94TChl} + 0.0214M - 0.1125, \tag{3.26}$$

where M varied from 0.75 to 3 in the GBR dataset (see Fig. 2.20).

To model the observed (see Fig. 2.20) shift in assemblage, and allow for the natural variability evident in the data, M was varied by a uniformly-distributed random number $\Re$ so that it spanned from 0.75 to 3:

$$M = 0.75 + 2.25\Re. \tag{3.27}$$

For low TChl values, the maximum fractional value of S_{Pro} was restricted to 1. The fraction of TChl attributable to Diatoms was then determined by:

$$S_{Diat} = 1 - S_{Pro}. \tag{3.28}$$

The chlorophyll specific absorption model input was then calculated as:

$$a^*_\phi(\lambda) = a^*_{Pro}(\lambda)S_{Pro} + a^*_{Diat}(\lambda)(1 - S_{Pro}), \tag{3.29}$$

where $a^*_{Pro}(\lambda)$ and $a^*_{Diat}(\lambda)$ and the chlorophyll specific absorption spectral end-members for *Prochlorococcus* and *Diatoms* (respectively).

Due to the Case 2 nature of coastal waters and the relatively low numbers of stations available in Case 1 conditions (i.e. outer shelf samples), the data set collected in the GBR was not sufficient to determine the spectral scattering properties of phytoplankton in isolation (also see Section 2.3.3.2.3). Instead, the Chl-specific scattering data of Morel (1987) (his Fig. 5b) was used to estimate a TChl-specific scattering end-members for oligotrophic waters (b^*_{Pro}) and eutrophic waters (b^*_{Diat}). These can then be mixed together in an equation analogous to Eq. 2.26:

$$b^*_\phi(\lambda) = b^*_{Pro}(\lambda)S_{Pro} + b^*_{Diat}(\lambda)(1 - S_{Pro}), \tag{3.30}$$

where the aforementioned graph of Morel (1987) was used to estimate $b^*_{Pro}(550) = 1.2$ and $b^*_{Diat}(550) = 0.12$.

This $b^*_\phi(550) = (1.2S_{Pro} + 0.12S_{Diat})$ mixing relationship satisfactorily reconstructed the $b^* = 0.3[TChl]^{-0.38}$ relationship from Morel (1987) with an RMS

error of approximately 13% for TChl values ranging from 0.15 to 10 μgl^{-1}.

For a given TChl value consistent with that used in Eq. 3.26, a phytoplankton scattering spectrum was formulated based on Eq. 2.26:

$$b_\phi(\lambda) = [TChl] b^*_\phi(550) \left(\frac{\lambda}{550}\right)^{-\gamma_\phi}, \tag{3.31}$$

where $\gamma_\phi = 2\sigma(2\Re - 1) + 0.65$; i.e. γ_ϕ was centered on the value of 0.65, but was allowed to randomly vary within two standard deviations $2\sigma = 0.14$ of the observed γ_p values calculated by Eq. 2.22. This assumes that $\gamma_p \approx \gamma_\phi$.

As is the case for phytoplankton scattering, blending was also performed on the Mie-modelled *Prochlorococcus* ($\widetilde{\beta_{Pro}}(\lambda, \psi)$) and Diatom ($\widetilde{\beta_{Diat}}(\lambda, \psi)$) phase functions determined in Section 2.3.3.2.5, and shown in Figs. 2.27a-c. After blending, the phase functions were re-normalised, as is required for the definition of phase functions (see Eq. 2.5 and 2.8):

$$\widetilde{\beta_\phi}(\lambda, \psi) = \frac{(1.2 S_{Pro} \widetilde{\beta_{Pro}}(\lambda, \psi) + 0.12 S_{Diat} \widetilde{\beta_{Diat}}(\lambda, \psi))}{2\pi \int_0^\pi (1.2 S_{Pro} \widetilde{\beta_{Pro}}(\lambda, \psi) + 0.12 S_{Diat} \widetilde{\beta_{Diat}}(\lambda, \psi)) \sin(\psi)}. \tag{3.32}$$

3.2.2.2 Non-algal Particulates

In Chapter 2, two different mass-specific absorption spectra were reduced from the GBR dataset; representing terrestrially-sourced mineral particles ($a^*_{min}(\lambda)$) and the other for pseudo-detrital or calcareous particles ($a^*_{det}(\lambda)$) (see Fig. 2.22). A blending scheme analogous to Eq. 2.44 was used to model the total a_{NAP} spectrum based on the two mass-specific basis vectors, and yielded TSS retrievals with 9% RMS error (see Fig. 2.22b):

$$a^*_{NAP}(\lambda) = a^*_{det}(\lambda)s_{det} + a^*_{min}(\lambda)s_{min}, \tag{3.33}$$

$$s_{min} = 1 - s_{det}, \tag{3.34}$$

where a^*_{NAP} is the mass specific non-algal particulate spectrum, S_{min} is the fractional contribution of minerals to a_{NAP} and s_{det} is the fractional contribution of detritus to a_{NAP}.

Even for a perfectly sampled population of non-mineral particulates, the application of the term 'detrital' to non-mineral absorption measurements determined with the filter-pad depigmentation method (Tassan & Ferrari 1995) is misleading. This is because the filter pad retains components of previously-living phytoplankton cells (i.e. that were living immediately prior to sampling), so a portion of the a_{NAP} spectrum will be correlated with TChl. By comparing the outer-reef TSS measurements with TChl, one finds that there is evidence of a relationship between the lower limit of TSS and TChl (see Fig. 3.10). By assuming that in these waters, $s_{min} = 0$, then modelling the lower limit provides an estimate of the functional relationship between s_{det}, TSS and TChl. By considering that s_{det} must be zero when TSS and TChl both equal, a simple square-root function was manually chosen to estimate the fraction of the oceanic/detrital basis vectors that are used to contribute to the overall a_{NAP} spectrum, namely

$$s_{det} = \frac{0.85\sqrt{TChl}}{TSS}, \tag{3.35}$$

where the coefficient 0.85 was chosen manually to approximate the lower limit shown in Fig. 3.10.

In real life, however, it is expected that there could be significant variability around this assumed relationship. In order to add more variability in the simulations, the random (right hand) term was added:

$$s_{det} = \frac{0.85\sqrt{TChl}}{TSS}\left(1 + \frac{(2\Re - 1)}{5}\right), \tag{3.36}$$

where the S_{det} fraction was limited between 0 and 1.

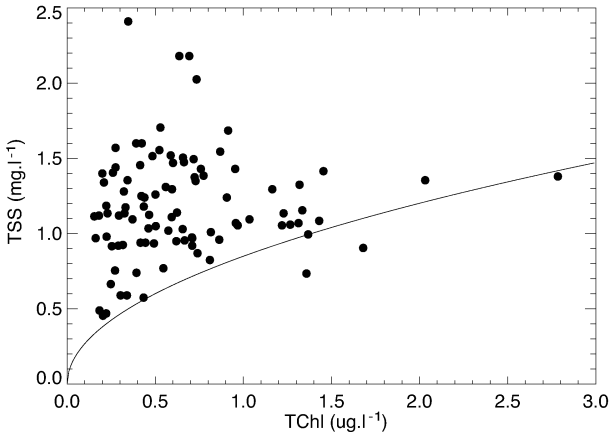

Figure 3.10: Outer-reef TSS and TChl, with the approximate lower-limit relationship (Eq. 3.35) overplotted.

As shown in Fig. 2.24, the TChl-corrected mineral scattering at 660 nm was determined by the linear relationship:

$$b_{min}(660) = 0.339[TSS] - 0.11. \tag{3.37}$$

It is assumed that, due to the considerable spread of the data points that was used to derive b^*_{min}, the y-intercept of 0.11 was ignored and assumed to be a consequence of methodological uncertainty. This uncertainty is prominent because four separate measurements (c_{pg}, a_ϕ, a_{NAP}, a_{CDOM}) needed to be combined (Eq. 2.49), so the uncertainties are additive. It is also worth mentioning at this point that, although never highlighted, if one is to regress the mean TSS and mean $b_p(555)$ values from Blondeau-Patissier et al. (2009) (their Table 2), the relationship obtained is $b_{NAP}(555) = 0.560[TSS]$. Future studies may find it beneficial

to analyse their dataset to estimate an equivalent b^*_{min} to compare with Eq. 3.37.

The mineral phase function was generated using the Fournier-Forand phase function, with a randomised input of $\mu = 2\sigma(2\Re - 1) + 0.65 + 3$ and an input spectral backscattering ratio generated by Eq. 3.38, which is a modification of Eq. 2.56 to include a randomised spectral slope based on the $2\sigma = 0.14$ variability of γ_b.

$$B_{min}(\lambda) = 0.0257 \left(\frac{\lambda}{660} \right)^{-2\sigma(2\Re-1)-0.578}. \tag{3.38}$$

3.2.2.3 CDOM

The absorption coefficient of CDOM was modelled as a function of DOC, as described below in Eq 3.39.

$$a_{CDOM}(\lambda) = a^*_{CDOM}(\lambda)[DOC - DOC_{inv}], \tag{3.39}$$

where the estimated optically inactive fraction of DOC, DOC_{inv} is approximately $0.65 mgl^{-1}$ (see Eq. 2.38). Accordingly, DOC concentration, in the modelling exercise of this section, was varied from 0.65 to $5.65 mgl^{-1}$ to provide $a_{CDOM}(\lambda)$ coefficients greater than zero.

3.2.2.4 Other Inputs

Hydrolight runs were performed for clear skies, for a variety of solar zenith angles (θ_s = 0°, 15°, 30°, 45° and 60°) and wind speeds (w =1, 2, 5 and 10 ms^{-1}). Computations were performed from 400 to 750 nm in 10 nm increments (36), so the total number of individual Hydrolight runs with unique IOP combinations was 86,400 (consisting of $5(\theta_s) \times 4(w) \times 5(TChl) \times 6(TSS) \times 4(DOC) \times 36(\lambda)$). Calculations were performed to provide data for just below the surface (0-), and just above the surface (0+). Due to the IOP blending approach, input phase functions needed to be re-discretised for each IOP combination. As a result of the wavelength dependence of, in particular, the *Prochlorococcus* phase function (see Fig. 2.27), each new wavelength also required a new discretisation.

3.3 Results

3.3.1 DALEC R_{rs} Measurements

Figure 3.11 shows the spatial distribution of quality-controlled DALEC measurements where coincident flow-though measurements were also made (described later in Section 2.2.4.4). The flow-through measurements are discussed later in Section 4.2.1.2. Figure 3.12a shows example spectra measured during a transect from Lodestone Reef towards Magnetic Island, near Townsville on the 31^{st} of January 2006. As the ship approached the coast, the DALEC R_{rs} measurements decreased in the blue (400 - 440 nm) and increased in the green (500 - 550 nm) as the particulate load increased. Explaining and understanding the changing shapes of the R_{rs} spectrum is assisted by reducing the R_{rs} spectrum into the IOPs of the substances in the water.

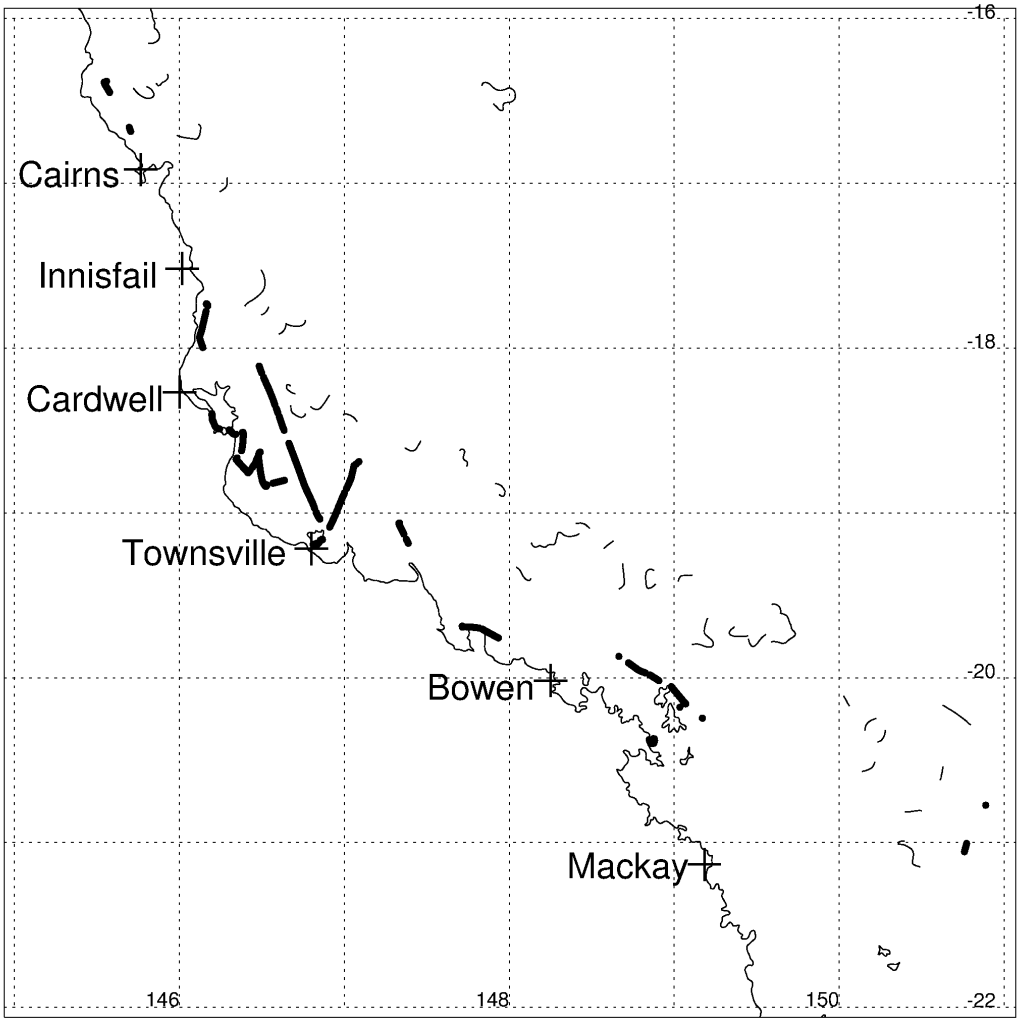

Figure 3.11: The locations of quality-controlled DALEC R_{rs} measurements where ancillary flow-through measurements were made. All transect data was recorded between Jan 4^{th} and Jan 31^{st}, 2006.

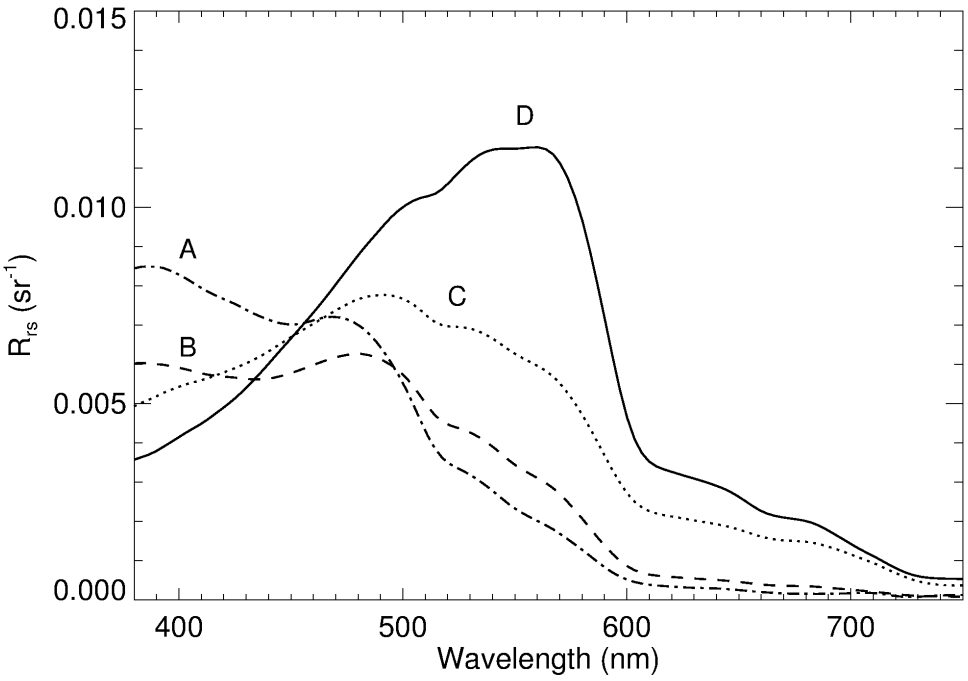

a)

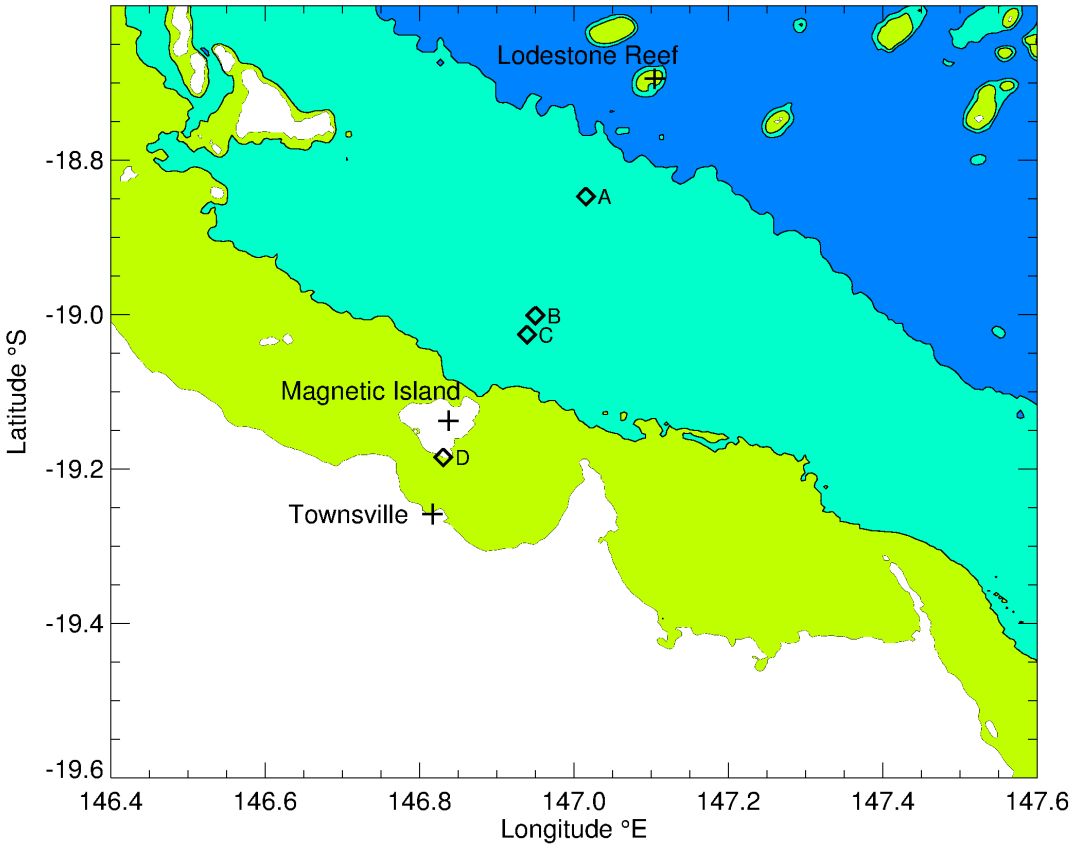

b)

Figure 3.12: a) Examples of DALEC R_{rs} measurements made on the 31^{st} of January 2006 from deep blue mid-lagoon water (label A), transitioning to brown water near Magnetic Island (label D). b) Locations of the example DALEC R_{rs} measurements shown in Fig. 3.12a. The 0-20 m, 20-40 and 40-100 m bathymetric contours shown respectively in yellow, cyan and blue.

3.3.2 Hydrolight Simulations

The Hydrolight-based synthetic dataset described in Section 3.2.2 was used to investigate the relationship between above-water R_{rs} and $\frac{b_b}{a+b_b}$, which is of primary importance to physics-based R_{rs} inversions. For brevity, the lower-case letter u is often substituted for the term $\frac{b_b}{a+b_b}$ following Eq. 3.40. u is used in Figures 3.13a-c.

$$u = \left(\frac{b_b}{a + b_b} \right). \tag{3.40}$$

Figure 3.13a shows the Hydrolight-computed relationship between above-water R_{rs} and u for 400 nm, 550 nm and 700 nm, for the entire range of concentrations shown in Table 3.3.

There is a slightly non-linear trend apparent in the data. It is also interesting to note that the wavelength dependence of the relationships between R_{rs} and u appears to be subtle.

For comparison, Fig. 3.13b shows the subsurface r_{rs} of the Hydrolight simulations performed at solar zenith angle $\theta_s = 0$ and sensor nadir view angle $\theta_v = 0$ at 550 nm, alongside the model fits of Lee et al. (1999) and Gordon et al. (1988). These models both exhibit the functional form shown in Eq. 3.41,

$$r_{rs} = g_0 u + g_1 u^2, \tag{3.41}$$

where lowercase r_{rs} denotes sub-surface remote sensing reflectance, and g_0 and g_1 are model coefficients (examples of which are shown in Table 3.4).

ID	Author	g_0	g_1
G88	Gordon et al. (1988)	0.0949	0.0794
L99	Lee et al. (1999)	0.0840	0.170
L02	Lee et al. (2002)	0.0895	0.1247
***	This study	0.0849	0.1211

Table 3.4: Published polynomial coefficients relating r_{rs} to u. L02 as published in Lee et al. (2002) was determined from the average of the G88 and L99 sets. All sets overplotted in Fig. 3.13b, labelled according to the ID column.

The Gordon et al. (1988) coefficients were optimised for oceanic conditions,

whereas the Lee et al. (1999) coefficients were optimized for coastal conditions. As a result, Lee et al. (2002) used the average of these two sets of values in order to equally represent coastal and oceanic waters. The bio-optical model Lee et al. (1999) used to generate their 'coastal' coefficients relied on chlorophyll-a based particle scattering, and the 'average particle' phase function described in Mobley (1994). The results of the present study are derived from concentration specific, but slightly randomized blends of molecular, Mie mono-dispersion (small phytoplankton), Mie polydispersion (large phytoplankton) and Fornier-Fourand based (mineral and detrital) phase functions in an attempt to better match the particle assemblages found in the GBR. Despite the differences in bio-optical modelling approaches, the coefficients calculated in this study closely match (5.2% for g_0 and 2.9% for g_1) the averaged coefficients of Lee et al. (2002) (Set L02 in Table 3.4).

The use of the simplistic 2^{nd} order polynomial relationship of Eq. 3.41 may be a consequence of the previously mentioned studies using a blend of only two phase functions (i.e. molecular and either 'average Petzold' (Mobley 1994, Petzold 1977) or Kullenberg (1974) for particles). By examining Fig. 3.13c, one can see that, at low values of u, a simple second order polynomial treatment, as in Eq. 3.41, cannot attempt to model the results of the observed synthetic Hydrolight runs, particularly at low u values.

The shortfall of Eq. 3.41 was recognised by Lee et al. (2004), who attributed the spread of data to the relative abundance of molecular scattering as opposed to particulate scattering (using Petzold's 'average particle' phase function). By partitioning the molecular and particulate scattering components, Lee et al. (2004) was able to determine more accurate parameters which related r_{rs} (subsurface) to u.

A similar partitioning approach was used in analysing this synthetic data set. However, a polynomial functional form (Eq 3.42) was used for the particulate

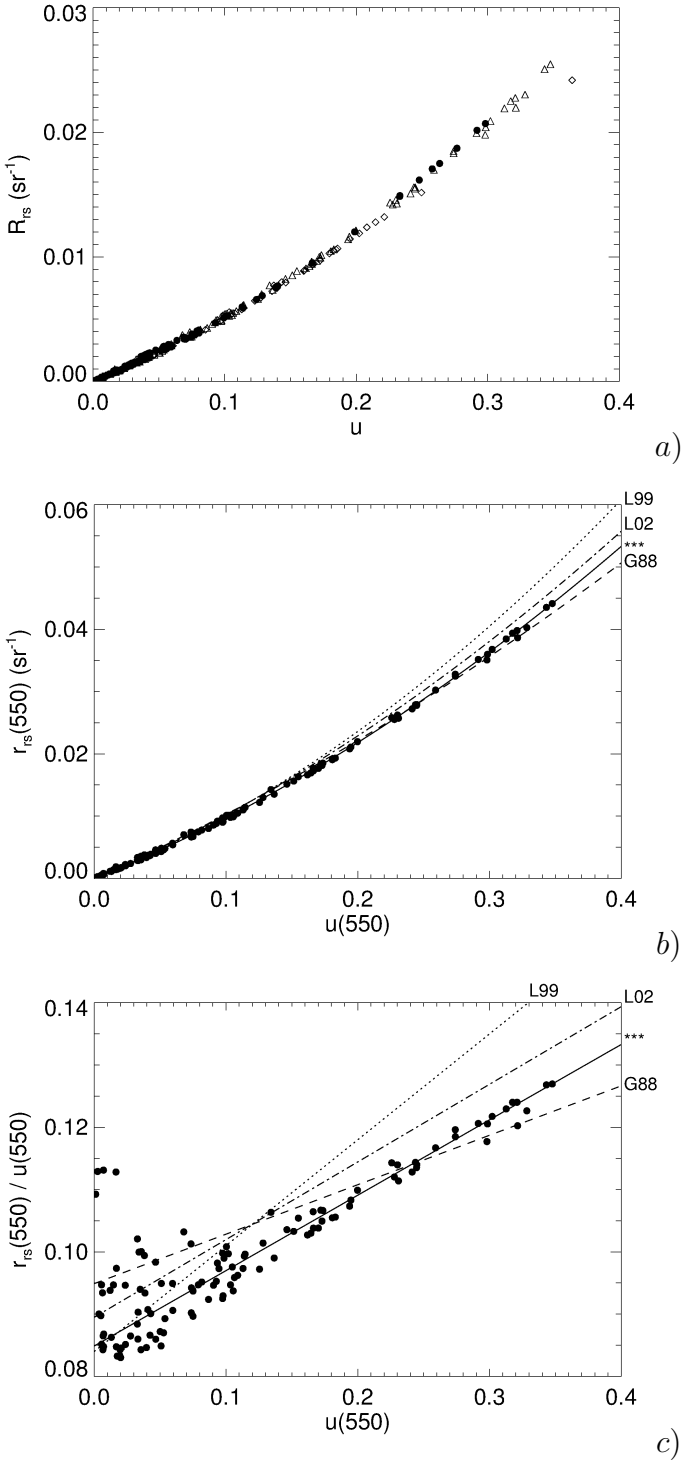

Figure 3.13: a) Above water nadir-viewed R_{rs} versus u for $\theta_s = 0$ (400 nm in diamonds, 550 nm in triangles and 700 nm in filled circles). b) Modelled subsurface nadir-viewed r_{rs} versus $u(550)$ for $\theta_s = 0$. The relationships of Gordon et al. (1988) (G88), Lee et al. (1999) (L99), Lee et al. (2002) L(02) and the parabolic model fit of this study (***) are shown. c) $u(550)$-normalised $r_{rs}(550)$ versus $u(550)$ similar to the plot in Lee et al. (2004), highlighting the deviations from the simplistic 2^{nd} order polynomial approach. The relationships of Gordon et al. (1988) (G88), Lee et al. (1999) (L99), Lee et al. (2002) L(02) and the parabolic model fit of this study (***) are shown.

contribution and coefficients were determined from above-water R_{rs},

$$R_{rs} = G_w \left(\frac{b_{bw}}{a + b_b} \right) + G_0 \left(\frac{b_{bp}}{a + b_b} \right) + G_1 \left(\frac{b_{bp}}{a + b_b} \right)^2 + G_2 \left(\frac{b_{bp}}{a + b_b} \right)^3, \quad (3.42)$$

where G_w, G_0, G_1 and G_2 are the polynomial model parameters, b_{bw} is the backscattering coefficient of water molecules, and b_{bp} is the backscattering coefficient of all particles (phytoplankton, detritus and minerals). For brevity, wavelength, geometry and sea state are omitted in the equation, but are described below.

A specific set of G_i (i denotes coefficient subscripts w, 0, 1 and 2) polynomial coefficients were determined using Levenberg-Markvardt optimisation (Markwardt 2009) for the modelled R_{rs} values determined for each wind speed (ws), solar zenith angle (θ_s), sensor view nadir angle (θ_v), sun-relative sensor view azimuth (ϕ_{az}) and wavelength (λ) combination. The resultant $G_i(\lambda, ws, \theta_s, \theta_v, \phi_{az})$ values were stored in a LUT which can be searched to retrieve the appropriate G_i coefficients for a measured $R_{rs}(\lambda, w, \theta_s, \theta_v, \phi_{az})$. Example G_i coefficients are shown in Fig. 3.14a.

For some analytical inversion approaches (i.e. Lee et al. (2002)), it is desirable to have knowledge of $\left(\frac{b_b}{a+b_b}\right)$ based on R_{rs} alone. In this case, the ratio between b_{bw} and b_{bp} is unknown, so Eq. 3.42 cannot be used directly. The Hydrolight synthetic dataset was used to determine an empirical polynomial relationship that could be applied to R_{rs} directly,

$$\frac{b_b}{a + b_b} = U_0 + U_1 R_{rs} + U_2 R_{rs}^2 + U_3 R_{rs}^3 + U_4 R_{rs}^4, \quad (3.43)$$

where U_0, U_1, U_2, U_3 and U_4 are the polynomial model parameters, and their spectral dependence is omitted for brevity.

Example spectral U_i coefficients are shown in Fig. 3.14c. As for the G model coefficients, the U model coefficients vary with wind speed, solar zenith angle, sensor view nadir angle, sun-relative sensor view azimuth and wavelength. The

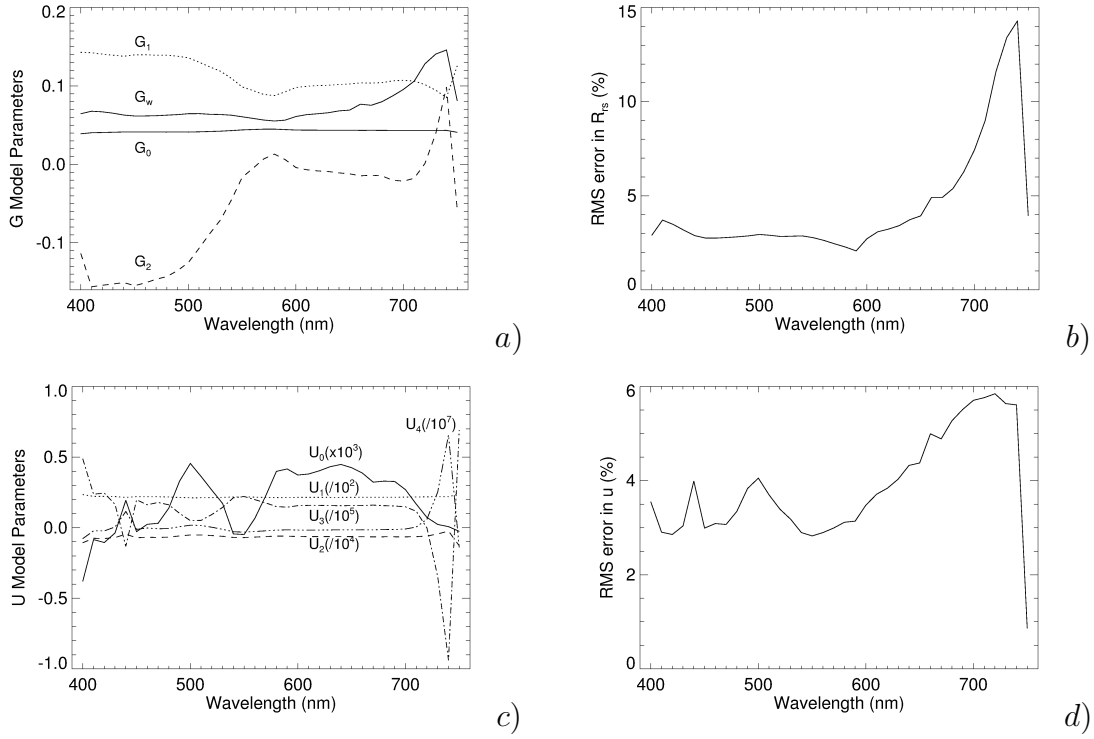

Figure 3.14: a) Spectral G_i model parameters for Eq. 3.42, for $\theta_s = 0$, $\phi_{az} = 135$, $\theta_v = 40$ and $ws = 1\ ms^{-1}$. b) RMS error when determining R_{rs} with Eq. 3.42 with the aforementioned model parameters and geometry from a). c) Spectral U_i model parameters for Eq. 3.43, for $\theta_s = 0$, $\phi_{az} = 135$, $\theta_v = 40$ and $ws = 1ms^{-1}$. d) RMS error when determining $\left(\frac{b_b}{a+b_b}\right)$ with Eq. 3.43.

U model values are also stored in a Look-Up-Table (LUT).

In comparing the RMS errors shown in Fig. 3.14b and d, one may be misled into concluding that the automatic conversion of R_{rs} into u yields a lower overall error, however it is important to realize that R_{rs} is between approximately 5% to 7% of u in this dataset (see Fig. 3.13a), and as such, will score higher RMS errors, especially in the red wavelengths due to there generally being very low R_{rs} in these regions.

3.3.3 Field Validation Measurements

Above water R_{rs} measurements were made with the DALEC, alongside surface ($\leq$ 2 m depth) *in situ* IOP measurements at several station visits in an attempt to collect data to assist evaluating the results of the aforementioned Hydrolight simulations which relate R_{rs} to u as in Fig. 3.13. The station visit locations are shown in Fig. 3.15, and details are provided in Table 3.5. The IOP methodology used in this section was described previously in Chapter 2. The individual spectra forming the validation dataset are shown in Figures 3.16-3.18.

Field-based comparisons of this nature are challenging because of the differing spatial scales involved between discrete IOP water sampling and the DALEC field of view. For example, each absorption measurement (a_{CDOM}, a_{ϕ} and a_{NAP}) was performed 'on station' with Niskin water samples taken from the middle of the ship, approximately 16 m from the viewing footprint of the DALEC which measures R_{rs}. Additionally, the b_{bp} measurements are taken from the hull intake, which is approximately 2 m under the surface of the water. Considering the time-consuming nature of discrete IOP absorption sampling and preparation, extensive vertical IOP sampling was not practical; although substances deeper than 2 m may contribute to R_{rs}. The coherence of the respective IOP and R_{rs} sampling times is also an issue. For each sampling location, an average DALEC R_{rs} and b_{bp} spectrum was calculated for a 15 minute window encompassing the discrete IOP sampling time, allowing the calculation of a standard deviations of

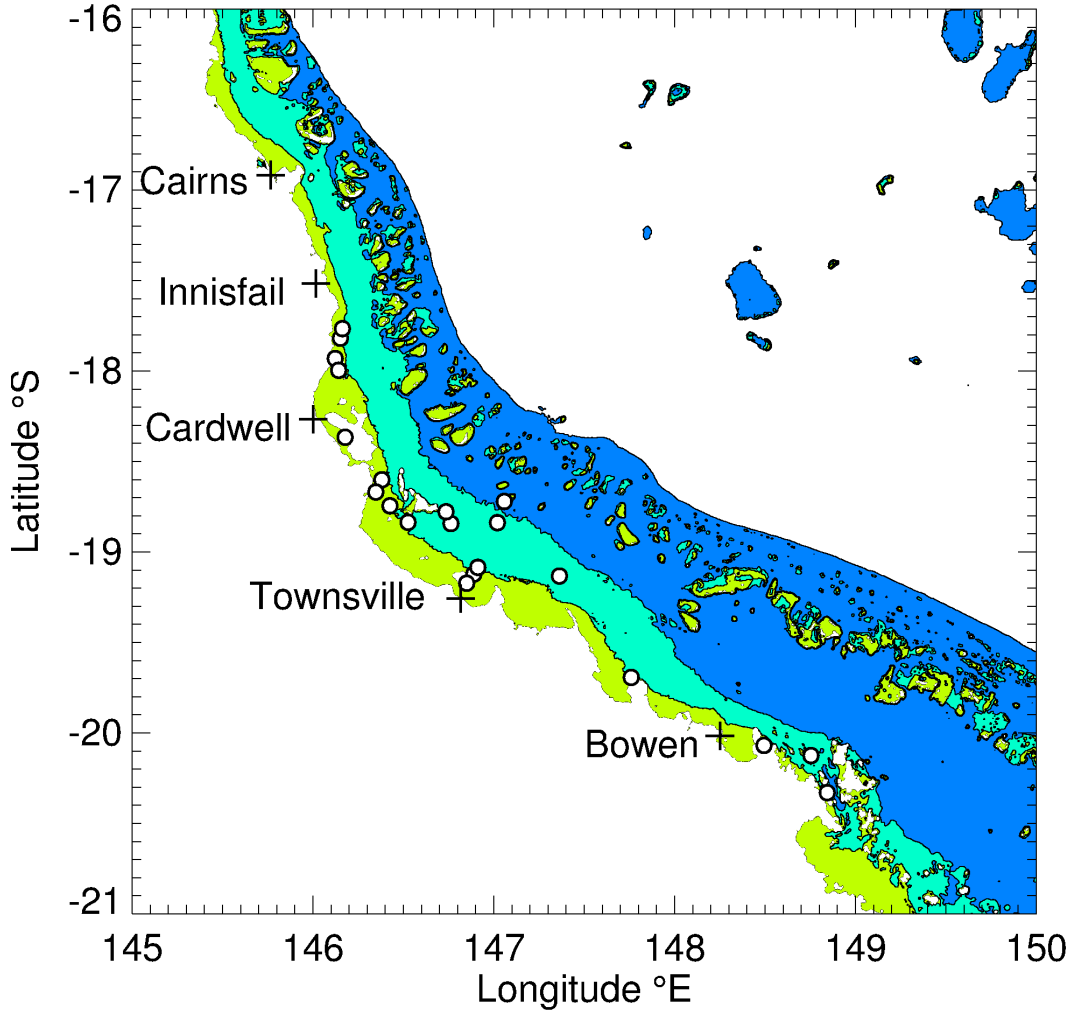

Figure 3.15: Locations (shown with white circles) in the GBR during January 2006 where concurrent quality-controlled DALEC R_{rs} and a_{NAP}, a_{ϕ}, a_{CDOM} and b_{bp} IOP measurements were made. The first (yellow) contour highlights waters shallower than 20 m, the cyan contour shows waters 20-40 m deep, and blue shows waters 40-100 m deep.

ID	Station ID	Day (Jan)	Local Time	Lat (°)	Lon (°)	θ_{rel} (°)	θ_s (°)	Wind (ms^{-1})	a-$a_w(442)$ (m^{-1})	$b_b(555)$ (m^{-1})	Spectral RMSE (%)
0	WQN035	22	11:03	-18.843	146.763	116	21	2.1	0.032	0.004	27.4
6	WQN051	24	13:00	-16.777	145.955	73	8	2.1	0.037	0.003	36.8
7	WQN060	28	9:45	-17.819	146.152	79	47	6.2	0.144	0.023	9.9
8	WQN061	28	11:00	-17.766	146.163	29	23	6.2	0.124	0.017	8.3
9	WQN062	28	12:50	-17.931	146.123	61	3	3.9	0.145	0.023	31.9
10	WQN063	28	16:35	-17.996	146.142	155	56	7.2	0.087	0.017	26.4
12	WQN066	29	9:00	-18.366	146.178	82	53	2.1	0.395	0.078	11.1
14	WQN068	29	11:00	-18.601	146.381	147	19	2.1	0.198	0.051	12
15	WQN069	29	12:35	-18.669	146.348	84	8	2.1	0.252	0.061	10.8
16	WQN070	29	14:100	-18.745	146.426	148	22	2.1	0.128	0.028	11.3
18	WQN072	30	15:00	-18.836	146.526	138	36	2.1	0.089	0.014	13.3
19	WQN073	30	16:25	-18.778	146.736	135	59	2.1	0.086	0.009	24.4
21	WQN076	31	11:05	-18.721	147.058	116	20	2.6	0.038	0.004	28.3
22	WQN077	31	12:05	-18.838	147.020	129	6	2.6	0.035	0.003	18.8
24	WQN079	31	13:40	-19.122	146.890	20	27	3.1	0.129	0.024	20
25	WQN080	31	14:38	-19.085	146.912	61	22	3.1	0.153	0.028	10.1
26	WQN081	31	15:30	-19.173	146.850	90	38	3.1	0.113	0.025	13.2
29	WQS059	7	15:00	-20.330	148.844	123	39	7.9	0.073	0.013	13.0
32	WQS069	9	11:48	-20.125	148.754	140	17	3.1	0.092	0.014	16.1
33	WQS070	9	14:10	-20.069	148.494	35	34	6.1	0.093	0.020	23.1
34	WQS072	10	10:25	-19.693	147.760	144	32	10.9	0.120	0.021	12.1
36	WQS076	10	15:00	-19.133	147.363	127	38	9.9	0.038	0.004	31.8

Table 3.5: Concurrent IOP and DALEC measurement times and locations, sun-relative DALEC view azimuth (θ_{az}), solar zenith angle (θ_s), wind speed, and total non-water absorption at 442 nm ($\beta = 2.0$) and $b_b(555)$ measurements sampled during the station. The final column shows the spectral RMS error between the similarity spectrum-corrected measured R_{rs} and IOP-based R_{rs} spectra (Individual spectra shown in Figs. 3.16 - 3.18).

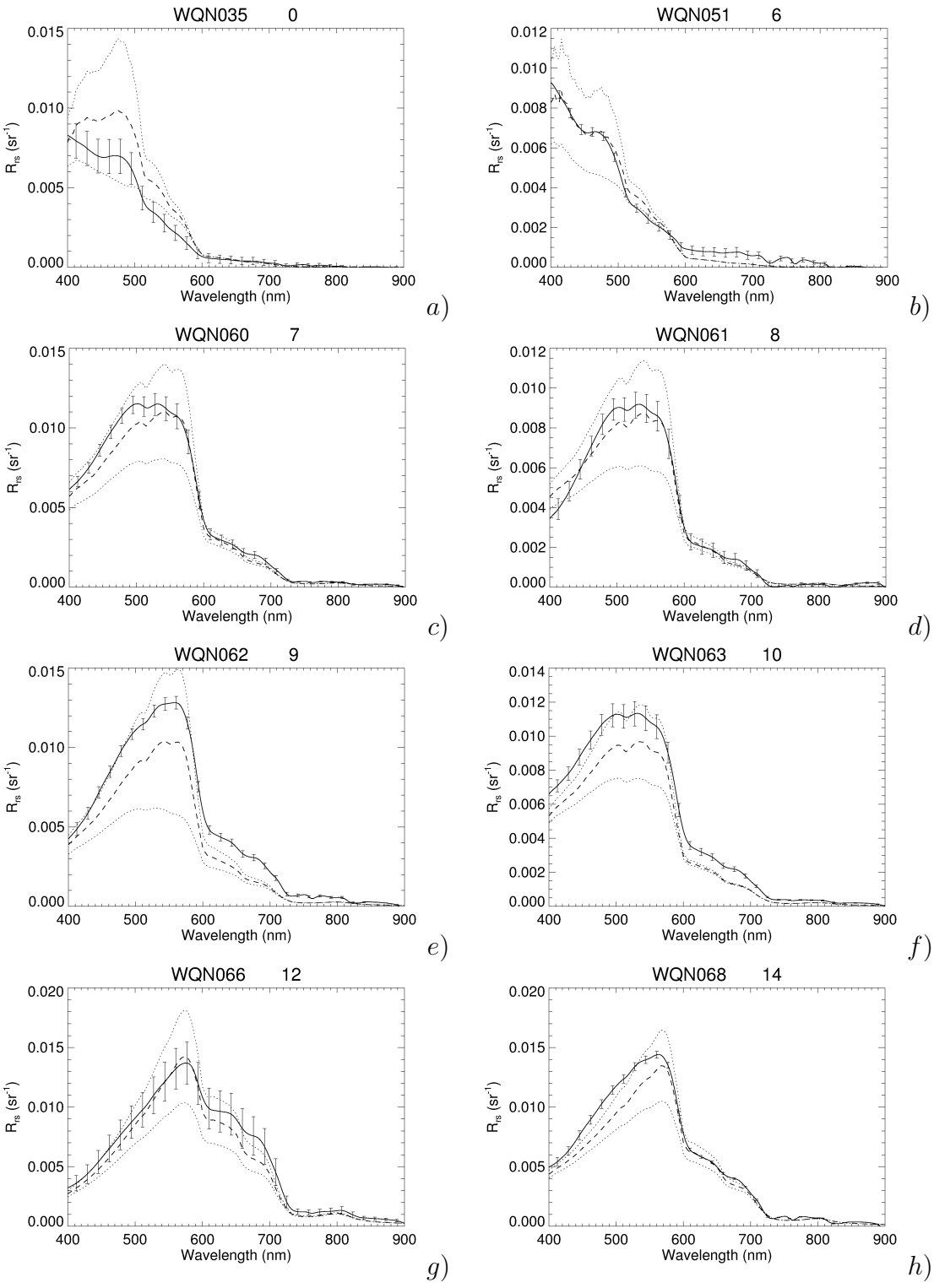

Figure 3.16: DALEC station average R_{rs} shown with the solid line and $\pm 1\sigma$ values are shown with error bars. The dashed line is the reconstructed R_{rs} spectrum based on IOP measurements from the same location and Eq. 3.42. The dotted lines show the uncertainty of the IOP-based R_{rs} reconstruction, calculated using partial differential calculus (Kirkup 1994). For these spectra, $\beta_f = 2.0$, $a_{NAP}(750) = 0$ and the measured R_{rs} spectrum was corrected with the similarity spectrum approach.

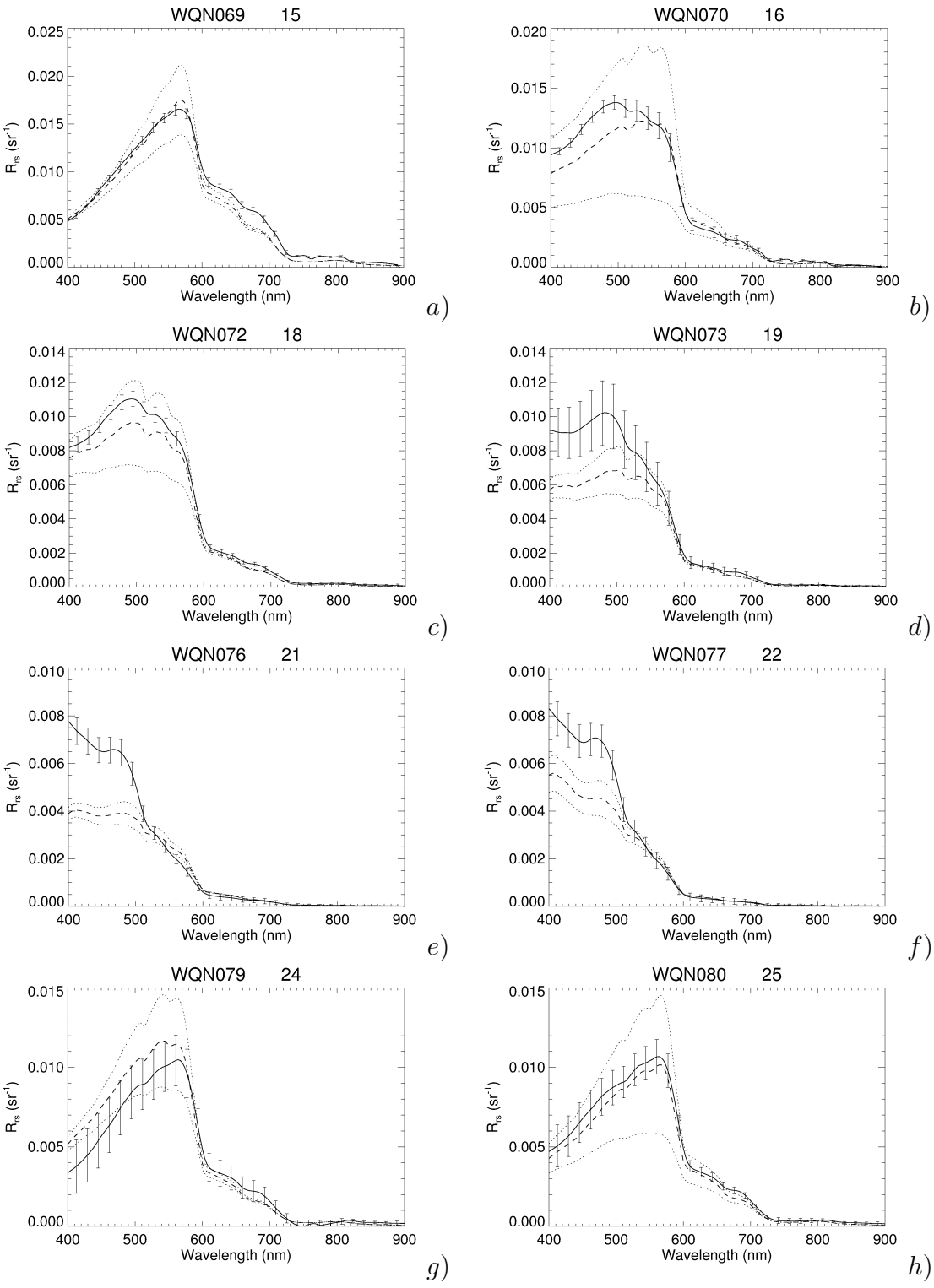

Figure 3.17: DALEC station average R_{rs} shown with the solid line and $\pm 1\sigma$ values are shown with error bars. The dashed line is the reconstructed R_{rs} spectrum based on IOP measurements from the same location and Eq. 3.42. The dotted lines show the uncertainty of the IOP-based R_{rs} reconstruction, calculated using partial differential calculus (Kirkup 1994). For these spectra, $\beta_f = 2.0$, $a_{NAP}(750) = 0$ and the measured R_{rs} spectrum was corrected with the similarity spectrum approach.

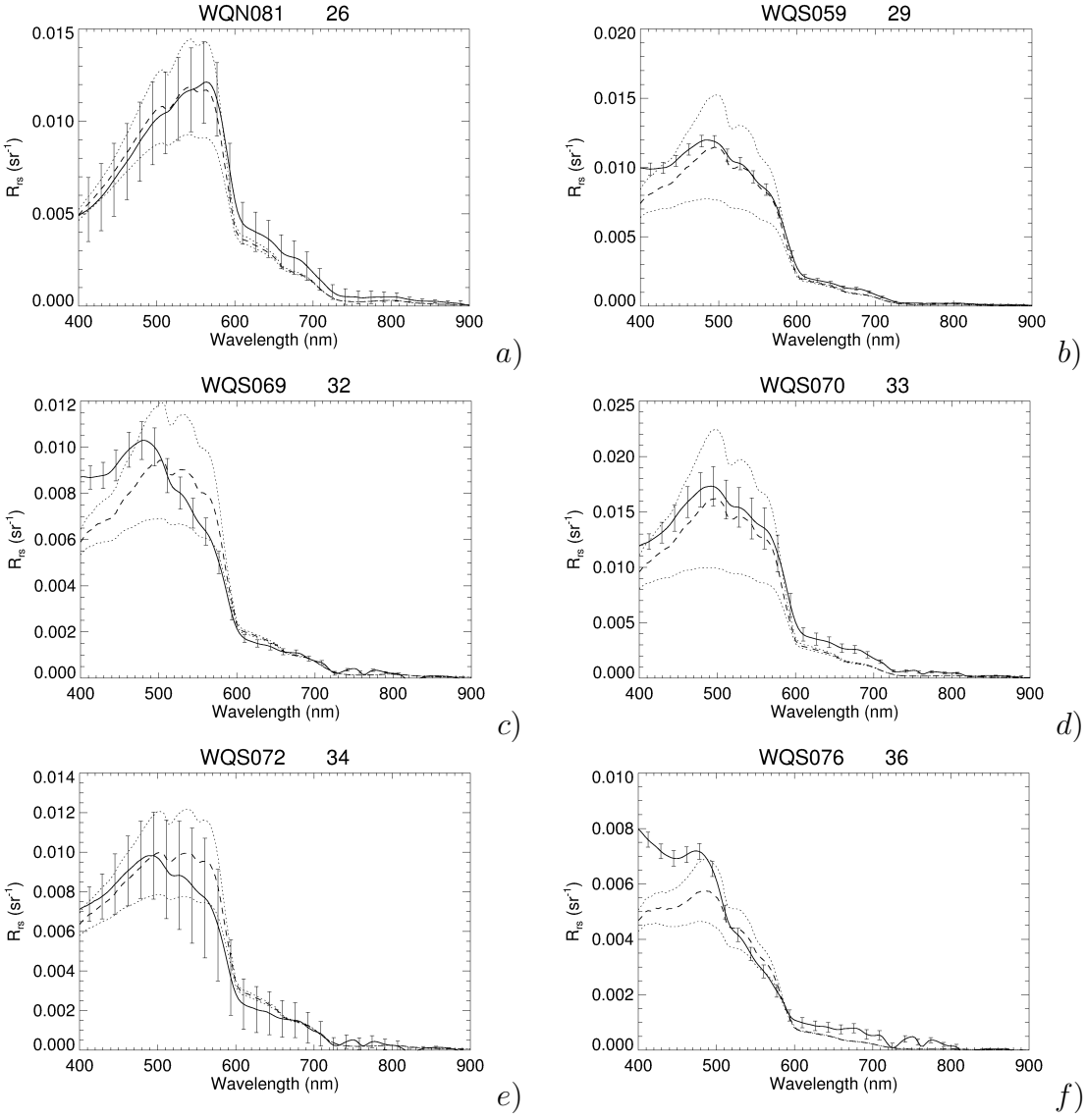

Figure 3.18: DALEC station average R_{rs} shown with the solid line and $\pm 1\sigma$ values are shown with error bars. The dashed line is the reconstructed R_{rs} spectrum based on IOP measurements from the same location and Eq. 3.42. The dotted lines show the uncertainty of the IOP-based R_{rs} reconstruction, calculated using partial differential calculus (Kirkup 1994). For these spectra, $\beta_f = 2.0$, $a_{NAP}(750) = 0$ and the measured R_{rs} spectrum was corrected with the similarity spectrum approach.

R_{rs} and b_{bp} to quantify spatiotemporal variability in the R_{rs} measurements and b_{bp}-derived measurements (see captions in Figures 3.16 - 3.24).

Confounding spatiotemporal issues aside, the overall uncertainties associated with combining multiple measurements of IOPs into R_{rs} (Eq. 3.42) or u (Eq. 3.43) are often large (see error bars in Figures 3.16 - 3.18). The forward conversion (Eq. 3.42) was used to convert measured IOPS into R_{rs}, because this is how most predictor-corrector inversion schemes work. The reverse conversion (Eq. 3.43) was also tested, because this function is useful for the QAA approach (Lee et al. 2002). To put the aforementioned uncertainties into context, the uncertainty of the input IOPs were propagated through Eq. 3.42, using partial differential calculus (Kirkup 1994). A conservative spectrally-flat uncertainty of 0.01 m^{-1} was assigned to the CDOM measurements (based on the baseline reproducibility of the spectrophotometer), and estimated uncertainties of 5% were assigned to both a_{phi} and a_{NAP} spectra, although the uncertainty is probably much larger when considering the pathlength amplification factor and scattering error uncertainties. The standard deviation of the on-station b_{bp} measurements was used as the uncertainty of b_{bp}.

The DALEC R_{rs} measurements may be contaminated by skylight reflection and sun-glint, although efforts were made to correct and quality control this contamination (see Eq. 3.24 and Table 3.2). During sampling from the Niskin bottle, the RV Lady Basten was usually positioned side-on and downwind of the Niskin bottle, to minimise the chance of wire tangles. Often this means that the DALEC relative azimuth angle (θ_{rel}) is non-optimal during station measurements, so data from some stations did not pass quality control procedures established in Table 3.2. Upon comparison between the IOP-based R_{rs} and the measured R_{rs} spectra, it was found that sometimes acceptable comparisons (i.e. spectral RMS errors between measured and modelled spectra $< 40\%$) were achieved in non-optimal relative azimuth angle (θ_{rel}) conditions. This may be indicative of the adequate performance of the above-water skylight correction method for those particular stations. However, a number of poor comparisons were observed for R_{rs} measure-

ments made when the solar zenith angle (θ_s) was greater than 60°. Considering the poor spectral fits, and that remote sensors typically don't image the GBR during high solar zenith angle conditions, these data were excluded from analysis. In addition, a small number of measured v.s. IOP-modelled R_{rs} spectra had radically different spectral features which could not be explained by sources of uncertainty previously evaluated. This type of mismatch was attributed to IOP sample mislabelling, and these samples were also excluded. Selective exclusion of this nature is considered acceptable in this aspect of the work because this dataset is primarily being used for a validation of the Hydrolight-based Look-up table approach, and not for deriving any quantitative calibration coefficients which would effect down-stream processing.

Although error bars between measured and modelled R_{rs} are both large (i.e. Fig. 3.19a), and most individual measured and modelled spectra are in agreement when considering these error bars, there may be trends identifiable in the data. The data shown in Figures 3.19a, 3.19c and 3.19e show comparisons between measured and IOP-modelled R_{rs} assuming negligible a_{NAP} absorption in the NIR, with $\beta_f = 2.0$, and the R_{rs} spectrum being corrected for residual skyglint by setting $R_{rs}(750) = 0$. Figures 3.19b, 3.19d and 3.19f show the same comparisons with the theoretical similarity-spectrum-based residual sky glint correction developed in this study. Differences between the two approaches are minor; offsets are slightly lower for the similarity-spectrum-based method, however slopes are slightly reduced. It is possible that at least in this validation data subset, the $R_{rs}(750) = 0$ yields more accurate comparsions with the IOP-based model. The confidence interval of the regression is large, making conclusions difficult. Considering GBR flood plume waters can get turbid, the similarity-spectrum method is preferred for subsequent DALEC processing. Without underwater E_d and L_u measurements for comparison, it is difficult to quantify residual skylight reflection artifacts in the corrected DALEC measurements. Atmospheric gas absorption features indicative of skylight reflection are sometimes apparent in the DALEC R_{rs} spectra, however it is unlikely that these wavelength regions will be utilised for IOP-based inversions.

The particulate absorption IOP measurements are subject to an unvalidated path-length amplification factor ($\beta_f = 2$ see Eq. 2.20) for GBR coastal particles, and these (β_f) coefficients are known to vary in the literature (i.e. Laurion et al. (2003), Cleveland & Weidemann (1993), Roesler (1998)). To understand the consequences of an uncertain pathlength amplification factor (previously assumed to be $\beta_f = 2.0$ (Roesler 1998)), the same measured vs IOP-modelled R_{rs} regressions were performed with different path-length amplification factors being applied to the measured filter pad-based IOP measurements. Laurion et al. (2003) determined coefficients closer to $\beta_f = 2.6$ and Kishino et al. (1985) reported values ranging from $\beta_f = 2.43$ to $\beta_f = 4.71$. Other researchers report the effective β_f is a non-linear function of the sample optical density (Cleveland & Weidemann 1993). The resultant plots using $\beta_f = 2.6$,3.0 and 4.0 are shown in Figs. 3.20 - 3.22. Increases of amplification factor increased the regression slopes between DALEC measured R_{rs} and IOP-based R_{rs} values and also generally reduced regression offsets.

In addition to the uncertain pathlength amplification factor, variations in the scattering corrections of these QFT absorption measurements exist; in particular, there is a question whether the non-algal particulate absorption measured in the NIR (i.e. 750 nm) is non-zero or not (Zaneveld et al. 1994, Bowers & Binding 2006, Mitchell et al. 2000, Babin & Stramski 2002). To investigate the effects of the uncertain nature of NIR a_{NAP} absorption, validation plots were generated with both $a_{NAP}(750) = 0$ and $a_{NAP}(750) \neq 0$ approaches (using $\beta_f = 2.0$ in Fig. 3.23 and $\beta_f = 4.0$ in Fig. 3.24), along with the similarity spectrum-based residual glint correction method. Figures 3.23 and 3.24 both show subtle degradation of performance when $a_{NAP}(750) \neq 0$. In both instances, the regression slope is reduced, but more significantly, the residual is increased. Based on this observation and consistent with the findings of (Babin, Morel, Fournier-Sicre, Fell & Stramski 2003), $a_{NAP}(750)$ will be set to 0 for subsequent work in this thesis.
Due to the low number of data points and large error bars in R_{rs} and IOP measurements, it is unclear which pathlength amplification factor to use in sub-

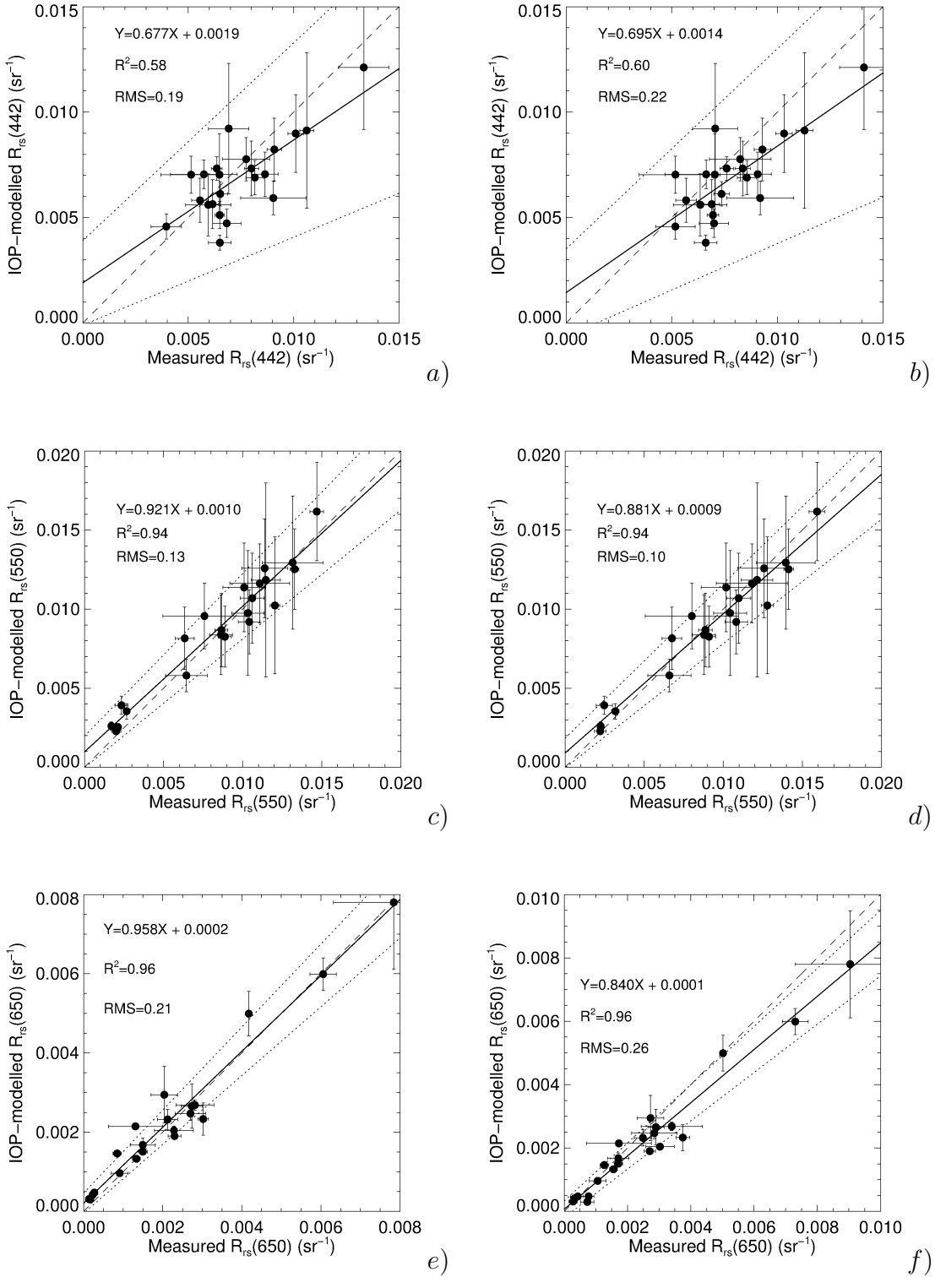

Figure 3.19: IOP-modelled ($\beta_f = 2.0$) R_{rs} based on Eq. 3.42 versus DALEC measured R_{rs} at 3 different wavelengths, for $R_{rs}(750) = 0$ residual skylight correction (left hand column a, c and e), and similarity-spectrum based residual skylight correction (right hand column, b, d and f). The solid line is a plot of the regression equation shown on the figure. The dashed line is the 1:1 line and the dotted lines are the $\pm 2\sigma$ confidence intervals of the linear regression.

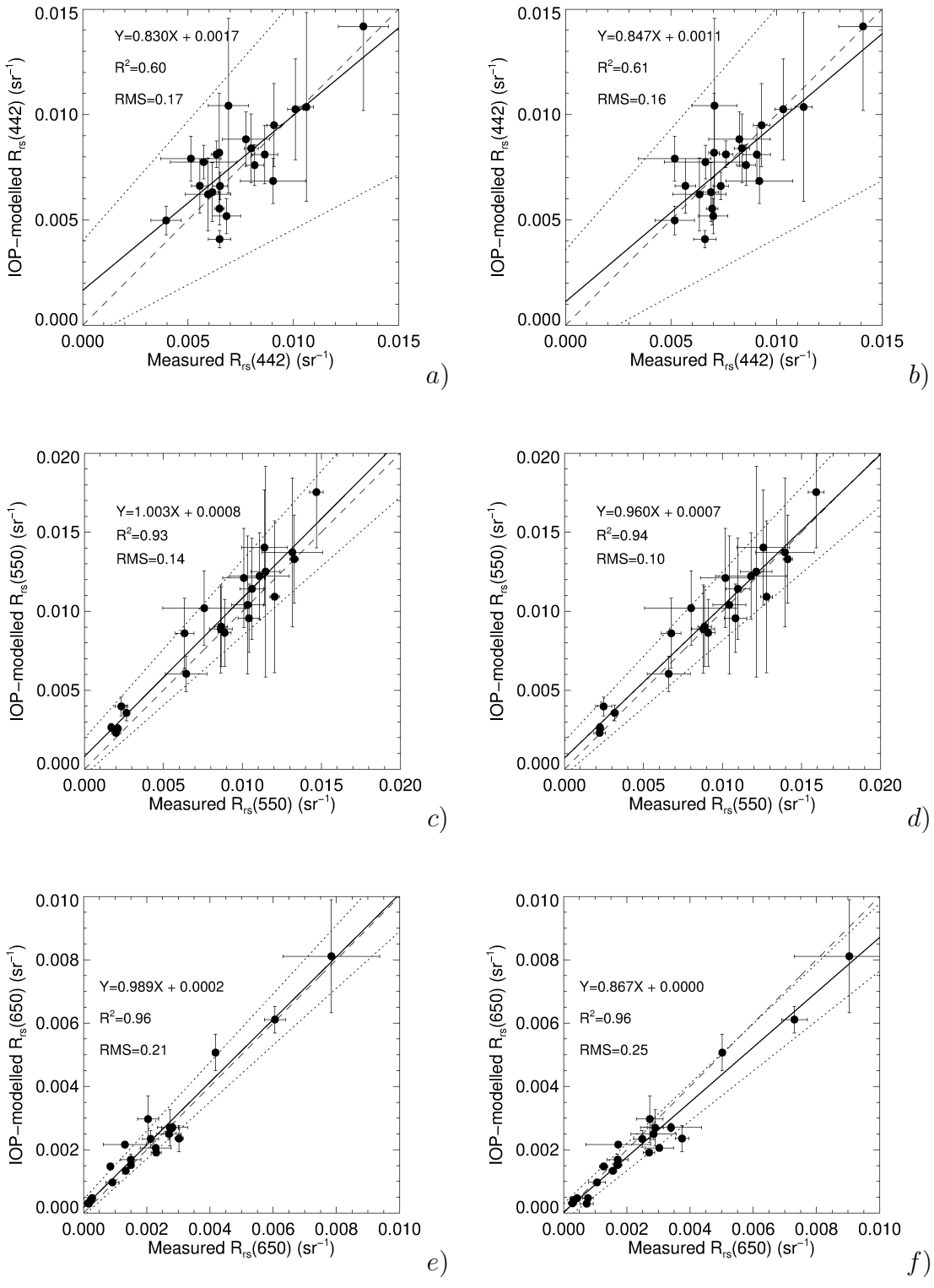

Figure 3.20: IOP-modelled ($\beta_f = 2.6$) R_{rs} based on Eq. 3.42 versus DALEC measured R_{rs} at 3 different wavelengths, for $R_{rs}(750) = 0$ residual skylight correction (left hand column a, c and e), and similarity-spectrum based residual skylight correction (right hand column, b, d and f). The solid line is a plot of the regression equation shown on the figure. The dashed line is the 1:1 line and the dotted lines are the $\pm 2\sigma$ confidence intervals of the linear regression.

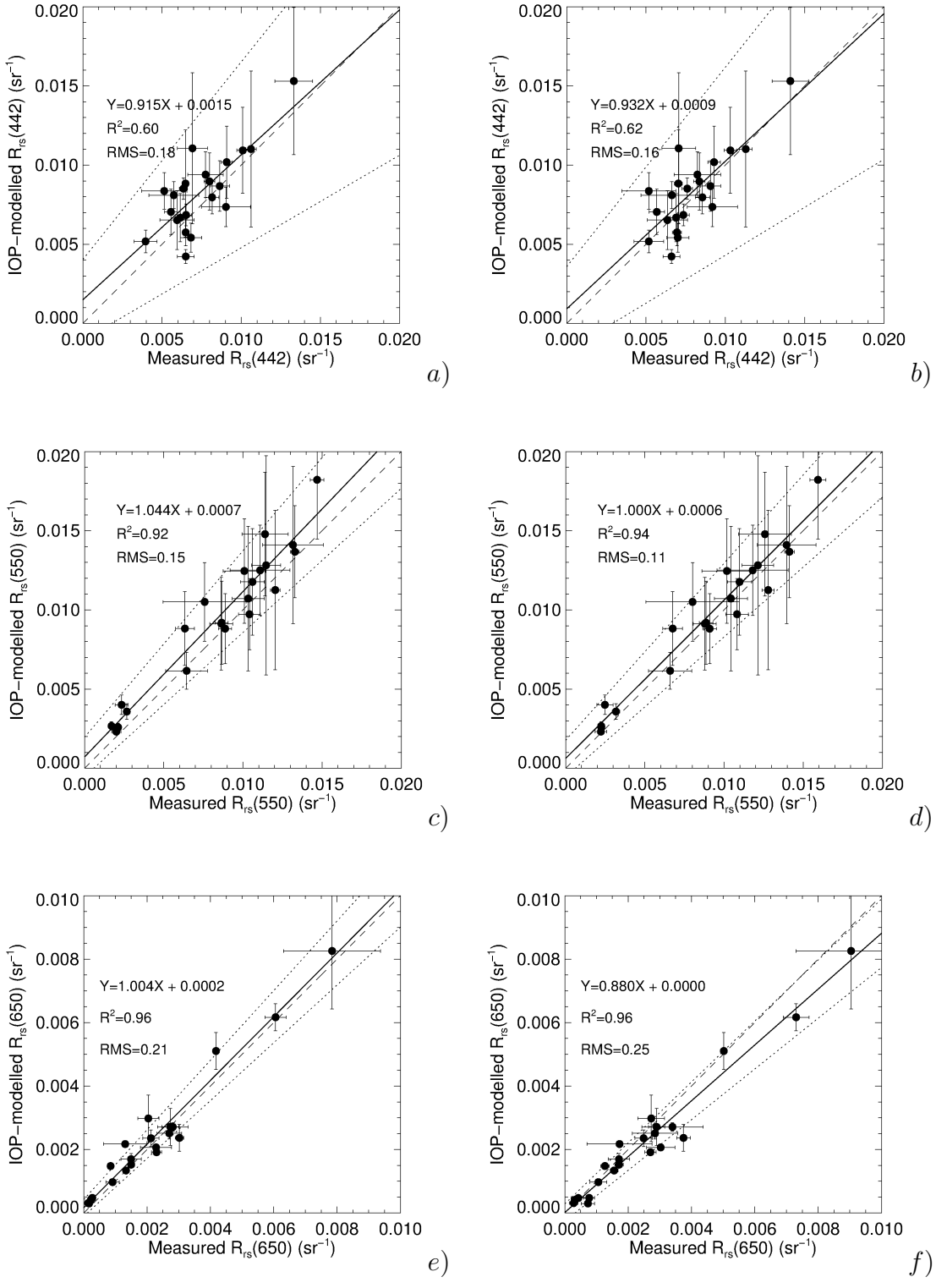

Figure 3.21: IOP-modelled ($\beta_f = 3.0$) R_{rs} based on Eq. 3.42 versus DALEC measured R_{rs} at 3 different wavelengths, for $R_{rs}(750) = 0$ residual skylight correction (left hand column a, c and e), and similarity-spectrum based residual skylight correction (right hand column, b, d and f). The solid line is a plot of the regression equation shown on the figure. The dashed line is the 1:1 line and the dotted lines are the $\pm 2\sigma$ confidence intervals of the linear regression.

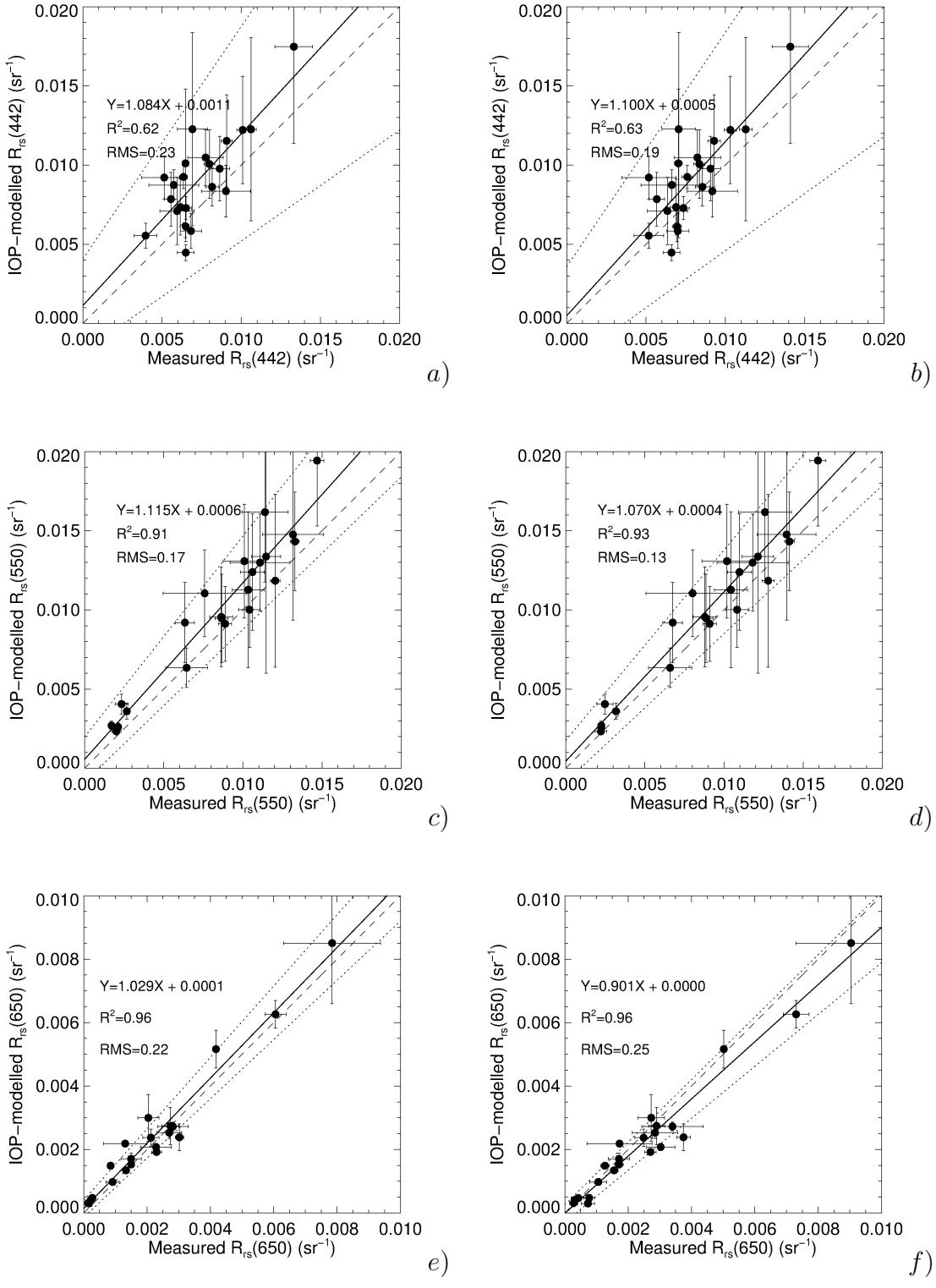

Figure 3.22: IOP-modelled ($\beta_f = 4.0$) R_{rs} based on Eq. 3.42 versus DALEC measured R_{rs} at 3 different wavelengths, for $R_{rs}(750) = 0$ residual skylight correction (left hand column a, c and e), and similarity-spectrum based residual skylight correction (right hand column, b, d and f). The solid line is a plot of the regression equation shown on the figure. The dashed line is the 1:1 line and the dotted lines are the $\pm 2\sigma$ confidence intervals of the linear regression.

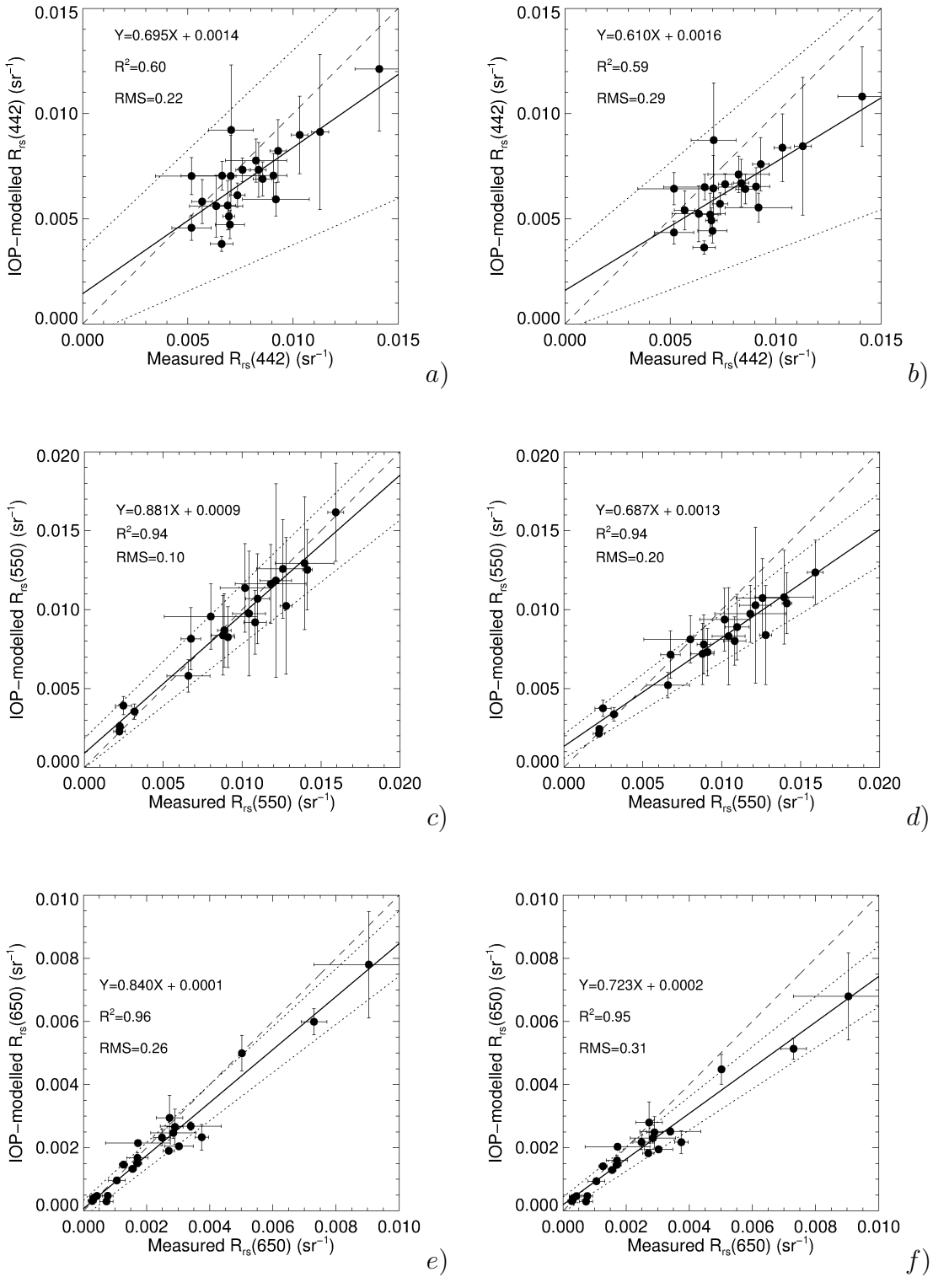

Figure 3.23: IOP-modelled ($\beta_f = 2.0$) R_{rs} based on Eq. 3.42 versus DALEC measured R_{rs} at 3 different wavelengths, for $a_{NAP}(750) = 0$ (left hand column a, c and e), and $a_{NAP}(750) \neq 0$ (right hand column, b, d and f). Similarity-spectrum based residual skylight correction was used in these plots. The solid line is a plot of the regression equation shown on the figure. The dashed line is the 1:1 line and the dotted lines are the $\pm 2\sigma$ confidence intervals of the linear regression.

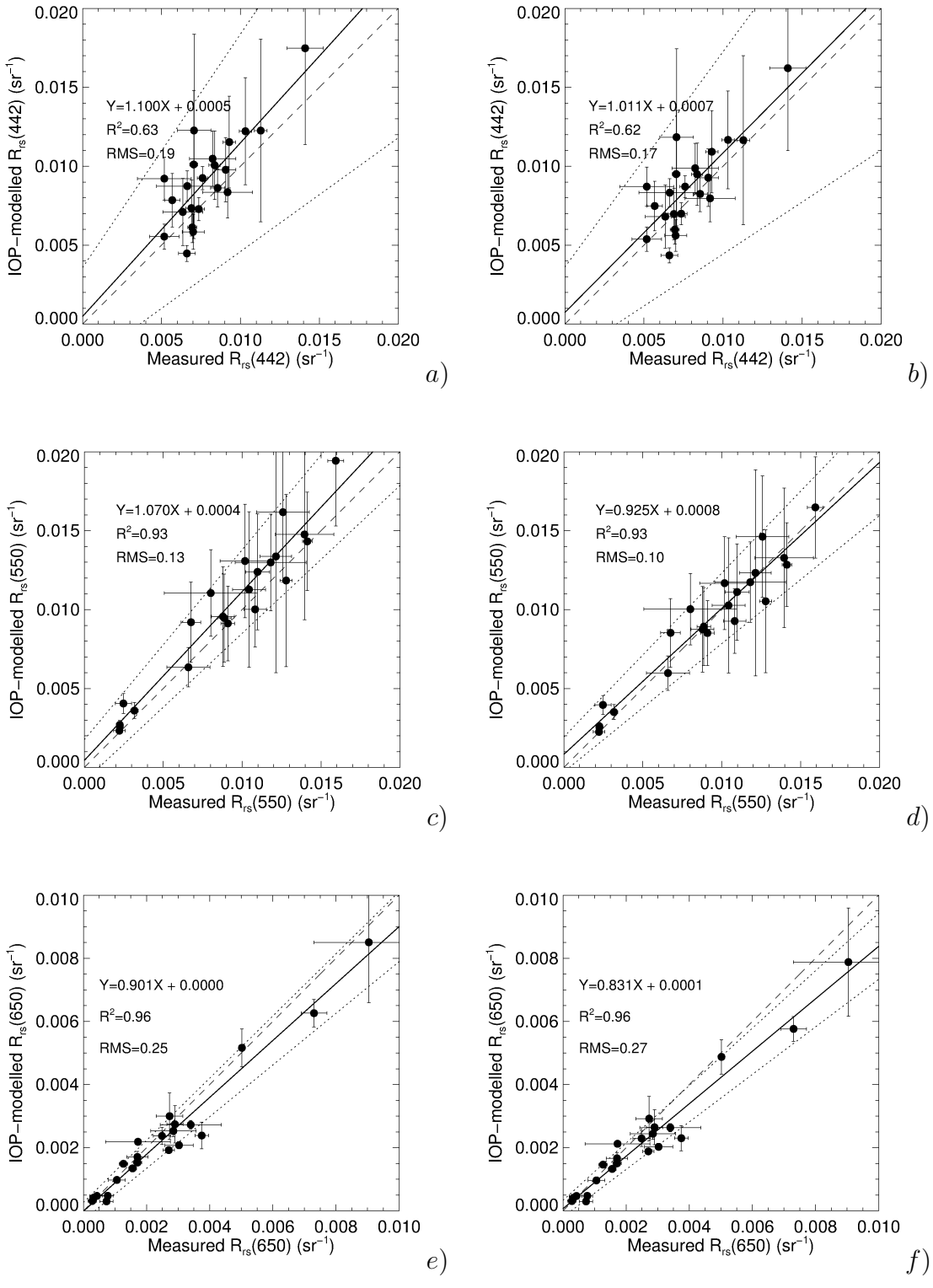

Figure 3.24: IOP-modelled ($\beta_f = 4.0$) R_{rs} based on Eq. 3.42 versus DALEC measured R_{rs} at 3 different wavelengths, for $a_{NAP}(750) = 0$ (left hand column a, c and e), and $a_{NAP}(750) \neq 0$ (right hand column, b, d and f). Similarity-spectrum based residual skylight correction was used in these plots. The solid line is a plot of the regression equation shown on the figure. The dashed line is the 1:1 line and the dotted lines are the $\pm 2\sigma$ confidence intervals of the linear regression.

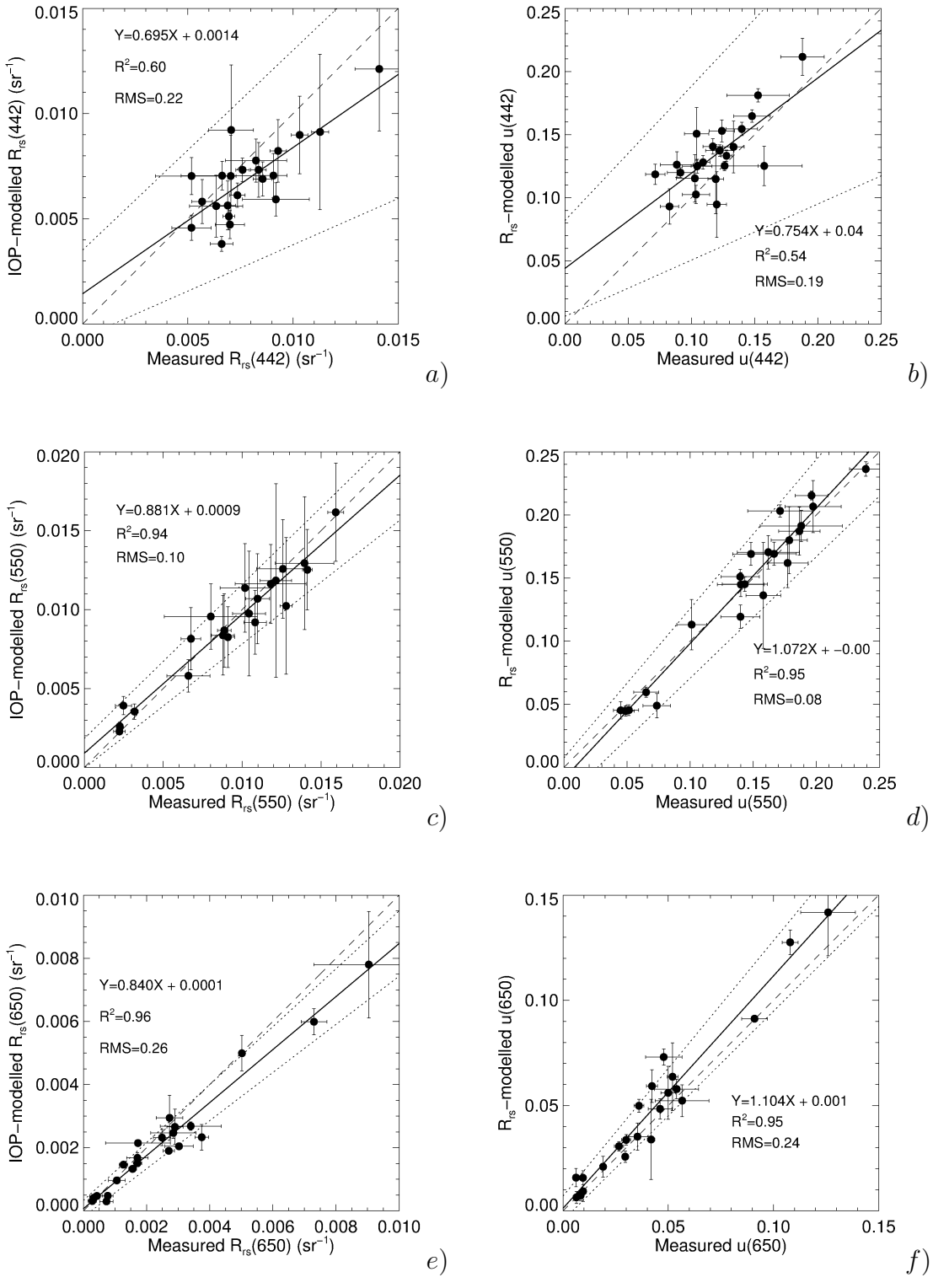

Figure 3.25: IOP-modelled ($\beta_f = 2.0$) R_{rs} based on Eq. 3.42 versus DALEC measured R_{rs} at 3 different wavelengths (left hand column a, c and e). DALEC-based u (Eq. 3.43) versus measured u at 3 different wavelengths (right hand column, b, d and f). The similarity-spectrum based residual skylight correction was used, and $a_{NAP}(750) = 0$. The solid line is a plot of the regression equation shown on the figure. The dashed line is the 1:1 line and the dotted lines are the $\pm 2\sigma$ confidence intervals of the linear regression.

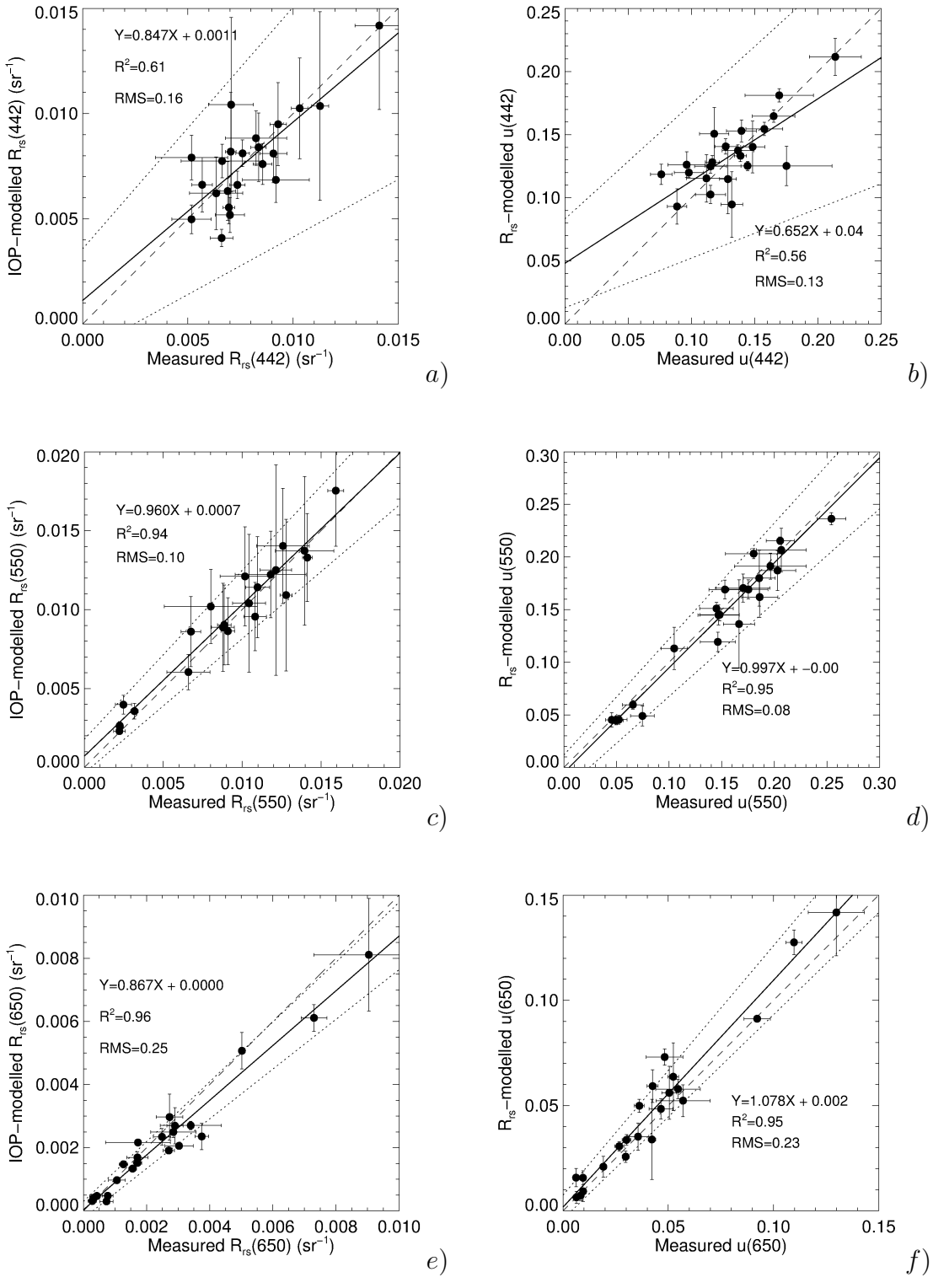

Figure 3.26: IOP-modelled ($\beta_f = 2.6$) R_{rs} based on Eq. 3.42 versus DALEC measured R_{rs} at 3 different wavelengths (left hand column a, c and e). DALEC-based u (Eq. 3.43) versus measured u at 3 different wavelengths (right hand column, b, d and f). The similarity-spectrum based residual skylight correction was used, and $a_{NAP}(750) = 0$. The solid line is a plot of the regression equation shown on the figure. The dashed line is the 1:1 line and the dotted lines are the $\pm 2\sigma$ confidence intervals of the linear regression.

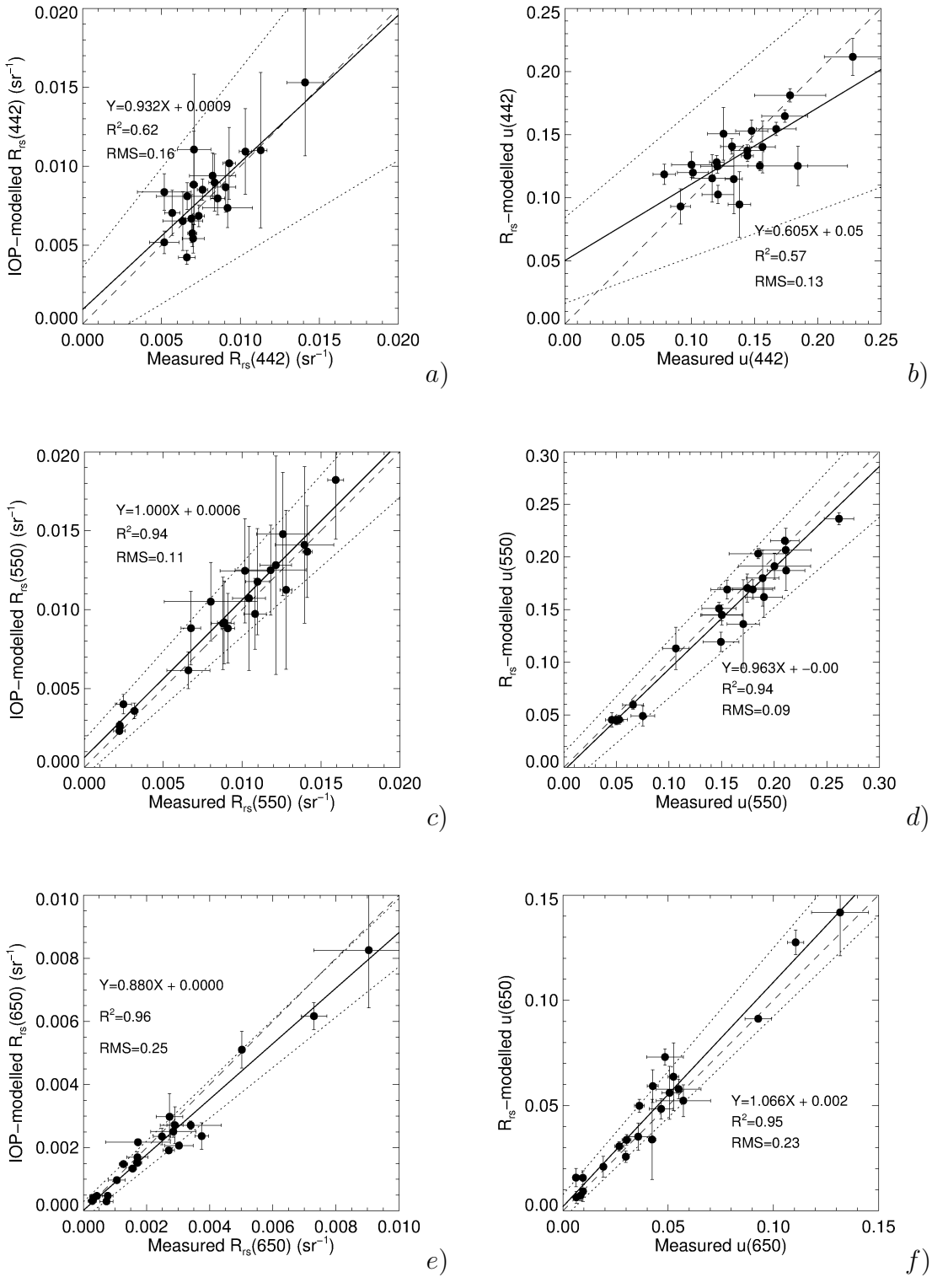

Figure 3.27: IOP-modelled ($\beta_f = 3.0$) R_{rs} based on Eq. 3.42 versus DALEC measured R_{rs} at 3 different wavelengths (left hand column a, c and e). DALEC-based u (Eq. 3.43) versus measured u at 3 different wavelengths (right hand column, b, d and f). The similarity-spectrum based residual skylight correction was used, and $a_{NAP}(750) = 0$. The solid line is a plot of the regression equation shown on the figure. The dashed line is the 1:1 line and the dotted lines are the $\pm 2\sigma$ confidence intervals of the linear regression.

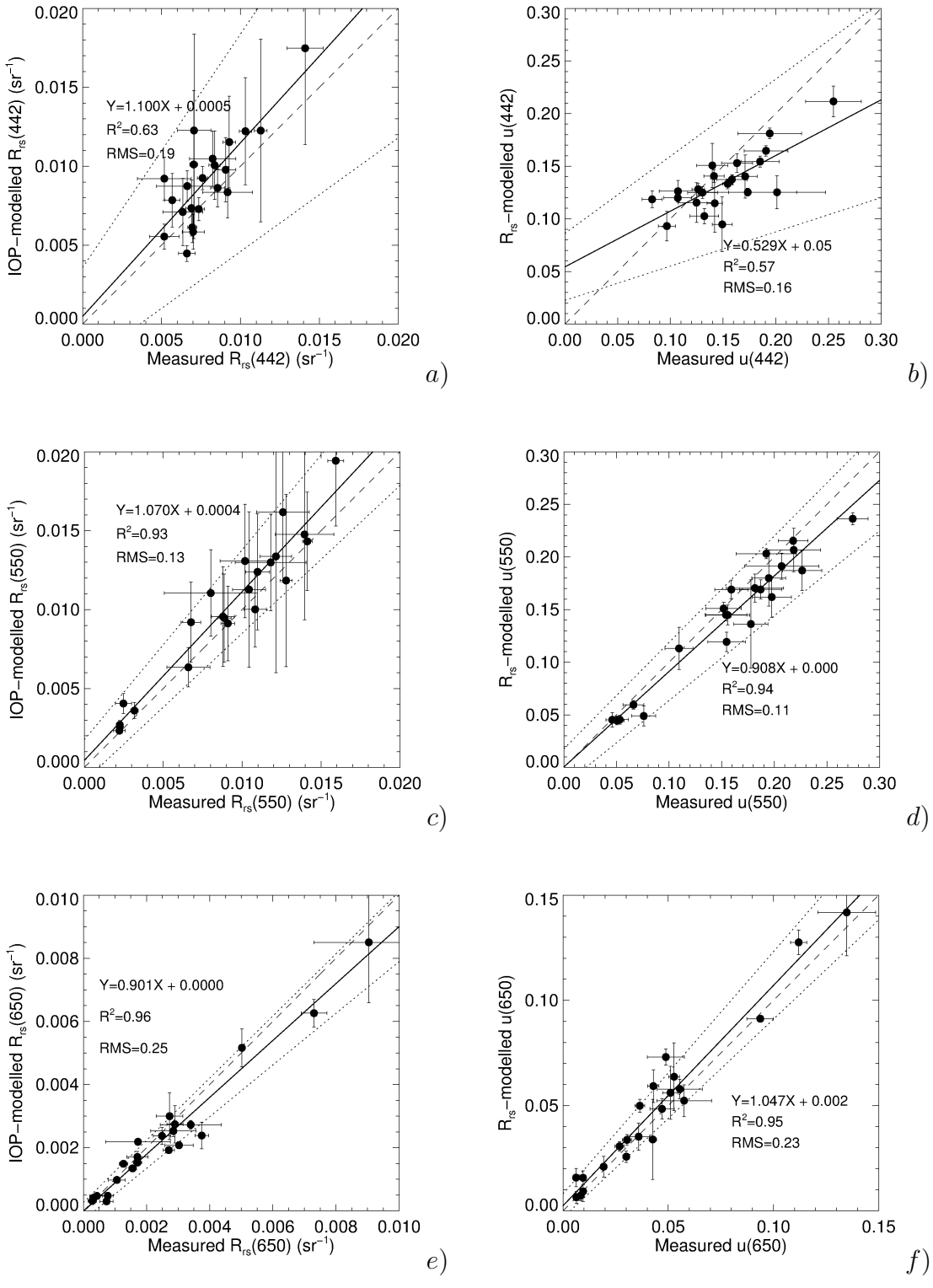

Figure 3.28: IOP-modelled ($\beta_f = 4.0$) R_{rs} based on Eq. 3.42 versus DALEC measured R_{rs} at 3 different wavelengths (left hand column a, c and e). DALEC-based u (Eq. 3.43) versus measured u at 3 different wavelengths (right hand column, b, d and f). The similarity-spectrum based residual skylight correction was used, and $a_{NAP}(750) = 0$. The solid line is a plot of the regression equation shown on the figure. The dashed line is the 1:1 line and the dotted lines are the $\pm 2\sigma$ confidence intervals of the linear regression.

sequent stages of the thesis. For now the, $\beta_f = 2.0$ will remain until further evidence presents itself to justify an alteration.

3.4 Summary

- The DALEC spectroradiometer was developed to measure the above-water R_{rs}. The DALEC calibration and data analysis protocols were described. The DALEC spectrometers exhibited non-linearity, so a non-linearity compensation factor was determined for the DALEC in order to ensure better radiometric accuracy. A method for correcting the above-water DALEC measurements for surface reflected skylight and sun glint was developed. This should also improve the accuracy of downstream DALEC-derived products.

- The GBR IOP models developed in Chapter 2 were used as input into extensive Hydrolight simulations tuned to cover the water quality concentrations observed in GBR waters. It was shown that the simulated R_{rs} signals contained information about the inherent optical properties in the water. The conversion factor from R_{rs} to u (and from u to R_{rs}) was determined for synthetic IOP (including the phase function) blends of phytoplankton, minerals and dissolved substances found in the GBR. These conversion factors were also functionalised in terms of wavelength, solar zenith angle, sun-relative azimuth angle and view angle so that R_{rs} measurements from either satellite or the DALEC can be converted into $\frac{b_b}{a+b_b}$. The conversion factors were stored in a Look-Up-Table (LUT) for further application.

- The Hydrolight-based LUT was applied to *in situ* IOP measurements and the LUT was generally able to reconstruct the DALEC measured R_{rs} spectrum within experimental uncertainties. Particulate absorption path-length amplification and NAP absorption null-point correction were investigated. The null point $a_{NAP}(750) = 0$ best reconciled the Hydrolight LUT-converted R_{rs} data with the *in situ* IOP measurements, so these values are used in subsequent analysis. Considering large experimental uncertainties, there is little firm evidence to support increasing the pathlength amplification factor (β_f) of the IOP measurements (and resultant models determined in Chapter). This pathlength amplification factor will be addressed later.

Chapter 4

Remote Sensing Reflectance Inversions

4.1 Introduction

The focus of this chapter is to combine the relationships between water quality parameters and IOPs in the GBR attained in Chapter 3.4, with the knowledge about the decomposition of R_{rs} into IOPs in Chapter 3, in order to *invert* R_{rs} spectra to produce estimates of the water quality parameters of interest (TChl, TSS and DOC).

The problem is approached in two stages. The first step is the partitioning of an individual R_{rs} measurement into its regionally (or water mass)-specific constituent IOP spectra; namely a_{CDOM}, a_{NAP}, a_{ϕ}, b_{bp}. From Chapter 3.4, these IOP spectra have been measured and documented for GBR waters. An example of the spectral shapes determined in Chapter 3.4 are again shown in Fig. 4.1.

In reality, R_{rs} measurements contain artifacts associated with sea surface reflections, calibration inaccuracies and instrumental noise. In addition, the inversion models are based on idealised, measured IOPs which represent only a finite set of conditions and contain methodological uncertainties and the potential for bias due to the simplifying assumptions applied (i.e. NIR scattering correction and pathlength amplification factor). Various spectral partitioning methods are tested

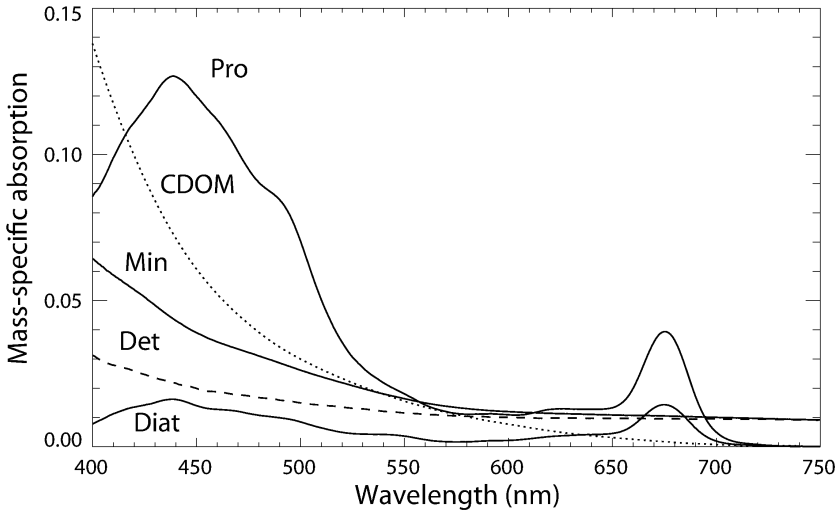

Figure 4.1: Mass-specific absorption end-members determined from the GBR dataset. Pro is *Prochlorococcus* and Diat is Diatom TChl-specific absorption ($l.\mu g^{-1}m^{-1}$). CDOM is the scaled DOC-specific CDOM absorption ($l.cg^{-1}m^{-1}$). Min is the (terrestrial) mineral and Det is the (oceanic) detrital TSS-specific absorption ($l.mg^{-1}m^{-1}$).

in this chapter, by applying them to field-measured R_{rs} spectra, using the discrete water-sample IOP measurements as validation data set. This IOP-based validation dataset is described in Section 4.2.1.1.

The second part of the problem is the extraction of information about water quality properties from the R_{rs}-derived IOP estimates. This involves the application of the mass-specific spectral IOP relationships determined in Chapter 3.4. To provide validation of these inversion-derived water quality parameters, a flow-through water quality logging system was developed to run simultaneously with the DALEC R_{rs} transects. This extensive dataset spans a large geographical coverage of GBR waters and water types, as shown previously in Fig. 3.11. This water quality parameter-based validation dataset is described in Section 4.2.1.2.

4.2 Methods

4.2.1 Validation Measurements

4.2.1.1 Coincident R_{rs} and IOP Data

To test whether the IOP models (and inherent assumptions) determined in Chapter 3.4 are applicable to the inversion of measured R_{rs} spectra, a dataset of concurrently-measured R_{rs} and IOP spectra was used. This coincident dataset was previously discussed in Chapter 3, Section 3.3.3 (and expressed in Figures 3.16 - 3.18 and Table 3.5). The IOP retrieval parameters of interest are $a_{\phi}(442)$, $a_{CDOM}(442)$ and $b_{bp}(555)$. It should be noted from the outset that the IOP spectra used here for validating the model represented a small (less than 5%) fraction of the entire IOP dataset which was used (amongst other water quality data) to create the IOP models in Chapter 3.4. Thus whilst the "validation" IOP data is not truly independent, it is considered acceptable for testing the operation of the numerical inversion techniques.

4.2.1.2 DALEC R_{rs} and Water Quality Transects

To assist the collection of a large number of samples across spatially variable coastal waters, a flow-through system was implemented which collected b_{bp} and chlorophyll fluorescence data simultaneously and complementary to the DALEC R_{rs} measurements. The DALEC and coincident flow-through water quality data were collected continually aboard the RV Lady Basten during daylight hours over approximately 20 days in January, 2006. Of these sampling days, only data from the days when the ship was in transit were used. The dates and locations of the sampling transects are shown in Table 4.1, and are shown on a map in Figure 4.2.

Jan. 2006	Description
4^{th}	Reef 20-344 to near High Peak Is.
7^{th}	Seaforth Is. (Lindeman) to Long Is.
8^{th}	North Whitsunday Is. to Border Is.
9^{th}	Cid Harbour to Bowen
10^{th}	Bowen to Central GBR Lagoon off Bowling Green Bay
14^{th}	Hook Is. to Deloraine
15^{th}	Deloraine Is. to Lindeman Is. via Edward Is.
16^{th}	Lindeman Is.
17^{th}	Long Is. to North Whitsunday Is.
18^{th}	Cateran Bay, Border Is. Only
19^{th}	Deloraine Is. to near Holbourne Is.
22^{nd}	Townsville to Otter Reef
23^{rd}	Cairns to Low Isles
24^{th}	Green Is. to Fitzroy Is.
28^{th}	Bedarra Is. to South Barnard Is.
29^{th}	South Through Hinchinbrook Channel to Orpheus Is.
30^{th}	Orpheus Is. to Central GBR Lagoon via Havanah Is.
31^{st}	Lodestone Reef to Townsville Harbour

Table 4.1: GBR cruise program on the R.V. Lady Basten in January 2006, during which DALEC and flow-through inversion validation measurements were collected. See Table 3.5 for more detail specific to the discrete measurements.

In the flow-through system, sea water was continually pumped using a diaphragm pump directly from the RV Lady Basten's hull intake, situated at about 2.0 m below the ocean surface. The intake had a coarse (2 mm) square mesh filter which rejected large particles. The pumped water was fed by hose to a 9 litre reservoir which served to provide an opportunity for large bubbles to re-join the

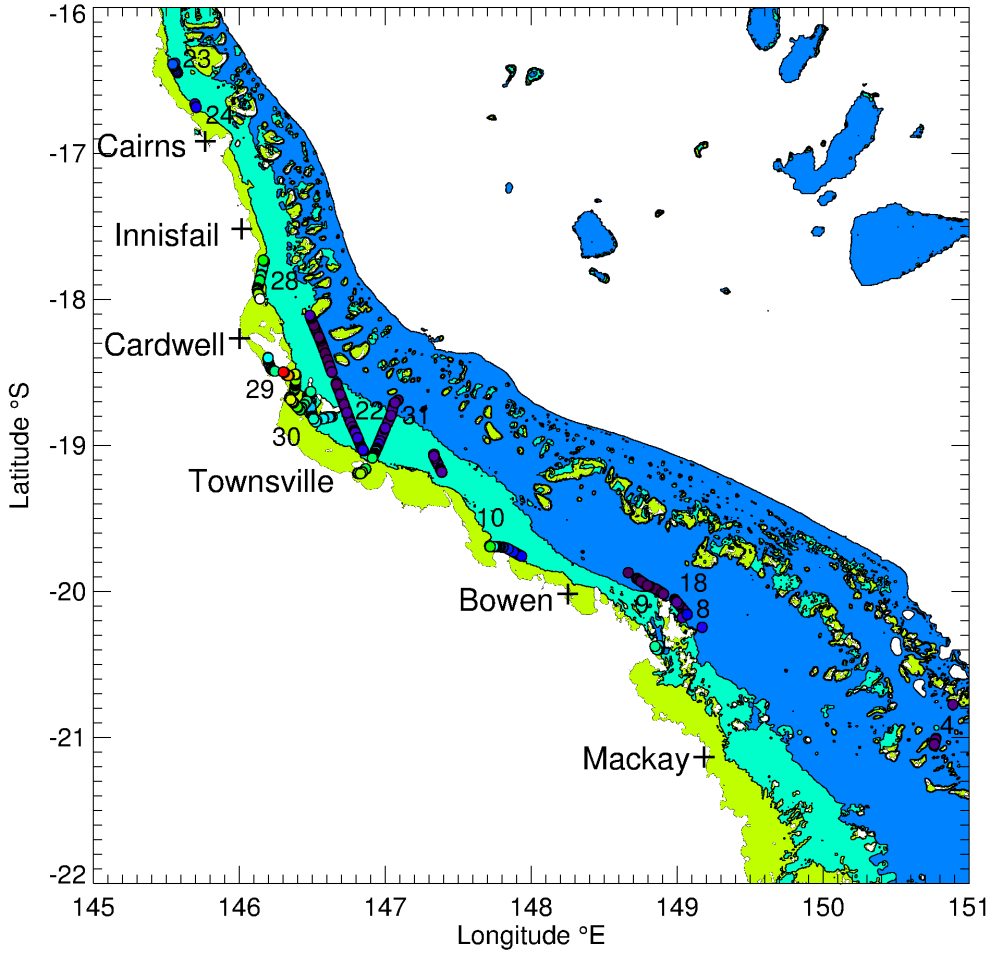

Figure 4.2: The locations of quality-controlled DALEC R_{rs} measurements where ancillary flow-through measurements were made. All transect data was recorded between Jan 4^{th} and Jan 31^{st}, 2006. The numbers on the map indicate the day of January 2006 when sampling occurred. Detail specific to the discrete measurements was provided previously in Table 3.5.

atmosphere (see Fig. 4.3). Inside the reservoir, a WETLabs FLNTU (Fluorometer and Nephelometric Turbidity Unit) device was housed in the center of the reservoir to sample the water passing through the reservoir (see Fig. 4.3). An inspection port was drilled into the reservoir to assist the routine daily cleaning and inspection of the FLNTU optical interface. The outflow of the reservoir was placed at the very lowest point to ensure the continual flushing of bubble-free, particle-laden water. The outflow was routinely inspected and no bubbles were seen, and time series observations of the optical data from the downstream Hydroscat instrument suggested no bubbles accumulated on the instrument optics. The outflow from the reservoir was brought via a hose to the custom-built Hydroscat chamber (see Fig. 4.4 and 4.5). Further details of the Hydroscat flow-through methodology are provided in the Chapter 3.4 Methods section.

To estimate the time lag of the system during cruising (10 knots), the delay between the start of a visible surface water plume front on the bow of the vessel (near the DALEC) and the first 'spike' of changed water quality parameter from each instrument (FLNTU and Hydroscat) was recorded. This was repeated a few times until average time lags were determined (15 and 45 seconds respectively, for the FLNTU and Hydroscat). The Hydroscat and the FLNTU are both designed to measure chlorophyll fluorescence and backscattering in a near-simultaneous fashion. Throughout the fieldwork, the FLNTU data was intermittent, and the FLNTU scattering data suffered from the adhesion of bubbles on the optical window. This was due to the FLNTU being placed inside the de-bubbling reservoir. Accordingly, most of the validation data came from the Hydroscat, which was fed from the outflow of the de-bubbling reservoir.

For the flow-through WQ dataset, the respective Hydroscat instrument responses (fluorescence and uncorrected $b_b(442)$) were directly calibrated to *in situ* $TChl$ and TSS (respectively) using discrete surface Niskin bottle grab sample data performed at station stops. This involved averaging the flow-through data for time intervals during the water sampling, and then performing regression analysis; the results of which are shown later in the Results section in Fig. 4.22a-c.

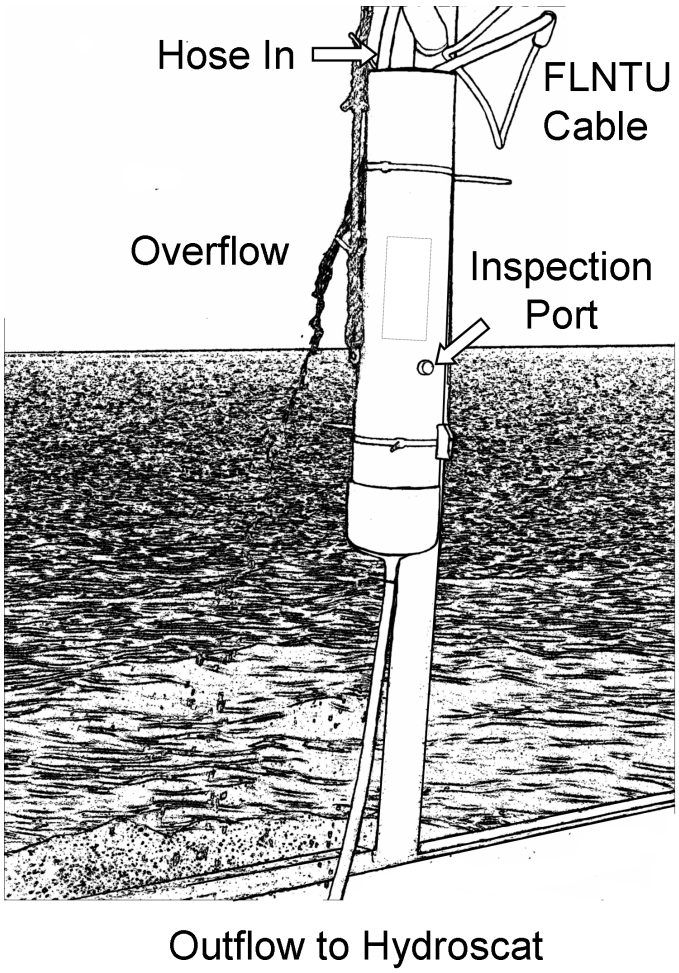

Figure 4.3: The custom-built de-bubbling reservoir / flow-through chamber for the FLNTU. The hull intake water was pumped into the top of the reservoir (Hose In), and was allowed to slightly overflow. The FLNTU optical window sits just above the inspection port, and faces down towards the outflow. The approximate position of the FLNTU is shown with the light rectangle.

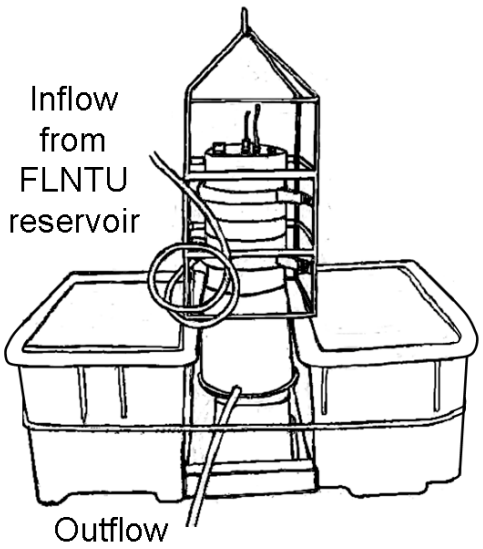

Figure 4.4: The Hydroscat flow-through sampler. Note this diagram was made during the setup stage of the experiment. Data was never collected with a double-loop in the inflow tube. All plumbing distances were minimised to reduce flow-through lag time.

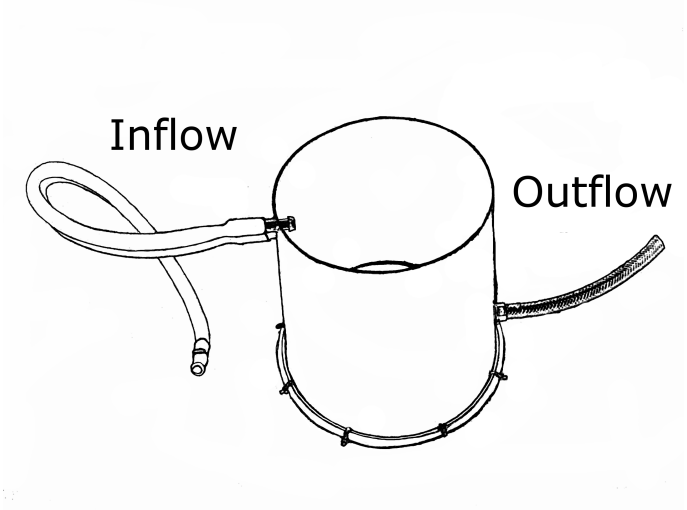

Figure 4.5: The custom-built flow-through chamber for the Hydroscat. The inlet is at the top of the chamber (on the left) and the outlet is on the right.

Particulate backscattering was calculated from the Hydroscat transect measurements using the methodology outlined in Section 2.2.4.4, and the spectral slope of backscattering (γ_{bb}) was calculated using Eq. 2.52.

4.2.2 Inversion Approaches

4.2.2.1 Predictor-corrector Inversion Schemes

A common remote sensing inversion scheme is the iterative predictor-corrector approach (Roesler & Perry 1995, Garver & Siegel 1997, Lee et al. 1999), whereby a mathematical procedure systematically varies parameters which alter the magnitude or shape of each constituent IOP spectrum, calculates $\left(\frac{b_b}{a+b_b}\right)$, and then converts this to a predicted R_{rs} spectrum. This part of the process is referred to as the 'forward model'. The results of the forward model of R_{rs} are then compared with the measured R_{rs} spectrum, and based on the spectral residual, the forward model parameters are corrected to yield a better second prediction. This cycle is repeated until the goodness-of-fit between the predicted and measured spectrum reach a required level. The IDL-version of a Levenberg-Marquardt predictor-corrector method MPFIT (Markwardt 2009) was used to vary the model parameters in this study.

Depending on the information content and exact nature of the forward model, this optimisation approach can be computationally expensive and may also be sensitive to the initial guesses of the inversion parameters, so convergence (the minimisation of the spectral goodness-of-fit) is not always guaranteed (Markwardt 2009). The performance of such an approach also relies on the ability of the forward model to correctly model the shape of the observed spectrum. Chapter 3.4 investigated the spectral shapes of GBR in-water constituents, and Chapter 3 dealt with developing a LUT which converts $\left(\frac{b_b}{a+b_b}\right)$ into above-water R_{rs}, so the required inputs to this predictor-corrector approach have been established.

The next section outlines some variants on the forward model IOP approach first published by Lee et al. (1999). Due to the potential for interference between each component of the forward model (i.e. spectral cancellation / compensation),

a number of forward model variants were developed and were tested using a nested FOR loop in the computation in order to determine the best performing combination of optical models for the retrieval of measured IOPs.

4.2.2.1.1 Absorption Model Variants

These models and associated coefficients were determined in Chapter 3.4. They are briefly summarised here, as these models are assessed later in the chapter. In Chapter 3.4, it was shown that the most accurate $TChl$ retrievals were derived when using different characteristic phytoplankton basis vectors to decompose a_{phi} measurements (see Table 2.8). It follows then, that provided the predictor-corrector retrieval is not confounded by the other spectral signatures which compose R_{rs}, then the basis vector approaches will be superior. Only these approaches are tested herein.

4.2.2.1.1.1 Phytoplankton: Two Spectrum Mixture In Chapter 3.4, it was shown that the combination of the picoplankton dominated *Prochlorococcus*, and highly-packaged Diatom-like basis vectors was able to yield the most accurate Total Chlorophyll (TChl) concentrations based on measured filter pad absorption spectra. The total phytoplankton absorption spectrum is represented by Eq. 4.1,

$$a_{\phi} = a^*_{\phi_{Pro}}[TChl_{Pro}] + a^*_{\phi_{Diat}}[TChl_{Diat}], \tag{4.1}$$

where $a^*_{\phi_{Pro}}$ is the TChl-specific absorption basis vector for *Prochlorococcus*, $a^*_{\phi_{Diat}}$ is the TChl-specific absorption basis vector for Diatoms, $TChl_{Pro}$ is the *Prochlorococcus* fraction of $TChl$ and $TChl_{Diat}$ is the Diatom fraction of $TChl$. The TChl-specific absorption basis vectors are in units of $l\mu g^{-1}m^{-1}$ and the TChl fractions are in units of μgl^{-1}. Note - the wavelength dependency of the basis vectors has been omitted for brevity.

4.2.2.1.1.2 Phytoplankton: Four Spectrum Mixture In Chapter 3.4, four phytoplankton basis vectors were described; *Prochlorococcus*, highly-packaged Diatom-like, *Trichodesmium* and *Synechococcus* (Morel et al. 1993). All four of these spectra are used by the optimisation code to model the range of phytoplank-

ton spectral shapes likely to be encountered in the GBR waters. This approach requires four parameters which, due to the TChl-specific normalised basis vectors for each phytoplankton type, are in units of $\mu g.l^{-1}$. The appropriate equation is:

$$a_\phi = a^*_{\phi_{Pro}}[TChl_{Pro}] + a^*_{\phi_{Syn}}[TChl_{Syn}] + a^*_{\phi_{Diat}}[TChl_{Diat}] + a^*_{\phi_{Trich}}[TChl_{Trich}], \tag{4.2}$$

where $a^*_{\phi_{Pro}}$ is the TChl-specific absorption basis vector for *Prochlorococcus*, $a^*_{\phi_{Syn}}$ is the TChl-specific absorption basis vector for *Synechococcus*, $a^*_{\phi_{Diat}}$ is the TChl-specific absorption basis vector for Diatoms, $a^*_{\phi_{Trich}}$ is the TChl-specific absorption basis vector for *Trichodesmium*. $TChl_{Pro}$ is the *Prochlorococcus* fraction of $TChl$, $TChl_{Syn}$ is the *Synechococcus* fraction of $TChl$, $TChl_{Diat}$ is the Diatom fraction of $TChl$ and $TChl_{Trich}$ is the *Trichodesmium* fraction of $TChl$. The TChl-specific absorption basis vectors are in units of $l\mu g^{-1}m^{-1}$ and the TChl fractions are in units of $\mu g l^{-1}$. Note, as before, the wavelength dependency of the basis vectors has been omitted for brevity.

4.2.2.1.1.3 Phytoplankton: Bricaud 1995 The approach of Bricaud et al. (1995) was used to functionalise the spectral absorption of GBR phytoplankton in Chapter 3.4. This a_ϕ model requires the variation of only one parameter, (TChl) in order to generate a spectrum, however this approach may lack the spectral detail of the four spectrum mixture.

$$a_\phi(\lambda) = A(\lambda)[TChl]^{B(\lambda)}, \tag{4.3}$$

where $A(\lambda)$ and $B(\lambda)$ are the regression-determined model coefficients determined in Chapter 3.4 (see Fig. 2.19 column 1, row 1).

4.2.2.1.1.4 Phytoplankton: Packaging The theoretical packaging approach of Morel (1991) was used and modified in this research to generalise the shift of phytoplankton spectral shape as a function of increased packaging. This model described by Eq. 4.4 requires the variation of only one parameter, (TChl) in order to generate a spectrum. However, it may also lack the spectral detail of the

four spectrum mixture,

$$a_\phi(\lambda) = A(\lambda)[TChl]Q^*, \tag{4.4}$$

where, Q^* is determined by Eq. 2.42 in Chapter 3.4.

4.2.2.1.1.5 Phytoplankton: Lee 1998 The final phytoplankton model investigated is based on Lee et al. (1998), where the full phytoplankton absorption spectrum is modelled as a function of $a_\phi(440)$, as shown below:

$$a_\phi(\lambda) = (A_0(\lambda) + A_1(\lambda)\ln[a_\phi(440)])a_\phi(440). \tag{4.5}$$

The spectral coefficients A_0 and A_1 were determined using the GBR dataset described in Chapter 3.4. The approach has been demonstrated to work with some success in inversion models (Lee et al. 1998).

4.2.2.1.1.6 $\mathbf{a_{CDOM}}$ and $\mathbf{a_{NAP}}$: Real Given the similar spectral shapes of a_{CDOM} and a_{NAP}, these are often modelled by a single exponential function (Lee et al. 1999), especially if the number of R_{rs} wavelengths is limited. Here, considering the hyperspectral measurements the DALEC provides, the unique GBR-specific spectral models are used. These are the mineral-dominated TSS-specific a_{NAP} spectrum shown in Fig. 2.22a and the DOC-specific a_{CDOM} spectrum shown in Fig. 2.17d. Two parameters TSS and DOC are used to scale the contributions of the two different basis vectors.

4.2.2.1.1.7 $\mathbf{a_{CDOM}}$ and $\mathbf{a_{NAP}}$: Exponential Formalisms Given the approximately exponential spectral shapes of a_{CDOM} and a_{NAP}, these can be represented by exponential functions:

$$a_{CDOM}(\lambda) = a_{CDOM}(442)(\lambda)e^{-S_{CDOM}(\lambda-442)}, \tag{4.6}$$

and

$$a_{NAP}(\lambda) = a_{NAP}(442)(\lambda)e^{-S_{NAP}(\lambda-442)}, \tag{4.7}$$

where $S_{CDOM} = 0.0165$ and $S_{NAP} = 0.009$, and were determined from exponential model fits from the respective mass specific absorption spectra (shown in Fig.

2.22a and Fig. 2.17d).

4.2.2.1.2 Backscattering Model Variants

4.2.2.1.2.1 b_{bp}: Standard Formalism As in Lee et al. (1999), the spectral backscattering spectrum, b_{bp} was modelled by Eq. 2.52.

$$b_{bp}(\lambda) = b_{bp}(555)\left(\frac{\lambda}{555}\right)^{-\gamma_{bb}}, \tag{4.8}$$

where the Levenberg-Markvardt optimisation is allowed to vary the spectral slope γ_{bb} from 0 to 5, encompassing the range observed the GBR data (see Fig. 2.25d).

4.2.2.1.2.2 b_{bp}: Empirically Constrained The second backscattering model is as in Eq. 4.8, but ties the magnitude of b_{bp} and the spectral slope γ together based on a general relationship determined in Chapter 3.4:

$$\gamma_{bb} = \frac{0.00380}{b_{bp}(555)} + 1.454. \tag{4.9}$$

4.2.2.1.2.3 b_{bp}: Blended Formalism The third inversion technique uses a blend of the double basis vectors $b_{bp_{det}}(\lambda)^*$ and $b_{bp_{min}}(\lambda)^*$ determined from the field measurements in Chapter 3.4, and are combined with a freely-varying optimised parameter s_{det}[1] to represent the shift of assemblage from mineral to organic scattering particles (see Eq. 2.55 and Fig. 2.26a), and then scaled by the optimised TSS parameter. The equations are as follows:

$$b_{bp_{det}}(\lambda)^* = 0.00302\left(\frac{\lambda}{555}\right)^{-3.347}, \tag{4.10}$$

$$b_{bp_{min}}(\lambda)^* = 0.01081\left(\frac{\lambda}{555}\right)^{-1.228}, \tag{4.11}$$

$$b_{bp}(\lambda) = \left[b_{bp_{det}}(\lambda)^* s_{det} + b_{bp_{min}}(\lambda)^*(1 - s_{det})\right] TSS. \tag{4.12}$$

[1] not to be confused with the uppercase S_{CDOM} and S_{NAP} variables in Eq. 4.6 and Eq. 4.7.

4.2.2.1.3 Inversion Variable Constraints and Initialistion

As mentioned previously, each model variant was systematically tested in a nested FOR loop in order to determine the best performing set of IOP inversion models for use with the predictor-corrector optimisation. The following Table 4.2 shows the variables which were optimised for each model. The minimum and maximum variable optimisation bounds are also shown, alongside the initial values of each variable. The full spectral R_{rs} data from 400 nm to 750 nm was used for the inversion.

Variable	Min	Max	Initialisation	Model	Reference.
$TChl_{Pro}$	0	10	Eq. 4.13, 4.14	two / four a^*_ϕ mix	Eq. 4.1, 4.2
$TChl_{Diat}$	0	10	Eq. 4.15, 4.18	two / four a^*_ϕ mix	Eq. 4.1, 4.2
$TChl_{Synn}$	0	10	Eq. 4.17	four a^*_ϕ mix	Eq. 4.2
$TChl_{Trich}$	0	10	Eq. 4.19	four a^*_ϕ mix	Eq. 4.2
$TChl$	0	10	Eq. 4.13	B95 and pack	Eq. 4.3, 4.4
$a_\phi(442)$	0	0.5	Eq. 4.32	Lee	Eq. 4.5
$a_{CDOM}(442)$	0	5	Eq. 4.34	all	Fig. 2.17d, Eq. 4.6
$a_{NAP}(442)$	0	5	Eq. 4.33	all	Fig. 2.22a, Eq. 4.6
$b_{bp}(555)$	0	1	Eq. 4.22	all	Eq. 4.8, Eq. 4.12
γ_{bb}	0	5	Eq. 4.23	standard b_{bp}	Eq. 4.8
s_{det}	0	1	Eq. 4.35, 3.35	b_{bp} blend	Eq. 4.12

Table 4.2: Predictor-corrector inversion constraints and initialisation. $TChl$ is in units of μgl^{-1}, and IOPs are in units of m^{-1}. s_{det} is dimensionless.

The $TChl$ variable was initalised by re-arranging Eq. 2.40 to solve for TChl:

$$TChl = \exp \frac{\ln\left(\frac{a_\phi(442)}{A}\right)}{B}, \tag{4.13}$$

where the model coefficients were estimated as $A = 0.04$ and $B = 0.4$.

The $TChl_{Pro}$ parameter was initialised by utilising Eq. 4.13 and re-arranging the model for S_{Pro}, with $M = 1.5$ (Eq. 2.48):

$$TChl_{Pro} = \left(\frac{M}{8.94TChl} + 0.0212M - 0.1125\right) TChl. \tag{4.14}$$

For the two-mixture phytoplankton model, the initial value for $TChl_{Diat}$ was set

with:

$$TChl_{Diat} = TChl - TChl_{Pro}. \tag{4.15}$$

For the four-mixture phytoplankton model, the initial values for $TChl_{Synn}$, $TChl_{Diat}$ and $TChl_{Tricho}$ were set so that each component contributed an equal contribution to $a_\phi(443)$ with:

$$a_{Synn} = a_{Diat} = a_{Trich} = \frac{a^*_{\phi_{Synn}} + a^*_{\phi_{Diat}} + a^*_{\phi_{Trich}}}{TChl - TChl_{Pro}}, \tag{4.16}$$

so the contributions became:

$$TChl_{Synn} = \frac{a^*_{\phi_{Synn}}}{a_{Synn}}, \tag{4.17}$$

$$TChl_{Diat} = \frac{a^*_{\phi_{Diat}}}{a_{Diat}}, \tag{4.18}$$

$$TChl_{Tricho} = \frac{a^*_{\phi_{Trich}}}{a_{Trich}}, \tag{4.19}$$

where the chlorophyll-specific absorption coefficients at 443 nm are $a^*_{\phi_{Trich}}$=0.054, $a^*_{\phi_{Synn}}$=0.124 and $a^*_{\phi_{Diat}}$=0.012 (Pathlength amplification factor $\beta_f = 2.6$).

The s_{det} initial parameter was estimated by Eq. 3.35, with an estimated TSS value based on Eq. 2.52 and the QAA-derived $b_{bp}(555)$ from Eq. 4.22.

4.2.2.2 Other Inversion Schemes

Two other inversion schemes are evaluated in this thesis. Namely, the Quasi-Analytical Algorithm (Section 4.3.2), and some other purely empirical approaches (Section 4.3.4). Both of these schemes rely on analysis and modelling of the validation measurements described in Sections 4.2.1.2 and 4.2.1.1, so the description and formulation of these approaches is left for the Results section.

4.3 Results

4.3.1 Predictor-Corrector IOP Inversion

To initially evaluate the IOP retrieval performance, each predictor-corrector algorithm variation (summarised in Table 4.2) was tested incrementally with each other in turn because each IOP model component may have an effect on another during the inversion. In addition, three different residual skylight correction methods were chosen. Firstly, $R_{rs}(750) = 0$, secondly, the theoretical similarity spectrum correction, and thirdly, a subset incorporating only the lowest 10% similarity spectrum-corrected reflectance measurements per station. This provided 180 sets of results for each retrieved water column optical property ($a_\phi(442)$, $a_{CDOM}(442)$, $a_{NAP}(442)$ and $b_{bp}(555)$). For each set, there were $N = 22$ stations available for analysis. Given the number of candidate algorithm combinations, a process of elimination is employed to select the best performing algorithm(s).

On average, each predictor-corrector inversion combination retrieved reasonable $R_{rs}(\lambda)$ reconstructions. The average spectral RMS error for all inversion variations (from 400 to 650 nm) was approximately 2.5% ($\sigma = 0.4\%$), with a minimum of 1.56% and a maximum of 3.46%. It should be noted, however, that some station sites for some inversion combinations failed to converge within the pre-defined 1000 iteration maximum. These combinations usually featured either the Pack, B-95 or Lee a_ϕ algorithm variants and the Blend b_{bp} algorithm variants. These combinations were excluded from further analysis as they are considered unreliable for the conditions encountered.

As a general test of the accuracy of the inversion models, the *in situ* non-water absorption $[a_t(442) - a_w(442)]$ and particulate backscatter ($b_{bp}(555)$) measurements were regressed with their inverted counterparts in order to calculate bias value for each parameter (i.e. the bias was calculated from the slope of the inverted v.s. *in situ* linear relationship). It is assumed that the best performing algorithms will have biases in both retrieved parameters close to unity. By comparing the bias of $a_t(442) - a_w(442)$ and $b_{bp}(555)$ (see Fig. 4.6a), certain populations can be resolved.

First, the population of retrievals using "Real" $a_{CDOM}(\lambda)$ and $a_{NAP}(\lambda)$ basis vectors (white plot symbols) deviated less from the ideal case, whereas the black plot symbols (the exponentially-modelled $a_{CDOM}(\lambda)$ and $a_{NAP}(\lambda)$ variants) typically showed greater deviation. In addition to the "Real" $a_{CDOM}(\lambda)$ and $a_{NAP}(\lambda)$ basis vectors which are considered successful algorithm candidates, a certain subset of the Lee $a_{\phi}(\lambda)$, exponential $a_{CDOM}(\lambda)$ and $a_{NAP}(\lambda)$ model results (shown in grey in Fig. 4.6a), also show potential.

The linear spread between $a_t(442) - a_w(442)$ and $b_{bp}(555)$ indicates that there is some interplay between retrieved absorption and backscattering. The dotted line indicates the line of best fit yielded when $a_{NAP}(750) \neq 0$. In this situation, $b_{bp}(555)$ inversions become lower in magnitude to compensate for decreased total absorption. Since $a_{NAP}(750) = 0$ yields average values closer to unity, the $a_{NAP}(750) = 0$ correction is preferred. Figure 4.6b shows the "Real" $a_{CDOM}(\lambda)$ and $a_{NAP}(\lambda)$ basis vector-based algorithms, and are colour coded in terms of residual glint correction. The grey plot symbols which denote the $R_{rs}(750) = 0$ based glint correction seem to yield more consistent $b_{bp}(555)$ retrievals (i.e. less data spread). However, it is clear that the $R_{rs}(750) = 0$ assumption does not hold in turbid waters. The similarity spectrum approach is still considered the best.

An initial inspection of the a_{ϕ} retrievals indicated that for the majority of the algorithm variants, a large proportion of the a_{ϕ} retrievals were negatively correlated with *in situ* a_{ϕ} measurements. Figure 4.7 shows example scatter plots of retrieved $a_{\phi}(442)$ v.s. measured $a_{\phi}(442)$ for 5 different retrieval approaches. In most cases, there are data points which deviate significantly from the dashed 1:1 line, and these are shown as hollow plot symbols. The hollow plot symbol data points were ignored in the calculation of the coefficients presented on Fig. 4.7.

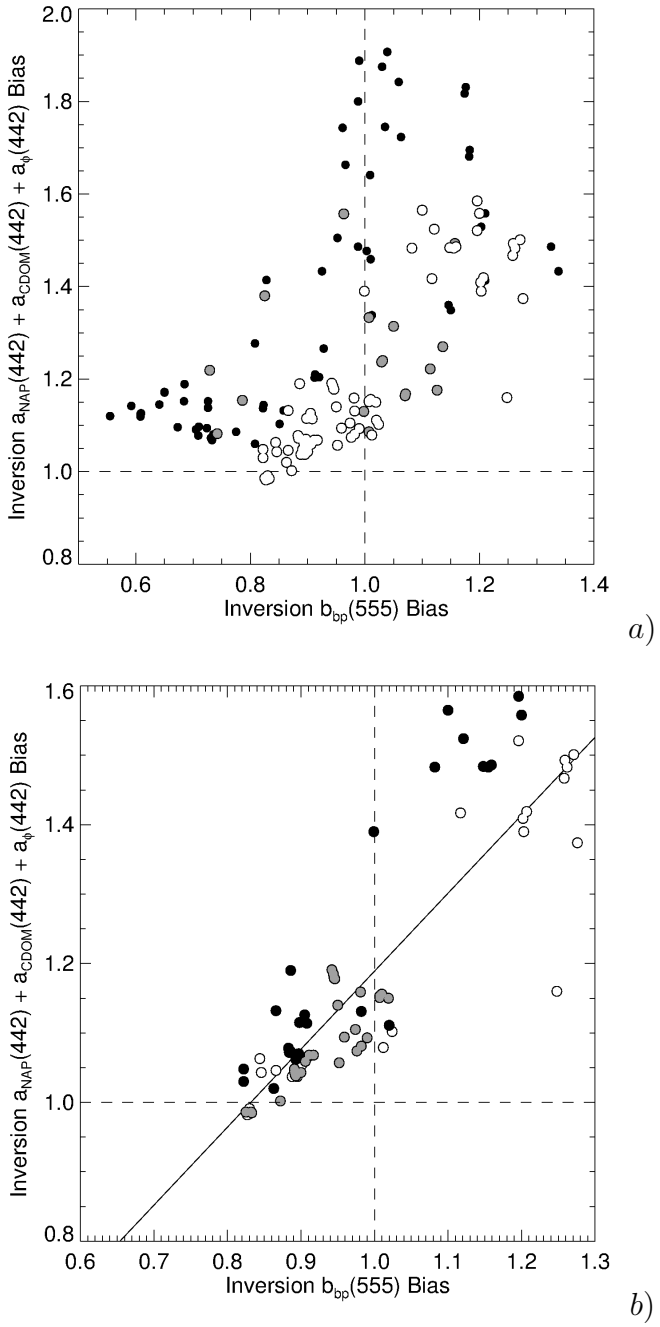

Figure 4.6: a) $[a_t(442) - a_w(442)]$ v.s. $b_{bp}(555)$ inversion biases for all 180 inversion algorithm combinations. White plot symbols show the "Real" spectral regression-derived $a_{CDOM}(\lambda)$ and $a_{NAP}(\lambda)$ basis vectors. Grey plot symbols are the Lee $a_\phi(\lambda)$ model variants with Exponentially-modelled $a_{CDOM}(\lambda)$ and $a_{NAP}(\lambda)$ basis vectors. Smaller, black plot symbols show all other combinations. The ideal unity-bias values for each axes are shown with the dashed line. The straight line is the line of best fit for all "Real" spectral regression-derived $a_{CDOM}(\lambda)$ and $a_{NAP}(\lambda)$ basis vector-derived inversions. The dotted line shows the same regression performed with the $a_{NAP}(750) \neq 0$ approach. b) As in a), but filtered to show only "Real" spectral regression-derived $a_{CDOM}(\lambda)$ and $a_{NAP}(\lambda)$ basis vector-based inversions. Plot symbols are colour-coded in terms of residual glint correction approach; the Similarity-Spectrum approach is in white, the 10% lowest similariy spectrum approach is in black, and grey denotes the $R_{rs}(750) = 0$ glint correction.

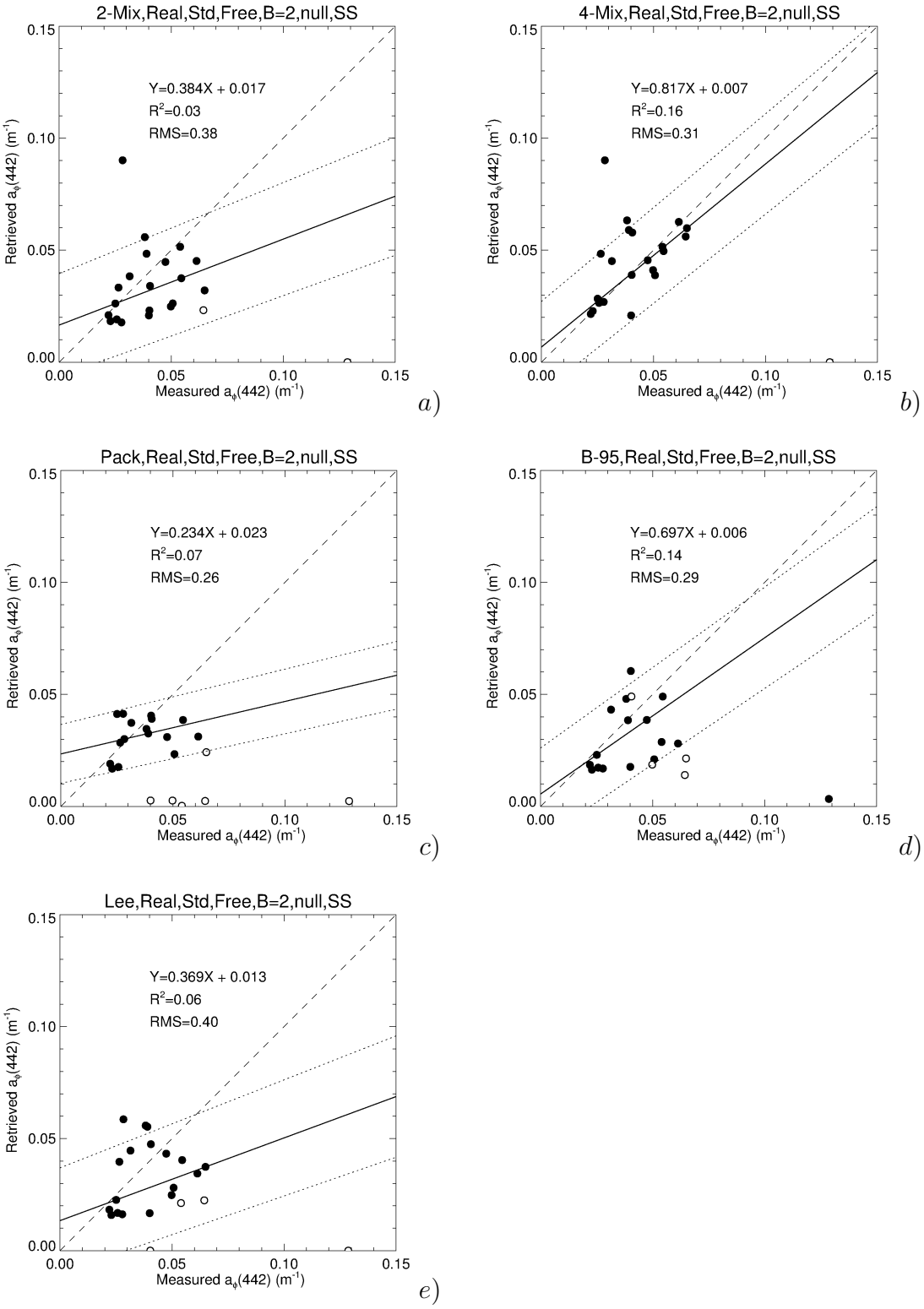

Figure 4.7: Example $a_\phi(442)$ retrievals for 5 different a_ϕ modelling approaches; a) 2 Spectrum Mixture, b) 4 Spectrum Mixture, c) Packaging, d) Bricaud 1995 and e) Lee 1998. Note the occurrence of very low $a_{phi}(442)$ inversions in most algorithm variants. The hollow plot symbols were identified as outliers and were excluded from subsequent analysis. The 1:1 line is shown as a dashed line.

Figure 4.8a - e provides an example of a_ϕ retrieval error v.s. the fractional contribution to the total non-water absorption $[a_t(442) - a_w(442)]$ for five different a_ϕ retrieval approaches. Figure 4.8f shows the overplotted results from all successful algorithm variants. In every case, a_ϕ retrieval error increases as the fractional contribution of a_ϕ is reduced. This may be interpreted as a lack of a_ϕ resolvable signal present in the R_{rs} spectrum in these conditions. In every algorithm variant, the error leads to an under-stated $a_\phi(442)$ value.

The retrieval data was filtered so that these erroneous values were removed (all data where the fractional contribution is less than 0.05). The removed data points are shown as hollow plot symbols in Figure 4.7. The threshold value of 0.05 can be used to quality control a_ϕ inversion products, however the exact value will be dependent of the exact algorithm variant being used. The lack of discrete IOP validation data makes this algorithm-specific value difficult to determine, however this will be addressed later with the flow-through dataset, where the data density is higher. Figure 4.8f also shows a large spread of algorithm performance (shown by large error bars) in the fractional range of 0.2 - 0.3. Further efforts must be made to identify the most robust algorithm variant combination, and the influence of the other IOPs should be considered.

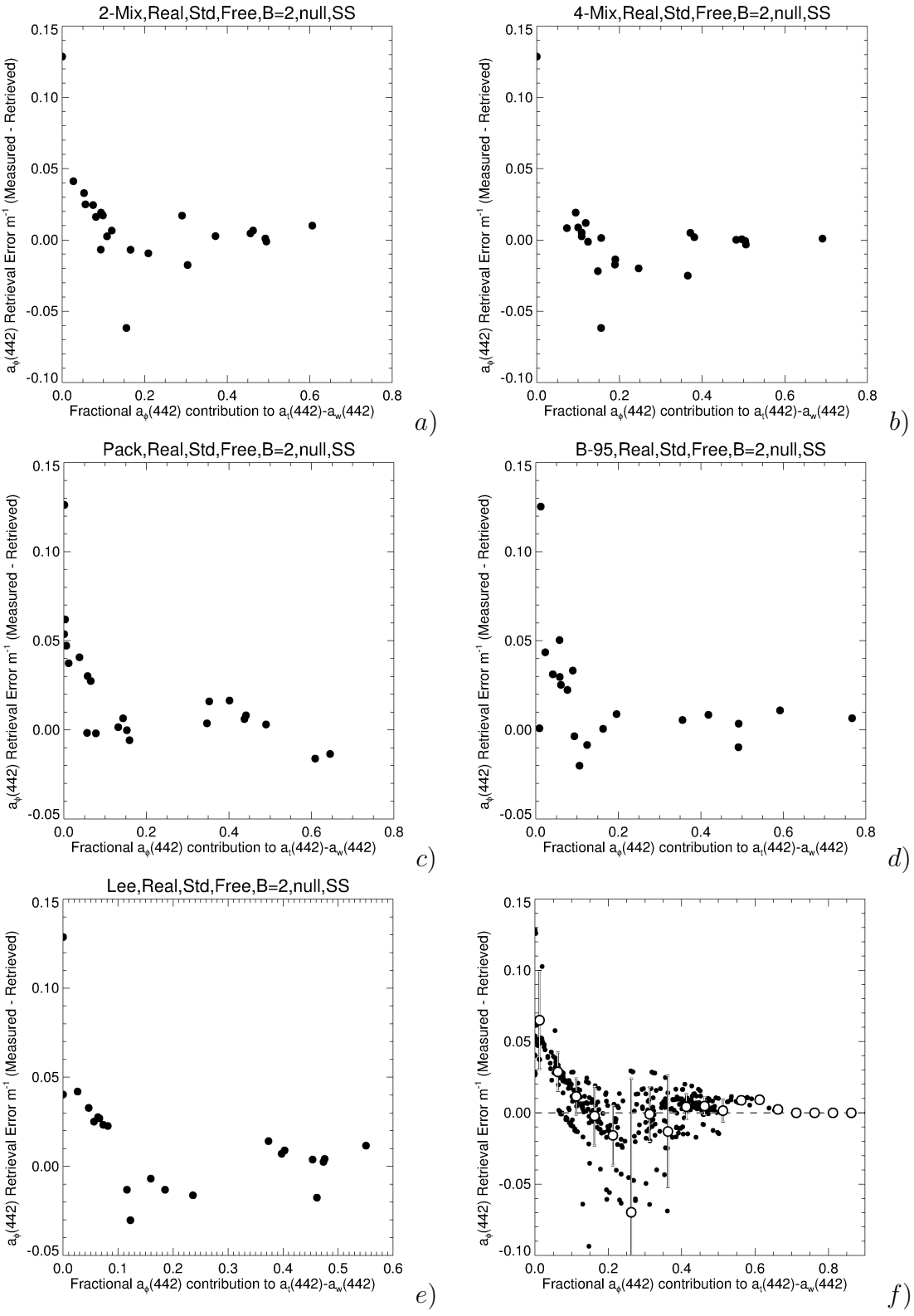

Figure 4.8: a-e) Examples of the $a_\phi(442)$ retrieval error versus the retrieved fractional contribution of a_ϕ to the total non-water absorption for five different model variants (note a_ϕ is expressed as a_{phi} in the plots). All show degradation in a_ϕ retrieval as the fractional contribution of a_ϕ is reduced past approximately 0.1 (10%). f) Results from all 720 variants overpotted. The white plot symbols are the average, ($\pm 0.0125 m^{-1}$) binned $a_\phi(442)$ errors, and the error bar magnitude is the standard deviation of each bin.

Figure 4.10 provides an example of a_{CDOM} retrieval error v.s. the fractional contribution to the total non-water absorption $[a_t(442) - a_w(442)]$ for five different a_{CDOM} retrieval approaches. This figure demonstrates that $a_{CDOM}(442)$ retrievals degrade as the fractional contribution of $a_{CDOM}(442)$ to non-water absorption $[a_t(442) - a_w(442)]$ increases. This is the opposite of the trend shown in $a_\phi(442)$ retrievals. Even when expressing the $a_{CDOM}(442)$ retrieval error as a percentage, the trend is apparent (see Fig. 4.11a). When the fractional contribution approaches 1, The retrieved $a_{CDOM}(442)$ coefficients are larger than what was measured, with the average slope between inverted vs measured being approximately 2.0 ($\sigma = 0.6$) (see Fig. 4.9 for an example). This may be an artifact of the a_{CDOM} contribution acting to compensate for inaccuracies of the a_ϕ spectral models. The a_ϕ spectral models are based on the Quantitative Filter Technique, and suffer from wavelength dependent uncertainties due to the uncertain pathlength amplification and scattering error processes. Alternatively, considering the similarity between the a_{CDOM} and a_{NAP} spectral shapes, the predictor-corrector inversion processs may over-retrieve a_{CDOM} at the expense of a_{NAP}. Figures 4.12a - e) show poor $a_{NAP}(442)$ retrievals for the same algorithm variants shown in Figs. 4.7 and 4.8. Here, when $a_{NAP}(442)$ contributes significantly to the total non-water absorption, it is generally understated. Figure 4.13 shows examples of the combined $a_{NAP}(442) + a_{CDOM}(442)$ retrievals v.s. the combined $a_{NAP}(442) + a_{CDOM}(442)$ measurements for 5 different inversion model variants. The agreement of these figures (as opposed to the $a_{NAP}(442)$ retrievals) suggests that generally the inversion models were unable accurately partition $a_{CDOM}(442)$ and $a_{NAP}(442)$, however accurate retrievals of the combined $a_{CDOM}(442) + a_{NAP}(442)$ are possible.

Fortunately, the non-algal particulates found in the GBR are known to scatter light, and $a_{NAP}(442)$ is highly correlated with $b_{bp}(555)$ (see Fig. 4.14). This high correlation provides an opportunity to tie the magnitude of the a_{NAP} spectrum to $b_{bp}(555)$ during the inversion process. This yields the example inversions shown in Fig. 4.16. Note that on average, even when $a_{NAP}(442)$ is tied to $b_{bp}(555)$, the resultant $a_{CDOM}(442)$ retrievals still yield slopes greater than 1, indicating a consistent spectral error in either the IOP models or the input R_{rs} measure-

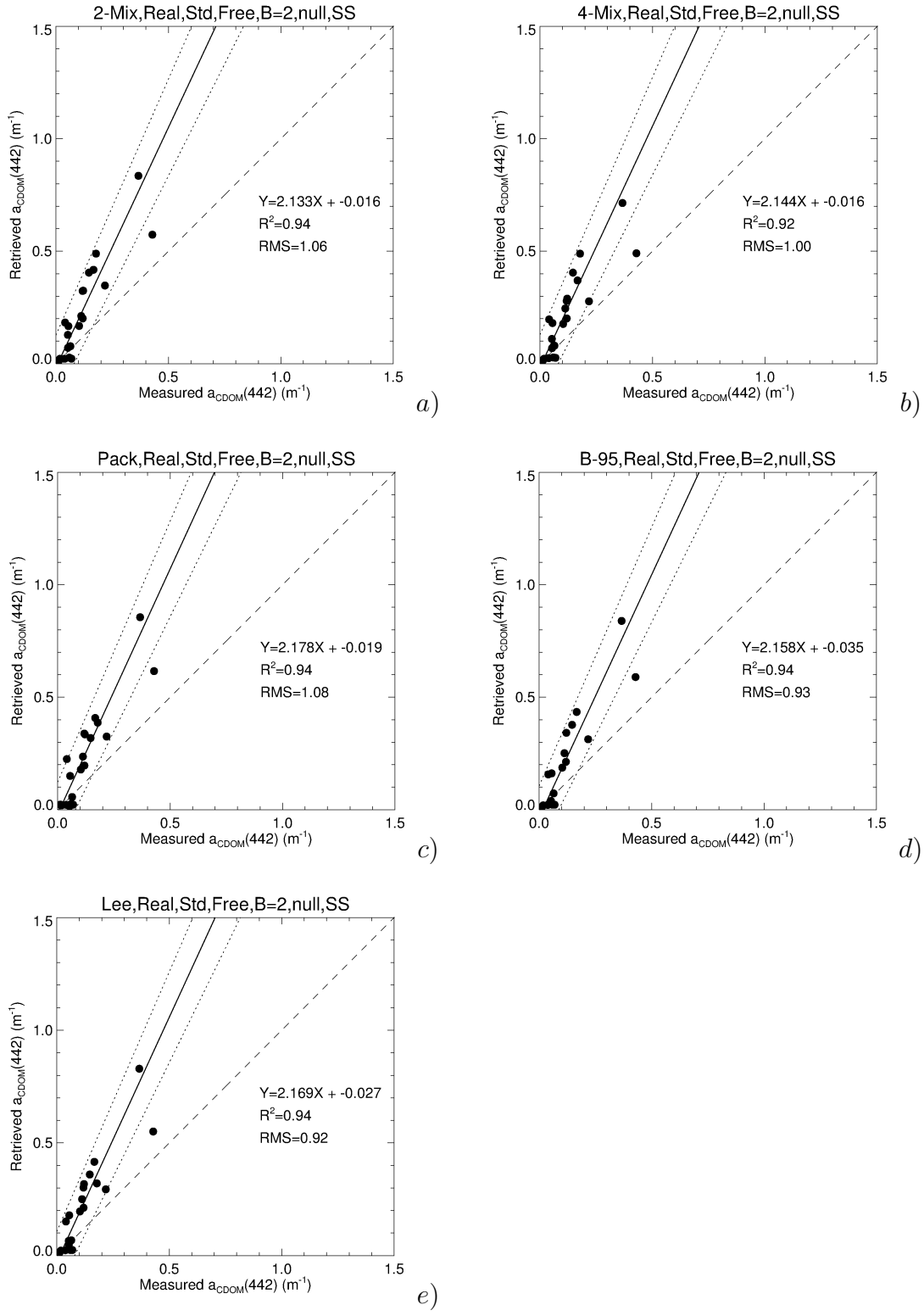

Figure 4.9: Example $a_{CDOM}(442)$ retrievals for 5 different a_ϕ modelling approaches; a) 2 Spectrum Mixture, b) 4 Spectrum Mixture, c) Packaging, d) Bricaud 1995 and e) Lee 1998. The 1:1 line is shown as a dashed line.

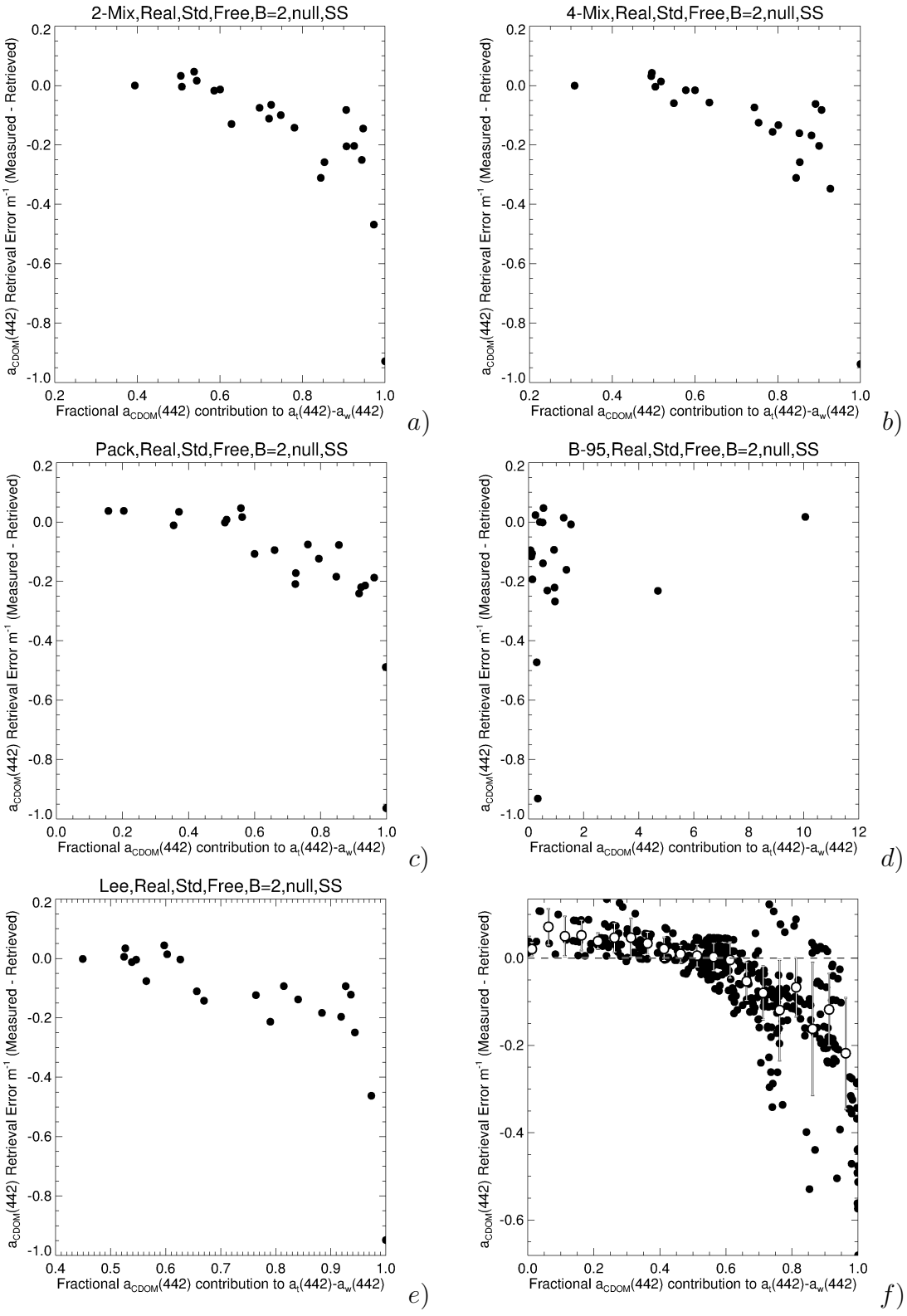

Figure 4.10: a-e) Examples of the $a_{CDOM}(442)$ retrieval error versus the retrieved fractional contribution of a_{CDOM} to the total non-water absorption for five different model variants. All show degradation in a_{CDOM} retrieval as the fractional contribution of a_{CDOM} increases. The 1:1 relationship is shown as a dashed line. f) Results from all 180 variants overpotted. The white plot symbols are the average, ($\pm 0.0125 m^{-1}$) binned $a_{CDOM}(442)$ errors, and the error bar magnitude is the standard deviation of each bin.

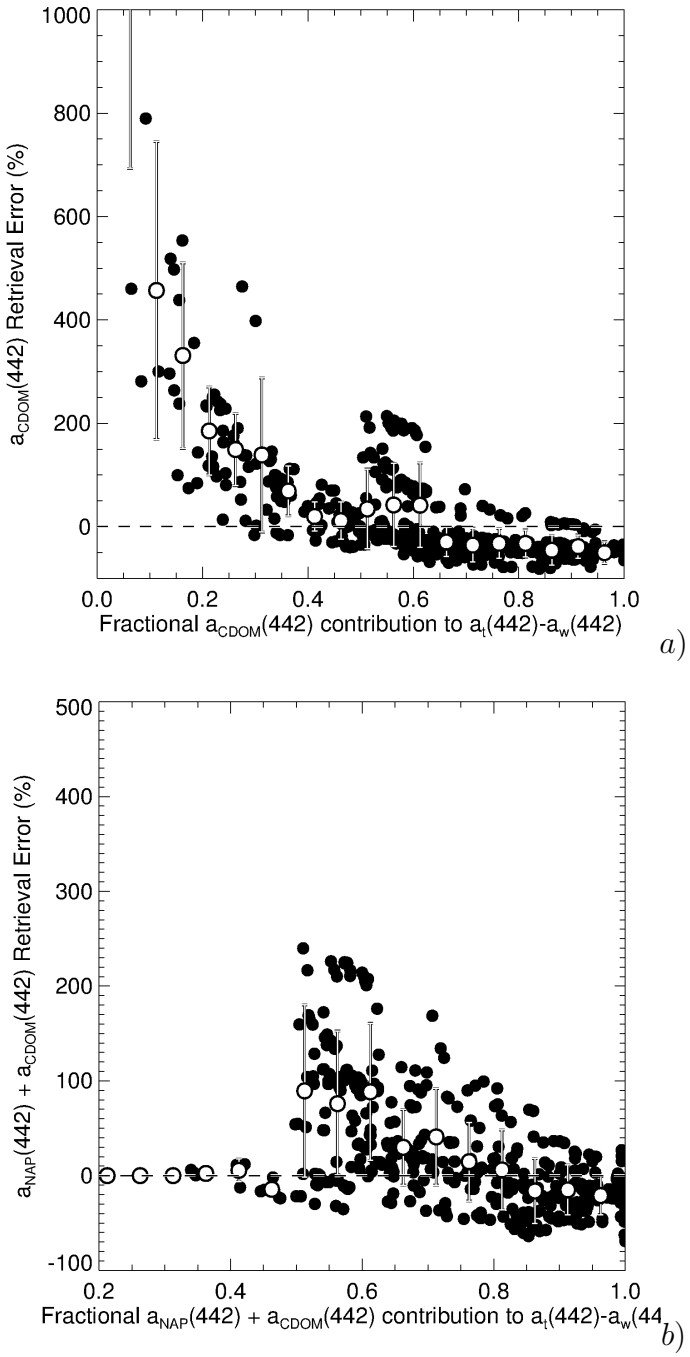

Figure 4.11: a) $a_{CDOM}(442)$ retrieval error expressed as a percentage versus the retrieved fractional contribution of a_{CDOM} to the total non-water absorption for all 720 model variants overplotted. The white plot symbols are the average, ($\pm 0.0125 m^{-1}$) binned $a_{CDOM}(442)$ percentage errors, and the error bar magnitude is the standard deviation of each bin. b) as in a), but for the combined $a_{NAP}(442) + a_{CDOM}(442)$ retrieval.

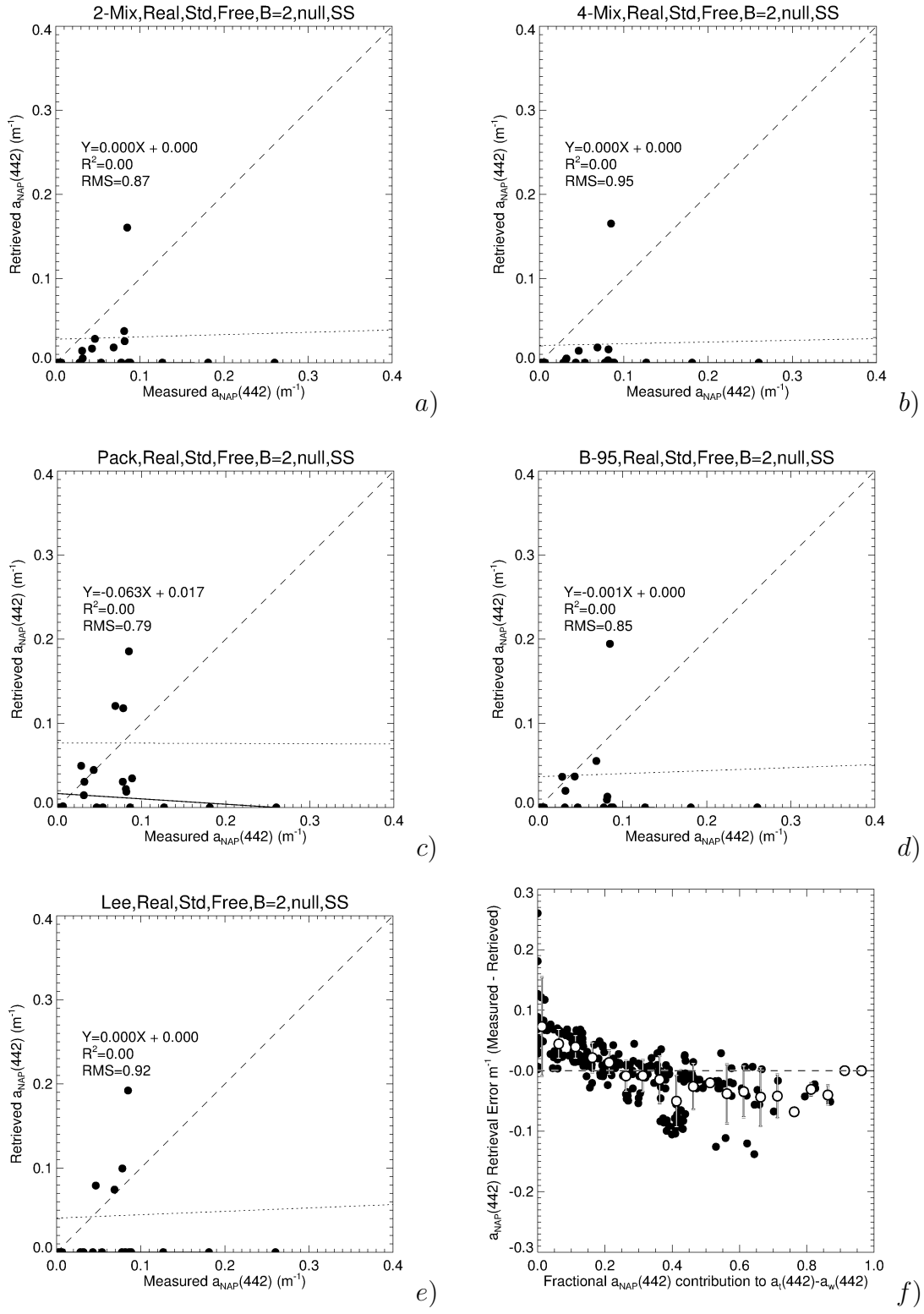

Figure 4.12: Example $a_{NAP}(442)$ retrievals for 5 different a_ϕ modelling approaches; a) 2 Spectrum Mixture, b) 4 Spectrum Mixture, c) Packaging, d) Bricaud 1995 and e) Lee 1998. Note the occurrence of very low $a_{NAP}(442)$ inversions in most algorithm variants. The 1:1 relationship is shown as a dashed line. f) Results from all 720 variants overpotted. The white plot symbols are the average, ($\pm 0.0125 m^{-1}$) binned $a_{CDOM}(442)$ errors, and the error bar magnitude is the standard deviation of each bin.

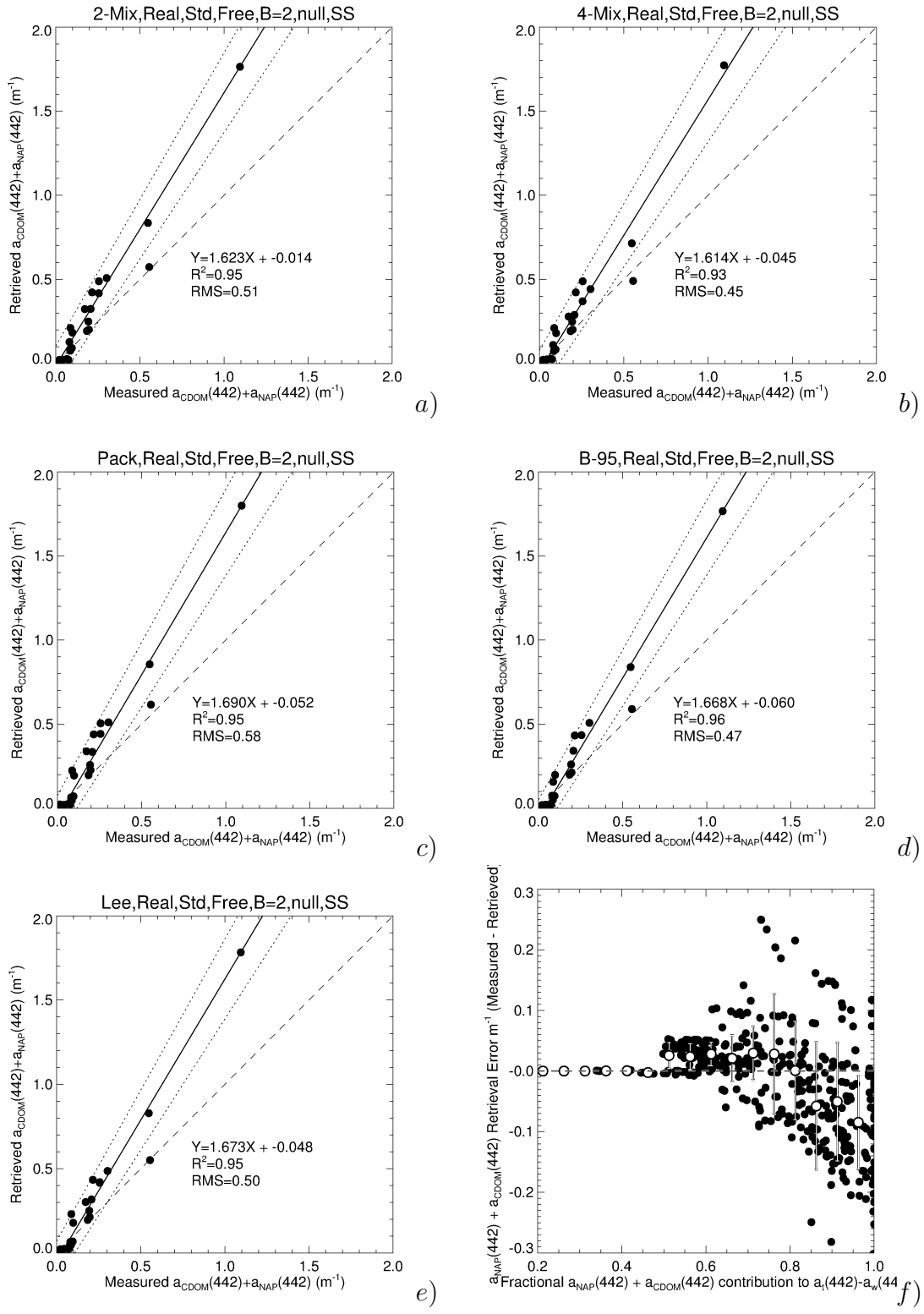

Figure 4.13: Example $a_{CDOM}(442) + a_{NAP}(442)$ retrievals for 5 different a_ϕ modelling approaches; a) 2 Spectrum Mixture, b) 4 Spectrum Mixture, c) Packaging, d) Bricaud 1995 and e) Lee 1998. The 1:1 relationship is shown as a dashed line. f) Results from all 720 variants overpotted. The white plot symbols are the average, ($\pm 0.0125 m^{-1}$) binned $a_{CDOM}(442) + a_{NAP}(442)$ errors, and the error bar magnitude is the standard deviation of each bin.

ments. Raman scattering might contribute to this error. Despite this, as long as correlation coefficients are high, the predictor-correct inversion approaches still show merit.

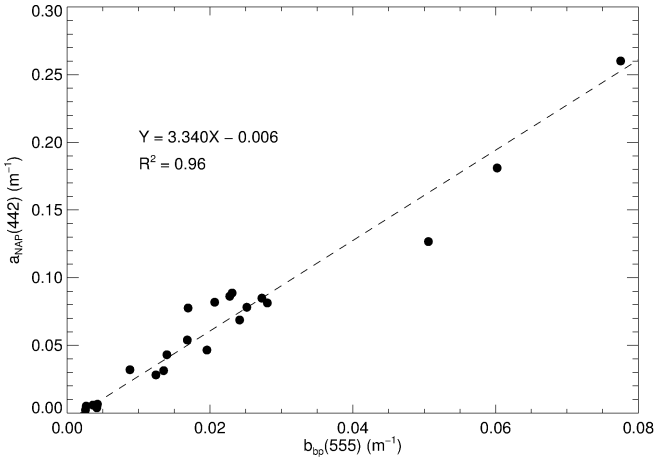

Figure 4.14: Measured $a_{NAP}(442)$ versus measured $b_{bp}(555)$ for the discrete IOP validation measurements. The slope of the relationship and R^2 correlation coefficient is shown on the plot.

To determine the best overall algorithm, the accuracy of all three IOP parameters should be evaluated simultaneously. Table 4.3.1 shows the inversion results of the 16 different approaches which survived elimination. Unfortunately, most a_ϕ retrievals have poor R^2 correlation coefficients. This is probably a consequence of the limited number and range of samples in this dataset, combined with spatial uncertainties between the R_{rs} and discrete IOP measurement. This serves to obfuscate the identification of the 'best' performing algorithm using this dataset. The comparison exercise has however, demonstrated that realistic inversion results can be achieved with the predictor-corrector approaches. The merits of the final 16 predictor-corrector methods will be tested later in the chapter with full transect measurements were the spatial variability between the algorithm inputs and measured outputs will be less significant.

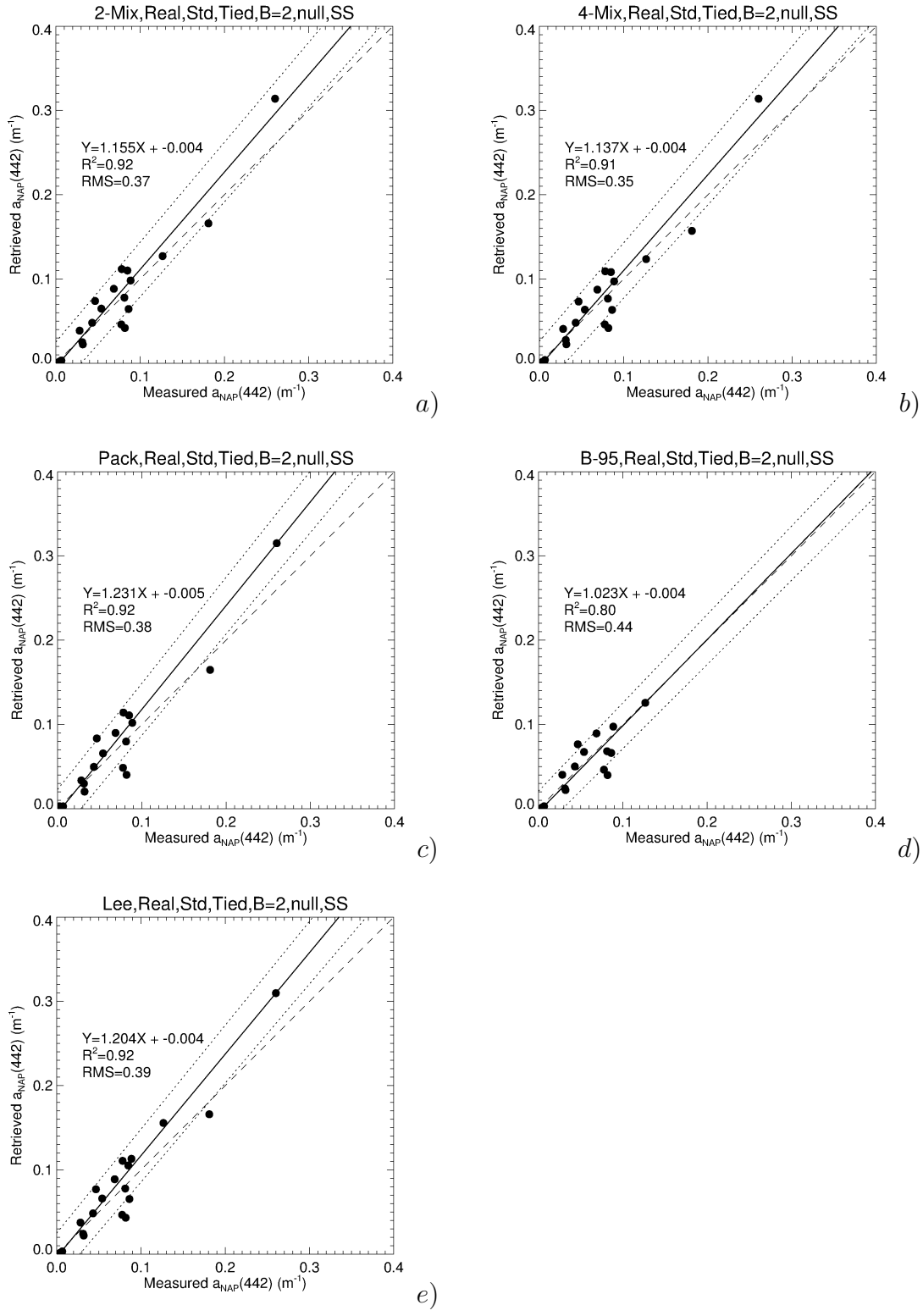

Figure 4.15: Example $a_{NAP}(442)$ retrievals for 5 different a_{ϕ} modelling approaches; a) 2 Spectrum Mixture, b) 4 Spectrum Mixture, c) Packaging, d) Bricaud 1995 and e) Lee 1998. Note the occurrence of very low $a_{NAP}(442)$ inversions in most algorithm variants. The 1:1 relationship is shown as a dashed line. f) Results from all 720 variants overpotted. The white plot symbols are the average, ($\pm 0.0125 m^{-1}$) binned $a_{CDOM}(442)$ errors, and the error bar magnitude is the standard deviation of each bin.

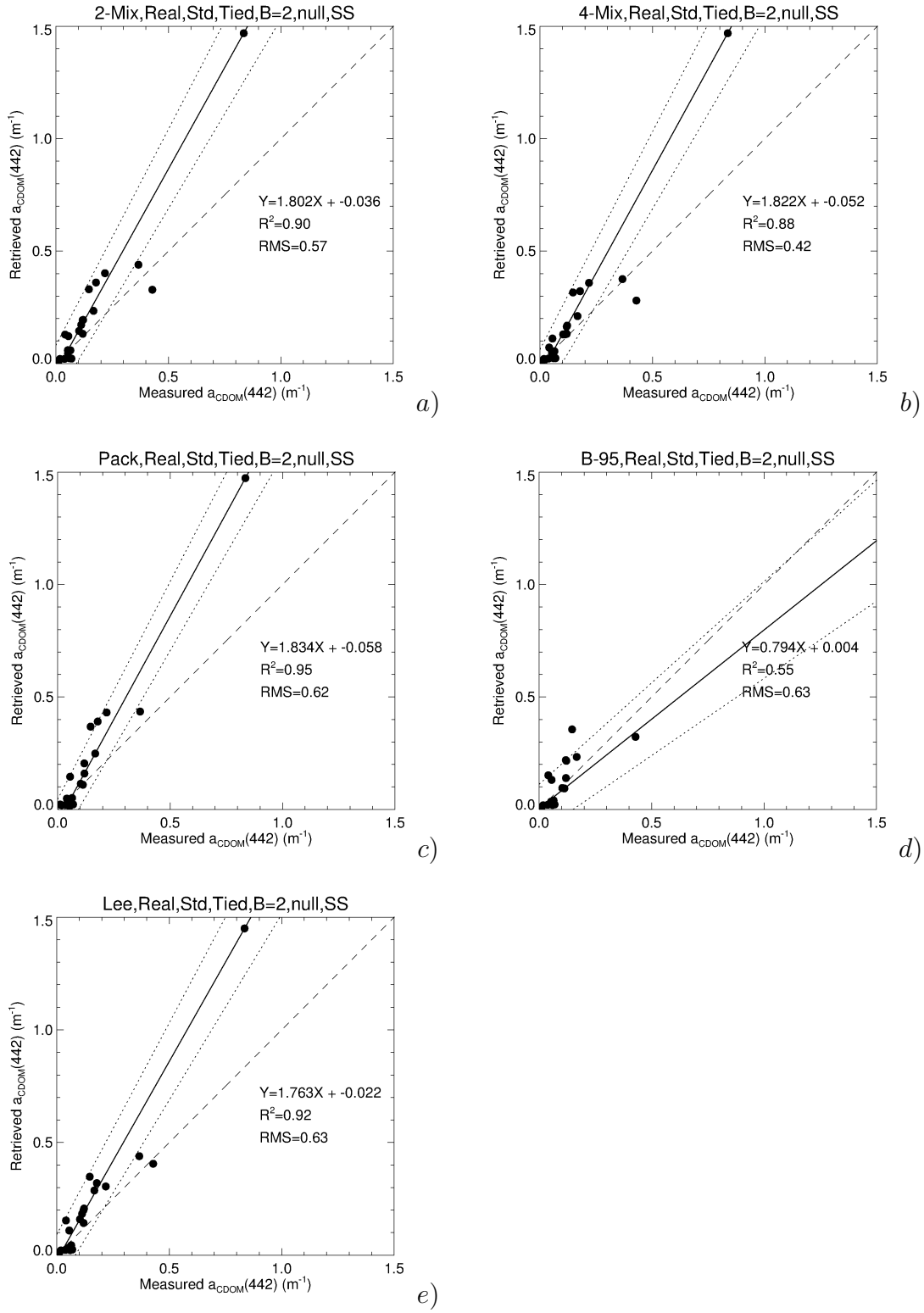

Figure 4.16: Example $a_{CDOM}(442)$ retrievals for 5 different a_ϕ modelling approaches; a) 2 Spectrum Mixture, b) 4 Spectrum Mixture, c) Packaging, d) Bricaud 1995 and e) Lee 1998. The 1:1 line is shown as a dashed line.

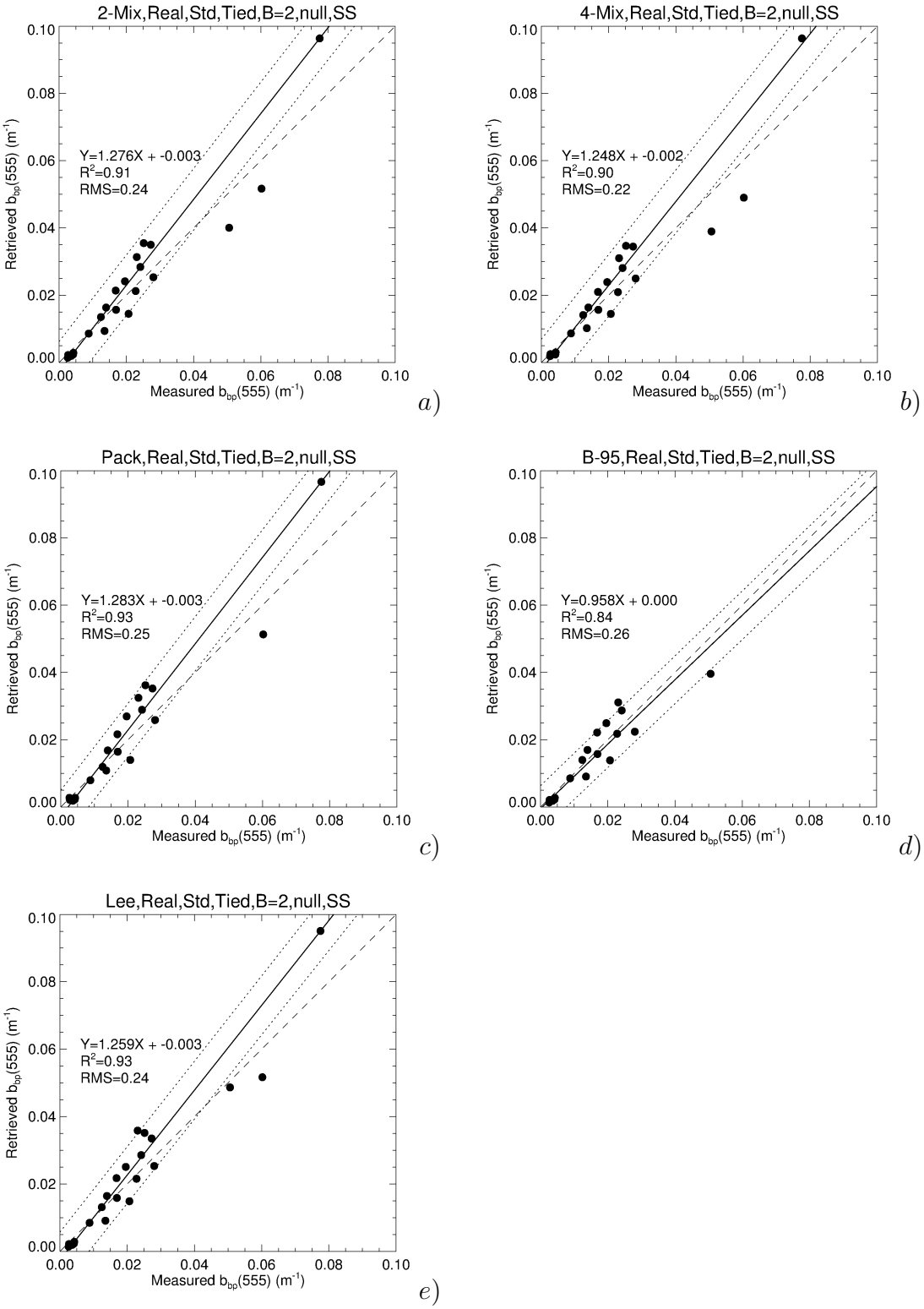

Figure 4.17: Example $b_{bp}(555)$ retrievals for 5 different a_ϕ modelling approaches; a) 2 Spectrum Mixture, b) 4 Spectrum Mixture, c) Packaging, d) Bricaud 1995 and e) Lee 1998. The 1:1 line is shown as a dashed line.

IOP	Model	Type			$a_t(442) - a_w(442)$		$a_\phi(442)$				$a_{CDOM}(442)$				$b_{bp}(555)$			
a_ϕ	a_{dg}	b_{bp}	Spec. (%)	Time (ms)	Offset (m^{-1})	Slope	R^2	RMS (%)	Offset (m^{-1})	Slope	R^2	RMS (%)	Offset (m^{-1})	Slope	R^2	RMS (%)	Offset (m^{-1})	Slope
2-Mix	Real	Std	1.91	81.8	-0.051	1.37	0.15	31.7	0.011	0.43	0.90	57.3	-0.036	1.80	0.91	24.0	-0.0026	1.28
2-Mix	Real	Emp	2.37	52.4	-0.025	1.04	0.23	32.3	0.013	0.47	0.93	41.5	-0.046	1.31	0.94	21.6	-0.0001	0.85
2-Mix	Real	Blend	2.32	73.5	-0.020	0.98	0.01	28.5	0.022	0.01	0.93	38.0	-0.038	1.27	0.92	20.8	0.0000	0.83
4-Mix	Real	Std	1.85	169.8	-0.031	1.16	0.19	27.4	0.016	0.45	0.88	42.0	-0.052	1.82	0.90	21.8	-0.0021	1.25
4-Mix	Real	Emp	2.06	84.0	-0.020	1.04	0.24	41.7	0.009	0.68	0.92	43.2	-0.047	1.28	0.94	19.3	0.0000	0.89
Pack	Real	Emp	2.54	58.5	-0.026	1.05	0.34	22.3	0.035	0.06	0.92	41.7	-0.042	1.30	0.93	20.7	0.0004	0.87
B-95	Real	Emp	2.41	46.5	-0.019	1.04	0.27	30.6	0.005	0.71	0.93	41.0	-0.046	1.31	0.93	22.0	-0.0003	0.89
B-95	Real	Blend	2.49	60.0	-0.020	0.98	0.26	27.5	0.006	0.68	0.92	38.1	-0.041	1.28	0.91	22.0	-0.0001	0.83
Lee	Real	Std	2.12	88.7	-0.067	1.49	0.44	30.2	0.000	0.79	0.92	63.3	-0.022	1.76	0.93	24.2	-0.0025	1.26
Lee	Real	Emp	2.35	61.5	-0.022	1.04	0.22	39.6	0.008	0.55	0.93	40.6	-0.044	1.30	0.92	21.8	-0.0003	0.90
Lee	Real	Blend	2.49	78.3	-0.025	0.99	0.00	43.8	0.012	0.31	0.93	36.8	-0.037	1.28	0.90	22.0	-0.0001	0.83
Lee	Exp	Emp	2.68	32.4	-0.035	1.09	0.81	51.1	-0.040	2.17	0.92	40.3	-0.033	1.08	0.89	23.0	-0.0013	1.01
Lee	Exp	Blend	2.77	77.4	-0.039	1.16	0.75	60.6	-0.055	2.74	0.91	35.3	-0.015	1.03	0.88	21.6	-0.0013	1.07

Table 4.3: Initial IOP inversion results for the $N = 22$ discrete measurements. The best performing algorithms used the similarity spectrum correction, $a_{NAP}(750) = 0$, and the magnitude of a_{NAP} was tied to $b_{bp}(555)$. Time denotes the average inversion time per spectrum in ms. Spec denotes the average RMS error of the model reproduction of the R_{rs} spectrum between 400 and 650 nm. Offset is the intercept of the linear regression between the Retrieved vs Measured IOP parameter. Slope is the gradient of the linear regression. R^2 is the correlation coefficient of the Retrieved vs Measured IOP data. RMS is the Root-Mean-Square error, expressed as a percentage.

4.3.2 Quasi-Analytical Algorithm

One approach to determine IOPs based on measured R_{rs} spectra is the Quasi-Analytical Algorithm (QAA) model of Lee et al. (2002). Since coincident R_{rs} and IOP data was collected at discrete stations (described in Chapters 2 and 3), empirical aspects of the QAA approach can be tuned specifically to the GBR waters sampled. The GBR-tuned QAA algorithmic approach developed in this study first converts R_{rs} into $\frac{b_b}{a+b_b}$ (shortened to u, as in Eq. 3.40) using Eq. 3.43, and then seeks to estimate the total absorption at a reference wavelength. Figures 4.18a and b reveals trends between *in situ* GBR measurements of absorption and remote-sensing derivable u (using Eq. 3.43). Based on these measurements, a useful empirical relationships specific to the GBR can be fitted:

$$a(555) = K_0 + K_1 \left(\frac{u(645)}{u(555)} \right) + K_2 \left(\frac{u(645)}{u(555)} \right)^2, \tag{4.20}$$

where a(555) is the total absorption coefficient at 555 nm, u(555) is the $\frac{b_b}{a+b_b}$ coefficient at 555 nm, and the polynomial model fit coefficients $K_0 = 0.0426$, $K_1 = 0.1284$, $K_2 = 0.4501$. The model fit is shown as a solid line in Fig. 4.18a. A similar equation utilising the wavelengths of the 1 km resolution MODIS bands is:

$$a(547) = J_0 + J_1 \left(\frac{u(667)}{u(547)} \right) + J_2 \left(\frac{u(667)}{u(547)} \right)^2, \tag{4.21}$$

where a(547) is the total absorption coefficient at 547 nm, u(547) is the $\frac{b_b}{a+b_b}$ coefficient at 547 nm, and the polynomial model fit coefficients $J_0 = 0.0314$, $J_1 = 0.3253$, $J_2 = 0.4725$. The model fit is shown as a solid line in Fig. 4.18b.

The next stage of the QAA-style algorithm approach uses the empirically estimated $a(555)$ (or alternatively, $a(547)$) and combines it with the analytical expression for u in order solve for $b_{bp}(555)$:

$$b_{bp}(555) = \frac{u(555)a(555)}{1 - u(555)} - b_{bw}(555), \tag{4.22}$$

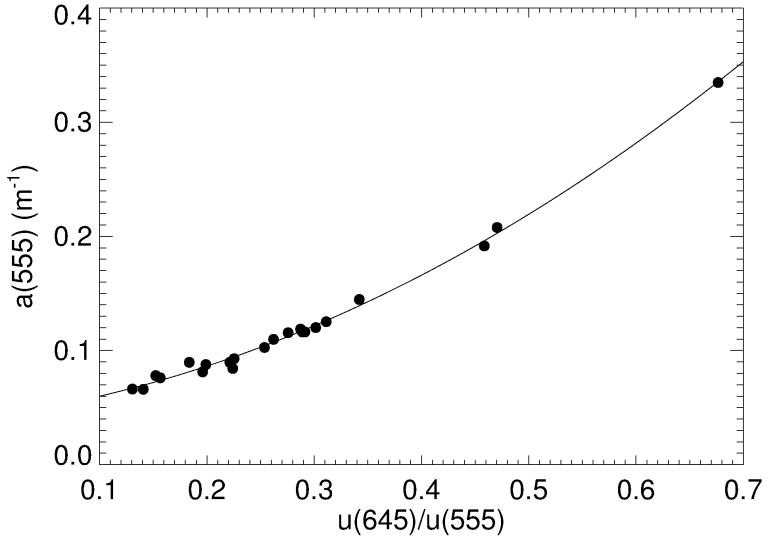

a)

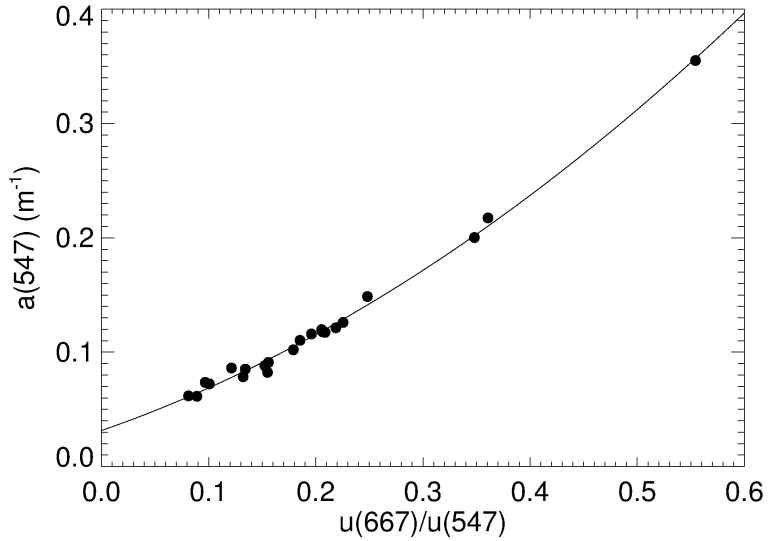

b)

Figure 4.18: a) Total absorption, a(555) versus u(645)/u(555) based on GBR IOP measurements described in Chapter 2. The solid line is a polynomial fit described by Eq. 4.20. b) Total absorption, a(547) versus u(667)/u(547) based on GBR IOP measurements described in Chapter 2. The solid line is a polynomial fit described by Eq. 4.21.

where $b_{bw}(555)$ is taken from Zhang et al. (2009).

Once $b_{bp}(555)$ is determined, the spectral slope of the b_{bp} spectrum (γ_{bb}) can be estimated so that the full backscattering spectrum can approximated using Eq. 4.8. An empirical relationship between $b_{bp}(555)$ and γ_{bb} was described in Chapter 2 (Eq. 2.54). This relationship was determined from a linear fit to the station-cropped IOP measurements and the inverse b_{bp} data. Now that the relationship between R_{rs} and u has been established, full transect flow-through Hydroscat and R_{rs} may be used to assess the applicability of Eq. 4.9. A subset (every 10^{th} data point) of the full transect data is shown in Fig. 4.19a. The relationship of Eq. 2.54 based on discrete IOP-only measurements is shown as a solid line overplotted in Fig. 4.19.

For higher $b_{bp}(555)$ values typical of extreme flood plume events, the dotted line does not predict the measurements made in the full-transect data. To make a more robust model, it was necessary to introduce a second function high-scattering waters in a piecewise fashion:

$$\gamma_{bb} = \begin{cases} \frac{0.00380}{b_{bp}(555)} + 1.454 & \text{for } b_{bp}(555) < 0.032m^{-1} \\ -3.32\ b_{bp}(555) + 1.68 & \text{for } b_{bp}(555) \geq 0.032m^{-1}, \end{cases} \tag{4.23}$$

where the first equation is Eq. 4.9, and the second equation is a linear fit of the data from $b_{bp}(555)$ data $\geq 0.02m^{-1}$.

As in Lee et al. (2002), γ_{bb} may also be empirically related to R_{rs} ratios. Examples of these ratio relationships were determined from *in situ* DALEC and Hydroscat measurements for the MODIS 1 km and 500 m bands. These are shown in Figures 4.19b and c. The modelled lines are generated with Eq.:

$$\gamma_{bb} = \gamma_{max} \left(1 - \exp^{AR+B}\right), \tag{4.24}$$

where γ_{max}, A, R and B are documented in Table 4.4.

Once a suitable γ_{bb} is determined, it is applied in Eq. 4.8 to estimate the backscat-

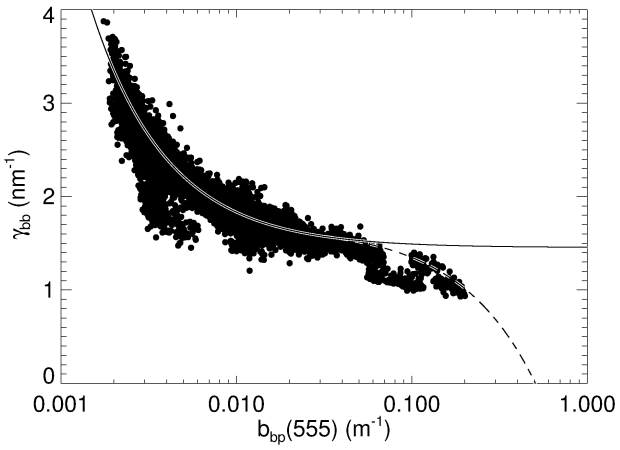

a)

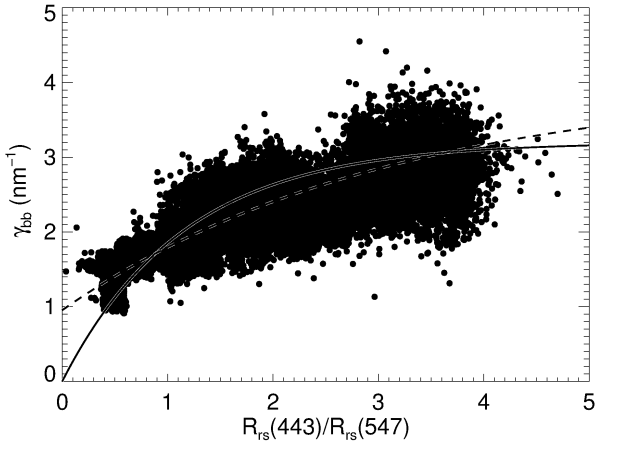

b)

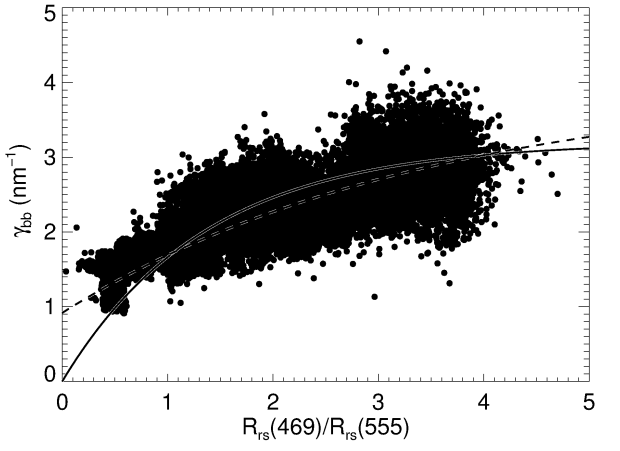

c)

Figure 4.19: a) Spectral backscattering slope γ_{bb} vs $b_{bp}(555)$ for every 10^{th} data point. The model described by Eq. 4.9 is shown in the solid line. An improved piecewise model (Eq. 4.23) is shown in the dashed line for $b_{bp}(555) \geq 0.032$. b) and c) Show the spectral backscattering slope γ_{bb} vs DALEC-measured reflectance ratios; the first (b) being applicable to 1 km MODIS bands and the other (c) for the 500 m bands. For each plot, two different models are featured which have different asymptotes. See Table 4.4 for details.

R	γ_{max}	A	B	ref.
$R_{rs}(443)/R_{rs}(547)$	4	-0.324	-0.272	Fig. 4.19b, dashed line
$R_{rs}(443)/R_{rs}(547)$	3.2	-0.865	0.000	Fig. 4.19b, solid line
$R_{rs}(469)/R_{rs}(555)$	4	-0.289	-0.260	Fig. 4.19c, dashed line
$R_{rs}(469)/R_{rs}(555)$	3.2	-0.733	0.000	Fig. 4.19c, solid line

Table 4.4: Model coefficients used to estimate γ_{bb} based on R_{rs} ratios. A and B are model fit parameters.

tering spectrum ($b_{bp}(\lambda)$) and then the total absorption $a(\lambda)$ can be determined using:

$$a(\lambda) = \frac{[1 - u(\lambda)][b_{bw}(\lambda) + b_{bp}(\lambda)]}{u(\lambda)}. \tag{4.25}$$

Once the $a(\lambda)$ is determined, $a_w(\lambda)$ can be subtracted and the absorption coefficients of each non-water subfraction can be deduced using empirical relationships determined from the IOP dataset in Chapter 3.4. The specific relationships of interest are shown in Figs. 4.20a-d. For the purposes of simplifying the process for the first stage of partitioning and, as in Lee et al. (2002), the combined a_{CDOM} and a_{NAP} is deduced. This sum is referred to as a_{dg}. The relative fractions of a_{dg} and a_ϕ can be deduced by observing the near-constant relationships between CDOM + NAP absorption (a_{dg}) and phytoplankton absorption (a_ϕ) at wavelengths of 412 nm and 443 nm (see Fig. 4.20a and b), where:

$$a_{res}(412) = a_{dg}(412) + a_\phi(412), \tag{4.26}$$

$$a_{res}(443) = a_{dg}(443) + a_\phi(443). \tag{4.27}$$

The empirical relationship in Fig. 4.20a expresses $a_{dg}(412)$ in terms of $a_{dg}(443)$:

$$a_{dg}(412) = M a_{dg}(443), \tag{4.28}$$

where $M = 1.569$.

Substituting Eq. 4.28 into Eq. 4.26:

$$a_{res}(412) = M a_{dg}(443) + a_{\phi}(412). \tag{4.29}$$

Re-arranging Eq. 4.27 to express $a_{dg}(443)$ in terms of $a_{res}(443)$ and $a_{\phi}(443)$:

$$a_{dg}(443) = a_{res}(443) - a_{\phi}(443). \tag{4.30}$$

The empirical relationship in Fig. 4.20b expresses $a_{\phi}(412)$ in terms of $a_{\phi}(443)$:

$$a_{\phi}(412) = N a_{\phi}(443), \tag{4.31}$$

where $N = 0.660$.

Substituting Eq. 4.31 and Eq. 4.30 into Eq. 4.29, and solving for $a_{\phi}(443)$ yields:

$$a_{\phi}(443) = \frac{a_{res}(412) - M a_{res}(443)}{-M + N}. \tag{4.32}$$

The partitioning of a_{dg} into the a_{CDOM} and a_{NAP} fractions can be made utilising the empirical GBR IOP dataset. In Fig.4.20c, it can be seen that there is a linear relationship between $a_{NAP}(443)$ and $b_{bp}(555)$ for the waters sampled. The equation of the line of best fit is described below:

$$a_{NAP}(443) = 3.340[b_{bp}(555)] - 0.006 \tag{4.33}$$

where the equation represented the measured $a_{NAP}(443)$ data with an RMSE of 35.6%.

Finally, the CDOM contribution may be estimated by:

$$a_{CDOM}(443) = a_{dg}(443) - a_{NAP}(443). \tag{4.34}$$

Figure 4.21 shows a comparison between the QAA retrieved $a_{\phi}(442)$, $a_{CDOM}(442)$ and $b_{bp}(555)$ coefficients and the respective *in situ* measured values. The algorithm performance is satisfactory, with RMS errors lower than approximately 30 % for all 3 IOPs. However, as was discovered in the previous predictor-

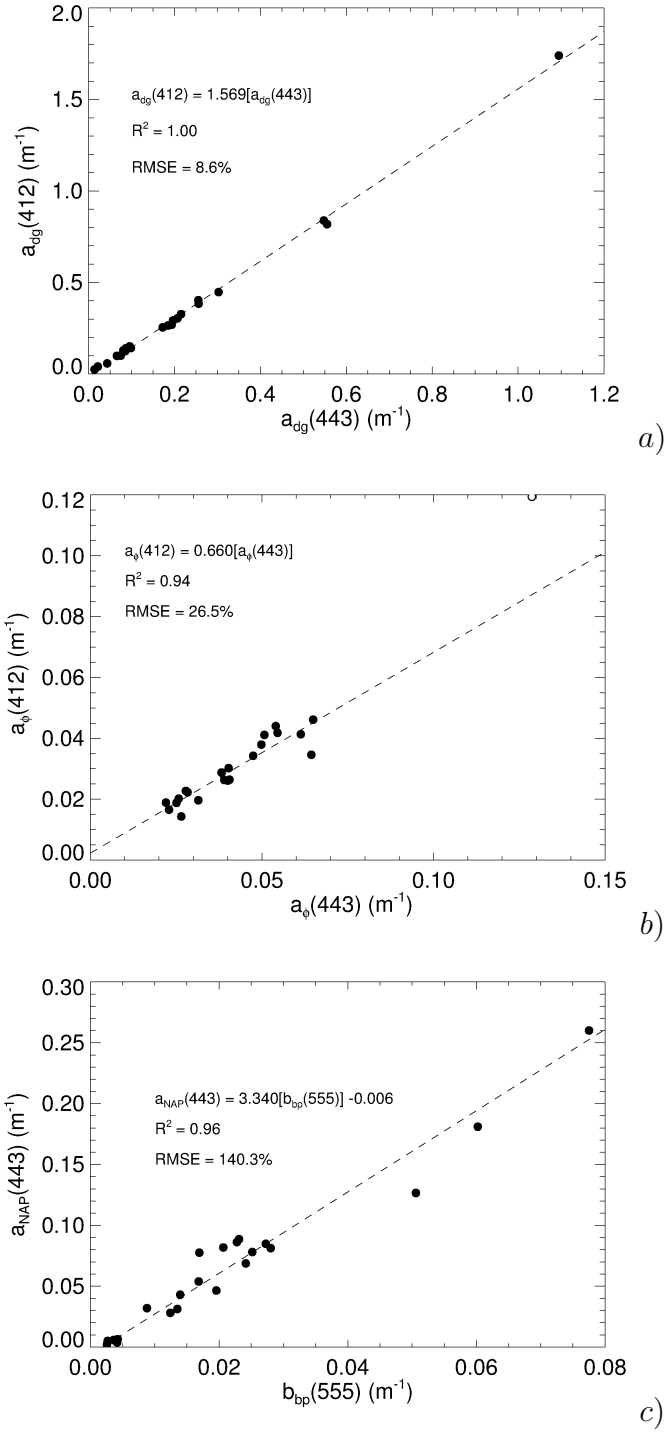

Figure 4.20: Linear empirical relationships between the absorption coefficients at 412 and 443 nm for: a) GBR combined NAP + CDOM absorption (the slope defines M in Eq. 4.32), b) GBR phytoplankton absorption (the slope defines N in Eq. 4.32). Data represented by the white plot symbol was omitted from the linear regression calculation as it was an outlier, potentially contaminated by residual non-algal particulates on the filter pad. c) The linear relationship between $a_{NAP}(443)$ and $b_{bp}(555)$. The RMSE of the linear models are shown on each plot, along with the R^2 correlation coefficients and equations.

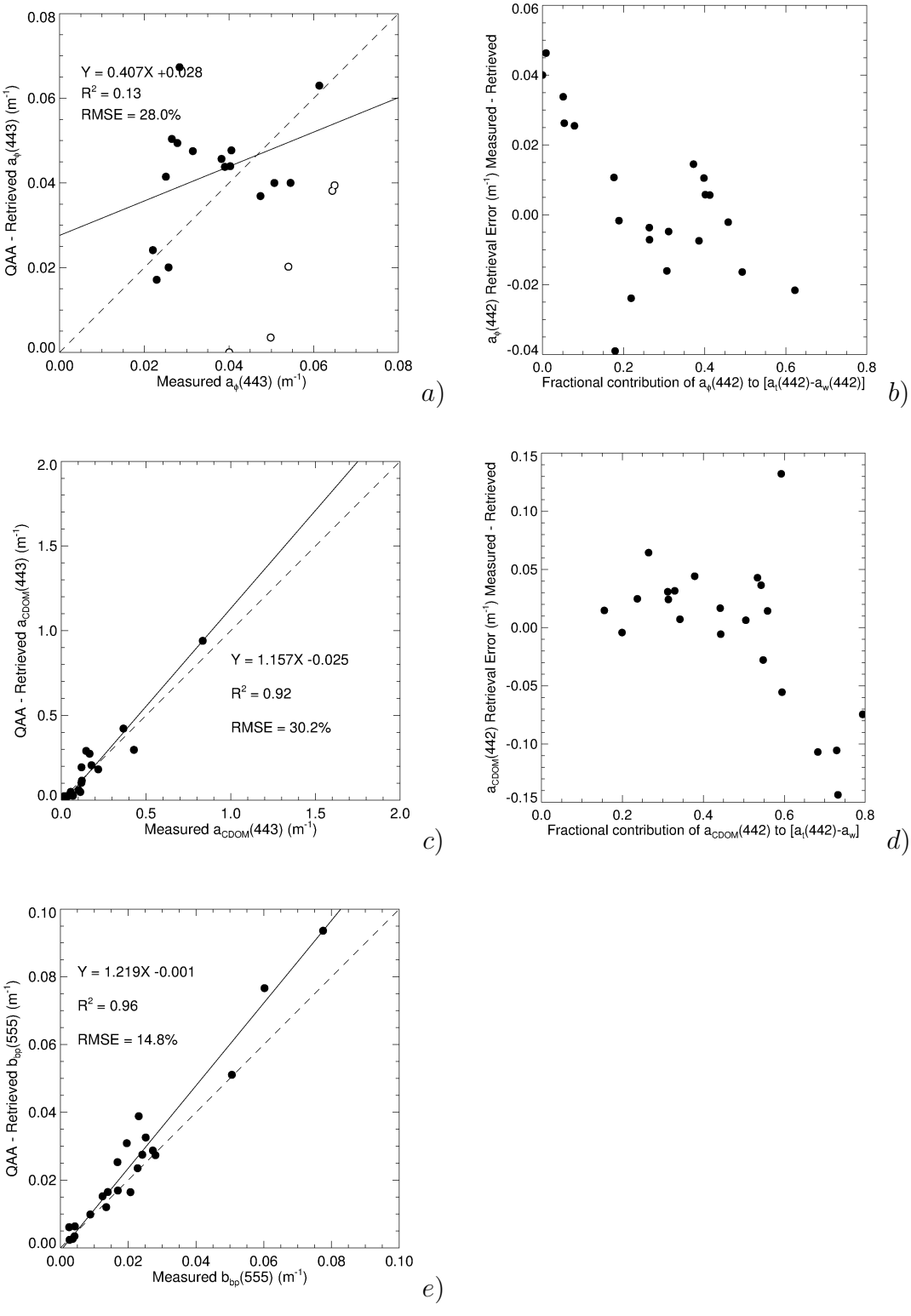

Figure 4.21: QAA retrieval results for: a) $a_\phi(442)$, c) $a_{CDOM}(442)$ and e) $b_{bp}(555)$. b) Shows the degradation in $a_\phi(442)$ retrieval performance when the relative contribution of $a_\phi(442)$ to $a_t(442) - a_w(442)$ is reduced. A fractional threshold of 0.1 was used to exclude poor $a_\phi(442)$ retrievals (shown as white plot symbols in a). d) Shows the degradation in $a_{CDOM}(442)$ retrieval performance when the relative contribution of $a_{CDOM}(442)$ to $a_t(442) - a_w(442)$ is reduced.

corrector approaches, $a_\phi(442)$ retrievals were poor when the fractional contribution of $a_\phi(442)$ to $a_t(442) - a_w(442)$ was low. A threshold of 0.1 was used to filter the retrievals (consistent with the predictor corrector approaches). Also similar to the predictor-corrector approach, the QAA-derived a_{CDOM} retrievals showed increasing error as the relative contribution of a_{CDOM} to $a_t(442) - a_w(442)$ increased. It is possible that for highly absorbing waters, the R_{rs} values at $412nm$ become too small to be accurately used for partitioning a_ϕ and a_{CDOM} contributions. Although (Lee et al. 2002) suggests using a longer reference wavelength in higher absorption waters, the approach used in this study included the 547/555 and 645 nm bands, so was already making use of the long wavelengths. If long wavelengths are required, then care must be chosen to avoid spectral regions in which fluorescence contribute significantly to the R_{rs} signal, as this would create additional errors. This further refinement is left for later work. In order to quality control the QAA-derived $a_{CDOM}(442)$ retrievals, a relative $a_{CDOM}(442)$ fractional contribution maximum threshold of 0.82 was used. This removed one outlier from Fig. 4.21c, as shown with a white plot symbol. The average computation time of the QAA approach was 1 ms, which is on average, about 50 times faster than the predictor-corrector apporaches. This computational speed is an important consideration when large volumes of data need to be processed.

The QAA allows the estimation of the phytoplankton absorption coefficient and the CDOM absorption coefficient, which are correlated to the respective water quality parameters TChl and DOC. Particulate backscatter ($b_{bp}(555)$) was determined earlier in the algorithm by Eq. 4.8, and 4.9. This $b_{bp}(555)$ value can then be used to determine TSS (see Fig. 2.25b). The accuracy of this algorithm approach with respect to water quality parameter retrievals will be evaluated with an *in situ* dataset, described later.

4.3.3 Water Quality Inversions

The coincident discrete Water Quality and time-averaged flowthrough calibration measurements are shown in Figures 4.22a-c. The RMS errors based on the Hydroscat data are 20% for $TChl$ and 15% for TSS. These errors are slightly higher than the relative replicability of discrete WQ measurements alone (See Table 2.7), suggesting that the spatial variability between the *in-situ* and flow-through measurements added to the uncertainty of calibration. The calibration of the the FLNTU $TChl$ data was shown to have a larger calibration RMS compared to the Hydroscat $TChl$, so was not used in further analysis.

The derived calibration coefficients were then applied to the flow-through Hydroscat data to compare with the R_{rs} - retrieved parameters. Unfortunately, no underway validation DOC data was collected other than discrete samples performed whilst on station.

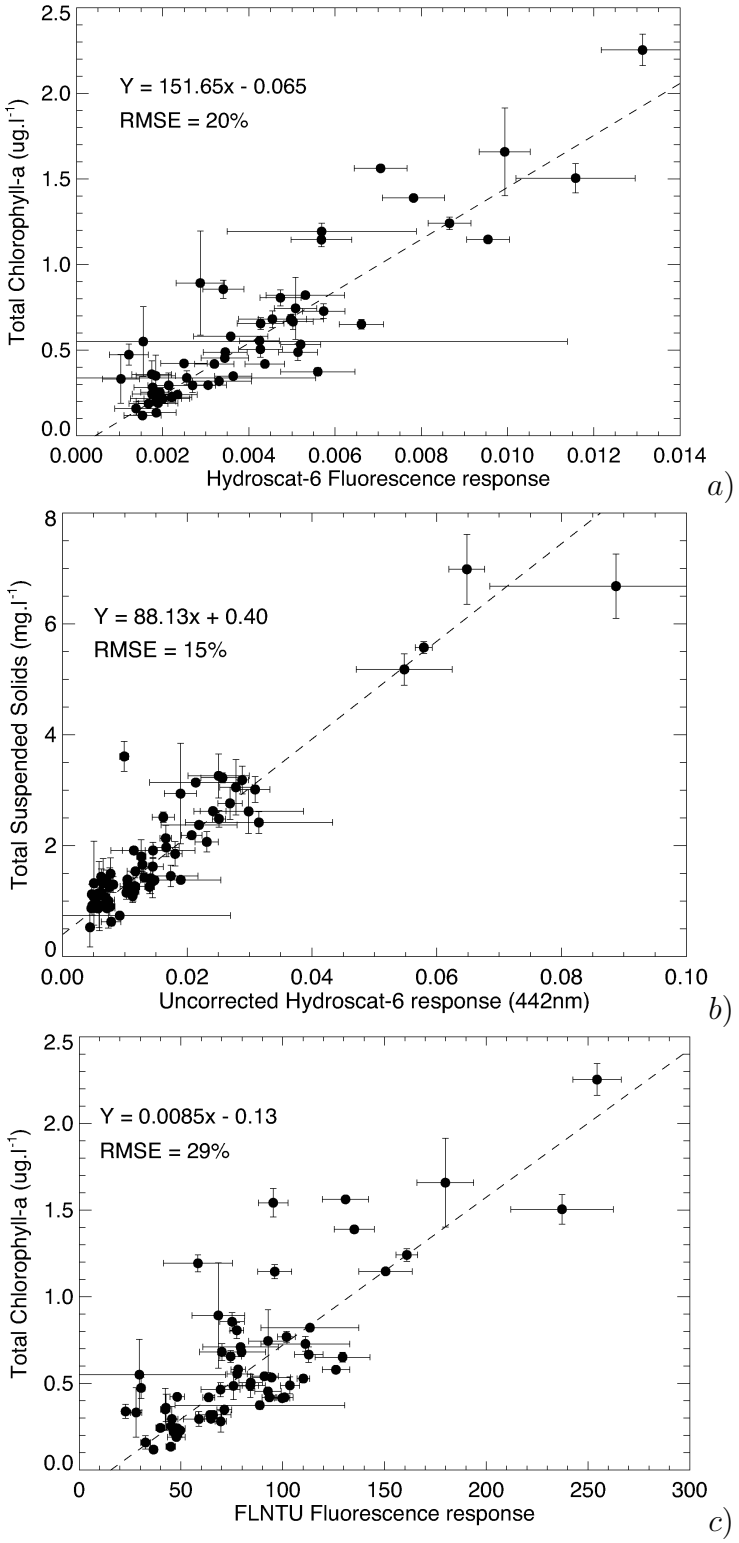

Figure 4.22: a) Niskin bottle TChl versus the Hydroscat fluorescence response. The linear regression shown was used to calibrate the Hydroscat response into TChl. b) Niskin bottle TSS versus the uncorrected Hydroscat scattering response at 442 nm. The linear regression shown was used to calibrate the Hydroscat response into TSS. c) Niskin bottle TChl versus the FLNTU fluorescence response. The linear regression shown was used to calibrate the FLNTU response into TChl.

4.3.4 Empirical DALEC transect retrievals

With the DALEC and flow-through system, it was possible to collect a substantial amount of data over very large spatial scales. Assuming the optical conditions characterising the GBR region were adequately represented during the field data collection, then direct empirical analysis of the field dataset may allow alternative and faster-performing algorithms applicable to the GBR to be adopted if their accuracy is satisfactory.

4.3.4.1 Empirical TSS

The most prominent observation from the data analyses is that DALEC-derived $u(645)$ and flow-through TSS are highly correlated (see Fig. 4.23a). The red 645 nm wavelength was chosen because the MODIS satellite produces a 250 m resolution image at this wavelength, so the algorithm will be applicable to MODIS image products. The $u(645)$ vs. TSS correlation is a result of the low absorption coefficients of CDOM and phytoplankton in this spectral region, combined with the fact that in the waters sampled, a significant portion of the scattering material contributing to $b_b(645)$ is readily captured on the filters used to quantify TSS.

As shown in Chapter 3, even perfectly measured above-water remote sensing reflectance is subject to variability caused by differences in sun-relative azimuth angle, solar zenith angle and wind speed. To remove these artifacts to make a more generally-applicable empirical relationship between R_{rs} and TSS, the R_{rs} was converted into u by Eq. 3.43 (as described in Chapter 3). Due to the general non-linearity of the TSS vs u relationship (see Fig. 4.23a), the following 2^{nd}-order polynomial was fit to relate TSS to u:

$$TSS = T_0 + T_1 u + T_2 u^2, \tag{4.35}$$

where $T_0 = 0.79$, $T_1 = 17$, and $T_2 = 193$. These coefficients represented the flow-through TSS data with a RMSE of 16.2% (see Fig.4.23b).

It is apparent that there is some spread in the u vs TSS data (see Fig 4.23a). This is possibly due to the fact that the highest suspended loads in this dataset were found in high CDOM and phytoplankton waters, whose absorption may contribute significantly to the reduction in $R_{rs}(645)$.

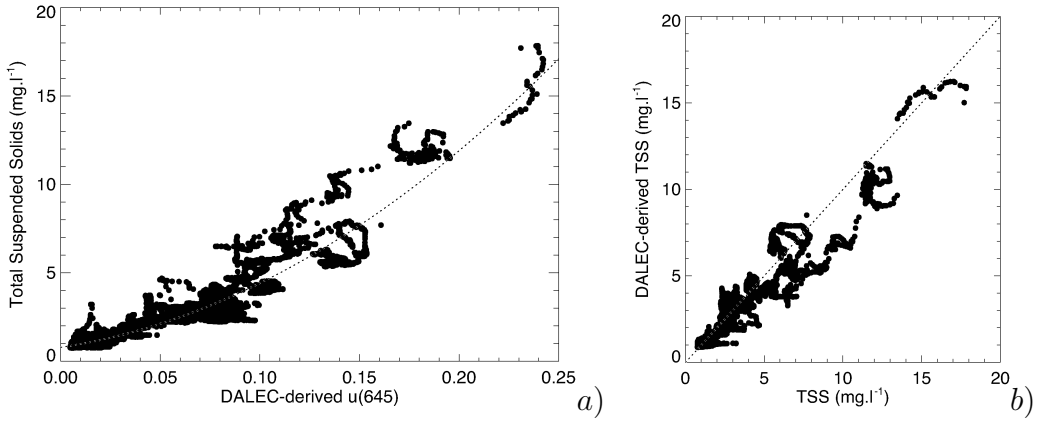

Figure 4.23: a) Flow-through TSS v.s. DALEC-derived u at 645nm. Dashed line shows the polynomial model 4.35. b) The empirically-retrieved (Eq. 4.35) TSS vs flow-through TSS.

4.3.4.2 Empirical TChl

The traditional empirical Maximum Band Ratio (MBR) ocean colour chlorophyll algorithms fail in turbid case-2 waters (Qin et al. 2007). These MBR algorithms are empirically tuned with large $TChl$ vs R_{rs} datasets collected mainly in case-1 waters. It is questionable whether regional or trophic variations on the relationship between $TChl$ and R_{rs} in coastal GBR are represented with the existing global MBR dataset. The standard MODIS OC3 MBR algorithm form is described below (O'Reilly et al. 2000):

$$TChl = 10^{A_0+A_1R+A_2R^2+A_3R^3+A_4^4}, \tag{4.36}$$

where

$$R = \log_{10}\left(\frac{R_{rs}(443) > R_{rs}(488)}{R_{rs}(547)}\right). \tag{4.37}$$

In Eq. 4.37, either $R_{rs}(443)$ or $R_{rs}(488)$ is chosen as the numerator, providing it produces the largest ratio when normalised by $R_{rs}(547)$. The coefficients $A_0 - A_4$ are respectively 0.2424, -2.7423, 1.8017, 0.0015 and -1.2280 for the OC3M algorithm determined from a large *in situ* dataset (O'Reilly et al. 2000).

By using the GBR *in situ* dataset, new polynomial coefficients can be determined for coastal GBR waters. Figure 4.24a shows the base-10 logarithm of TChl v.s. R dataset collected in this study for the entire range of GBR waters encountered. Here, R was calculated by Eq. 4.37, which utlilises MODIS 1 km spatial resolution bands at 443, 488 and 547 nm. Two different polynomials were used in a piecewise fashion to describe the data (see Table 4.5). By inspection, it was decided that combining two polynomials in a piecewise fashion best represented the data and would lend itself to more stable extrapolations if imagery is processed outside of the regression dataset range. The dotted line describes the relationship of the OC3M algorithm. Clear differences are seen between the OC3M fit and the GBR-tuned polynomial, however for low chlorophyll concentrations, differences are much smaller; in the vicinity of 0.025 μgl^{-1}. Small differences may be due to differences in laboratory Chl methodology or issues with calibrating the flow-through chlorophyll fluorometer. For higher $TChl$ waters, there is substantial deviation. This is likely due to the presence of other in-water constituents (see TSS-based colour code in Figure 4.24c).

Bands (nm)	Range	A_0	A_1	A_2	A_3	A_4
$(443, 488, 547)$	$R \leq 0.0587$	-0.2177	-1.1977	4.4589	-22.3351	25.7503
1 km	$R > 0.0587$	-0.1856	-1.6446	1.6587	-1.9631	0
$(469, 555)$	$R \leq 0.0281$	-0.2521	-0.6111	2.4902	-11.0464	0
500 m	$R > 0.0281$	-0.2380	-1.0844	1.3553	-2.8821	0

Table 4.5: GBR-specific piecewise polynomial model coefficients for 1 km and 500 m resolution Band Ratio TChl algorithms.

Coastal waters are usually spatially variable, and there is a need to monitor TChl in close proximity to the shoreline. In this case, it could be beneficial to use the higher spatial resolution MODIS bands. Using the 500 m resolution MODIS bands centered at 469 nm and 555 nm similar to the work of Franz et al. (2006),

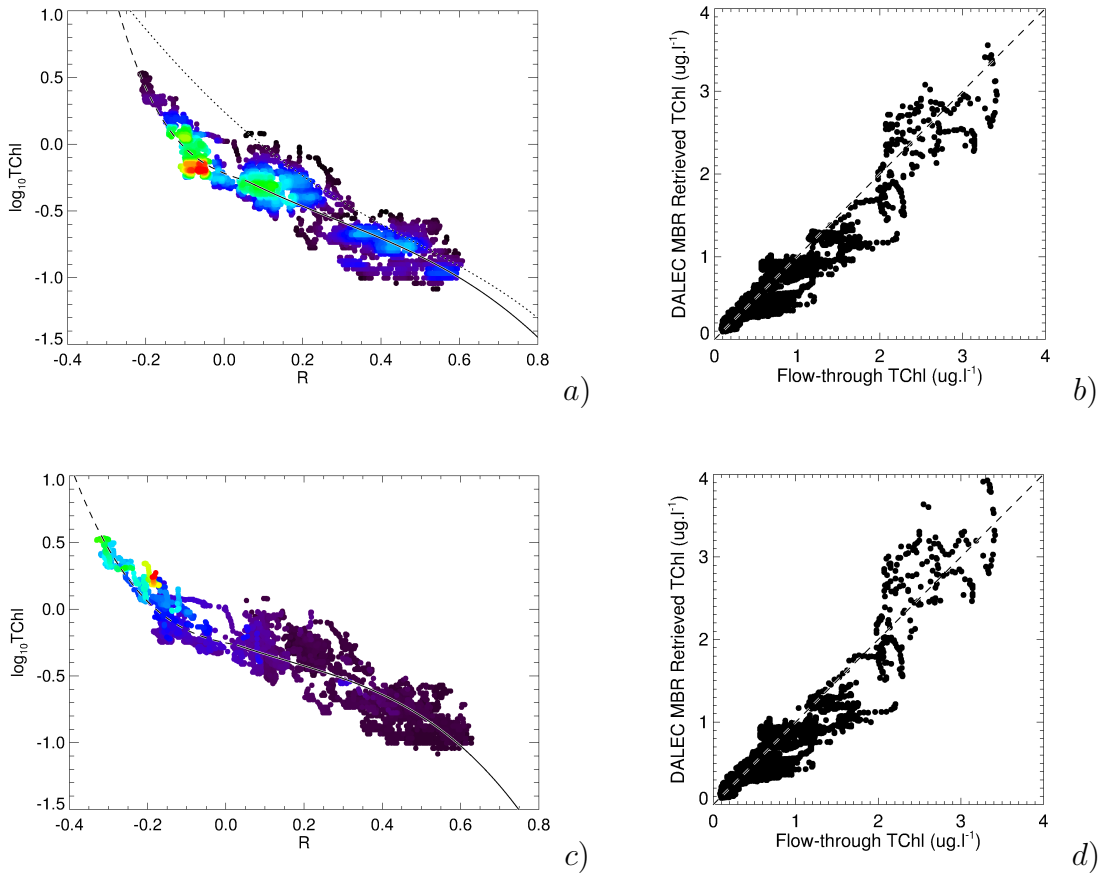

Figure 4.24: a) Polynomial fits to determine the empirical band ratio coefficients for the GBR dataset using the 1 km bands (Eq .4.37). The dashed line is a fourth-order polynomial and then solid line is a third order (see Table 4.5). The dotted line is the OC3M MBR relationship for comparison. Note, colour-coding of the plot symbols is based on data density, where red is highest and black is the lowest density. The b) The empirically-retrieved TChl v.s. flow-through TChl using piecewise polynomials described in Eq. 4.5. The 1:1 line is shown with the dashed line. $RMSE = 0.227$. c) Polynomial fit to determine the empirical band ratio coefficients for the GBR dataset using the 500 m bands, where $R = \log_{10}\left(\frac{R_{rs}(469)}{R_{rs}(555)}\right)$. The dashed line is the first third-order polynomial and the solid line is the second third order (see Table 4.5). Note, the plot symbols here are colour-coded in terms of Total Suspended Solids, where low TSS is violet and high TSS is Red. d) The empirically-retrieved TChl vs flow-through TChl. The 1:1 line is shown with the dashed line. $RMSE = 0.225$.

a GBR-tuned MBR algorithm can be determined to allow the estimation of $TChl$ at 500 m resolution.

Figure 4.24c presents two 3^{rd} order polynomial fits to parameterise the tuned band ratio TChl algorithm based on the flow-through $TChl$ and DALEC R_{rs}, where in this 500 m algorithm, $R = \log_{10}\left(\frac{R_{rs}(469)}{R_{rs}(555)}\right)$.

When processed with the DALEC R_{rs} data using essentially identical synthesied spectral bands, both the 1 km and 500 m algorithms retrieve the flow-through $TChl$ with an RMSE of approximately 23% (see Figs. 4.24b and d). It should be noted that other constituents correlated to DOC and TChl are expected to vary R, however this dataset demonstrates that these other constituents must correlate well with $TChl$. As a result, the satisfactory 23% RMSE retrieval of $TChl$ is achieved. This result is surprising, as this retrieval error is lower than the RMS of retrieving $TChl$ from an *in situ* measured $a_\phi(\lambda)$ (see Table 2.8). This, combined with the simplicity in image processing and superior spatial resolution may make this empirical approach superior to full-spectrum inversions for some applications, however empirical tuning to the local conditions is important.

In terms of absorption, a_{CDOM} can be 5 to 10 times greater than a_ϕ in the blue region, and generally, areas of high a_{CDOM} also have high $TChl$ concentrations (see Fig.4.25). Considering this, the MBR algorithm determined for the GBR (Eq. 4.36) is undoubtedly strongly influenced by the presence of a_{CDOM} because a_{CDOM} is exponential in spectral shape so will effect R in Eq. 4.36. Additionally, a_{NAP} can easily be in the same order of magnitude as a_ϕ. Despite this, the MBR $TChl$ algorithm has been shown to perform satisfactorily with the input dataset (Fig. 4.24b). However, use of the algorithm should be applied with caution in that it is sensitive to the relative abundances of different optical fractions encountered during the transect fieldwork. This algorithm would be expected to perform worst for phytoplankton blooms occurring in very clear water, however these regions are probably adequately measured using the standard OC3M algorithm (O'Reilly et al. 2000), and it is very easy to determine a threshold between

coastal and case 1 regions based on the empirical TSS algorithm (Eq. 4.35) in order to blend the two algorithmic approaches if necessary. A TSS threshold at around 1.5 $\pm$ 0.5 mgl^{-1} should suffice, however this should be confirmed with visual appraisal of a number of scenes.

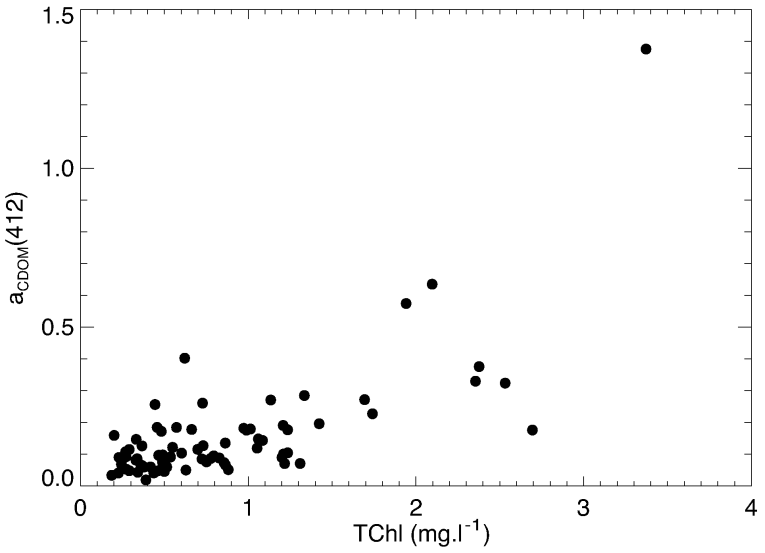

Figure 4.25: Coincident discrete a_{CDOM} vs $TChl$ measurements for the GBR showing weak correlation.

An alternative empirical approach used to estimate $TChl$ is via the MODIS chlorophyll Fluorescent Line Height (FLH) algorithm (Abbott & Letelier 1999). The MODIS sensors have 1 km bands positioned at 667, 678 and 748 nm, which are able to resolve the spectral signature of the water leaving radiance (L_w) due to phytoplankton pigment fluorescence. The tuned FLH used in this study uses the R_{rs} product and is calculated by first establishing a "baseline" equal to the extrapolated R_{rs} value at 678 nm determined from only the 667 nm and 748 nm bands. The FLH is then calculated by the measured $R_{rs}(678)$, minus the baseline:

$$FLH = R_{rs}(678) + \frac{(678-667)(R_{rs}(667) - R_{rs}(748))}{(748-667)} - R_{rs}(667). \qquad (4.38)$$

In the original radiance-based FLH product, the FLH signal is a function of $TChl$ and other parameters (Abbott & Letelier 1999):

$$FLH_{Lu} = [TChl]a^*_\phi(676)E_{PAR}\phi_f, \qquad (4.39)$$

where FLH_{Lu} is the radiance-based Fluorescent Line Height, ϕ_f is the fluorescence quantum yield, $a^*_\phi(676)$ is the chlorophyll-specific absorption coefficient, $[TChl]$ is the Total Chlorophyll concentration, E_{PAR} is known or easily estimated from remote sensing (Carder et al. 2003). However, for the R_{rs}-based FLH, this E_{PAR} term becomes less significant. $a^*_\phi(676)$ varies slightly with phytoplankton pigment packaging, but can be modelled as a function TChl (see Chapter 3.4).

The main unknown in Eq. 4.39 is ϕ_f; the fluorescence quantum yield which has been reported to vary from 0.0015 to 0.1, with a mean of 0.0035 (Abbott & Letelier 1999). This parameter is defined as the fraction of energy absorbed by TChl that is released in the form of fluorescence, and thus provides information about the physiological state of the phytoplankton. Although not expressed in Eq. 4.39, in practice, the fluorescent line height is affected by the presence of scattering and absorbing minerals and also CDOM. The respective mass-specific absorption coefficients of a_{NAP} and a_{CDOM} are low in the far red / NIR wavelength region which the FLH uses, and in case-1 waters, it is possible that these could be ignored. In coastal GBR waters, this should be assessed. By utilizing the forward model which creates R_{rs} spectra, the sensitivity of the FLH to increasing concentrations of a_ϕ, a_{CDOM}, b_{bp} (and associated a_{NAP}) was assessed. TSS was varied from 0.7 up to 30 mgl^{-1} and DOC (i.e. CDOM) was varied from 0.66 up to 30 mgl^{-1}. These ranges are outside of the magnitudes sampled during the field campaigns. Figure 4.26a and b show how the FLH is contaminated by increasing concentrations of a_{CDOM}, and b_{bp} (and co-varying a_{NAP}). The most significant changes in FLH are associated with increases in b_{bp}, however a_{CDOM} also effects the FLH. To further demonstrate how b_{bp} (i.e. TSS) influences the FLH, Figure 4.27 shows plots of the FLH vs TChl (a,b) and FLH vs TSS (c). The best correlation is derived from the FLH v.s. TSS plot and not TChl, so the FLH has been demonstrated to not perform as a reliable estimator of Chlorophyll in coastal GBR waters.

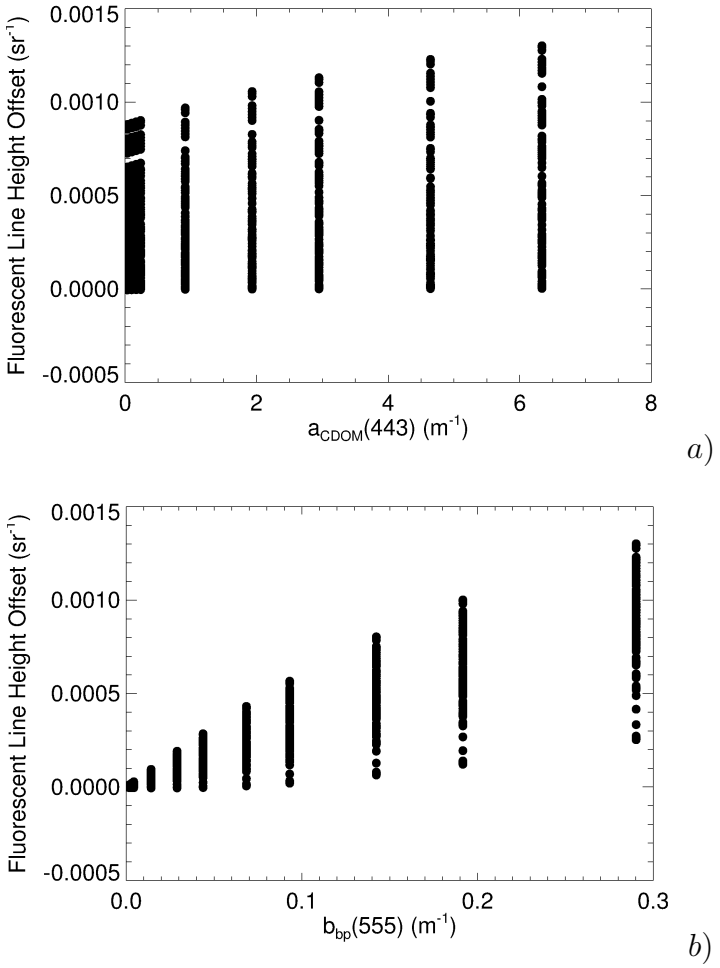

Figure 4.26: Fluorescent Line Height Offset error versus a) $a_{CDOM}(443)$ and b) $b_{bp}(555)$. Each vertical 'line' of data points is produced by variations in the other parameters (the most influential being b_{bp}). TSS was varied from 0.7 up to 30 mgl^{-1} and DOC (i.e. CDOM) was varied from 0.66 up to 30 mgl^{-1}.

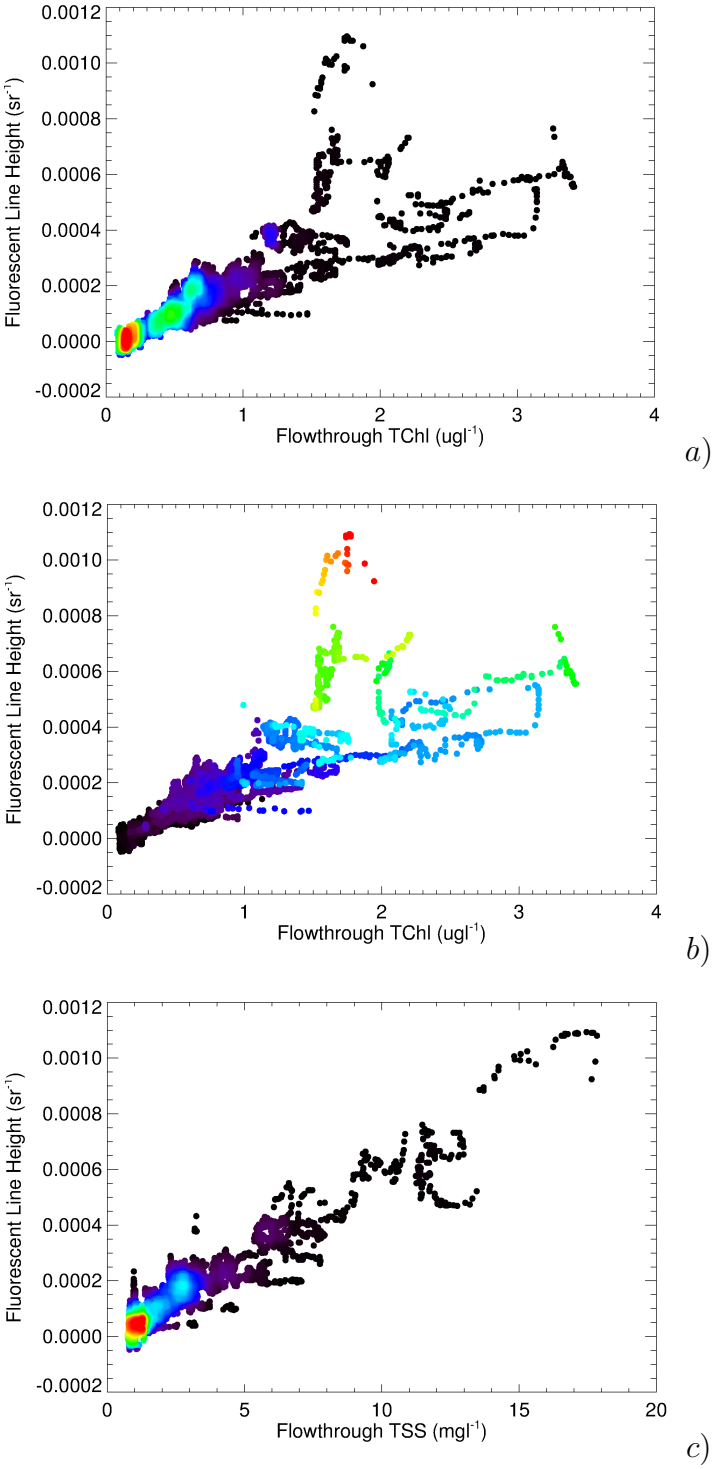

Figure 4.27: The DALEC-based Fluorescent Line Height using flow-through measurements from the January field trip. The data points are colour coded by a) data density (black to red corresponds with low to high densities) and b) TSS from black ($\approx 0.5\ mgl^{-1}$), up to red ($\approx 18\ mgl^{-1}$). c) FLH algorithm versus flow-through measurements of TSS, showing better visual correlation than for TChl in b).

4.3.5 IOP-based DALEC transect retrievals

The analysis performed with the discrete IOP dataset was difficult given the spatial variability of the coincident IOP and R_{rs} measurements, however through a process of elimination, it was concluded that the "Real" a_{CDOM} and a_{NAP} basis vectors lead to more accurate IOP retrievals. It was also concluded that approaches with $a_{NAP}(442)$ tied to b_{bp} could potentially lead to better $a_{CDOM}(442)$ retrievals, and that $a_{NAP}(750) = 0$. Apart from these findings, conclusions about which combination of a_ϕ or b_{bp} inversion approach is the most appropriate would ideally be drawn analysing by a much larger dataset, where the possible effects of occasional spatial mis-matches are reduced. Such a dataset was collected during the DALEC transects.

As the inversion process is known to be affected by the type of IOP models used, a variety of IOP model combinations were tested. In Chapter 3.4, it was observed that increasing the number of phytoplankton basis vectors improved the TChl retrieval based on $a_\phi(\lambda)$ measurements. This approach, along with the more simplistic one-parameter $a_\phi(\lambda)$ phytoplankton absorption models were tested in the hyperspectral inversion scheme (2-Mix, 4-Mix, B-95, Lee and Pack). Given that all three backscattering models performed similarly (see Table 4.3.1), all three variants described in Section 4.2.2.1.2 were tested (Std, Blend, and Emp). Inversions were performed with both a freely-varying $a_{NAP}(442)$ and also $a_{NAP}(442)$ tied to b_{bp} .

The daily quality-controlled DALEC transect datasets were merged and co-located with the flow-through water quality data by applying a time lag to the flow-through measurements. To reduce inversion processing time, every 10^{th} R_{rs} spectrum was inverted using the aforementioned variants of the predictor-corrector algorithms. This provided $10 \times 3 = 30$ sets of results, excluding the QAA method. The total number of inverted data points for comparison with flow-through water quality measurements was approximately 5000 (i.e. 5000 points per inversion combination).

4.3.5.1 Particulate Backscattering Retrievals

In general, $b_{bp}(555)$ retrievals for all model variants were highly correlated with the flow-through TSS measurements. Six example $b_{bp}(555)$ retrievals are shown in Fig. 4.28. The scatter plots have subtle differences which effect the correlation coefficients and thus accuracy of TSS retrievals based on $b_{bp}(555)$.
By using the *in situ* validation flow-through dataset, a more accurate relationship between the DALEC inverted ($b'_{bp}(555)$) product and TSS can be formulated:

$$TSS = M[b'_{bp}(555)] + O, \tag{4.40}$$

where M is the empirically-tuned slope and O is the tuned offset (shown in Table 4.6), and the $b_{bp}(555)'$ is primed to indicate it is an inverted parameter.

This re-tuning approach compensates for any potential biases in the IOP-based inversions. Two TSS retrieval examples are shown in Fig. 4.29.

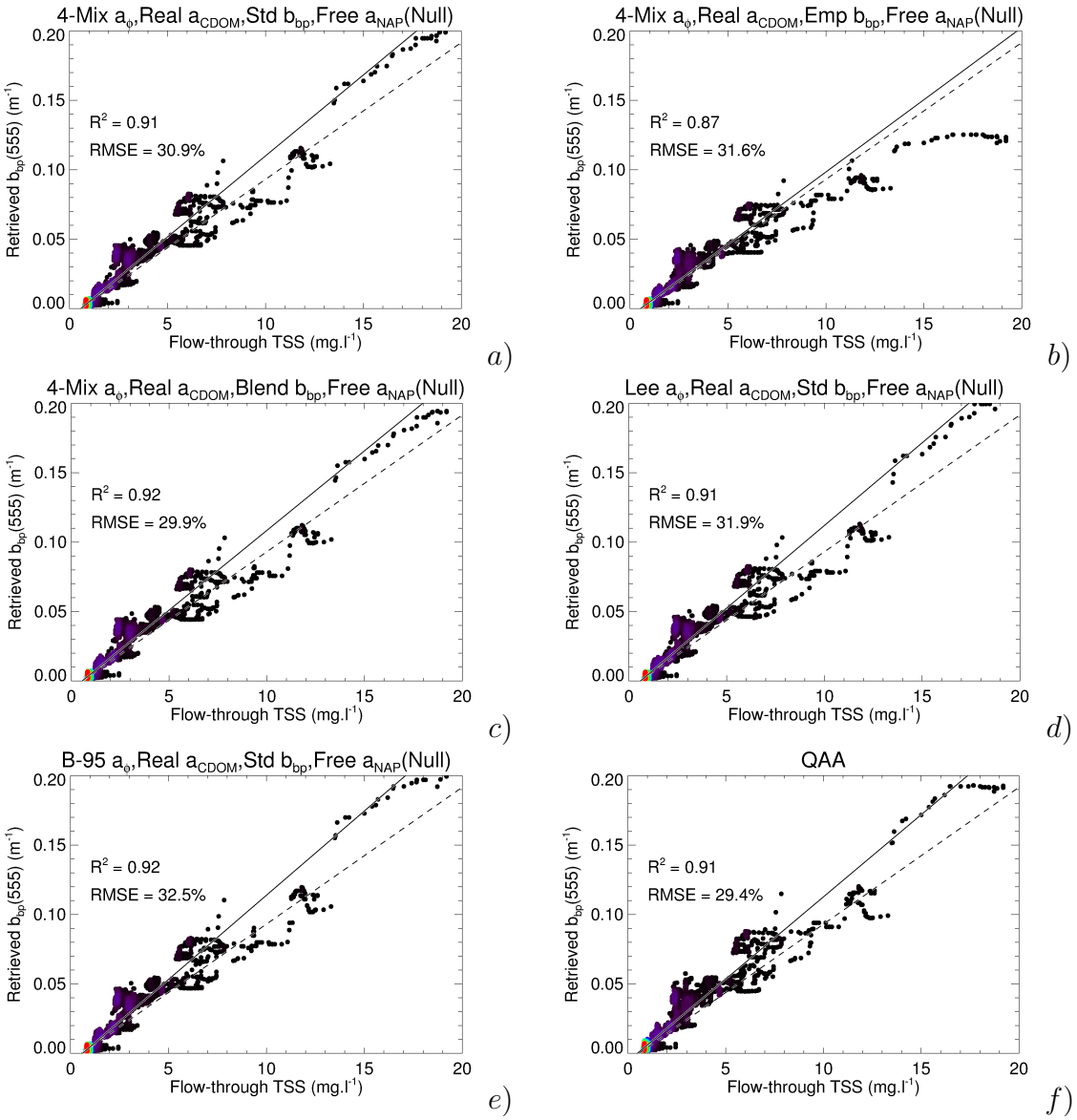

Figure 4.28: Example $b_{bp}(555)$ retrievals vs flow-through TSS for: a) The 4 phytoplanton mixture, Real a_{CDOM}, free b_{bp} model, b) The 4 phytoplanton mixture, Real a_{CDOM}, Empirically-tied b_{bp} model, c) The 4 phytoplanton mixture, Real a_{CDOM}, basis vector blend b_{bp} model, d) The GBR-adapted Lee phytoplankton model, Real a_{CDOM}, free b_{bp} model, e) The B-95, Real a_{CDOM}, free b_{bp} model and f) The GBR-tuned QAA. The dashed lines show the relationship described by Eq. 2.53. The solid lines show the regression of the retrieved v.s. flow-through TSS. The plots are colour coded in terms of data density (black to red corresponds with low to high densities).

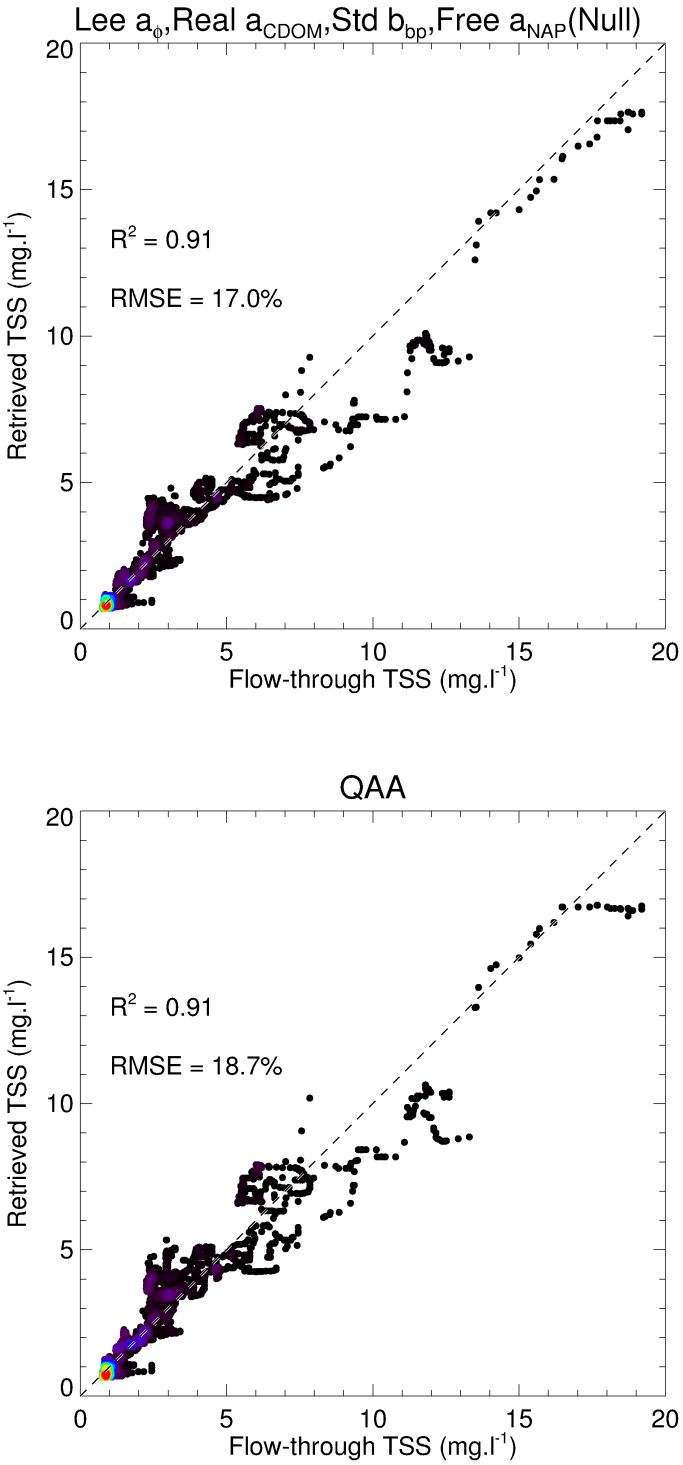

Figure 4.29: Two examples of the Eq. 4.40 retrieved TSS vs flow-through TSS comparison for a) GBR-tuned Lee phytoplankton, Real a_{CDOM} and Standard free b_{bp} algorithm variant and b) The QAA. The dashed line is the 1:1 line. The plots are colour coded in terms of data density (black to red corresponds with low to high densities). The results of the best performing algorithm variants are shown in Table 4.6.

4.3.5.2 Phytoplankton Absorption

Unlike the $b_{bp}(555)$ retrievals, all algorithm variants produced widely varying a_ϕ retrievals in some conditions. To qualitatively investigate the accuracy of the a_ϕ retrievals, they were compared with the flow-through TChl measurements. Six example a_ϕ retrieval v.s. TChl plots are shown in Figure 4.30. Although the general shape of the power-law (B-95) relationship between a_ϕ and TChl is exhibited in Figs 4.30a - f, there are some retrievals which clearly deviate from this trend. For the case of the 2-Mix variants (ie Fig. 4.30b), some of these outliers could be due to a distinct phytoplankton population with varying chlorophyll-a specific absorption coefficients, however there are a number of retrievals where the retrieved $a_\phi(442)$ values are lower than the lowest TChl-specific $a_\phi(442)$ encountered (see straight dotted lines on each plot in Fig. 4.30). These retrievals are considered erroneous, and thus presents a limitation to the accuracy of TChl retrievals based on the $a_\phi(442)$ v.s. TChl relationship. Fortunately, some algorithm variants are more robust.

Figure 4.31 shows the same retrievals as shown in Figs. 4.30a, c and e, however the plot symbols are colour coded in terms of fractional a_ϕ contribution to total non-water absorption $(a_t - a_w)$ in the first column, and the second column is plotted in terms of total non-water absorption $(a_t - a_w)$. By observing the colour scales in Figs. 4.31a, c and e, it can be seen that $a_\phi(442)$ retrievals generally deviate further from the 'B-95' power-law trend as the fractional contribution of $a_\phi(442)$ decreases. This likely represents the Levenberg-Marquart optimisation straying into an incorrect local minimum solution in turbid waters.

Each inversion algorithm variant was evaluated based on its ability to retrieve the measured flow-though TChl values from inverted $a_\phi(442)$. The number of complete $a_\phi(442)$ failures (i.e. $a_\phi(442) = 0$) for each variant was recorded and expressed as a data retention % in Table 4.6. Algorithm failures were then removed from the dataset and the B-95 model curve was fitted to the retrieved $a_\phi(442)$ data (i.e. Fig. 4.30) for each inversion variant. Re-arranging Eq. 2.40 to solve

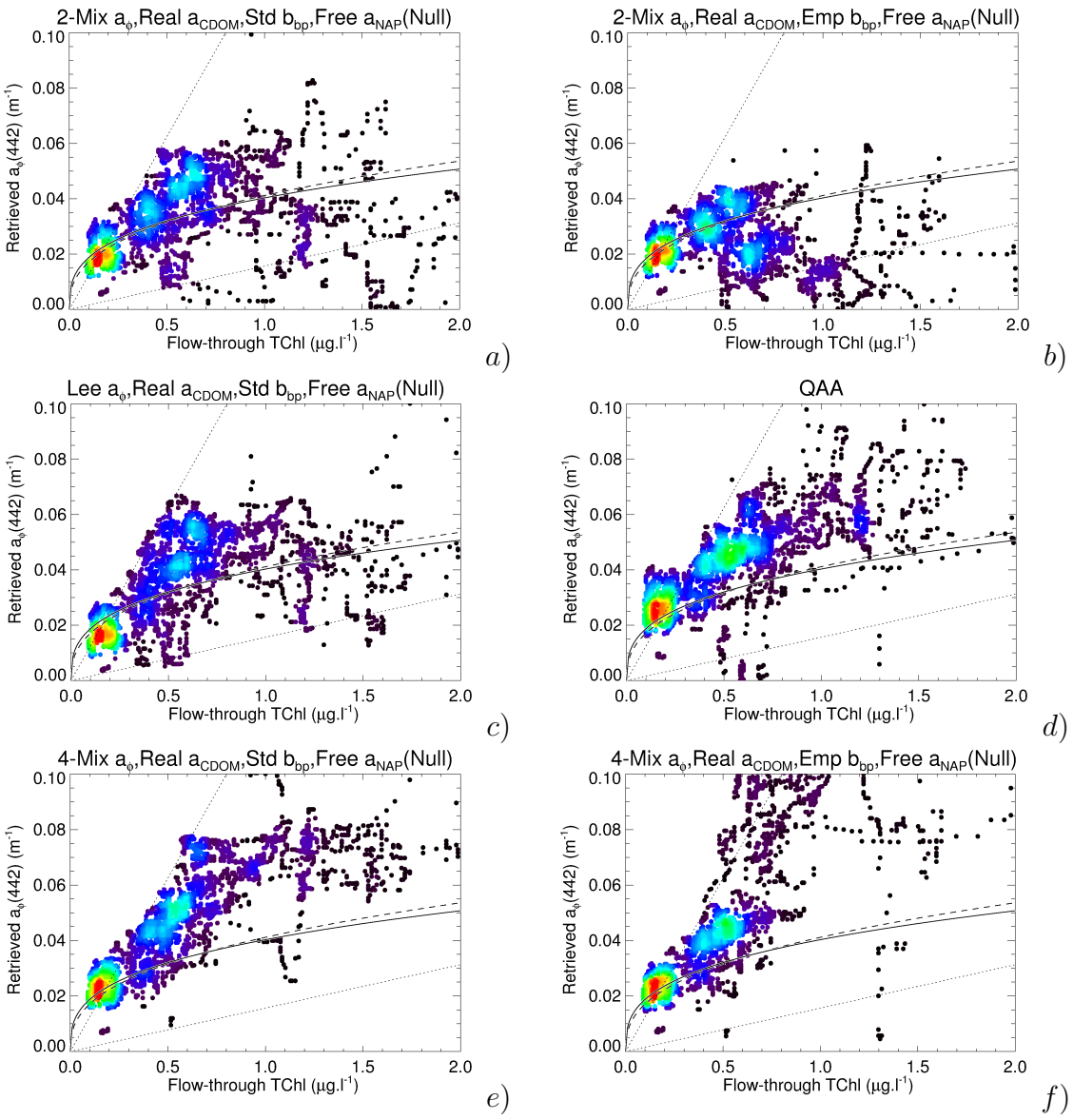

Figure 4.30: Six examples of retrieved $a_\phi(442)$ v.s. flow-though measured TChl for: a) The 2 phytoplanton mixture, Real a_{CDOM}, free b_{bp} model, b) The 2 phytoplanton mixture, Real a_{CDOM}, Empirically-tied b_{bp} model, c) The GBR-adapted Lee phytoplankton model, Real a_{CDOM}, free b_{bp} model, d) The GBR-tuned QAA, e) The 4 phytoplanton mixture, Real a_{CDOM}, free b_{bp} model and f) The 4 phytoplanton mixture, Real a_{CDOM}, Empirically-tied b_{bp} model. The dashed line is the B95 relationship developed in Chapter 3.4, and the solid line is the exact B95 relationship of Bricaud et al. (1995). The plots are colour coded in terms of data density (black to red corresponds with low to high densities). The straight, dotted lines show the extrema of the slightly packaged *Prochlorococcus* (upper) and the highly packaged Diatom (lower) end members identified in Chapter 3.4. All plots were limited to the same range, although outliers exist outside the shown range for all four variants.

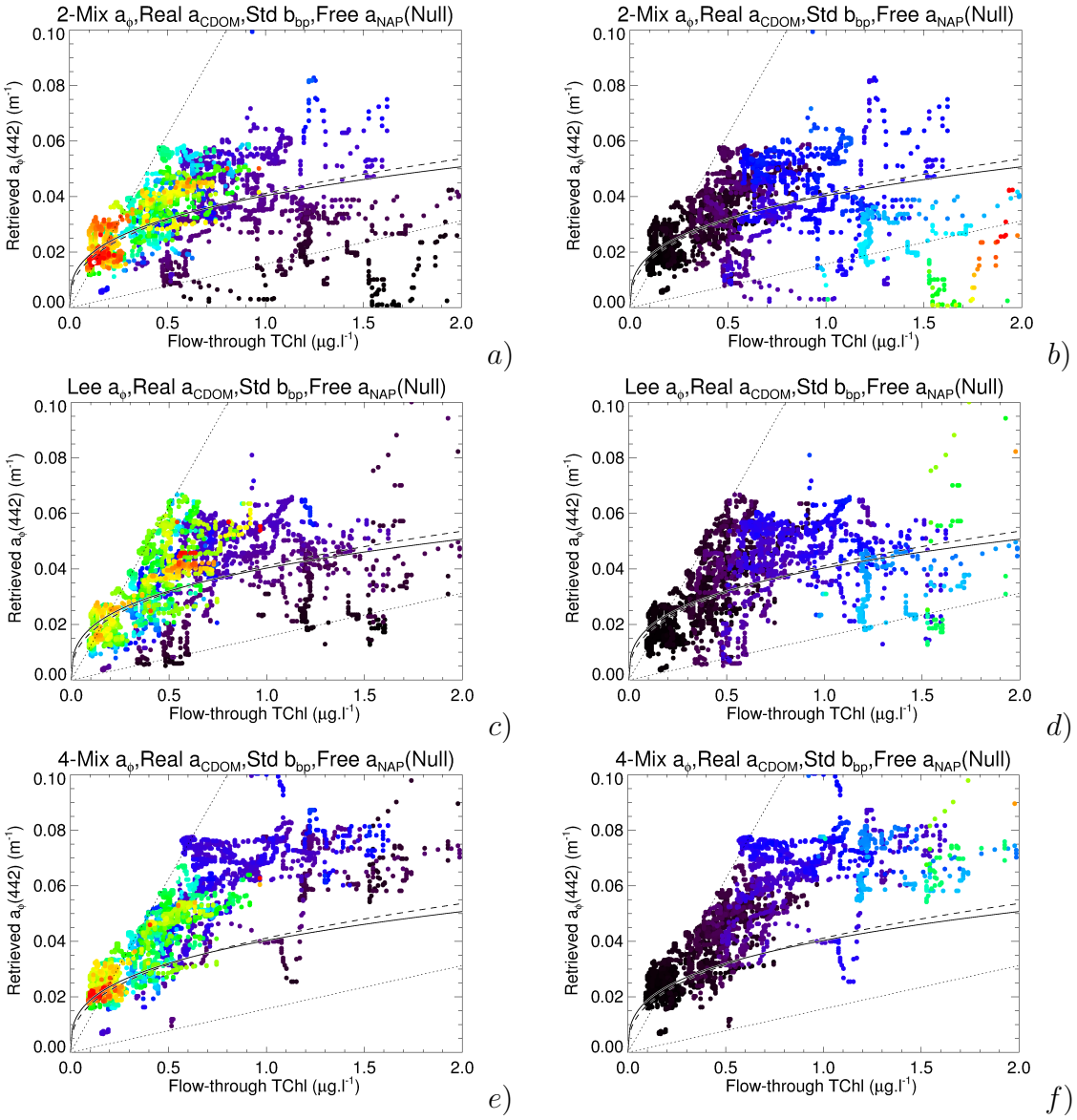

Figure 4.31: As in Fig. 4.30a, c and e, but symbols are colour coded according to a) Fractional a_ϕ contribution to total non-water absorption ($a_t - a_w$), with the highest values shown in red (80%), fading through yellow, green, blue and then finally to black. b) Colour coded according to total non-water absorption ($a_t - a_w$). As in Fig. 4.30a, c and e, the dashed lines in all plots show the B95 relationship developed in Chapter 3.4, and the solid line is the exact B95 relationship of Bricaud et al. (1995). The straight, dotted lines show the extrema of the slightly packaged *Prochlorococcus* (upper) and the highly packaged Diatom (lower) end members identified in Chapter 3.4.

for TChl yields:

$$TChl = \exp \frac{\ln\left(\frac{a_\phi(442)}{A}\right)}{B}, \tag{4.41}$$

where the model coefficients A and B are determined from the retrieved a_ϕ values and the flow-through TChl dataset. The tuned A and B coefficients are listed in Table 4.6. An example of the Eq 4.41 model curve TChl retrieval is shown in Fig. 4.32, and the results of other algorithm combinations are shown later in Table 4.6.

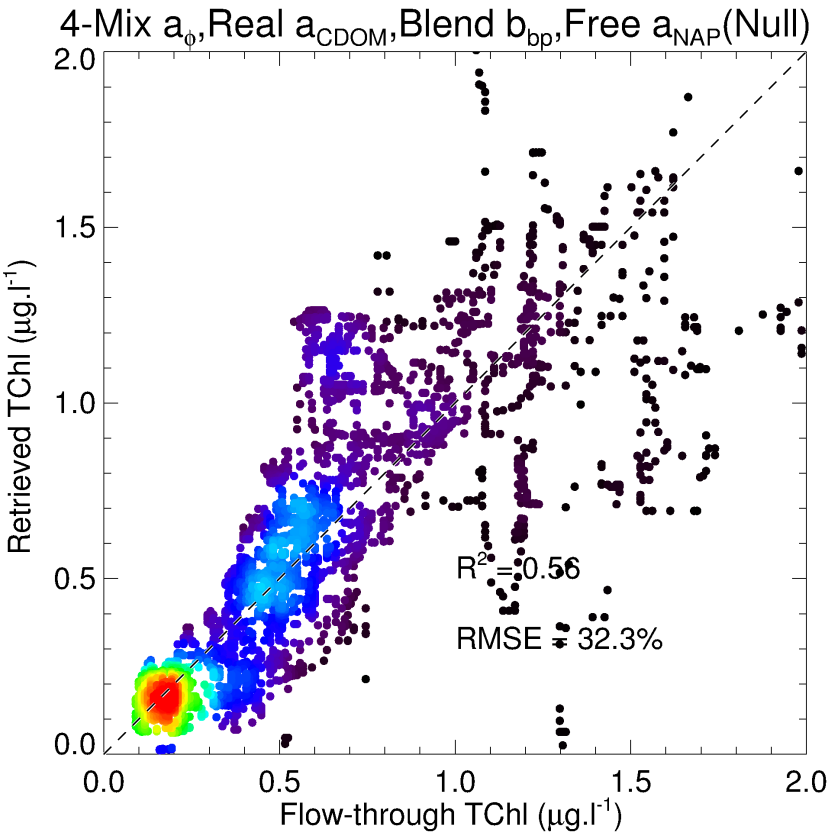

Figure 4.32: An example of the corrected (Eq. 4.41) retrieved $TChl$ vs flow-through $TChl$ comparison for the 4-Mixture *in situ*-derived "Real" a_{NAP} and a_{CDOM} basis vector variant. The dashed line is the 1:1 line. The plots are colour coded in terms of data density (black to red corresponds with low to high densities). This algorithm retained 100% of the data.

For the 2-Mix and 4-Mix inversion variants, TChl can also be calculated by summing the optimised weights of each chlorophyll-specific basis vector. The weights are in units of $\mu g l^{-1}$ and are described in Eq. 4.2. For example, for the 4-Mix

variant, the total TChl is calculated as:

$$TChl = TChl_{Pro} + TChl_{Syn} + TChl_{Diat} + TChl_{Trich}, \tag{4.42}$$

where the subscripts denote the TChl concentration for each of the 4 chlorophyll specific phytoplankton basis vectors (also see Eq 4.2). The 2-Mix algorithm is similar, but contains only $TChl_{Pro}$ and $TChl_{Diat}$ contributions.

The retrieval of TChl based on Eq. 4.42 may potentially yield information about the functional groups of phytoplankton with distinctive pigment suites and should provide greater accuracy TChl retrievals. Two examples of an Eq. 4.42 based retrieval is shown in Fig. 4.33. These example plots show that despite the general accuracy of the a_ϕ retrievals (i.e. Fig. 4.30e), the Mix-based algorithms retrieve erroneous TChl values if the mass-specific absorption basis vectors are used to calculate TChl (i.e Eq. 4.42). The 2-Mix and 4-Mix retrieval methods are very sensitive to the mass-specific coefficients of the phytoplankton basis vectors used. To assess which basis vectors lead to the greatest retrieval error, the RMS error in the TChl retrieval was plotted as a function of the relative contributions of each phytoplankton type (see Fig. 4.34). Figure 4.34d highlights that in particular, very large errors in TChl retrieval occur when $TChl_{Diat}$ is the dominant contributor to the total TChl. Given that the total a_ϕ appears fairly accurate, the error demonstrated by Figure 4.34d could suggest that the diatom-like chlorophyll-specific absorption basis vector ($a^*_{\phi_{Diat}}$) determined from field measurements is erroneous. This may be a result of issues associated with variable pathlength amplification in the highly turbid waters for which the $a^*_{\phi_{Diat}}$ was determined.

To correct the magnitude of $a^*_{\phi_{Diat}}$, the inverted $TChl_{Diat}$ was compared with the residual TChl (i.e. $TChl - TChl_{Pro} - TChl_{Synn} - TChl_{Tricho}$). An example of this residual comparison is shown in Fig. 4.35a. In every variant case, the retrieved $TChl_{Diat}$ value was approximately 4 times greater than the residual value. By applying a scaling factor to correct $a^*_{\phi_{Diat}}$, greatly improved TChl retrieval can be achieved, as shown in Fig. 4.33b. A list of calculated scaling factors and offsets are shown in the final retrieval results Table 4.6.

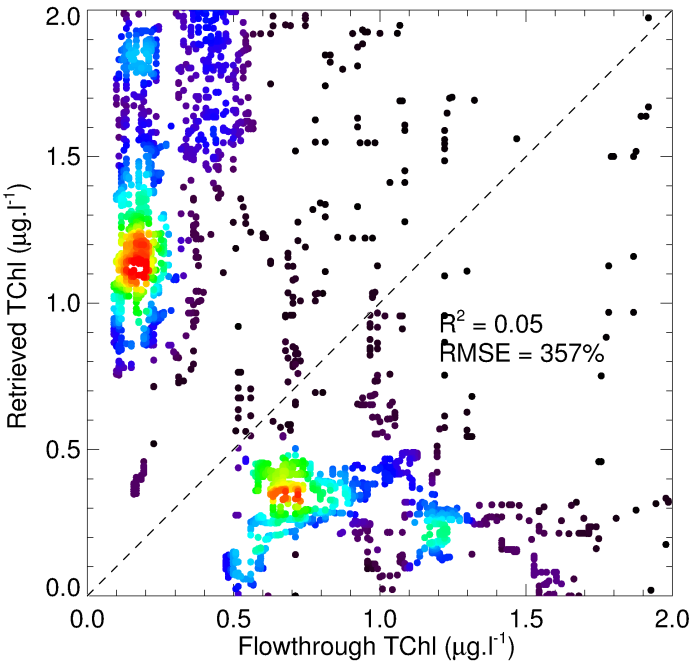

a)

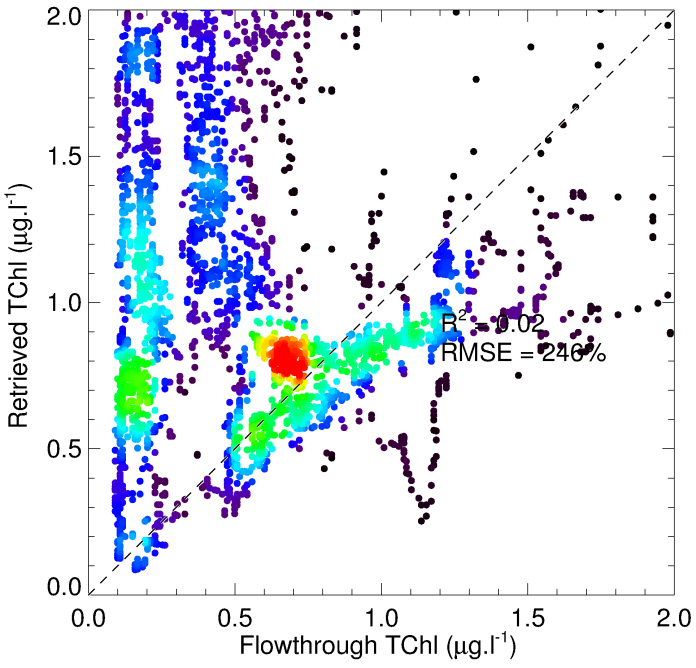

b)

Figure 4.33: Two examples of the optimised weights retrieved $TChl$ vs flow-through $TChl$ comparison. a) is the 2-Mixture, Real a_{CDOM} basis vector and Standard b_{bp} variant, with a TChl calculated by Eq. 4.1. b) is the 4-Mixture, Real a_{CDOM} basis vector and Standard b_{bp} variant, with a TChl calculated by Eq. 4.2. The dashed line is the 1:1 line. The plots are colour coded in terms of data density (black to red corresponds with low to high densities).

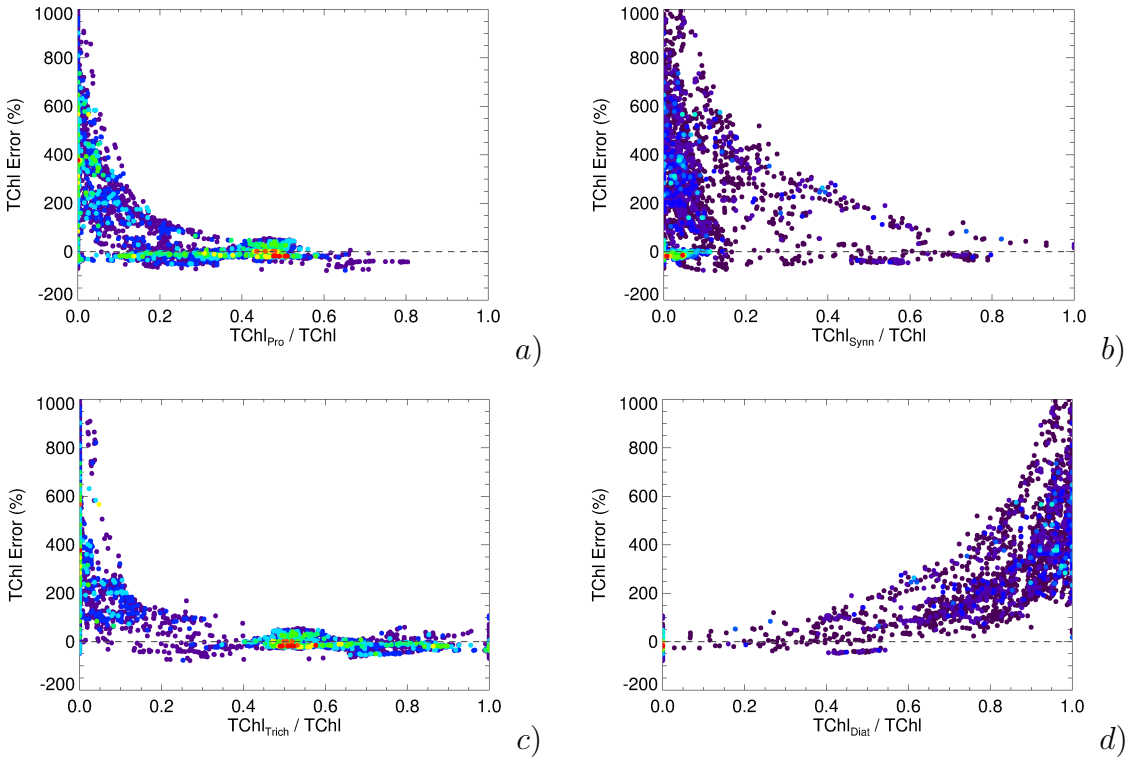

Figure 4.34: Example of the percentage error in retrieved TChl as a function of the relative contribution of TChl from a) *Prochlorococcus*, b) *Synnechococcus*, c) *Trichodesmium* and d) Diatoms. The plots are colour coded in terms of data density (black to red corresponds with low to high densities)

Unfortunately DOC or a_{CDOM} proxy data from the flow-through system was collected; however a_{CDOM} retrievals varied from near-zero to approximately 3 m^{-1}; within the range encountered during the discrete sampling presented in Chapter 3.4.

The best overall algorithm was selected by firstly considering the RMSE of the TChl retrievals, and then also considering the data retention %. Algorithm perfomance data is shown in Table 4.6. Table 4.6 shows the most accurate TChl came from the 4-Mixture, Real-modelled a_{CDOM}, Standard b_{bp} and freely-varying a_{NAP} algorithm, yielding a TChl RMSE of 26.6% for the entire dataset. The best performing algorithm for b_{bp} retrieval had an RMSE of 16.5%, however the approach that the best TChl was only marginally worse performing with an RMSE of 17.2%, so the 4-Mixture, Real-modelled a_{CDOM}, Standard b_{bp} approach is con-

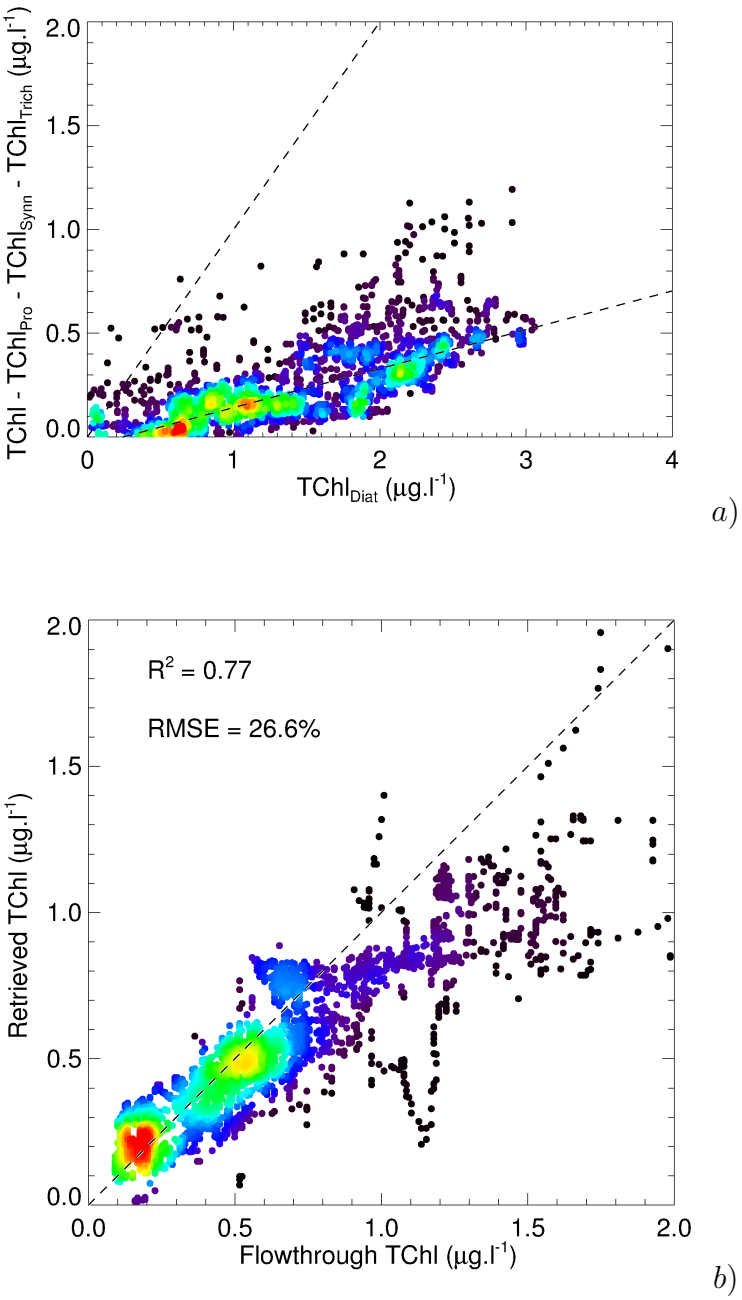

Figure 4.35: a) The residual TChl vs $TChl_{Diat}$ for the 4-Mixture, Real a_{CDOM} basis vector inversion variant. The dashed line is the 1:1 line. The plots are colour coded in terms of data density (black to red corresponds with low to high densities). The solid line is the median slope of the dataset. b) An example of the corrected optimised weights (Eq. 4.2) retrieved $TChl$ vs flow-through $TChl$ comparison for the *in situ*-derived 4-Mix, Real a_{CDOM} basis vector variant. The data shown here is the $TChl_{Diat}$ corrected equivalent of Fig. 4.33. The dashed line is the 1:1 line. The plots are colour coded the same as for a).

a_ϕ model	b_{bp} model	a_{NAP} type	**B-95 TChl** RMSE	R^2	A	B	**Mix TChl** RMSE	R^2	Offset	Slope	Valid %	**TSS** RMSE	R^2	Offset	Slope
2-Mix	Blend	Free	267.	0.03	0.036	0.183	49.4	0.00	0.023	0.173	98.5	17.8	0.89	0.678	75.48
2-Mix	Std	Free	210.	0.04	0.038	0.208	47.6	0.00	0.031	0.169	99.0	17.8	0.89	0.698	72.56
2-Mix	Emp	Free	7.73	0.00	0.026	0.048	76.1	0.00	0.384	0.039	91.8	20.1	0.84	0.647	91.11
4-Mix	Blend	Free	**32.3**	**0.56**	0.064	0.514	**27.1**	**0.75**	**-0.04**	**0.191**	**100**	**17.0**	**0.91**	**0.665**	**76.68**
4-Mix	Std	Free	**32.3**	**0.58**	0.066	0.536	**26.6**	**0.77**	**-0.04**	**0.187**	**100**	**17.2**	**0.91**	**0.679**	**74.55**
4-Mix	Emp	Free	40.3	0.48	0.093	0.696	49.2	0.56	-0.04	0.204	100	18.6	0.87	0.670	79.57
B-95	Blend	Free	80.0	0.39	0.045	0.472	n.a.	n.a.	n.a.	n.a.	99.9	16.5	0.92	0.687	74.32
B-95	Std	Free	71.5	0.43	0.048	0.521	n.a.	n.a.	n.a.	n.a.	100	16.6	0.91	0.707	72.18
B-95	Emp	Free	37.8	0.69	0.071	0.611	n.a.	n.a.	n.a.	n.a.	99.9	17.7	0.90	0.699	78.52
Lee	Blend	Free	55.5	0.36	0.049	0.509	n.a.	n.a.	n.a.	n.a.	99.6	16.9	0.91	0.677	75.22
Lee	Std	Free	50.5	0.39	0.051	0.550	n.a.	n.a.	n.a.	n.a.	99.8	17.0	0.91	0.696	72.95
Lee	Emp	Free	36.0	0.49	0.091	0.768	n.a.	n.a.	n.a.	n.a.	100	18.8	0.90	0.687	79.11
Pack	Blend	Free	83.1	0.30	0.039	0.322	n.a.	n.a.	n.a.	n.a.	96.5	16.7	0.90	0.689	74.20
Pack	Std	Free	61.1	0.43	0.043	0.381	n.a.	n.a.	n.a.	n.a.	99.8	16.9	0.90	0.706	72.55
Pack	Emp	Free	51.7	0.50	0.049	0.411	n.a.	n.a.	n.a.	n.a.	100	17.5	0.88	0.697	78.83
QAA	n.a.	n.a.	38.6	0.35	0.062	0.531	n.a.	n.a.	n.a.	n.a.	96.8	18.7	0.91	0.628	72.33

Table 4.6: The 15 simultaneous TChl and TSS retrievals and associated tuning parameters. For 2-Mix and 4-Mix algorithms, two different TChl products were available; one is derived from a B-95 model regression with the tuning parameters A and B (Eq. 4.41), and the other uses the fractional TChl contributions (Eq. 4.42), including the slope and offset with which to alter $a^*_{diat}(442)$. The best-performing $TChl$ techniques are shown in bold. The TChl Valid % shows the percentage of the data which is retained after removing $a_\phi(442) = 0$. n.a. denotes where the information is not applicable.

sidered satisfactory for TSS inversions. The QAA retrieved TChl with an RMSE of 38.6% for 96.8% of the dataset.

4.4 Summary

This Chapter dealt with the application of the DALEC, discrete IOP and the flow-through system data to develop and / or validate a number of R_{rs} inversion approaches. A series of physics-based predictor-corrector inversion techniques were tested, based on different IOP modelling approaches.

- It was shown that for the discrete IOP dataset, the 4-Mixture phytoplankton absorption model yielded the most accurate R_{rs} reconstruction and the most stable $a_{\phi}(442)$ retrievals.
- For the DALEC transect water quality inversions, the most stable inversion came from the 4-Mix, Real a_{CDOM} and Standard b_{bp} approach where the spectral slope (γ) was allow to freely vary. These approaches may provide additional information about phytoplankton functional groups in the GBR.
- The 4-Mix, Std. b_{bp} predictor-corrector TChl RMSE was 32.3% (B-95 tuning) or 26.6% (Tuned 2-Mixture sum), with a coincident TSS retrieval RMSE of 17.2%. In contrast, an empirical TSS algorithm was derived and shown to have a 16.2% RMSE. A GBR-tuned maximum band ratio algorithm was determined and was shown to retrieve TChl with a 23% RMSE. Whilst the RMSE of the physics-based TChl retrieval is higher than the purely empirical MBR approach, it should be noted that the physics-based approach should provide a more reliable image across the whole GBR region, with reduced artifacts due to the presence of confounding in-water constituents and additional information about varying phytoplankton assemblages.
- The fluorescence-based FLH algorithm was shown to be affected by b_{bp}, so is considered unsuitable for TChl inversion in these coastal waters.

Chapter 5

Validation and Application to MODIS

5.1 Introduction

Chapter 4 dealt with the application and tuning of a number of water quality estimation algorithms for use with data collected from the DALEC *in situ* spectroradiometer. The DALEC has been demonstrated to be a useful tool for monitoring surface water quality parameters. Combining the DALEC with a surface water sampling flow-through system significantly adds to the number of data points available for algorithm training or validation, compared with discrete sampling. The knowledge gained from inverting DALEC R_{rs} measurements is also relevant to multi-wavelength ocean colour satellite sensors such as the MODIS. The synoptic and near-daily coverage of the MODIS sensors provides a wealth of ocean colour information for the GBR region, however its performance has not been demonstrated in the turbid, coastal GBR region.

The first step to utilising the MODIS sensor in turbid, coastal waters is to demonstrate the radiometric accuracy of the MODIS reflectance products. MODIS images of turbid coastal regions usually require specialist atmospheric correction procedures because standard operational NASA processing relies on the zero R_{rs} in the NIR bands (748 and 869 nm) (Gordon & Wang 1994). This so-called 'black pixel' condition is generally not met in coastal waters (Siegel et al. 2000)

and specifically not in the GBR. Work by Franz et al. (2006) has suggested the ocean colour community utilise the higher resolution SWIR atmospheric MODIS bands for turbid waters. This extends the applicability of the black pixel assumption because is more likely that hydrosols are invisible due to very high water absorption coefficients in the NIR. The atmospheric correction approach used with MODIS imagery can greatly affect image quality and care must be taken when using the MODIS SWIR bands, as they are not designed to view the ocean and their low signal-to-nose ratios lead to noisy (grainy) images. Wang & Shi (2007) published a method which decides whether the SWIR bands are required for atmospheric correction or not; thus the algorithm is able to shift from the 748 and 869 nm NIR black pixel assumption, out to the 1240 and 2130 nm SWIR bands when appropriate. This approach should ensure that the quality of clear water imagery is maintained whilst the atmospheric correction accuracy of turbid waters within the same scene is improved.

One significant benefit of the DALEC instrument developed in this thesis is that it can be used to validate the choice of atmospheric correction procedures applied to MODIS scenes in a given region. As the DALEC is a transecting device, it can be deployed during a satellite overpass and a number of DALEC spectra can be recorded within one MODIS pixel. The DALEC samples R_{rs} every 3.3 nm in the visible region at approximately 10 nm FWHM (Full Width Half Maximum) spectral resolution. The MODIS R_{rs} products are fixed at certain discrete wavelengths, and most of the bands have spectral resolutions around 10 nm FWHM. Considering the similarity in spectral resolution of the two different sensors, an average DALEC reflectance value can be calculated for comparison with the satellite pixels recorded within the same time-frame. Like all satellite match-up approaches, the quality of this comparison is dependent on the inter-pixel spatial variability encountered and the number of measurements made within one pixel. Considering this, the DALEC sampling approach would seem better suited to coastal waters where large gradients in water quality parameters are often expected.

Although the spectral coverage of MODIS is less than that of the DALEC, the MODIS bands were positioned specifically for extracting information about phytoplankton and CDOM (Sathyendranath 2000). Given the generally smoothly-varying spectral IOP signatures found in GBR waters, direct transfer of DALEC or IOP spectral relationships to MODIS imagery should be possible. Preempting the application of these DALEC-derived relationships to the MODIS sensor, the empirical algorithm coefficients (i.e. Eq. 4.35 and 4.36) were determined specifically for MODIS bands. Additionally, the spectral inversion code (and embedded IOP basis vectors) used to invert the DALEC R_{rs} data was written in such a way that the user simply has to provide the center wavelengths of the input R_{rs} bands. A 10 nm FWHM gaussian convolution of all inversion spectra is performed around these centers. This is also considered satisfactory for application to MODIS within the scope of this thesis work. However, assessing the impact of the spectral band shapes on the output water quality parameter maps is left for refinement in further work.

This study determined five new algorithms which show promise in the GBR region, and these are summarised below:

Name	Algorithm Description	MODIS Bands (nm)	Res (m^2)	RMSE (%)	Ref.
GTSS	Empirical TSS	645	250	16.2	Eq. 4.35
GCHL1	Band Ratio TChl	469, 555	500	22.5	Eq. 4.36
GCHL2	Band Ratio TChl	443, 488, 547	1000	22.7	Eq. 4.36,4.37
GINV	Predictor-corrector Inversion (TChl, TSS and DOC)	all 9 (412 − 748)	1000	25.7, 17.7, 10**	

Table 5.1: Summary of algorithms which show potential in GBR waters, with the associated MODIS spectral bands, the spatial resolution of the bands and the RMSE determined for each algorithm. The GINV RMSE were estimated from the DALEC-based retrievals and are for $TChl$, TSS and DOC (respectively). ** This RMSE is determined from the IOP-coincident dataset only.

In this chapter, data from the DALEC spectroradiometer is used to help choose an appropriate MODIS atmospheric correction method and then vicariously calibrate the MODIS imagery in turbid, coastal waters using a limited *in situ* match-

up dataset. Secondly, the vicariously calibrated MODIS R_{rs} pixel values are then used as input into the empirical and predictor-corrector spectral inversion schemes previously demonstrated with the DALEC data (see Table 5.1).

5.2 Methods

MODIS imagery is able to capture a wide expanse of the Queensland coast, so within one particular scene, a wide variety of water quality (and IOP) conditions should be present. This diversity is most prominent during the wet season where flood plumes are most likely to be present; typically bringing the highest TChl, TSS and DOC concentrations out to the ocean. The DALEC spectroradiometer was deployed daily during all ship operations when winds were less than 15 knots. On the 31^{st} of January 2006, the DALEC continuously measured the changing reflectance from deep water on the outer reef, towards the turbid waters of Magnetic Island, near Townsville. During this transect at approximately 1:50 pm local time, the MODIS Aqua sensor recorded multispectral imagery over the area which allows a comparison between *in situ* DALEC and MODIS R_{rs}. It should be noted that the MODIS image was recorded within a few minutes, whereas DALEC data was recorded within a time window approximately 2 hours before and after the MODIS image collection. Unfortunately, the only turbid-water MODIS matchup scene suffers from pixel saturation, sun glint, light clouds and thin trichodesmium further offshore. A true colour representation of the "match-up" scene is shown in Figure 5.1. Fortunately, there is still usable data from the MODIS image.

5.2.1 Atmospheric Correction / Validation

SEADAS (OBPG 2011) processing software was used to perform a variety of atmospheric corrections to produce a series of MODIS R_{rs} images for the 31^{st} of January 2006 match-up. All image variants were left uncorrected for the Bidirectional Reflectance Distribution Function (BRDF) (brdf_opt=0). In addition to

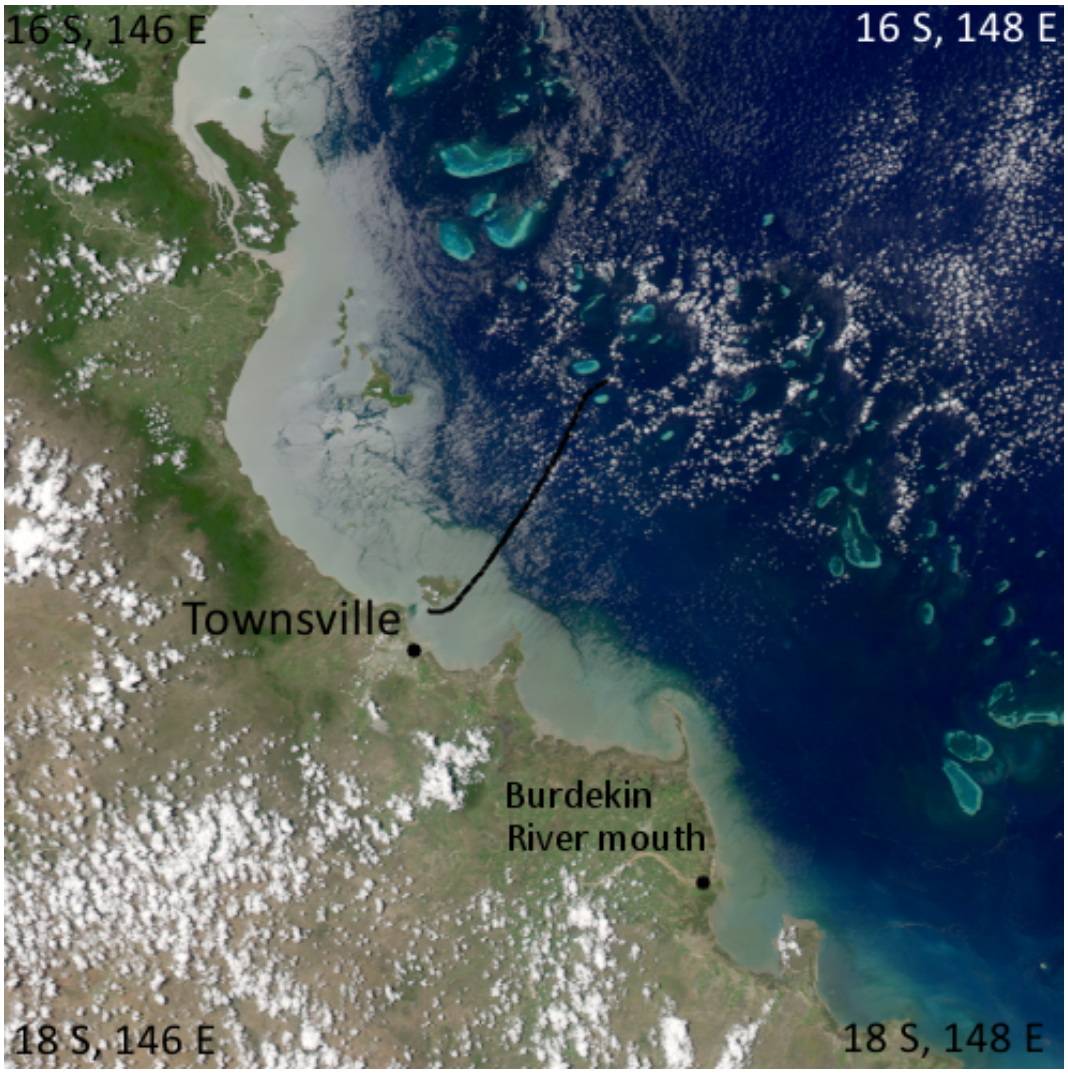

Figure 5.1: MODIS pseudo true colour image recorded on the 31^{st} of January 2006. The approximate ship track from where DALEC measurements were made is shown with a black line. The transect started near the top centre of the image and ended near Townsville. Thin, white cloud is seen offshore over the reef matrix. Moderate glint is apparent in some offshore pixels and appears grey in colour. High glint is apparent in the turbid inshore waters near the coast, and particularly to the North of Townsville.

the R_{rs} product, wind speed, sun and sensor azimuth and zenith geometry products were also generated to provide input to the spectral BRDF lookup table developed in Chapter 3. Flagged pixels were included in the processing (maskland=0, maskbath=0, maskcloud=0 ,maskglint=0, maskhilt=0, maskstlight=0 and filter_opt=0). Pixels were later screened to remove areas where absorbing aerosols (ABSAER), atmospheric correction failure (MAXAERITER or ATMFAIL), cloud or ice (CLDICE) or trichodesmium (TRICHO) was detected. All processing included gas_opt=15, which denotes atmospheric correction for Ozone, CO2, NO2 and H2O. Both glint_opt=0 and glint_opt=1 were tested. Table 5.2 shows the SEADAS-specific atmospheric correction parameters trialled on the matchup scene.

5.2.2 Water Quality Algorithms

The R_{rs}-based empirical and inversion algorithms were applied to the atmospherically-corrected MODIS data. The algorithm outputs were then compared to the average flow-through TChl or TSS measurements recorded coincident with each given pixel. Each GINV (predictor-corrector) algorithm variant was tested as done previously in Chapter 4. Previously, it was shown that inversions in inshore waters suffered from poor retrievals when the fractional contribution of the inverted $a_\phi(443)$ to $(a_t(443) - a_w(443))$ was less than between 10 and 20%. This occurs closer to the coast, when total non-water absorption at 443 nm $(a_t(443) - a_w(443))$ reaches above about $0.2m^{-1}$. In these situations, the QAA initialisation of $a_\phi(443)$ could have large errors. Considering that the MODIS-based empirical GTSS, GCHL2 and GCHL2.1 outputs are shown to perform acceptably in the matchup scene, these may be able to also assist in intialising the GINV inversion approach. To test whether the initialisation parameters in Table 4.2 influenced the inversion results, 3 different initialisations were tested on the vicariously calibrated MODIS R_{rs} dataset. The first was using fixed values of $TSS = 2.0mgl^{-1}$, $TChl = 2.0\mu g^{-1}$, $a_\phi(443) = 0.06m^{-1}$, $a_{CDOM}(443) = 0.06m^{-1}$ and $a_{NAP}(443) = 0.06m^{-1}$ and $b_{bp}(555) = 0.015m^{-1}$. The second was based on the empirical MODIS TChl and TSS algorithms (and IOP models). The empirical intitialiser used the GCHL2.1 algorithm for TChl, $a_\phi(443) = 0.044TChl^{0.37}$

Reference	Type	aer opt	aer wave short (nm)	aer wave long (nm)	other parameters
Gordon & Wang (1994)	Fixed Maritime 90% RH	4	859	1240	-
	Fixed Maritime 99% RH	5	859	1240	-
	Fixed Coastal 70% RH	7	859	1240	-
	Fixed Coastal 90% RH	8	859	1240	-
	Fixed Coastal 99% RH	9	859	1240	-
	2-band	-1	748	869	-
	2-band	-1	859	1240	-
	2-band	-1	1240	2130	-
Gordon & Wang (1994) Bailey et al. (2010)	2-band, NIR	-3	748	869	-
	2-band, NIR	-3	859	1240	-
	2-band, NIR	-3	1240	2130	-
Ziauddin et al. (2010)	Fixed Pair	-4	859	1240	40,79,1
	Fixed Pair	-4	859	1240	40,79,0.5
	Fixed Pair	-4	1240	2130	40,79,1
	Fixed Pair	-4	1240	2130	40,79,0.5
Ziauddin et al. (2010) Bailey et al. (2010)	2-band RH, NIR	-2	748	869	-
	2-band RH, NIR	-2	859	1240	-
	2-band RH, NIR	-2	1240	2130	-
	Fixed Pair, NIR	-5	859	1240	40,79,1
	Fixed Pair, NIR	-5	859	1240	40,79,0.5
	Fixed Pair, NIR	-5	1240	2130	40,79,1
	Fixed Pair, NIR	-5	1240	2130	40,79,0.5
Ruddick et al. (2000)	MUMM	-10	1240	2130	α=default
		-10	859	1240	α=default
		-10	748	869	α =default
		-10	1240	2130	$\alpha = 21.8$
		-10	859	1240	$\alpha = 26.0$
		-10	748	869	$\alpha = 1.67$
Wang & Shi (2007)	2-band, SWIR	-9	748	869	(1240,2130)
	2-band, SWIR	-9	859	1240	(1240,2130)
	2-band, SWIR	-9	1240	2130	-

Table 5.2: SEADAS atmospheric correction parameters used on the matchup image. The three numbers in the last column for Fixed Pair models refer to the aeromodmin, aeromodmax and aermodrat parameters (respectively). The constrained models correspond to relative humidities between 80 and 95 percent (model name r80f95v01 to r95f00v01, respectively). (OBPG 2011).

(see Fig. 2.18c), the GTSS algorithm for TSS, Eq. 2.53 to initialise $b_{bp}(555)$, Eq. 4.33 to initialise $a_{NAP}(443)$ and $a_{CDOM}(443) = \frac{[TChl]}{MK}$, where M is 1.569 from Eq. 4.28 and $K = 8$ is estimated from the slope of the data in Fig. 4.25. The third initialisation model was the QAA approache as used on the DALEC R_{rs} and described in Table 4.2.

5.3 Results

5.3.1 Atmospheric Correction / Validation

Figure 5.2a and b shows the DALEC $R_{rs}(412)$ matchup time series and the corresponding MODIS pixel values processed with the current default SEADAS atmospheric correction procedure, without (a) and with (b) residual glint correction (glint_opt). The glint_opt=0 setting compares better with the DALEC data recorded between 10:30 and 12:30 (clear, mid-lagoon waters), however in moderately turbid waters, the glint_opt=1 setting yields a better fit. Although DALEC data was available from 14:00 to 15:00 the corresponding MODIS pixels were flagged due to saturated bands (both 748 nm and 869 nm were saturated). In an attempt to avoid saturated bands, the model selection wavelength pair (aer_wave_short and aer_wave_long) was shifted to 859 nm and 1240 nm, however the $R_{rs}(412)$ retrievals are less consistent (see Fig. 5.2c and d). It is likely that these wavelengths suffer from reduced signal to noise, and so transfer the errors via the atmospheric correction onto the resultant $R_{rs}(412)$ product. Furthermore, the 859 nm and 1240 nm pair still do not yield any pixel information from 14:00 to 15:00. It is possible that the aer_opt=-2 relies on one of the saturated bands for another part of the processing chain, limiting its application in the turbid waters of this matchup scene.

Figures 5.3 and 5.4 show results as in 5.2, however with the aer_opt=-3 and aer_opt=-1 settings (respectively). These approaches use the older and reduced set of atmospheric models in the model selection. There are minor differences in the the $R_{rs}(412)$ retrievals, although it appears that the aer_opt=-2 and aer_opt=-3 approaches remove more pixels in turbid waters, whereas the aer_opt=-1 shows slightly negative $R_{rs}(412)$ values in the same areas ($\approx -0.002sr^1$ from 14:00 to

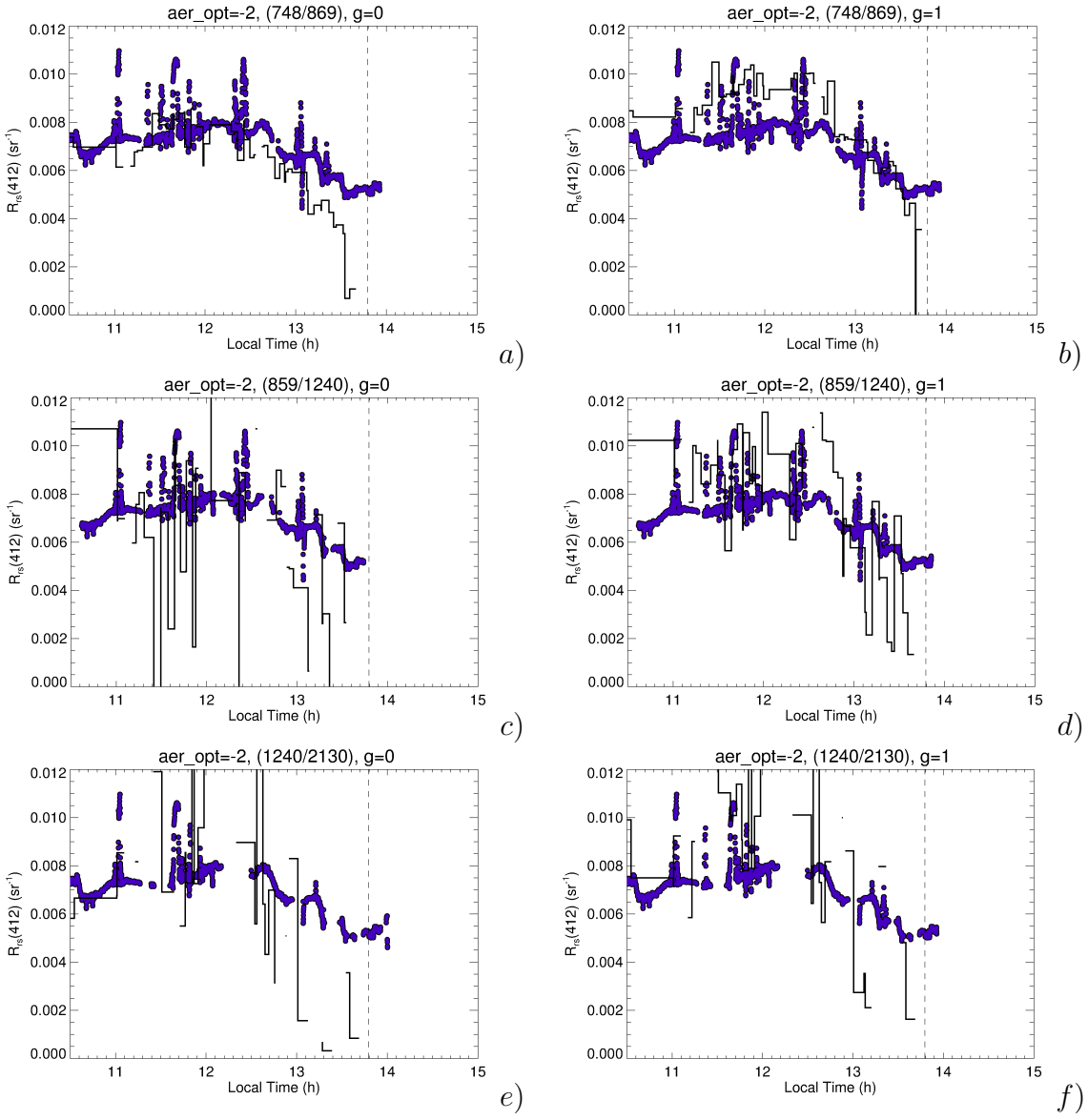

Figure 5.2: DALEC $R_{rs}(412)$ transect time series (circular plot symbols) and corresponding MODIS overpass pixel values (black line) for 6 different SEADAS atmospheric correction variations. The aer_opt settings are shown in the title of each plot, along with aer_wave_short and aer_wave_long in parentheses. g denotes the glint_opt setting used during processing.

15:00, negative data not shown).

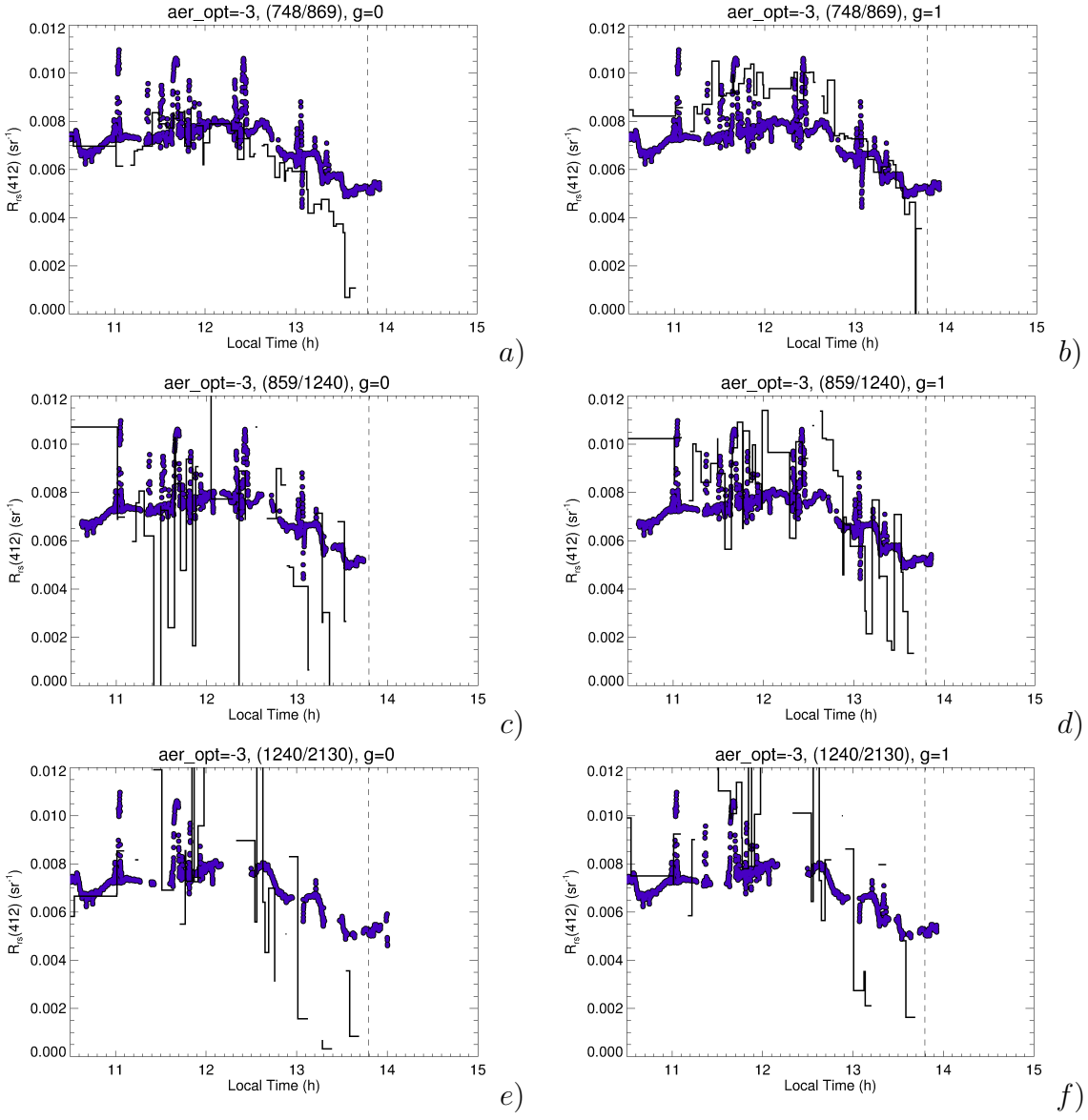

Figure 5.3: DALEC $R_{rs}(412)$ transect time series (circular plot symbols) and corresponding MODIS overpass pixel values (black line) for 6 different SEADAS atmospheric correction variations. The aer_opt settings are shown in the title of each plot, along with aer_wave_short and aer_wave_long in parentheses. g denotes the glint_opt setting used during processing.

All aforementioned approaches (aer_opt=-1, -2 and -3) use two NIR bands to estimate both the aerosol contribution and the spectral nature of the aerosol contribution (see Table 5.2 for the wavelength bands tested). If one or both of the NIR bands is saturated, then the atmospheric correction model selection is likely to fail, resulting in the loss of R_{rs} information in the turbid waters of the matchup scene. Interestingly, even when aer_wave_short and aer_wave_long are

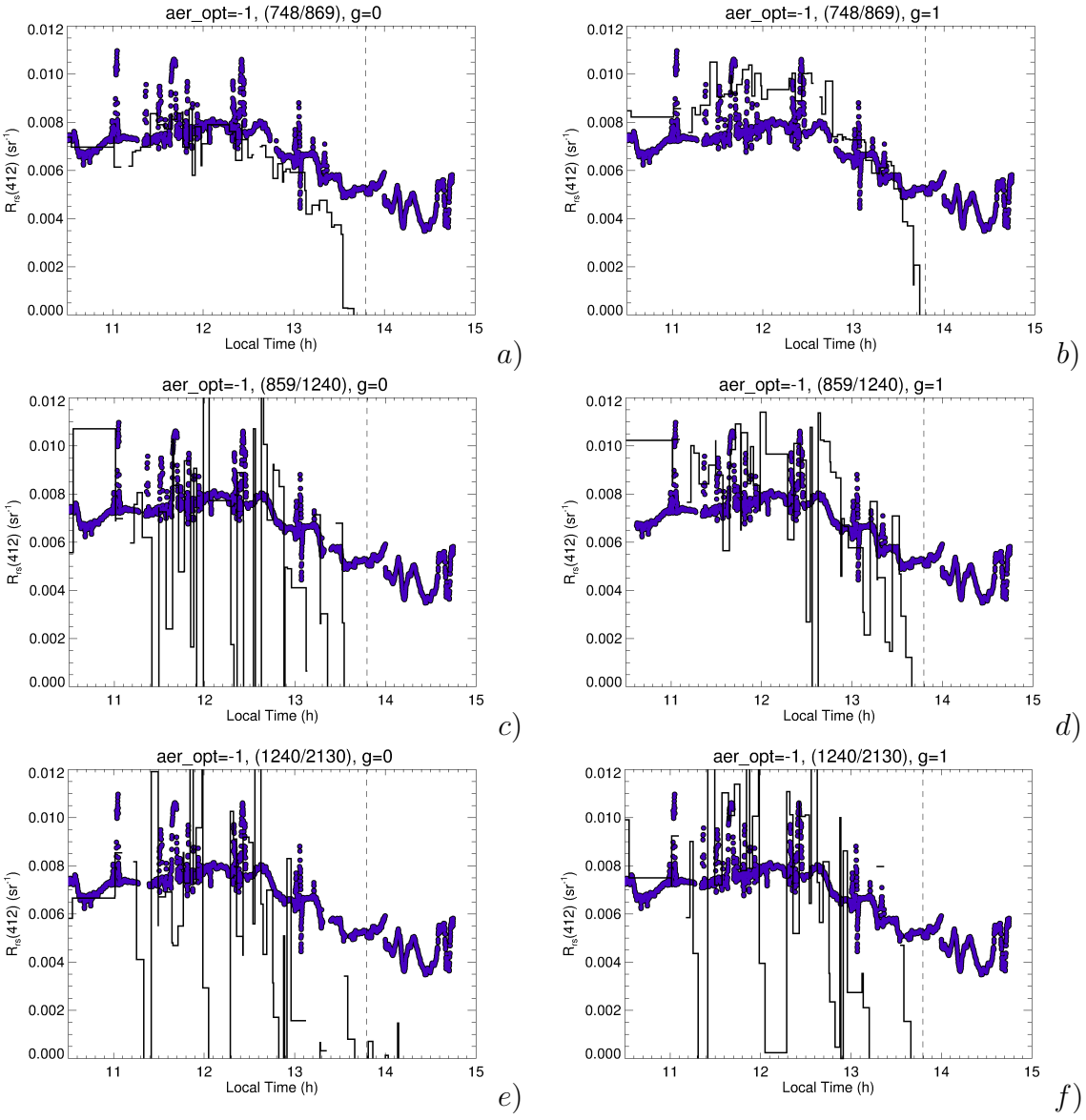

Figure 5.4: DALEC $R_{rs}(412)$ transect time series (circular plot symbols) and corresponding MODIS overpass pixel values (black line) for 6 different SEADAS atmospheric correction variations. The aer_opt settings are shown in the title of each plot, along with aer_wave_short and aer_wave_long in parentheses. g denotes the glint_opt setting used during processing.

set to bands that are not saturated, SEADAS still yields spurious data (i.e. bad data from 14:00 to 15:00 in the lower plots c and d from Figure 5.2 to 5.4). In an attempt to circumvent this issue, a select few matchups were made using constrained aerosol models and non-saturated aer_wave_short and aer_wave_long combinations (859 nm and 1240 nm). First, five different fixed models were chosen (aer_opt=4, 5, 7, 8 and 9); corresponding to the older Maritime 90%, Maritime 99%, Coastal 70%, Coastal 90% and Coastal 99% relative humidity models (Gordon & Wang 1994). The Maritime atmosphere model-based time series are shown in Fig. 5.5, and the Coastal atmosphere model results are shown in Fig. 5.6. From these results, it can be seen that the Fixed Coastal model atmospheric correction approaches yield reasonable or at least non-zero $R_{rs}(412)$ values for this matchup. It is not clear whether the NIR correction approach of Bailey et al. (2010) or the Gordon & Wang (1994) model selection approach is causing invalid turbid water pixels.

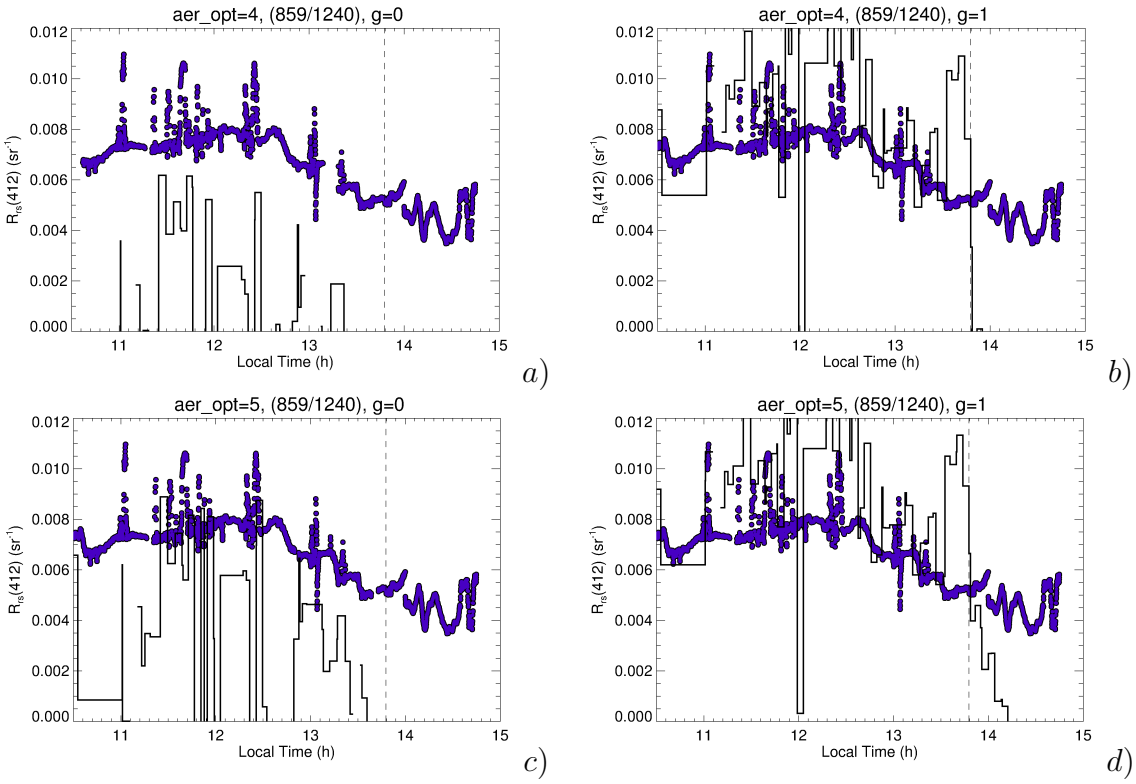

Figure 5.5: DALEC $R_{rs}(412)$ transect time series (circular plot symbols) and corresponding MODIS overpass pixel values (black line) for 4 different SEADAS atmospheric correction variations. The aer_opt settings are shown in the title of each plot, along with aer_wave_short and aer_wave_long in parentheses. g denotes the glint_opt setting used during processing.

By introducing a constrained Fixed Pair model selection based on the models of Ziauddin et al. (2010) with and without the NIR correction (Figs. 5.7 and 5.8), it can be seen that the NIR correction does not produce valid data. In these situations, is may be more appropriate to fix an aerosol model and not perform the Bailey et al. (2010) NIR correction. It also appears as though the 1240/2130 wavelength-based model selection is more accurate in the most turbid waters compared with 859/1240. This is because the ocean is more 'black' in longer wavelength regions.

The Wang & Shi (2007) atmospheric correction approach utilizes the concept of the black pixel similar to Gordon & Wang (1994), however the algorithm assesses a "turbidity index" (based on Top-of-Atmosphere reflectance measurements at 748 nm and 1240 nm (Shi & Wang 2007)) and switches the model selection bands from the NIR to SWIR (Short-Wave InfraRed) pairs to achieve the darkest ocean pixels possible for model selection in turbid waters. This ensures that the SWIR bands, which are generally more grainy in appearance due to lower signal to noise ratios on the detectors are only used when it is necessary to do so. The Wang & Shi (2007) approach appears to work satisfactorily for clearer waters (ie using the standard 748/869 bands), however also breaks down in turbid waters (See Fig. 5.9). It is possible that if either the 748 nm or 869 nm band is used for calculating the model selection in SEADAS, when these reach near saturation, the turbidity index may provide spurious results which can effect when or if the model selection bands shift from the NIR to SWIR.

A final turbid water atmospheric correction approach was tested on the matchup data. The approach of Ruddick et al. (2000) was used. This approach using the 1240 and 2130nm bands yielded accurate $R_{rs}(412)$ values in the turbid, glint-effected pixels, as opposed to many of the other atmospheric correction combinations.

From the time series matchup comparisons, it is clear that there are differences between glint and non-glint corrected MODIS R_{rs} values for a given atmospheric correction approach, and for some, setting glint_opt=1 often lead to artifacts in the $R_{rs}(412)$ data. As the DALEC measurements were glint-corrected using Eq.

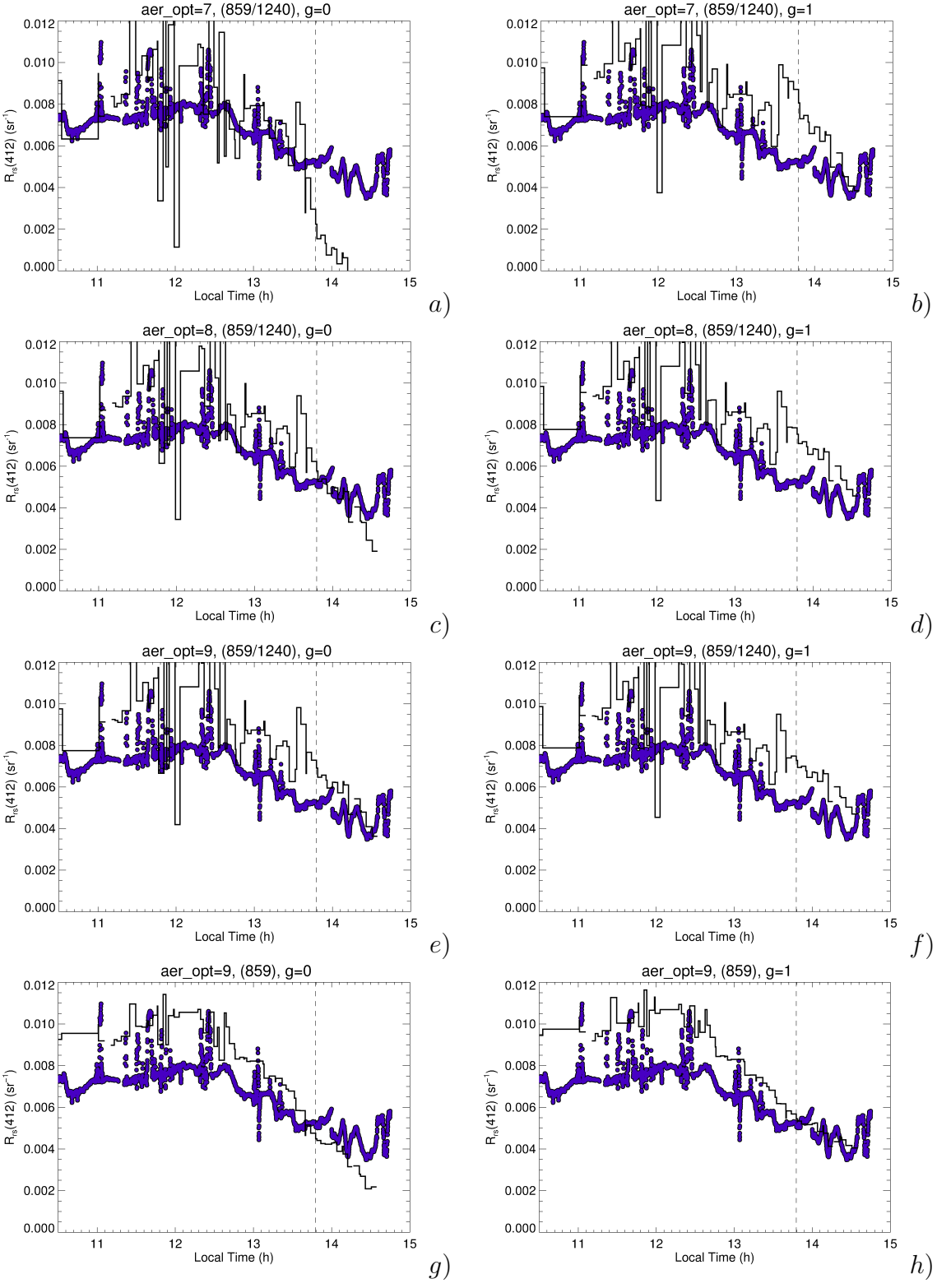

Figure 5.6: DALEC $R_{rs}(412)$ transect time series (circular plot symbols) and corresponding MODIS overpass pixel values (black line) for 6 different SEADAS atmospheric correction variations. The aer_opt settings are shown in the title of each plot, along with aer_wave_short and aer_wave_long in parentheses. g denotes the glint_opt setting used during processing.

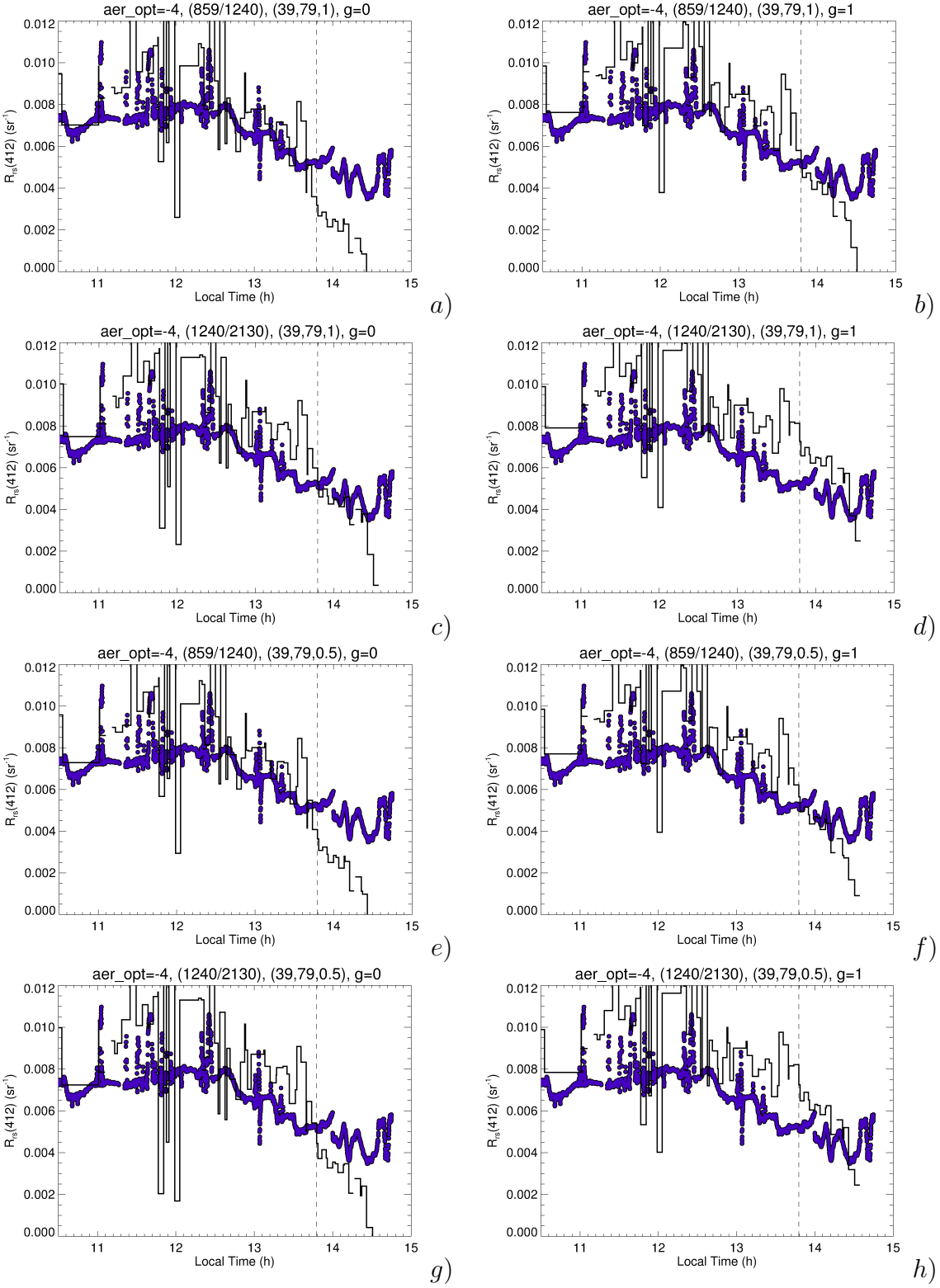

Figure 5.7: DALEC $R_{rs}(412)$ transect time series (circular plot symbols) and corresponding MODIS overpass pixel values (black line) for 6 different SEADAS atmospheric correction variations. The aer_opt settings are shown in the title of each plot, along with aer_wave_short and aer_wave_long in parentheses. g denotes the glint_opt setting used during processing.

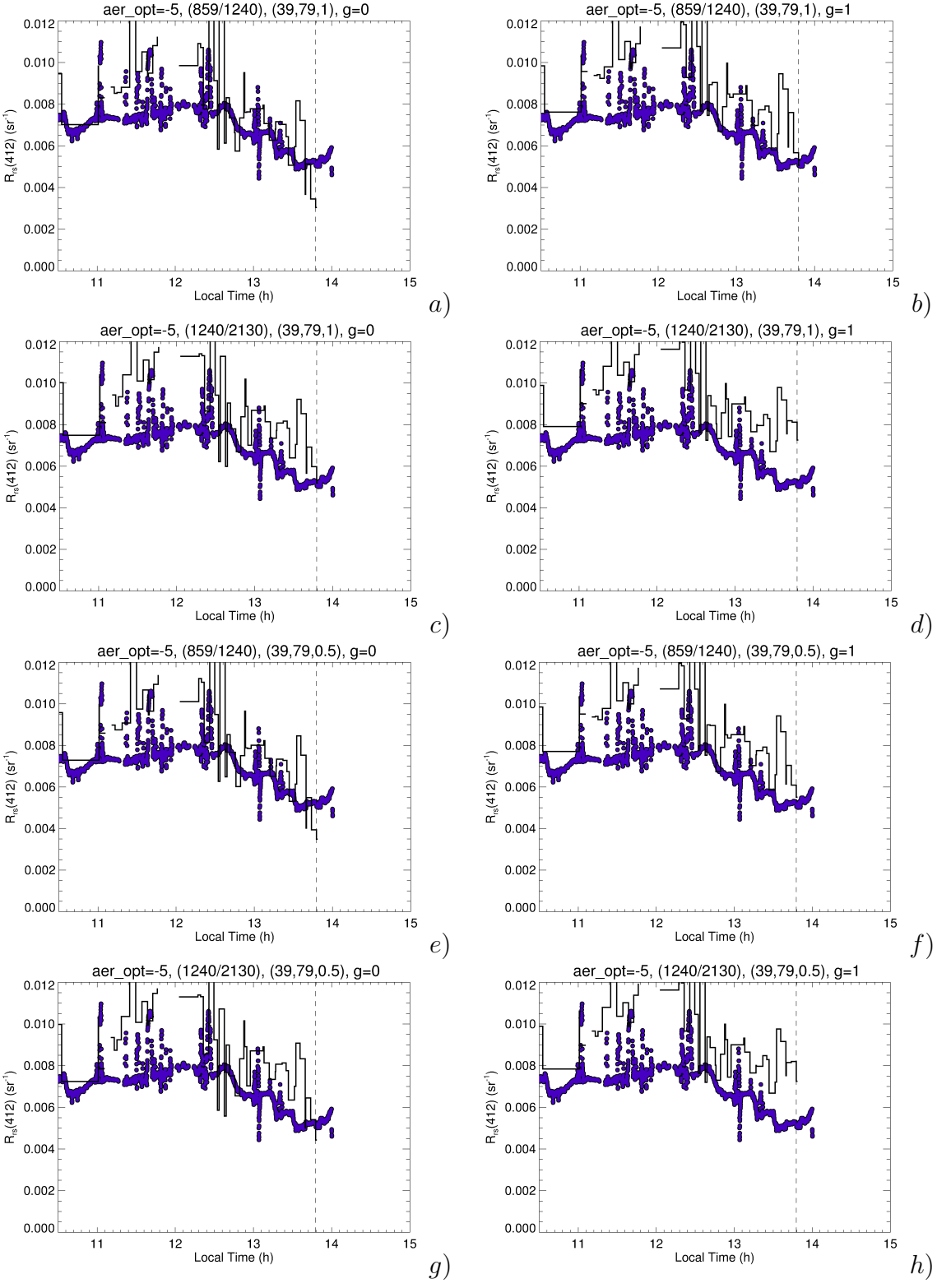

Figure 5.8: DALEC $R_{rs}(412)$ transect time series (circular plot symbols) and corresponding MODIS overpass pixel values (black line) for 6 different SEADAS atmospheric correction variations. The aer_opt settings are shown in the title of each plot, along with aer_wave_short and aer_wave_long in parentheses. g denotes the glint_opt setting used during processing.

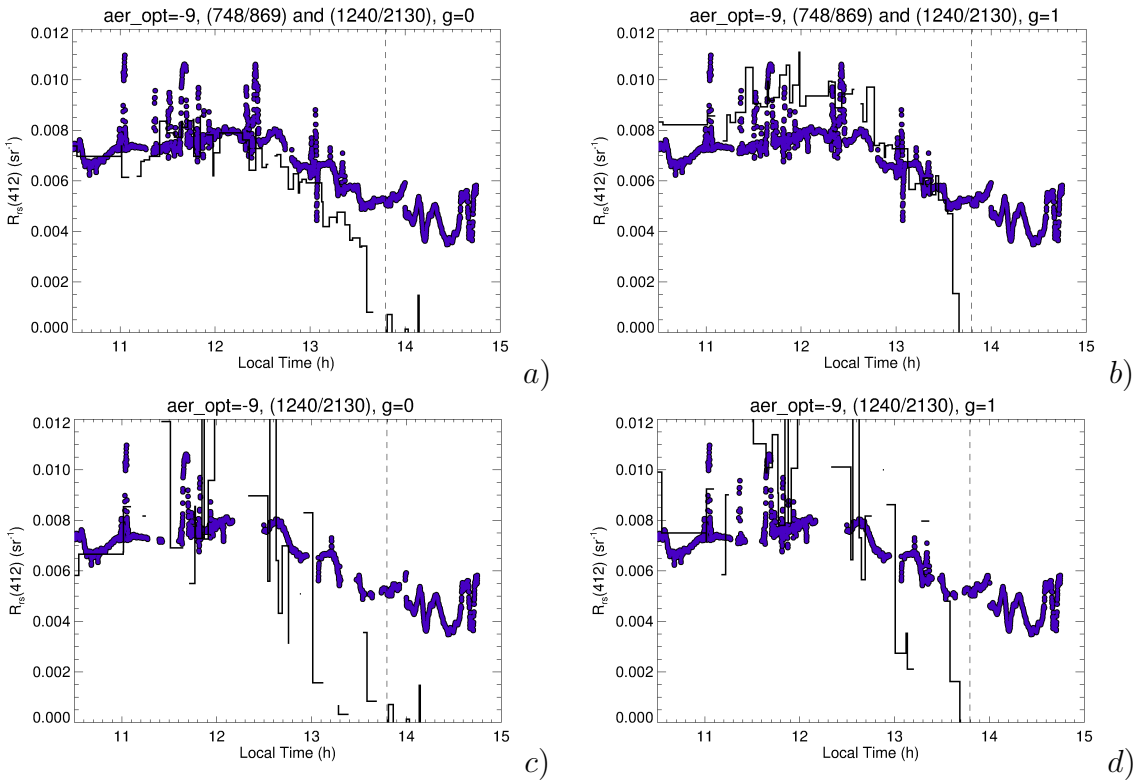

Figure 5.9: DALEC $R_{rs}(412)$ transect time series (circular plot symbols) and corresponding MODIS overpass pixel values (black line) for 4 different SEADAS atmospheric correction variations. The aer_opt settings are shown in the title of each plot, along with aer_wave_short and aer_wave_long in parentheses. g denotes the glint_opt setting used during processing.

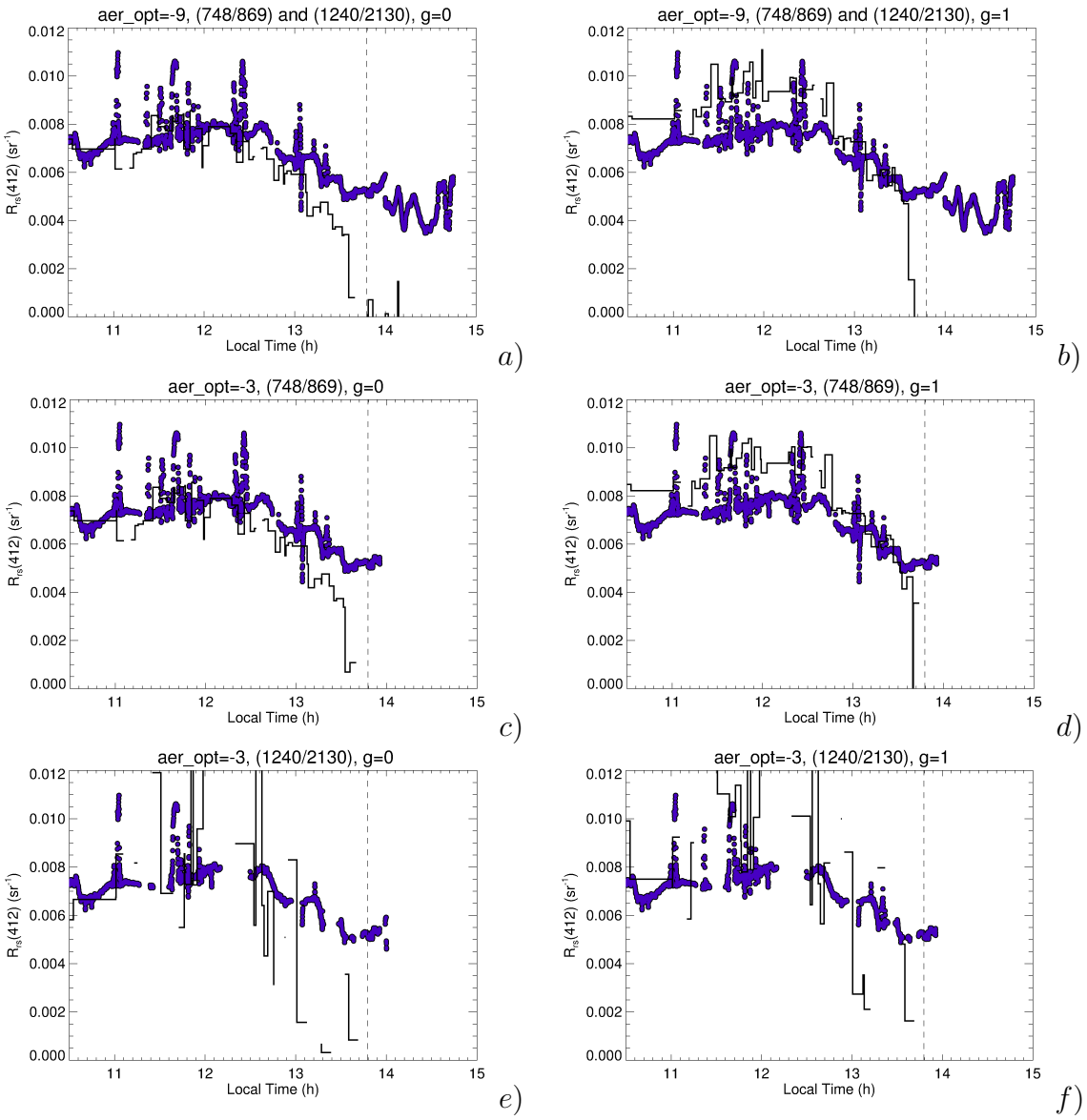

Figure 5.10: DALEC $R_{rs}(412)$ transect time series (circular plot symbols) and corresponding MODIS overpass pixel values (black line) for 6 different SEADAS atmospheric correction variations. The aer_opt settings are shown in the title of each plot, along with aer_wave_short and aer_wave_long in parentheses. g denotes the glint_opt setting used during processing. The first row (a and b) is the Wang & Shi (2007) method. The second row is the standard SEADAS method of Ziauddin et al. (2010), Bailey et al. (2010), which should be identical to the Wang & Shi (2007) method in low-turbidity waters. The last row is the standard SEADAS method of Ziauddin et al. (2010), Bailey et al. (2010), with the model selection bands shifted to (1240/2130).

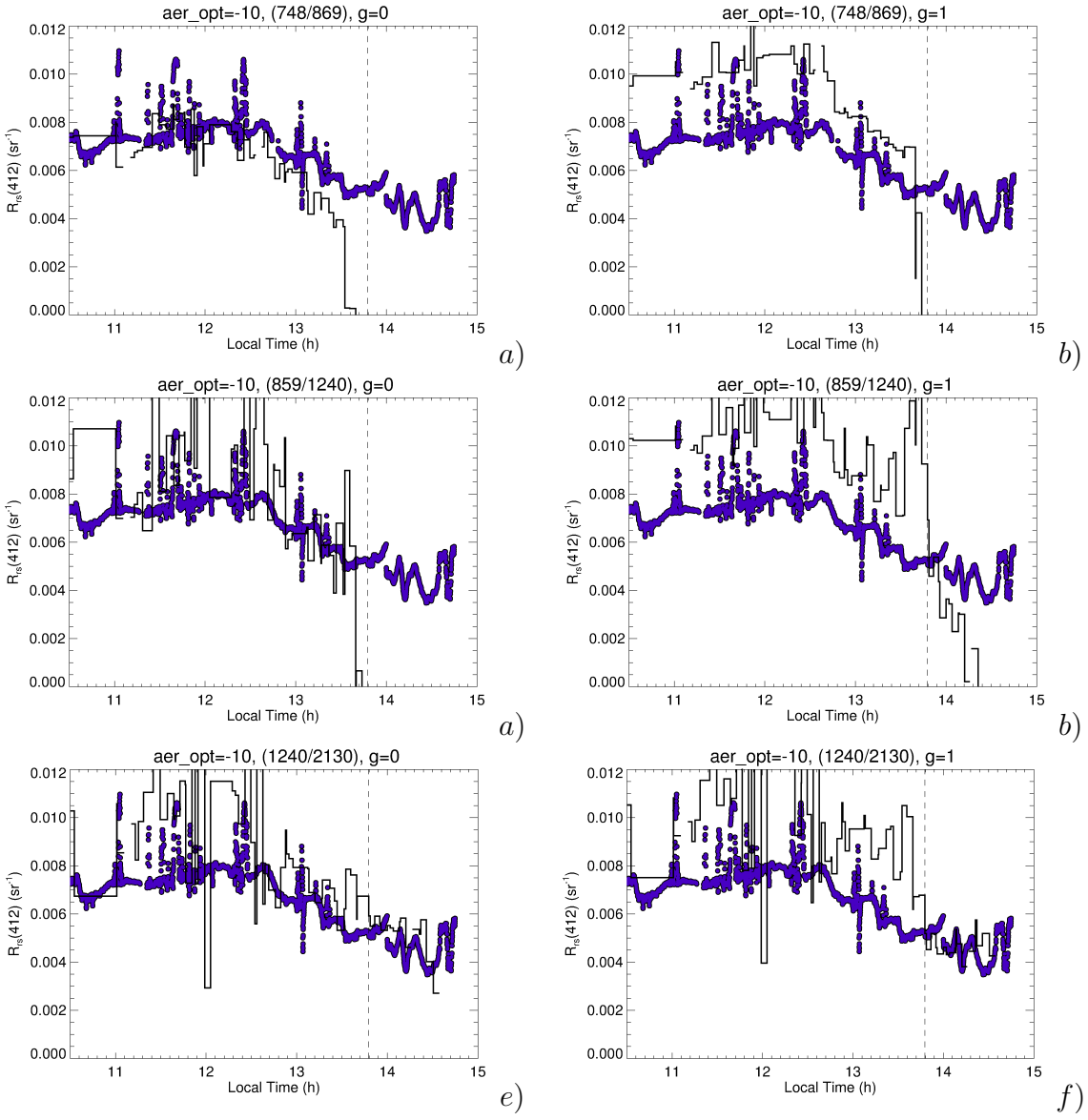

Figure 5.11: DALEC $R_{rs}(412)$ transect time series (circular plot symbols) and corresponding MODIS overpass pixel values (black line) for 4 different SEADAS atmospheric correction variations. The aer_opt settings are shown in the title of each plot, along with aer_wave_short and aer_wave_long in parentheses. g denotes the glint_opt setting used during processing.

3.21, it is considered appropriate to investigate manually applying residual glint correction to the MODIS data prior to further comparison. For every MODIS spectrum, ϵ was calculated by fitting Eq. 3.21 to the MODIS spectrum, and then subtracted from the entire spectrum. All aforementioned atmospheric correction variants were processed with and without the additional Eq. 3.21 correction. The RMS error of each MODIS reflectance band was calculated by comparison with the DALEC R_{rs} data.

For the atmospheric correction procedures relying on 748 and 869 nm, 16 transect matchups were useable. When the 859, 1240 or 2130 nm bands were utilised, 31 transect matchups were usable (except for bands 547, 667 and 678, which saturated in 15 of the 31 co-incident pixels). Table 5.3 lists the best performing atmospheric correction methods, sorted in order of the average RMS errors of R_{rs} products from 412 to 645 nm. Although the standard processing methods yielded low RMS errors, these techniques used the 869 nm band, which saturated in the turbid inshore waters. The best performing atmospheric correction approach yielding all 31 pixels was the Fixed Coastal 99% RH model (aer_opt=9), with residual glint correction, and the additional ϵ correction was not applied.

Figures 5.12 and 5.13 show the time series of the 1km resolution MODIS bands, along with the ϵ corrected MODIS data and co-incident DALEC data. The same information is conveyed in the scatter plots in Figs. 5.15 and 5.16, however 3 pixels were removed from analysis due to large fluctuations in the DALEC data within these pixels. The RMS errors of each wavelength, along with other regression parameters are presented in Table 5.4. The level of agreement between MODIS and DALEC is encouraging, however not ideal. It is likely that there is an issue with the atmospheric correction of the MODIS data for this particular matchup. Considering the DALEC sea-level measurements are available, these measurements were used to vicariously calibrate the MODIS pixel values so that empirical algorithms based on DALEC measurements can be applied to the matchup MODIS scene. These slope and offset coefficients are provided in Table 5.4.

The empirical GTSS and GCHL1 products were processed with the fixed aerosol model (Coastal 99% relative humidity), with either 859 or (859/1240) nm bands

RMS $R_{rs}(412)$	RMS $R_{rs}(\lambda)$	N	glint opt	ϵ?	Type	aer opt	aer wave short (nm)	aer wave long (nm)	other parameters
16.2	20.9	16	1	no	2-band RH, NIR	-2	748	869	-
16.2	20.9	16	1	no	2-band, NIR	-3	748	869	-
17.7	31.2	16	0	yes	Fixed Pair	-5	859	1240	40,79,1
18.8	20.6	16	1	yes	2-band RH, NIR	-2	748	869	-
18.8	20.6	16	1	yes	2-band, NIR	-3	748	869	-
19.1	21.6	16	1	no	2-band	-1	748	869	-
19.2	21.7	16	1	no	MUMM	-10	748	869	$\alpha = 1.67$
19.2	34.6	16	0	yes	Fixed Pair	-5	859	1240	40,79,0.5
19.8	**26.7**	**28**	**1**	**no**	**Fixed Coastal 99% RH**	**9**	**859**	**859**	**-**
21.2	51.4	16	1	yes	MUMM	-10	748	869	$\alpha = 1.67$
22.3	28.7	28	1	yes	Fixed Coastal 99% RH	9	859	859	-
22.9	26.2	16	1	yes	2-band	-1	748	869	-
22.9	17.5	16	0	yes	2-band RH, NIR	-2	748	869	-
22.9	17.5	16	0	yes	2-band, NIR	-3	748	869	-
23.3	22.4	16	0	yes	Fixed Pair	-5	1240	2130	40,79,1
23.5	16.1	16	0	yes	2-band	-1	748	869	-
23.5	23.8	16	0	yes	Fixed Pair	-5	1240	2130	40,79,0.5
23.9	37.1	16	0	no	Fixed Coastal 99% RH	9	869	869	-
24.5	49.4	16	0	yes	MUMM	-10	748	869	α =default

Table 5.3: The best performing atmospheric correction procedures compared with *in situ* DALEC R_{rs} spectra. The list is sorted in ascending RMS error of $R_{rs}(\lambda)$, where λ denotes wavelengths from 412 to 645 nm. The Fixed Coastal 99% RH model is highlighted because it performs adequately in the turbid and glint effected matchup. ϵ denotes where additional; glint correction was performed (i.e. Eq. 3.21)). See 5.2 for references.

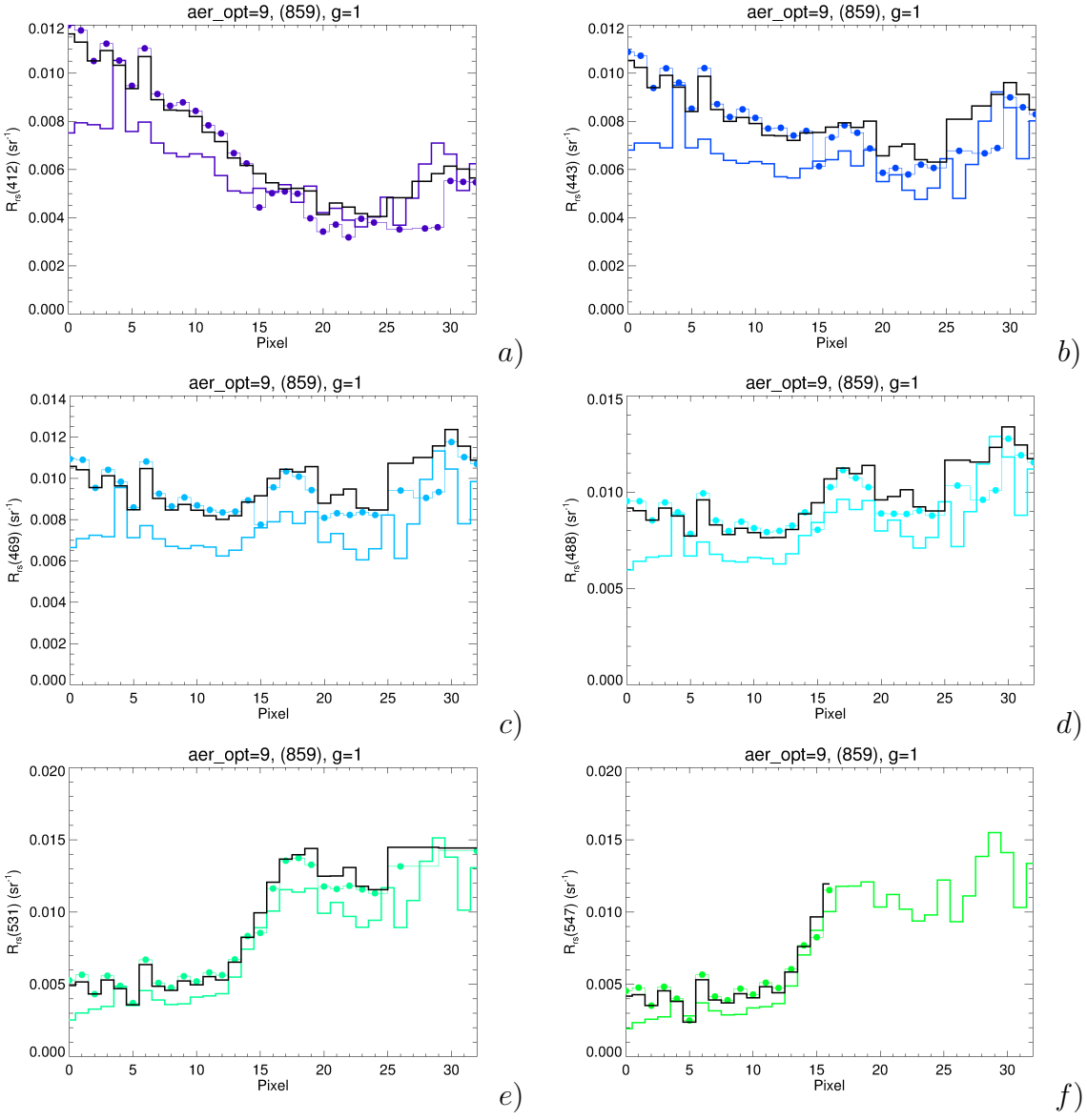

Figure 5.12: DALEC R_{rs} transect pixels and corresponding MODIS overpass pixel values for 6 different wavelengths, with the 99% Relative Humidity Fixed aerosol model (859). The original SEADAS MODIS pixel values are shown in black. The DALEC transect is shown in colour. The additionally glint-corrected MODIS outputs are shown with coloured, circular plot symbols. Note that the 547 nm band saturated from pixel 15 onwards, where excessive glint and elevated turbidity was present.

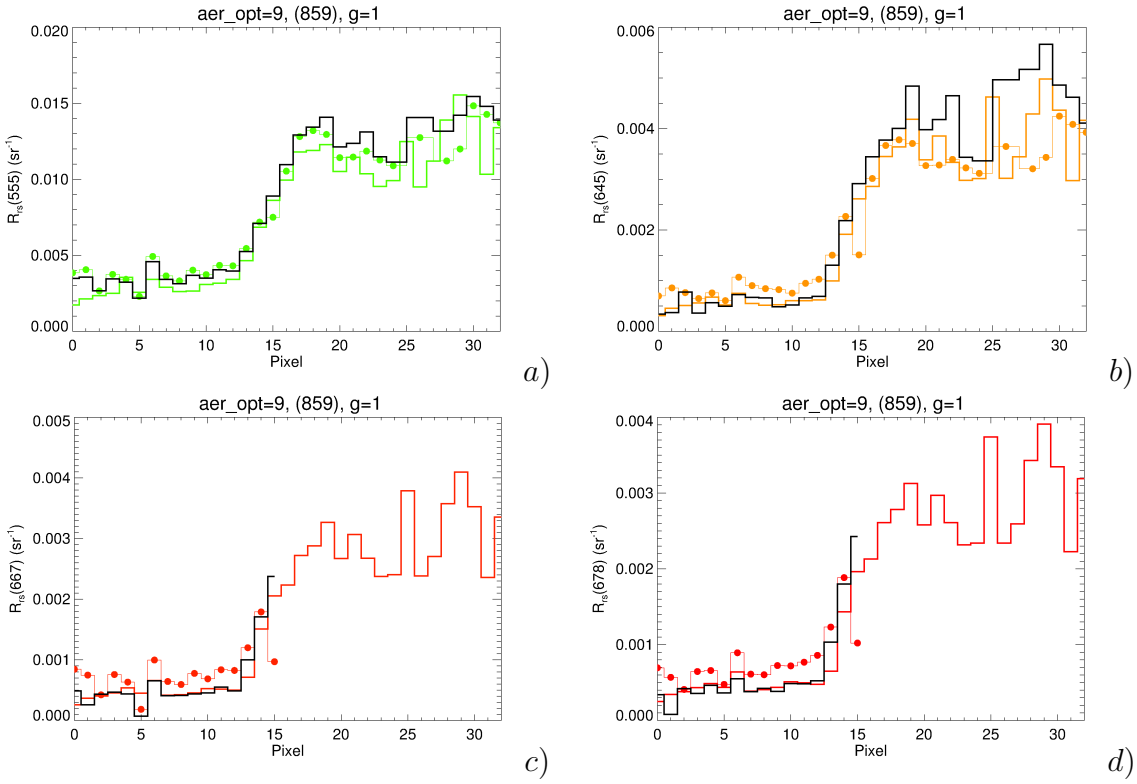

Figure 5.13: DALEC R_{rs} transect pixels and corresponding MODIS overpass pixel values for 4 different wavelengths, with the 99% Relative Humidity Fixed aerosol model (859). The original SEADAS MODIS pixel values are shown in black. The DALEC transect is shown in colour. The additionally glint-corrected MODIS outputs are shown with coloured, circular plot symbols. Note that the 667 and 678 nm bands saturated from pixel 15 onwards, where excessive glint and elevated turbidity was present.

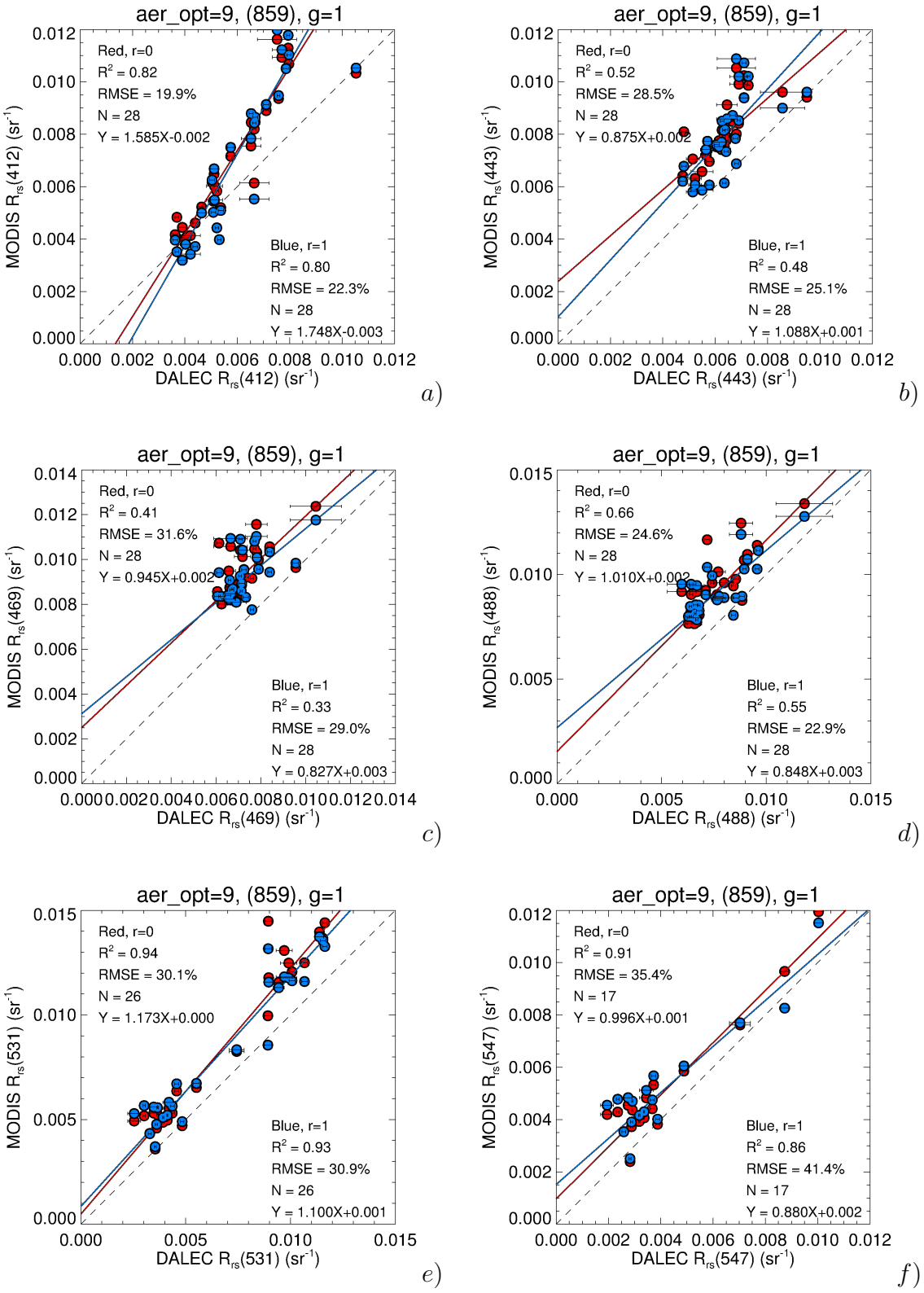

Figure 5.14: DALEC $R_{rs}(412)$ transect pixels v.s. corresponding MODIS overpass pixel values for 6 different wavelengths, with the 99% Relative Humidity Fixed aerosol model (859). The original SEADAS MODIS pixel values are shown with red plot symbols. The additionally glint-corrected ($r = 1$) MODIS outputs are shown with blue plot symbols. Note that the 547 nm band saturated in 15 of the 31 pixels, where excessive glint and elevated turbidity was present.

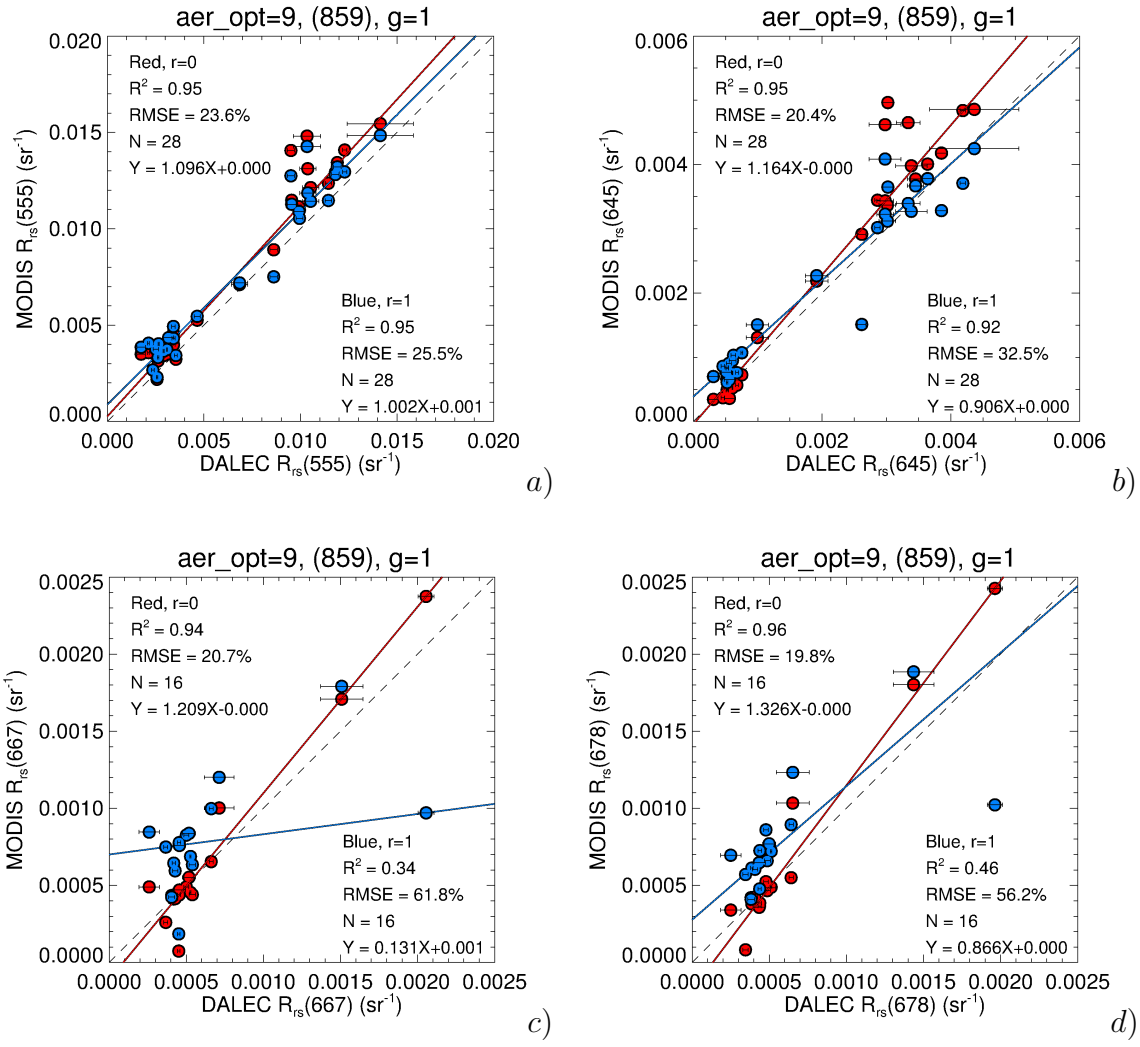

Figure 5.15: DALEC $R_{rs}(412)$ transect pixels v.s. corresponding MODIS overpass pixel values for 4 different wavelengths, with the 99% Relative Humidity Fixed aerosol model (859). The original SEADAS MODIS pixel values are shown with red plot symbols. The additionally glint-corrected ($r = 1$) MODIS outputs are shown with blue plot symbols. Note that the 667 and 678 nm bands saturated in 15 of the 31 pixels, where excessive glint and turbidity was present.

Band (nm)	R^2	RMSE (%)	Offset	Slope
412	0.82	19.9	-0.0021	1.585
443	0.52	28.5	0.0024	0.875
469	0.41	31.6	0.0025	0.945
			(0.0034)	(0.810)
488	0.66	24.6	0.0015	1.010
531	0.94	30.1	0.0005	1.173
547	0.91	35.4	0.0010	0.996
555	0.95	23.6	0.0003	1.096
			(0.0005)	(1.069)
645	0.95	20.4	0.0000	1.164
			(0.0000)	(1.072)
667	0.94	20.7	-0.0001	1.209
678	0.96	19.8	-0.0002	1.326

Table 5.4: Individual Regression Parameters for the matchup between the DALEC and the glint-corrected (g=1), 99% Relative Humidity Fixed aerosol model (859) MODIS pixels for each 1km band wavelength. Coefficients in brackets represent the same regressions but performed on the 500 or 250 m resolution data. Note that when R_{rs} varied less, the correlation coefficient R^2 and the regression slope deviated further from unity. The slopes and offsets are used later as vicarious calibration coefficients for processing the matchup MODIS image.

being used to determine the aerosol concentration. Use of the individual 859 nm band enables a pure 250 m resolution image to help resolve coastal features. Despite 859 nm typically not having non-zero reflectance in turbid waters, errors in the atmospheric correction is minimal at 645 nm, as revealed by the good agreement between the uncorrected MODIS and DALEC in the $R_{rs}(645)$ time series plots in Figs. 5.13b and 5.16e, as well as the near-unity slope and near-zero offsets shown in Table 5.4. These potential errors can be assessed by comparing with the DALEC $R_{rs}(645)$ data, or operationally on a scene-by-scene basis by comparing with the spatially binned 500 m $R_{rs}(645)$ products which utilise the potentially more accurate 869, 1240 or 2130 nm band-based atmospheric correction. Taking this into account, the benefit of having a pure 250 m resolution empirical TSS image may outweigh any drawbacks associated with atmospheric correction errors for certain empirical applications. From comparing the two columns in Fig. 5.16, it can be seen that introducing the 1240 nm band for model selection does not improve the accuracy of the high resolution R_{rs} products for this particular

matchup.

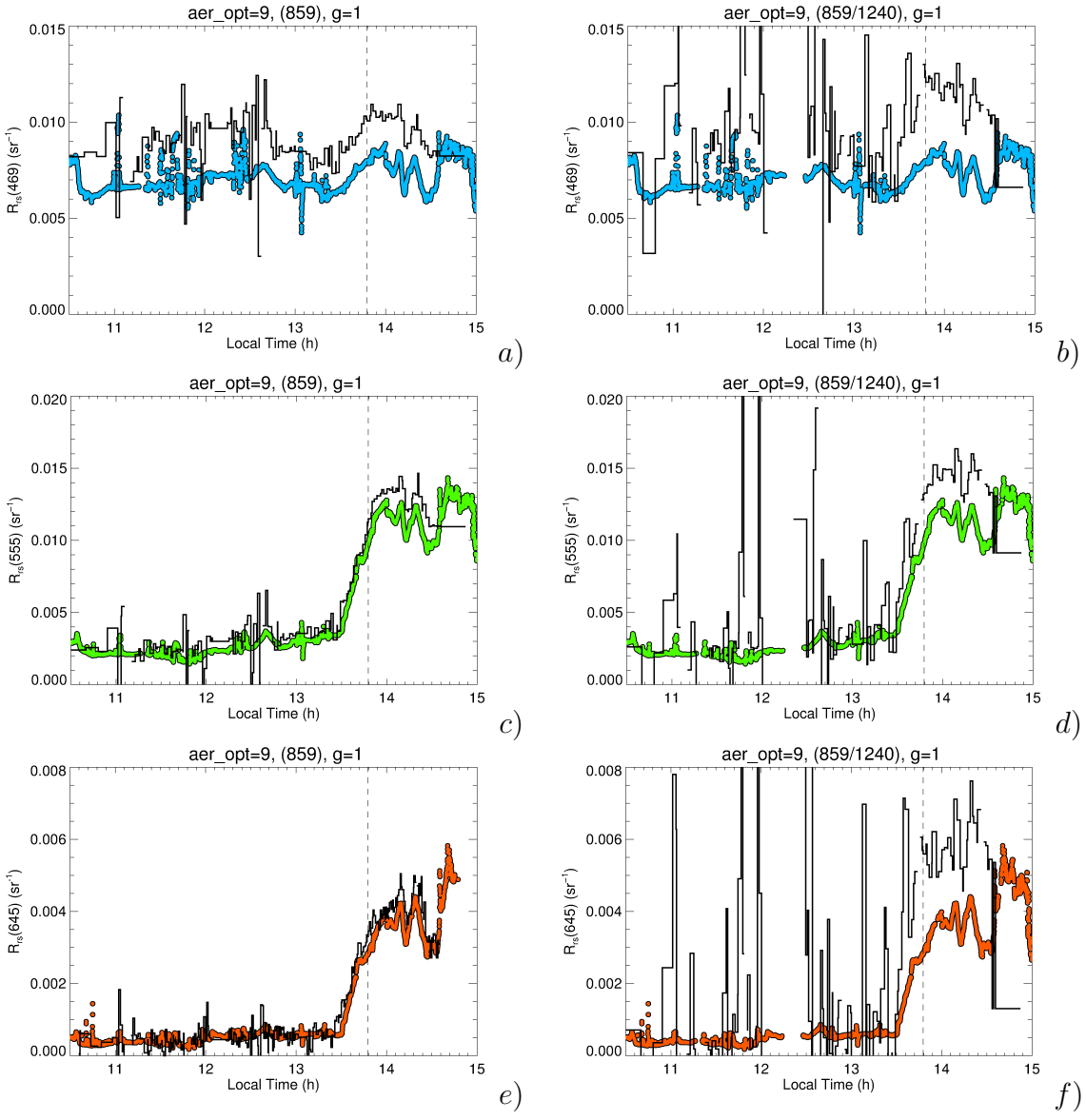

Figure 5.16: DALEC R_{rs} transect pixels and corresponding MODIS overpass pixel values for 3 different wavelengths, with the Coastal 99% Relative Humidity Fixed aerosol model using 859 nm only (a,c and e), and using 859/1240 (b,d and f). The original SEADAS MODIS pixel values are shown in black. The DALEC transect is shown in colour.

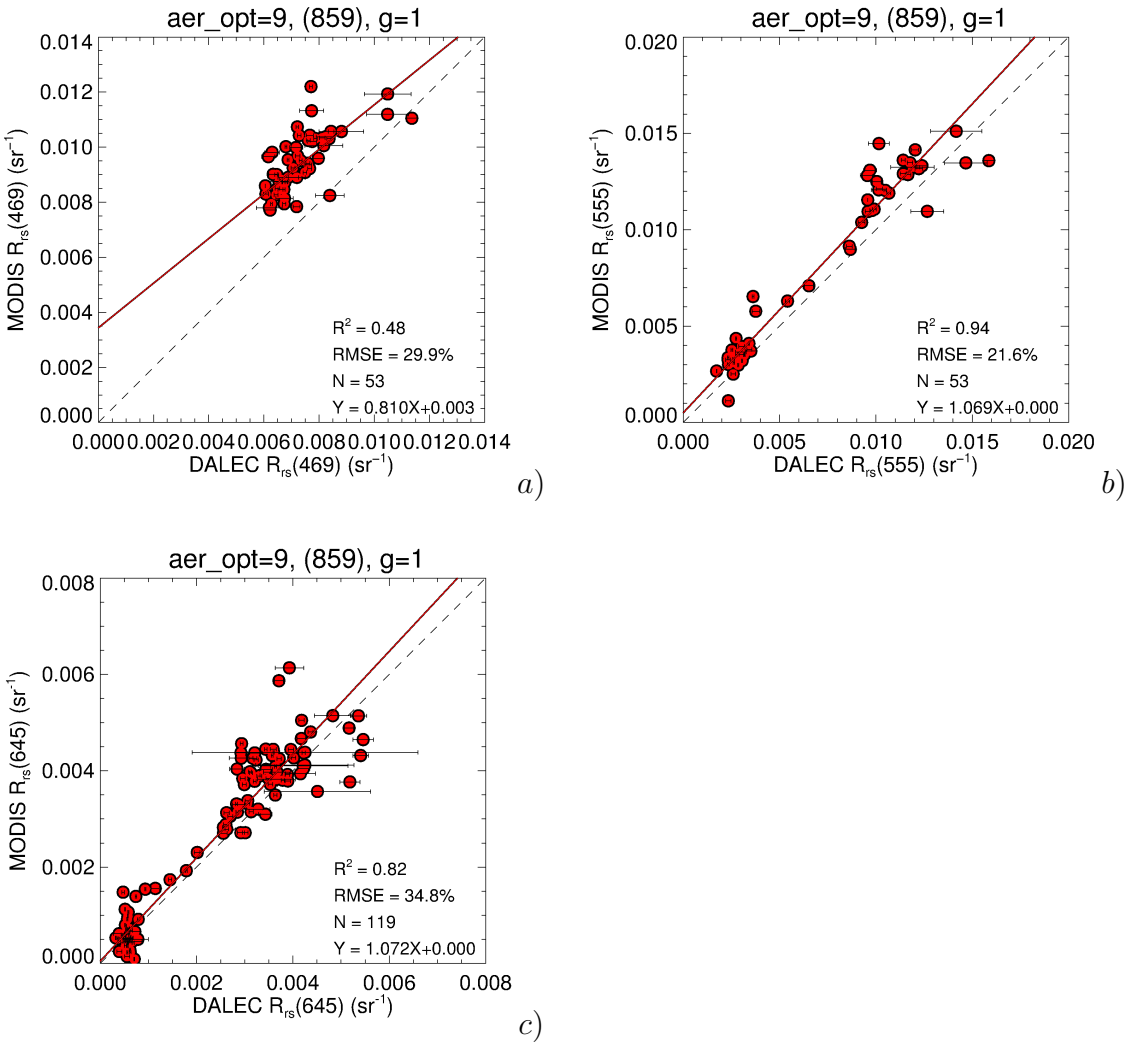

Figure 5.17: DALEC R_{rs} transect pixels v.s. corresponding High resolution MODIS overpass pixel values for 3 different wavelengths, with the 99% Relative Humidity Fixed aerosol model (859). The original SEADAS MODIS pixel values are shown with red plot symbols.

5.3.2 Empirical Algorithms

5.3.2.1 GTSS - Empirical Total Suspended Solids (250m)

The R_{rs} validation data in Figs. 5.16e and 5.18c shows that the MODIS $R_{rs}(645)$ band compares well with the DALEC. The vicarious calibration coefficients were applied to the MODIS data, and was then converted into Total Suspended Solids using Eqs. 3.43 and 4.35. The MODIS data yielded TSS retrievals with an estimated RMSE of 13.5% (based on a comparison with the flow-through TSS data). Figure 5.18a and b shows the pixel-based measurements along with the *in situ* flow-through TSS measurements. The processed GTSS image is shown in Fig. 5.21. This image has the sharpest detail possible from MODIS because the 859nm band used for atmospheric correction is also 250m resolution. In this scene, small, scatterred clouds and their shadows can be seen around the outer reef and mid-lagoon waters towards the center and upper right of the image. Dark filament structures can also be seen in mid lagoon waters and these are caused by atmospheric correction issues associated with floating *Trichodesmium* (this can be verified by viewing the true colour image in Fig. 5.1). The magnitude of the error is approximately 0.5 mgl^{-1} in this scene. Near land, there is sometimes erroneously high values which should be masked out. These are most likely due to stray light from a bright target influencing the imager. A 5m depth mask was applied to the imagery, which covers areas in the image which may result in artifacts from bottom reflection in clear waters. Towards the glint-effected region (see Fig. 5.1), the GTSS product appears marbled, which represents a reduced product accuracy in glint-effected regions.

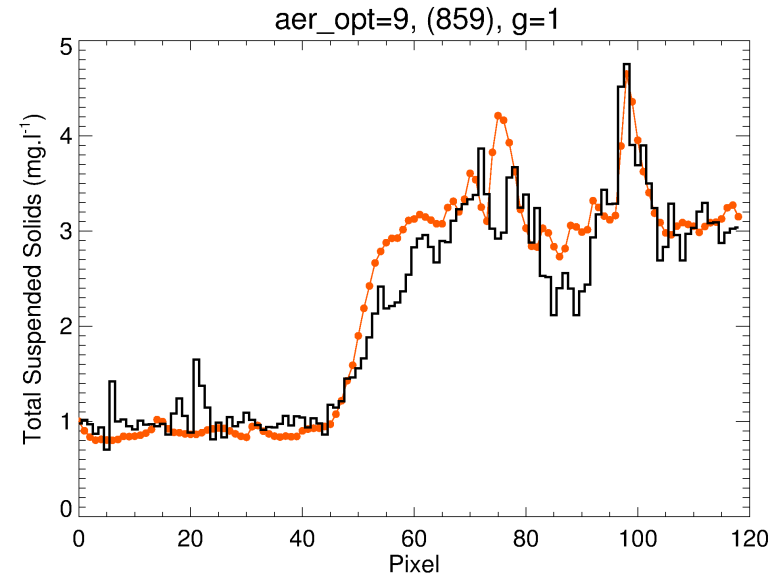

a)

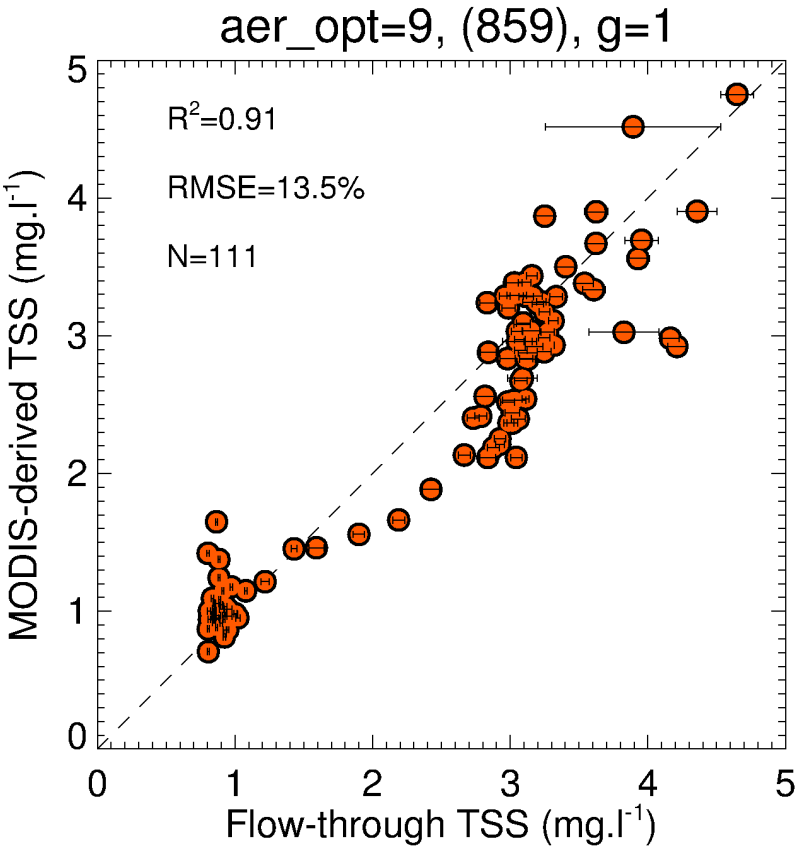

b)

Figure 5.18: The Flow-through measured TSS vs MODIS empirical algorithm-based TSS retrievals a) The pixel-resolved time series and b) The comparison scatter plot.

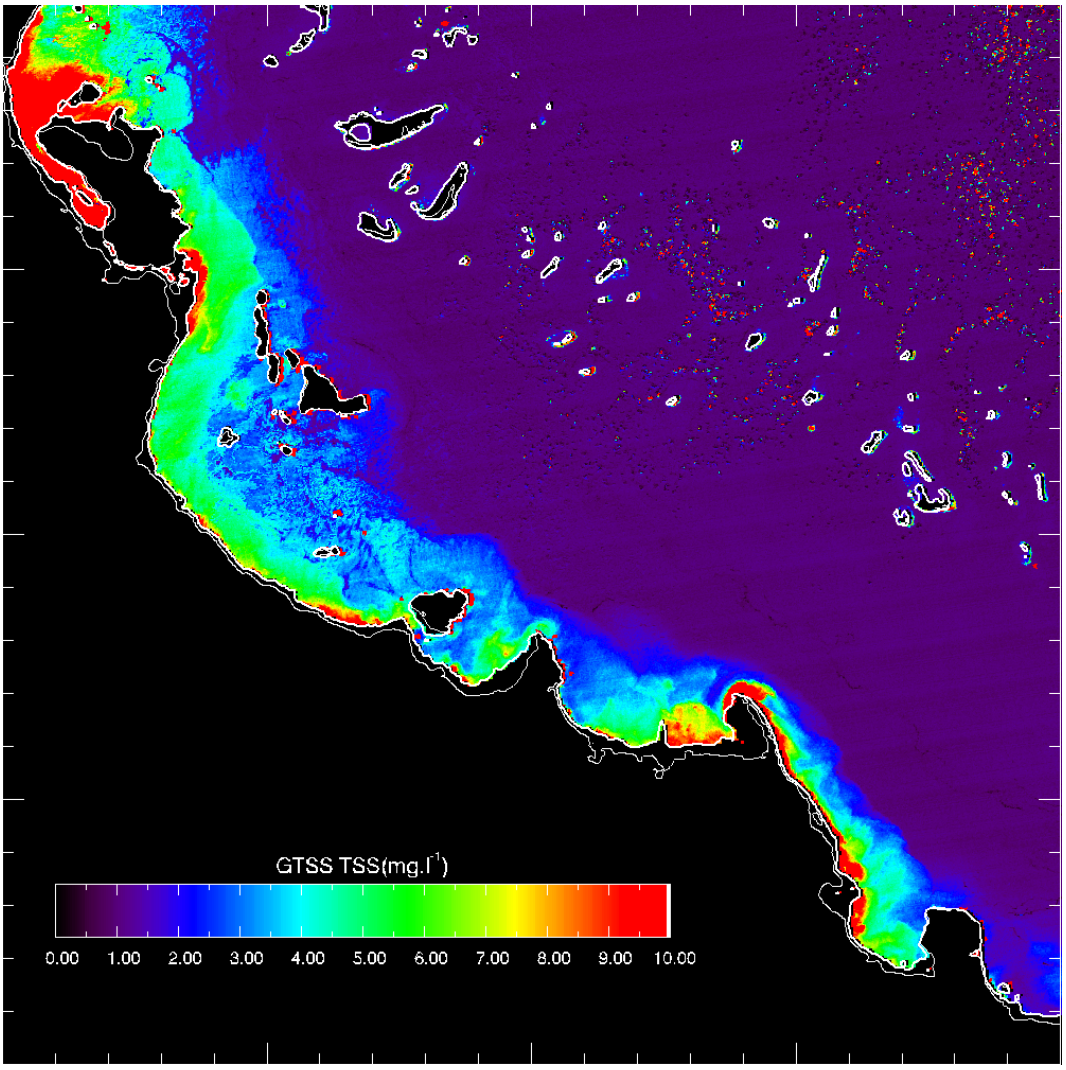

Figure 5.19: The 250m resolution empirical GTSS TSS algorithm output. This product had a RMSE of 13.5% when compared with flowthrough data (N=111), but note marbling effect to the North-east of Townsville.

5.3.2.2 GCHL1 - Empirical Chlorophyll-a (500m)

The R_{rs} MODIS data in Fig. 5.16a and c (i.e. 469 and 555 nm) appeared to be noisy in clear waters encountered prior to approximately 13:30 local time. There were patchy clouds in this area, and it is possible that the increased resolution of these bands (as opposed to the standard 1km bands) make the influence of clouds more apparent. In more turbid waters away from clouds, the time series appeared more smooth. The higher spatial resolution of these bands gives an opportunity to resolve more coastal features, so an empirical TChl algorithmic approach considered beneficial. Unfortunately, the 469 nm band appears constantly higher than the equivalent DALEC measurements. The source of the difference is most likey atmospheric correction, as the atmosphere can account for up 90% of the reflectance signal measured by the satellite. Other possible sources of difference include an over-correction of the DALEC data for sky-glint, spectral bandwidth differences between the MODIS 469 nm and equivalent DALEC 469 nm, or calibration issues with the MODIS 469 nm band. By vicariously calibrating the MODIS R_{rs} signals, possible errors due to atmospheric correction are reduced.
Figure 5.20a and b show comparisons between the MODIS-based GCHL1 outputs and the coincident flow-through TChl measurements for different conditions. From these plots, it can be seen that vicariously calibrating the MODIS data improved the TChl retrievals. Further, a re-regression of the band ratio polynomial coefficients from this scene (referred to as GCHL1.1, see Table 5.5) improved the TChl retrieval from an RMSE of 40.9% down to 18.7% for this matchup. Retrieval differences between these two algorithms are in the order of 0.3 $\mu g.l^{-1}$, and this uncertainty is possibly consequence of other in-water constituents having an effect over the band ratios. It should also be recognised that the area that is glint-effected, so this may also effect the spectral shape of the input MODIS data. Figures 5.21 and 5.22 shows the original GCHL1 and GCHL1.1 algorithm (respectively) applied to the MODIS matchup scene. The GCHL1.1 produces higher TChl values in mid-shelf and offshore waters which is consistent with the *in-situ* flow-through fluorometer measurements, however these elevated readings may be a fluorometer calibration artifact (possibly biofouling). In off-shore waters, it is expected that the TChl would be lower than 0.1 $\mu g.l^{-1}$, however the

GCHL1.1 algorithm appears to plateau around this level for realistic R values. In these more oceanic waters away from terrestrial influences, it is also expected that the NASA OC3m algorithm product is accurate. OC3m also produces Chl values lower than 0.1 $\mu g.l^{-1}$ in these waters (See Fig. 5.25). Although in this particular case, the GCHL1.1 algorithm reduces the RMSE compared to an *in situ* dataset measured one particular day, it is probably more accurate to routinely apply the GCHL1 algorithm which was developed with a larger dataset collected over many days and oceanographic conditions. It should be noted, however that there are significant differences in the magnitude of the coastal 'bloom' features towards the lower right of the image between the GCHL1 and GCHL1.1 algorithms. Whilst having a high spatial resolution TChl product is enticing, more work is required to assess the stability and accuracy of the derived TChl values.

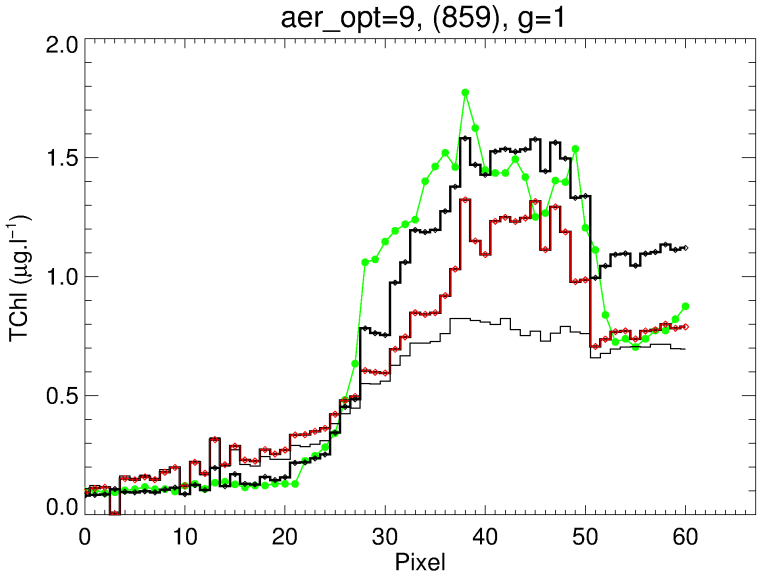

a)

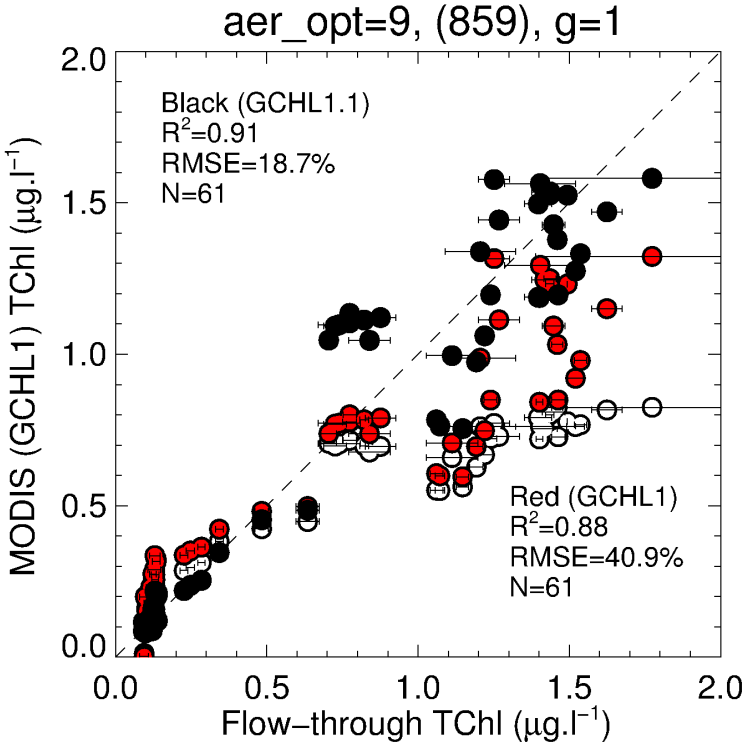

b)

Figure 5.20: a) The pixel-resolved time series of the flow-through measured TChl and MODIS empirical algorithm-based (GCHL1). The uppermost green trace with circular plot symbols is the flow-through (fluorometer) TChl concentration. The thick black line is the MODIS-retrieved GCHL1 output with vicarious calibration applied to $R_{rs}(469)$ and $R_{rs}(555)$. The thin black line is the MODIS-retrieved GCHL1 output without vicarious calibration. b) The comparison TChl scatter plot with the vicarious calibration data shown with red plot symbols (no error bars), and the vicariously calibrated GCHL1 outputs shown in green (with error bars based on the standard deviation of the flowthrough TChl concentrations recorded within each pixel.)

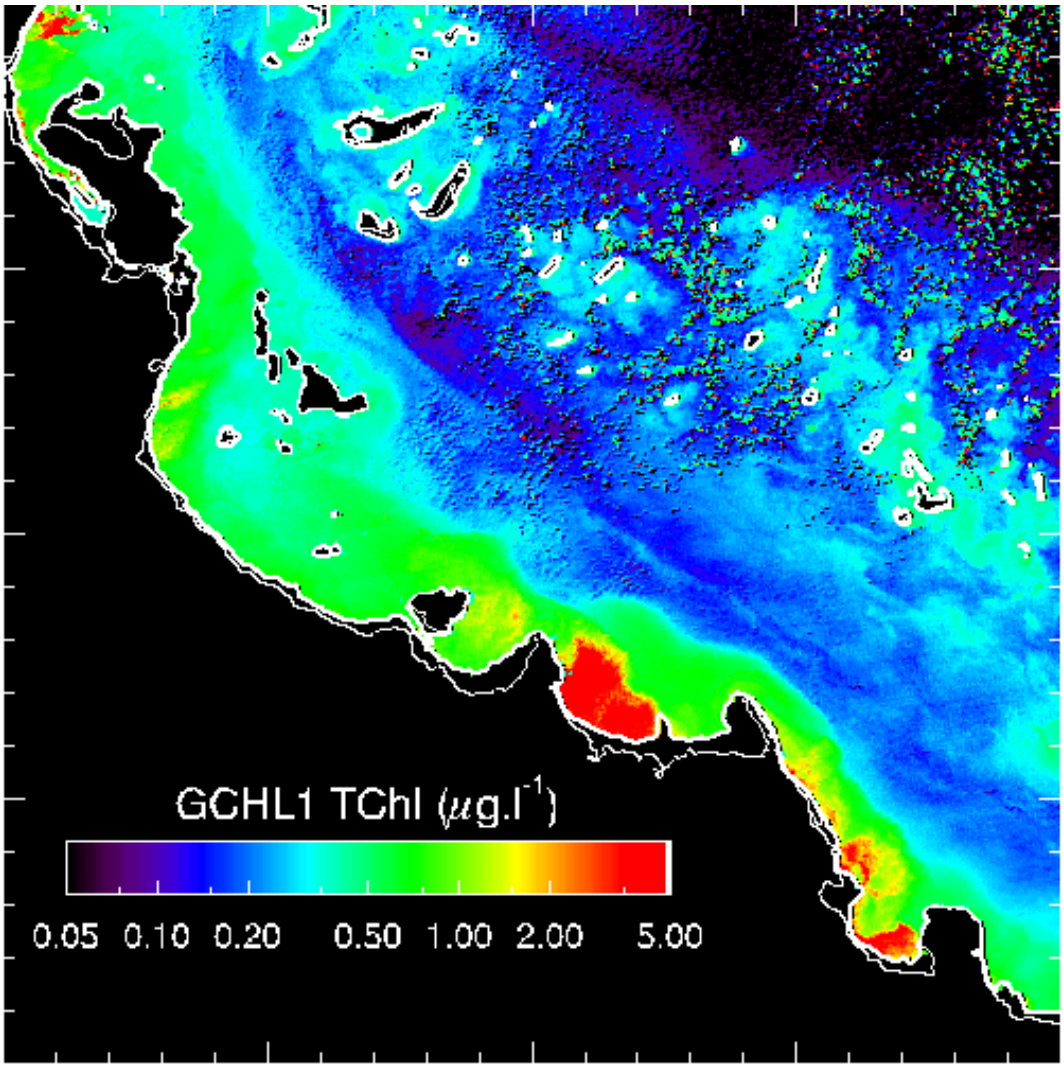

Figure 5.21: The 500m resolution GCHL1 TChl algorithm output.

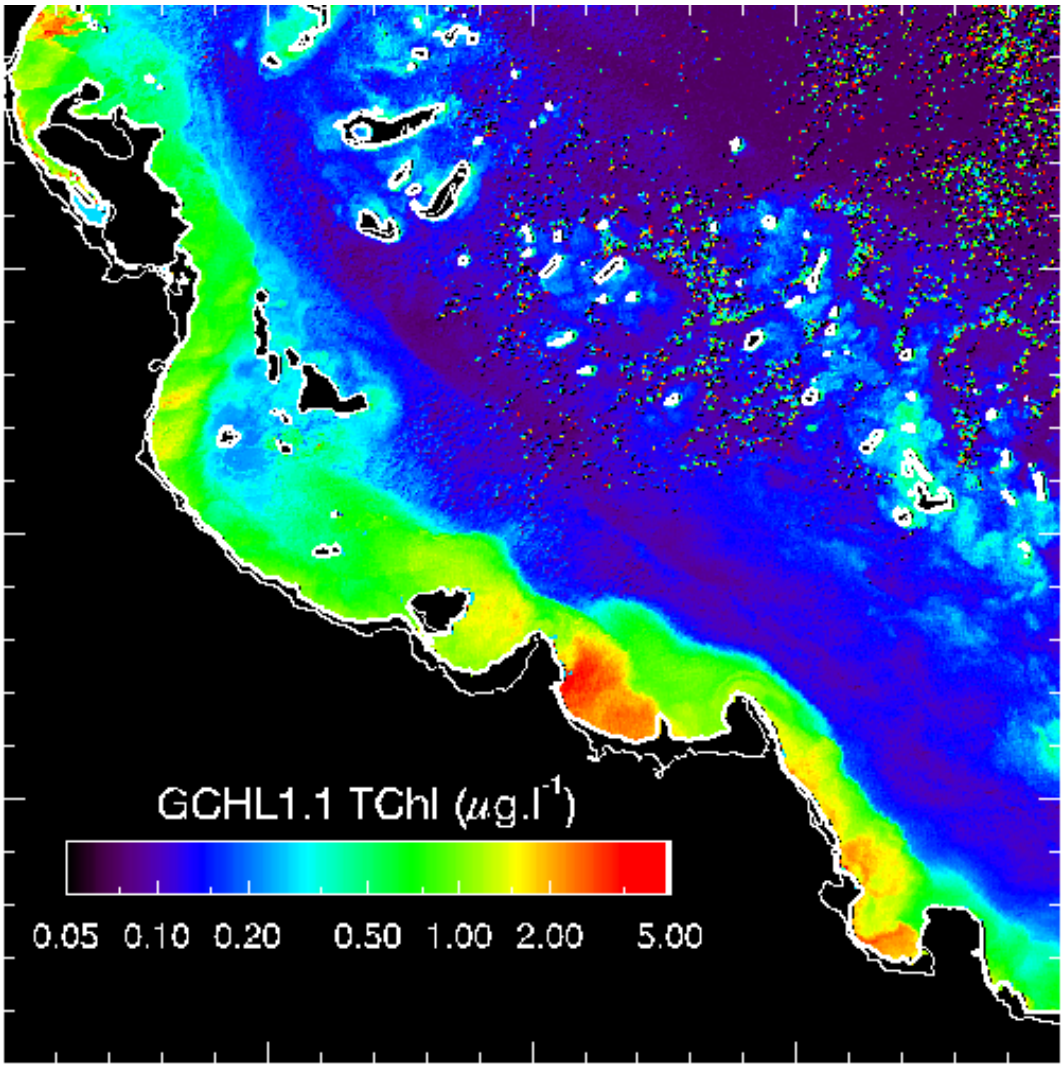

Figure 5.22: The 500m resolution GCHL1.1 TChl algorithm output.

5.3.2.3 GCHL2 - Empirical Chlorophyll-a (1km)

The pixel-resolved time series of the 1km empirical MODIS GCHL2 algorithm is shown in Fig. 5.23, alongside the NASA OC3m equivalent and an empirically re-tuned (GCHL2.1) algorithm specifically for the matchup scene. The GCHL2.1 algorithm output performs slightly better than the GCHL2 algorithm (18.8% vs 40.6% RMSE), and significantly better than the OC3m algorithm which overstates TChl by approximately 250% and has an RMSE of 155.7%. The GCHL2.1 algorithm coefficients are shown in Table 5.5. Figures 5.24 and 5.25 show the GCHL2 and GCHL2.1 algorithm match-up images (respectively). The standard NASA OC3m algorithm (similarly applied to vicariously-calibrated MODIS R_{rs} bands) is shown in Fig. 5.26 for comparison. Note, in addition to vicarious calibration, saturated bands in the glint effected regions were replaced with spectrally interpolated data from non-saturated bands. If this was not done, most coastal pixels would be invalid because of saturation in the $R_{rs}(547)$ band. Similar to differences between GCHL1 and GCHL1.1, the GCHL2 image shows a higher TChl concentration in coastal waters than the matchup-based re-tuned GCHL2.1. It is likely that the ratio of a_{cdom}, a_{ϕ} and a_{NAP} encountered on this day was slightly different to the bulk average ratios experienced during data collection. As with the 500m bands, the difference in TChl concentration between the bulk and revised algorithms illustrates the sensitivity of the empirical TChl algorithm approach to changes in in-water IOPs. A further demonstration of this effect can be made by using the spectral forward model described in Chapter 3 to simulate the maximum band ratio, R in different scenarios. Figures 5.27a-d show how variations in IOP concentrations and spectral shapes effect the MBR which is used as the basis for the empirical TChl algorithms. Due to the variability exhibited in these plots which correspond to potential errors in TChl of hundreds of percent in ceratin conditions, the reader is cautioned against using a purely empirical approach to estimate TChl in coastal GBR waters.

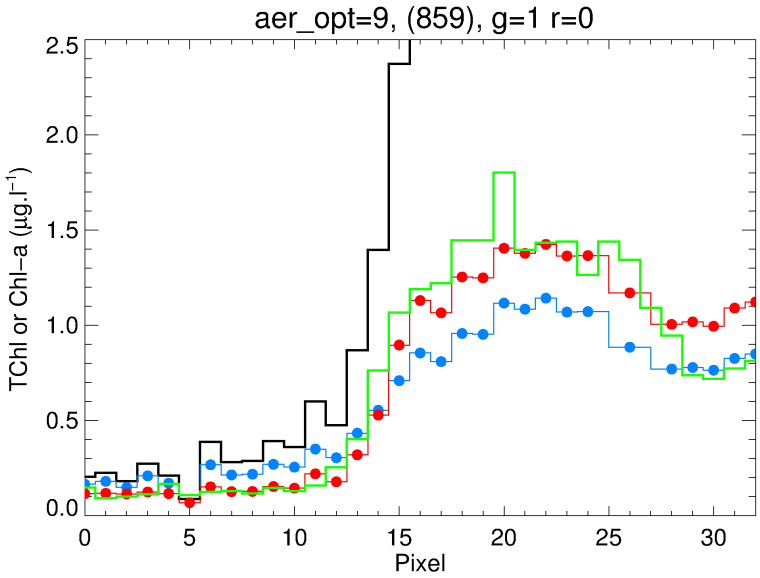

a)

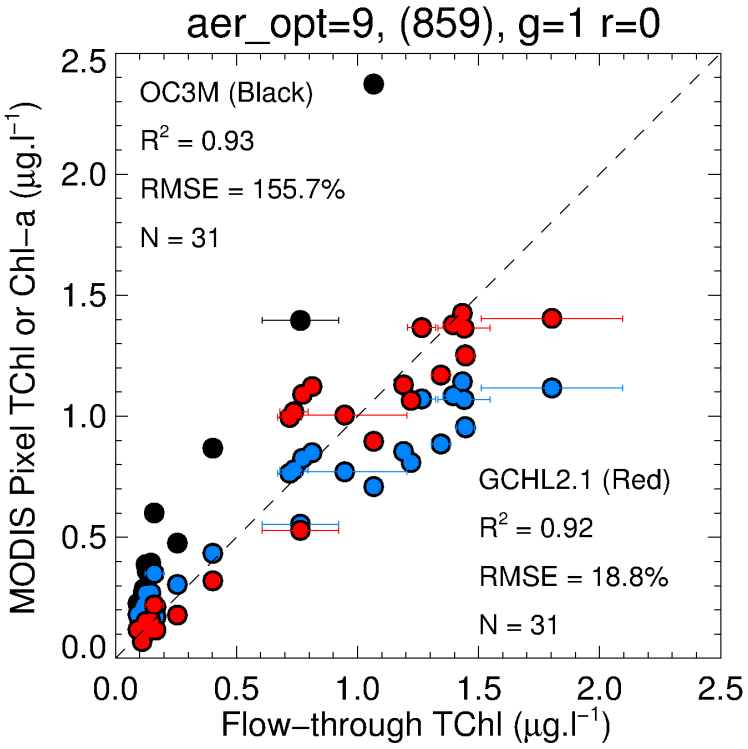

b)

Figure 5.23: a) The pixel-resolved time series of the flow-through measured TChl and MODIS empirical algorithm-based (GCHL2). The green trace is the coincident flow-through (fluorometer) TChl concentration. The red line with circular plot symbols is the GCHL2.1 algorithm. The thick black line is the standard OC3m algorithm, which approaches $5 \mu g l^{-1}$ (data off scale). The thin blue line with circular plot symbols is the MODIS-retrieved GCHL2 output. b) Scatter plot with MODIS OC3m (black), GCHL2.1 (red) and GCHL2 (blue), compared with the flow-through TChl. Error bars are based on the standard deviation of the flow-through TChl concentrations recorded within each pixel.

Bands (nm)	A_0	A_1	A_2	A_3	A_4
$(443, 488, 547), R < 0.564$ **GCHL2.1**, 1 km	-0.17644	-2.76423	0.00592	1.3316	-7.9275
$(469, 555)$ **GCHL1.1**, 500 m	-0.19229	-1.87829	-0.17335	1.33157	0

Table 5.5: Re-tuned matchup-specific polynomial model coefficients for 1 km and 500 m resolution Band Ratio TChl algorithms. Due to the minimal data collected in very clear waters during the match-up, GCHL2.1 reverts back to the GCHL2 coefficients for $R \geq 0.564$.

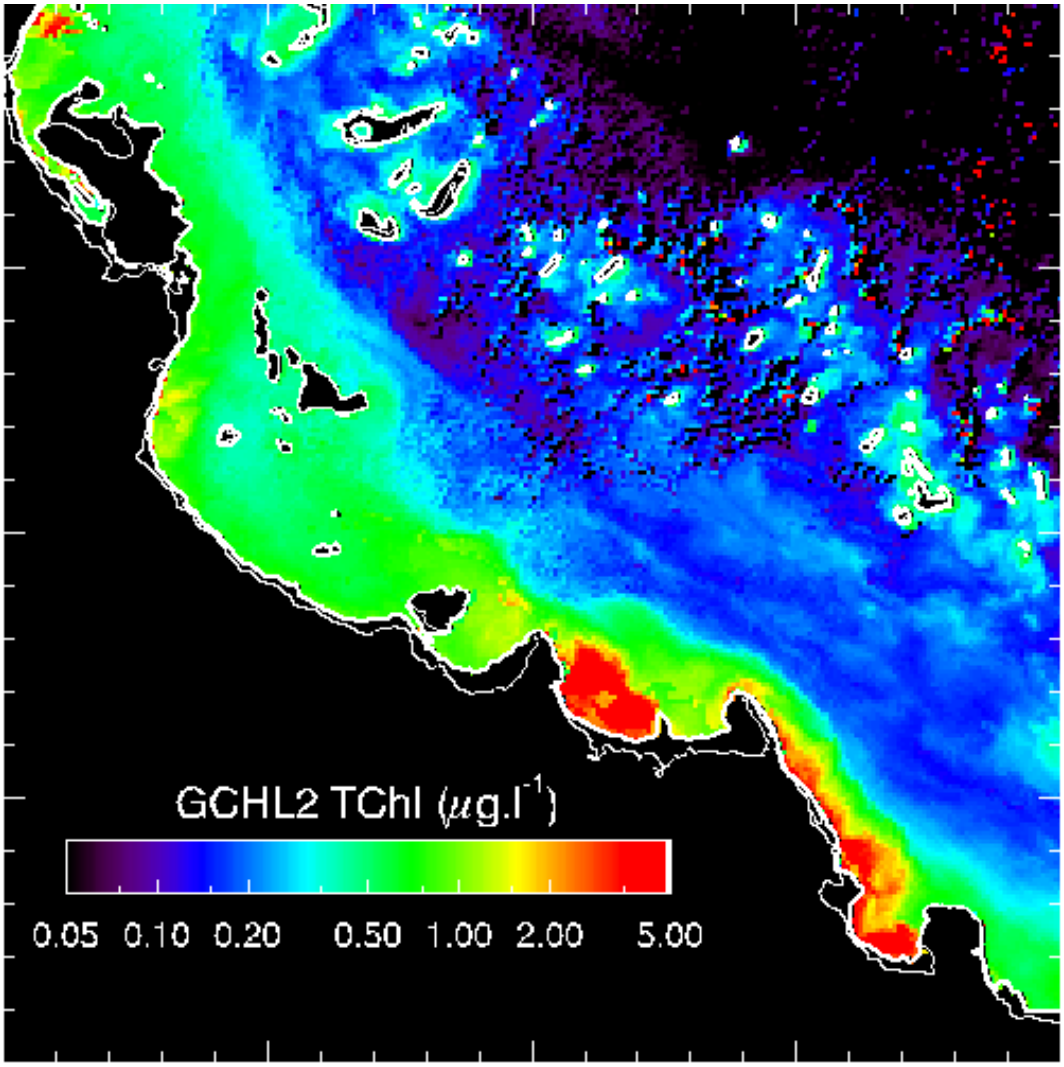

Figure 5.24: The 1km resolution GCHL2 TChl algorithm output.

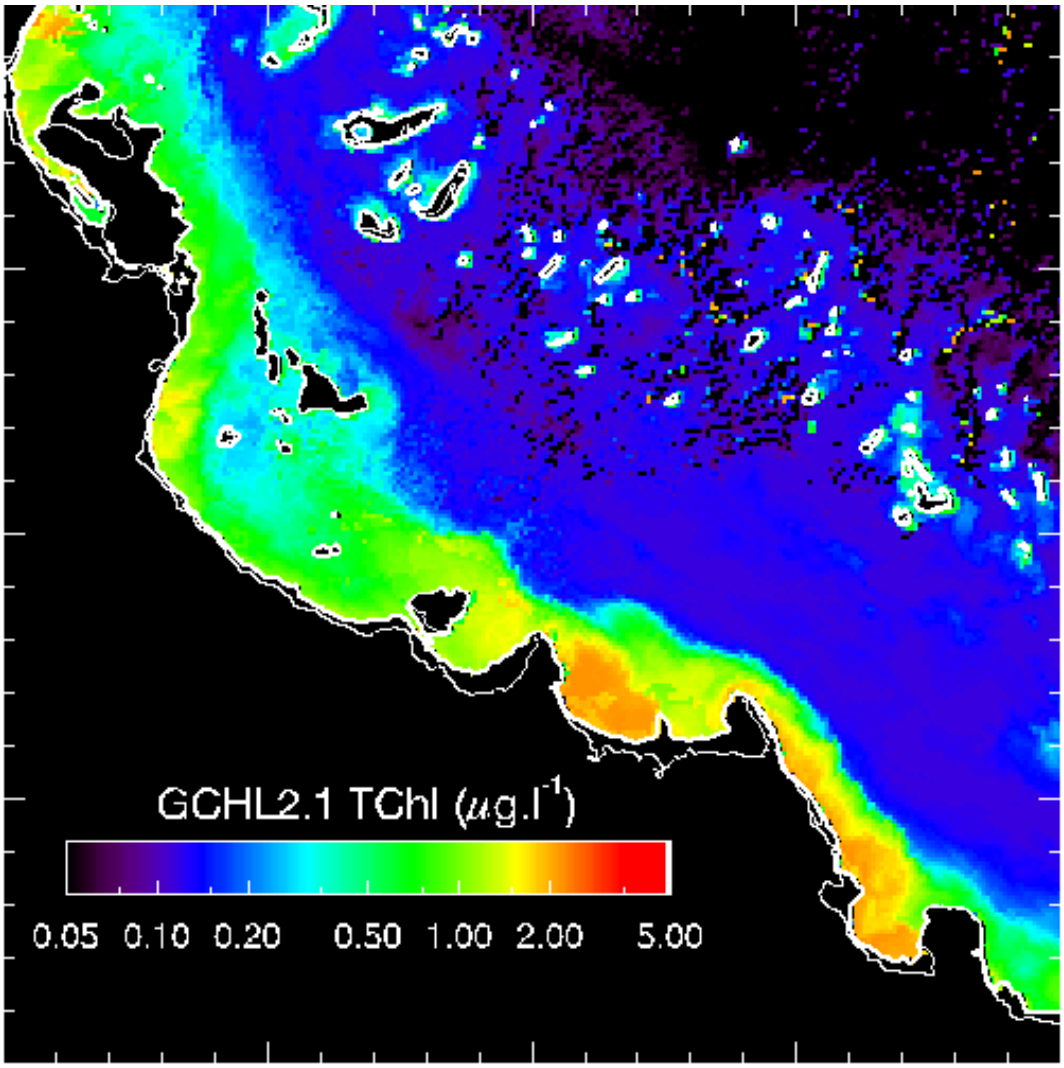

Figure 5.25: The 1km resolution GCHL2.1 TChl algorithm output.

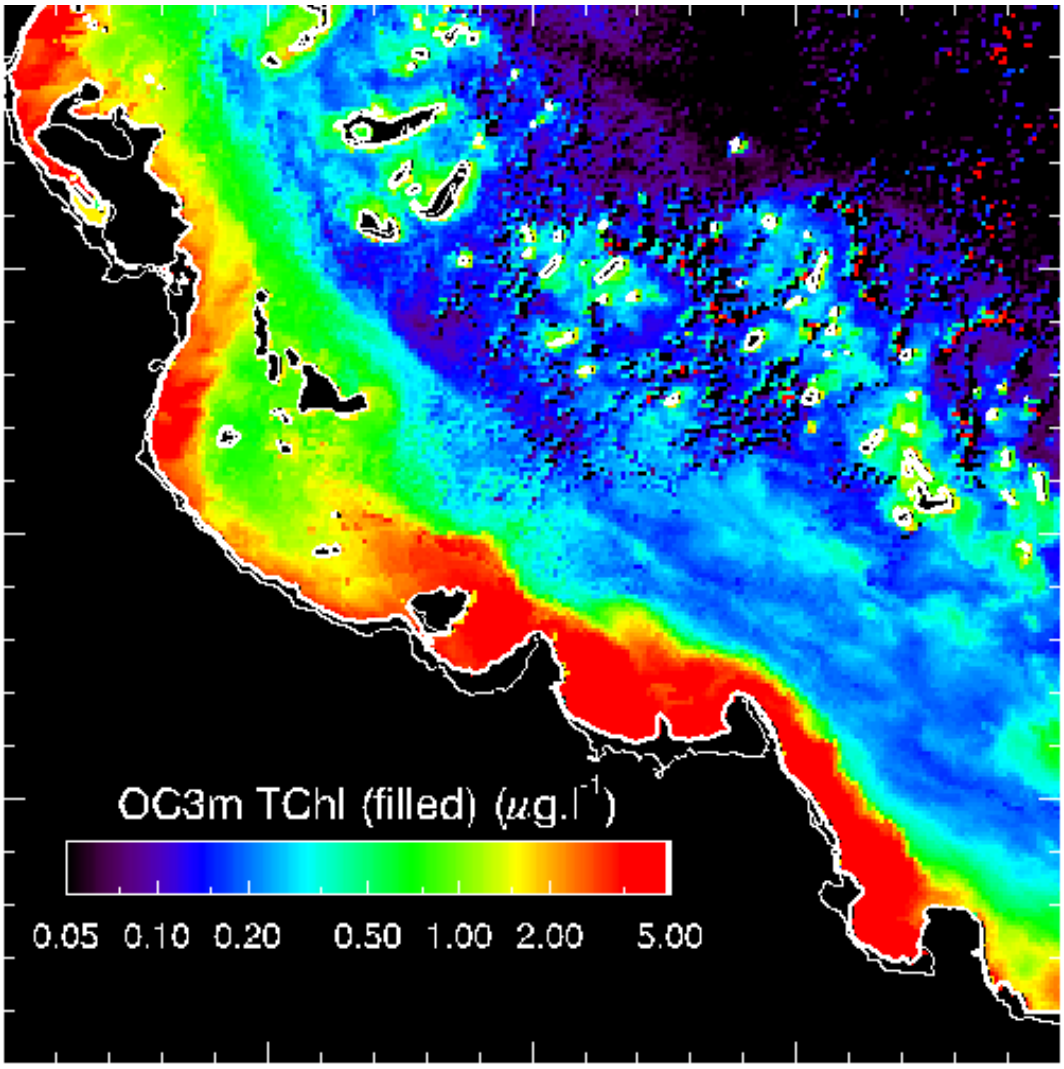

Figure 5.26: The 1km resolution NASA OC3m Chl-a algorithm output (with modified atmospheric correction and spectral in-filling to correct for saturation, consistent with all other matchup images.)

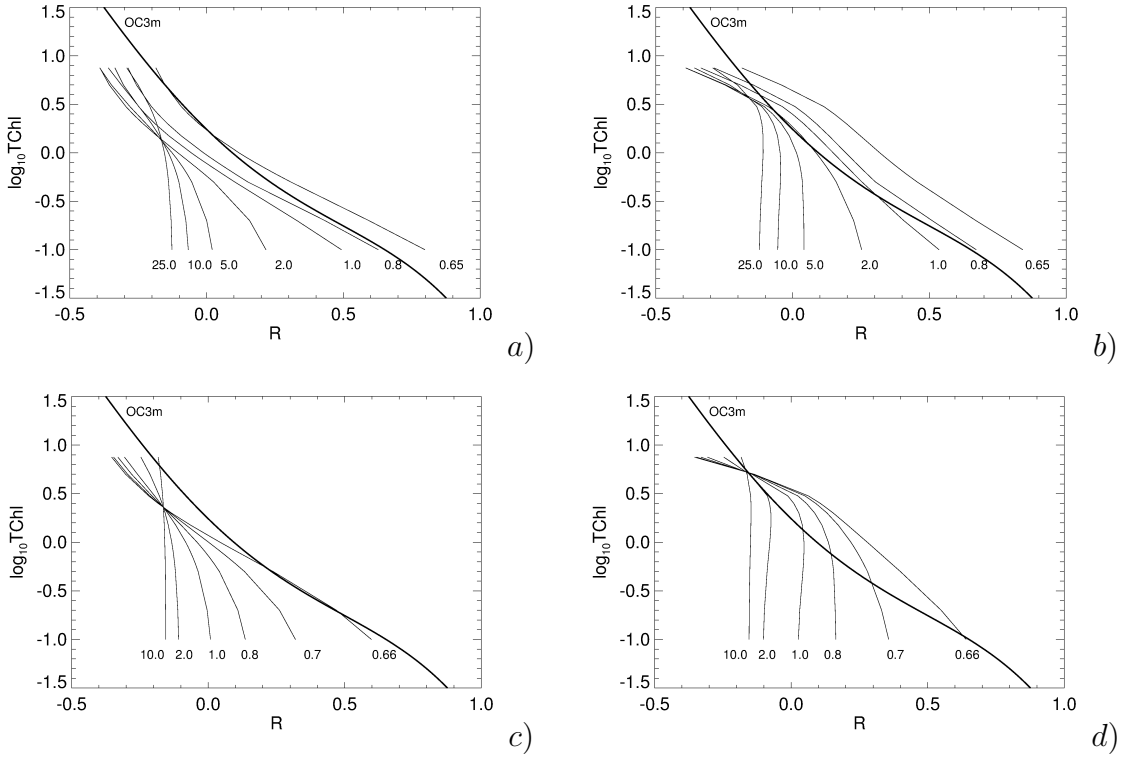

Figure 5.27: a) Simulated Maximum Band Ratio (R) vs log_{10}TChl. Each joined line is a series of TChl concentrations from 0.1 to 8 μgl^{-1}. Each separate line are the MBR results for different TSS concentrations (see annotations, TSS mgl^{-1} units suppressed for clarity). In this simulation, only the *Prochlorococcus* basis vector was used (i.e. $S_{Pro} = 1$). b) As in a, but with S_{Pro} varying as a function of TChl (Eq. 3.26) to simulate the transistion from oligotrophic to eutrophic waters. c) As in a, but each line is for a different DOC concentration (see annotations, DOC mgl^{-1} units suppressed for clarity). TSS is held fixed at 0.8 mgl^{-1}, and $S_{Pro} = 1$. d) as in c, but with S_{Pro} varying as a function of TChl (Eq. 3.26). The OC3m polynomial is overplotted on all graphs for reference.

5.3.2.4 GINV

Earlier in Chapter 4, it was shown that with DALEC R_{rs} data as input, the predictor-corrector inversion outputs needed to be empirically tuned to the water quality parameters to get acceptable accuracy. The same applies when using vicariously calibrated MODIS R_{rs} as input. This is due to one or more of the following: errors in the spectral shapes of the IOP basis vectors (due to pathlength amplification, de-pigmentation, and / or sigma correction uncertainties discussed previously), or errors in the spectral shape of the input R_{rs} measurements themselves. The outputs of each GINV algorithm variant were empirically tuned to match the flow-through TChl and TSS measurements. The results for the TChl retrievals and associated tuning parameters (A and B from Eq. 2.40) are shown in Table 5.6, along with the 1 km empirical GCHL2 and GCHL2.1 results for reference.

The best performing algorithm was the 4-Mixture phytoplankton absorption model, with $b_{bp}(555)$ begin tied to the spectral slope γ, and $a_{NAP}(442)$ being a free parameter. This algorithm achieved an RMSE of 26.9%, and valid data from 27 of the 31 useable matchup pixels. Four suspect inversions ($\frac{a_\phi(443)}{a_\phi(443)+a_{CDOM}(443)+a_{NAP}(443)} < 0.15$) were removed. This algorithm combination only achieved this level of accuracy with the empirical initialisation approach. Figure 5.29 shows the markedly different retrievals from the same algorithm but with different initialisation conditions. Fortunately, in this scene the empirical algorithms were fairly accurate, however the initialisation of the Levenberg-Markquardt predictor-corrector method needs further work to establish this inversion method on an operational basis.

The 4-Mix basis vector approach also yields the fractionated TChl contributions of 4 represetative types of phytoplankton, however the retrievals only accounted for approximately 50% of the flowthrough TChl. Fig. 5.31 shows the uncorrected output TChl retrievals for each different phytoplankton basis vector. In this algorithm, the relative fraction of *Prochlorococcus* is initialised with the empirical TChl value for each pixel. Each other basis vector is initialised equally in terms of $a_\phi(443)$ contribution so that no particular basis vector is biased during the inversion (see Table 4.2 for more details). The time series in Fig. 5.31

Type	b_{bp} type	a_{NAP} free?	Init.	RMSE %	R^2	N	Offset	Slope	A	B
GCHL2.1	-	-	-	18.8	0.93	31	0.046	0.918	-	-
4-Mix	**Std**	**Yes**	**Emp**	**26.9**	**0.89**	**27**	**-0.013**	**1.107**	**0.078**	**0.567**
4-Mix	Emp.	Yes	Emp	30.4	0.90	27	0.001	1.14	0.075	0.604
4-Mix	Emp	No	Emp	34.7	0.82	27	0.000	1.026	0.063	0.634
2-Mix	Emp	Yes	QAA	36.0	0.81	20	0.004	1.009	0.064	0.805
2-Mix	Blend	Yes	QAA	36.0	0.91	20	0.005	1.001	0.055	0.767
Lee	Blend	No	Emp	36.5	0.94	16	0.008	0.990	0.075	0.711
2-Mix	Std.	No	Emp	36.9	0.72	24	-0.004	1.045	0.048	0.662
2-Mix	Emp	No	Emp	37.4	0.70	24	-0.005	1.051	0.049	0.650
4-Mix	Blend	No	Emp	39.0	0.74	26	0.001	1.056	0.073	0.564
4-Mix	Blend	Yes	Emp	39.6	0.79	27	0.001	1.044	0.077	0.567
4-Mix	Std.	No	Emp	40.0	0.75	27	0.000	1.044	0.063	0.590
2-Mix	Std.	Yes	QAA	40.4	0.74	19	0.004	1.011	0.065	0.825
2-Mix	Std.	Yes	QAA	44.0	0.75	20	-0.008	1.022	0.166	0.851
GCHL2	-	-	-	40.6	0.91	31	0.186	0.627	-	-
Lee	Std.	Yes	QAA	46.1	0.77	12	-0.027	1.051	0.119	0.901

Table 5.6: MODIS-based TChl Algorithm Retrieval parameters, sorted by RMSE. All GINV inversions used the GBR-specific a_{CDOM} and a_{NAP} spectral shapes. b_{bp} type denotes the model used for the b_{bp} spectrum. The best GINV results in this dataset were achieved by keeping $a_{NAP}(443)$ a free parameter. Init refers to the initialisation method used. The Emp intitialiser used GCHL2.1 for TChl, $a_\phi(443) = 0.044TChl^{0.37}$ (see Fig. 2.18c), GTSS for TSS, Eq. 2.53 to initialise $b_{bp}(555)$, Eq. 4.33 to initialise $a_{NAP}(443)$ and $a_{CDOM}(443) = \frac{[TChl]}{MK}$, where M is 1.569 from Eq. 4.28 and $K = 8$, estimated from the slope of the data in Fig. 4.25. All other parameters were initialised as described previously in Table 4.2, which also describes the QAA initializer. Offset and Slope are the linear regression coefficients of the retrieved TChl v.s. flow-through TChl. A and B are the re-tuning parameters applied to the GINV retrieved $a_{phi}(442)$ to yield TChl.

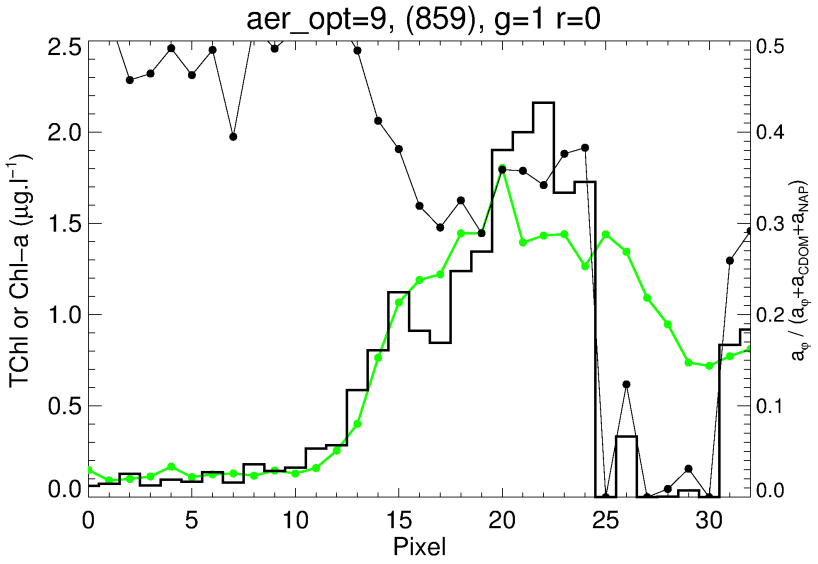

a)

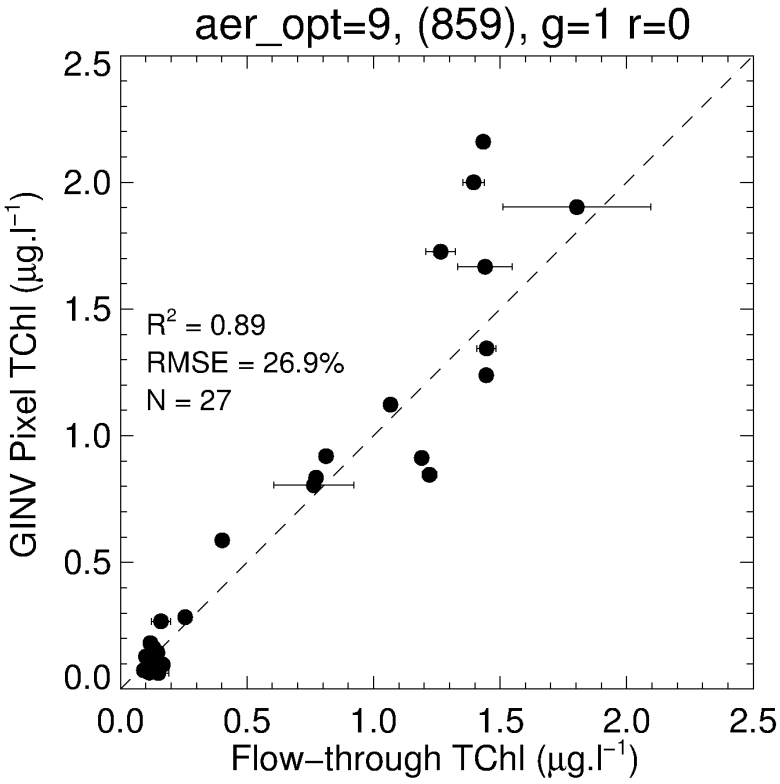

b)

Figure 5.28: The best performing MODIS-based retrieval from the matchup image a) The pixel-resolved time series, with the flow-through TChl in green, the retrieval in black bars and the fractional contribution of $a_\phi(442)$ to $a(442)-a_w(442)$ overlayed with black plot symbols. b) The comparison scatter plot. This inversion scheme used the "4-Mix" model, with $a_{NAP}(442)$ being a free inversion parameter. The GBR-specific a_{CDOM} and a_{NAP} spectral shapes were used, with the empirical b_{bp} spectral model which held γ tied to $b_{bp}(555)$. Note that only 27 pixels yielded reliable TChl information.

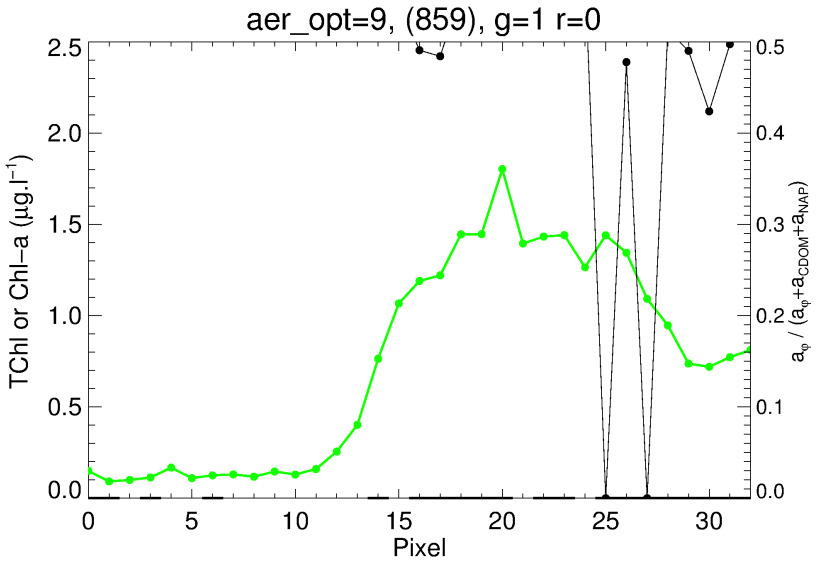

a)

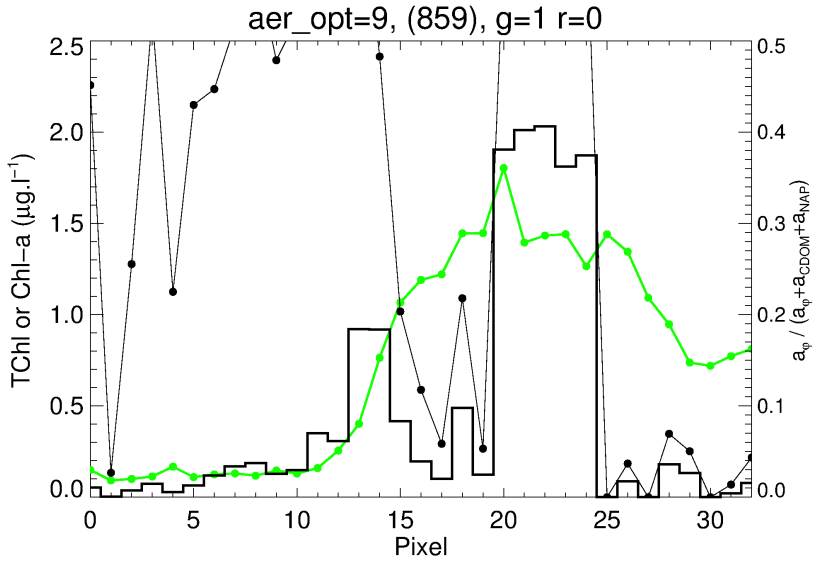

b)

Figure 5.29: The same algorithm combination as in Fig. 5.23a, but with different initialisation values. a) was initialised with fixed parameters and b) was initialised with the QAA.

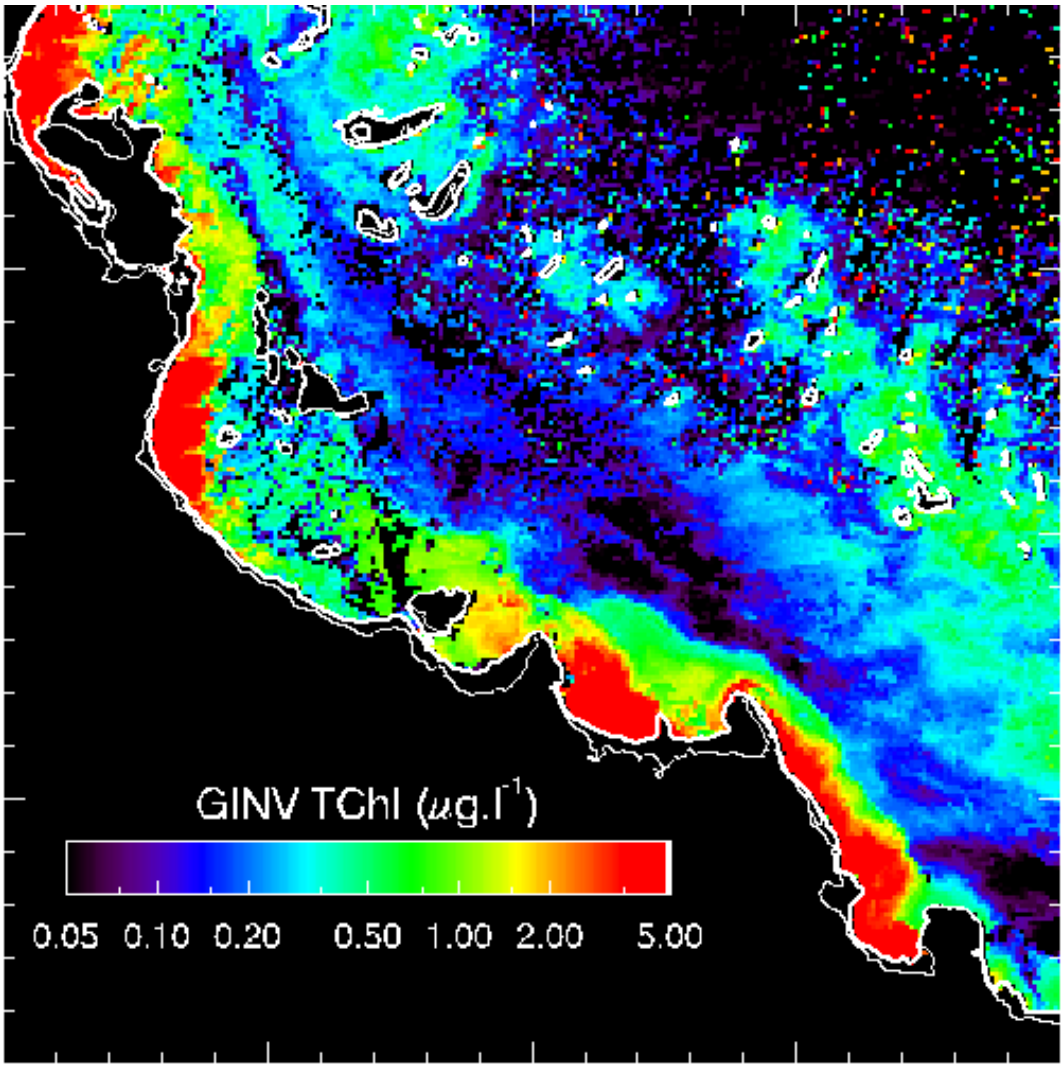

Figure 5.30: The 1km resolution GINV TChl algorithm output.

indicates that further off the coast at the start of the transect, TChl is mainly contributed by *Prochlorococcus* and then towards the coast, *Synechococcus* contributes the most TChl. This is compatible with the findings of Crosbie & Furnas (2001), however this trend is influenced by the initial conditions provided to the predictor-corrector inversion algorithm. Unfortunately, the overall magnitude of the sum of these TChl components is approximately half of the flowthrough TChl value. It is possible that the overall magnitudes of the chlorophyll-specific basis vectors used to invert this matchup scene are not representative of the actual phytoplankton encountered on that day. This may be due to the methodological uncertainties associated with determining the chlorophyll-specific basis vectors in the first place (and that the *Synechococcus* basis vector was taken from another study (Morel et al. 1993)). Furthermore, photoadaptation is known to change the TChl-specific absorption properties of a given phytoplankton type. The retrievals of the different phytoplankton types is also dependent on the initialisation approach (data not shown). Apart from assigning an initial S_{Pro} value based on empirical TChl value, the other 3 phytoplankton-representative absorption spectra are initialised equally in magnitude at 443 nm.

Unfortunately, no complementary datasets such as fractionation or HPLC pigment analysis were available for validation of the phytoplankton basis vector magnitudes. Validation and optimisation of these images is left for further work. The images of each component are shown in Fig. 5.32. The most dominant basis vectors were the *Prochlorococcus* and *Synechococcus* vectors. There appears to be artifacts in the image close to the coast in the glint-effected region towards the top left of the scene. There appears to be some striping artifacts in the GINV TChl approach. It is unclear whether this is will be a prominent feature in all TChl images processed with the GINV technique, however it is worth mentioning that these stripes are much less evident in the empirical MBR algorithms. It may be possible to use either the 500m or 1km resolution empirical TChl results to correct these image artifacts, however this is left for future work.

The GINV algorithm also outputs a TSS product at 1km resolution. Most algo-

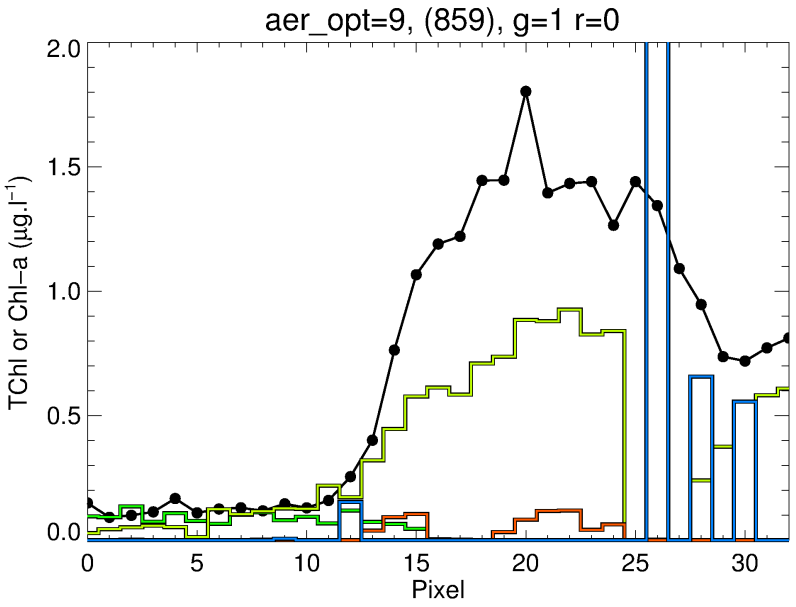

a)

Figure 5.31: Raw TChl output for each basis vector. The black line with circular plot symbols is the flow-through TChl. The *Prochlorococcus*, *Synechococcus*, *Trichodesmium* and diatom retrievals are shown in green, yellow, orange and blue (respectively).

rithm variants were fairly accurate (between 8.5 and 33 % RMSE), however for consistency and computational efficiency, only the GINV algorithm variant that produced the most accurate simultaneous TChl retrieval is presented. It had a TSS retrieval RMSE of 11.9% (See Figure 5.33). The GTSS TSS algorithm evaluated at 1km resolution is also shown on this plot for comparison, and it yielded a slightly worse RMSE of 14.6%. The high resolution 250m GTSS product may be able to used to sharpen the more accurate GINV TSS algorithm to combine the benefits of each algorithm. This is left as further work.

The GINV DOC inversion transect data is shown in Fig. 5.35. As no flow-through data was available, the pixel-coincident discrete station site DOC values were overplotted. After removing the outlier with large error bars, a slope and offset was determined from linear regression between the inversion algorithm-retrieved $a_{CDOM}(443)$ and the *in situ* DOC data. The inversion algorithm-retrieved $a_{CDOM}(442)$ was converted to DOC using Eq. 5.1. The MODIS matchup scene is shown in Fig. 5.36. The image shows elevated DOC features consistent with river plumes, unfortunately no extensive validation data was collected.

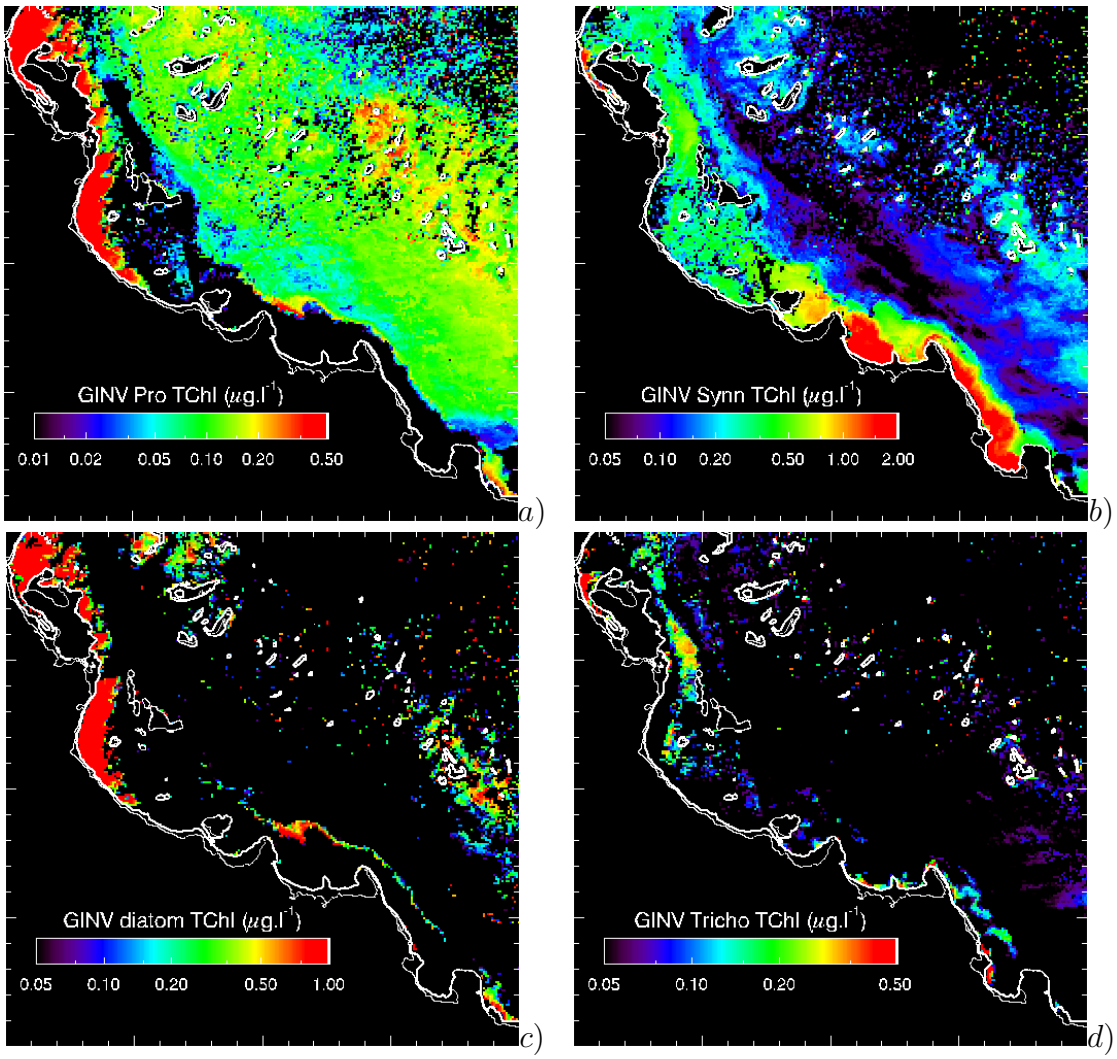

Figure 5.32: The 1km resolution GINV Phytoplankton basis vector TChl algorithm output a) *Prochlorococcus*, b) *Synechococcus*, c) diatoms and d) *Trichodesmium*. Note that these inversions were shown to be inaccurate (see Fig. 5.31).

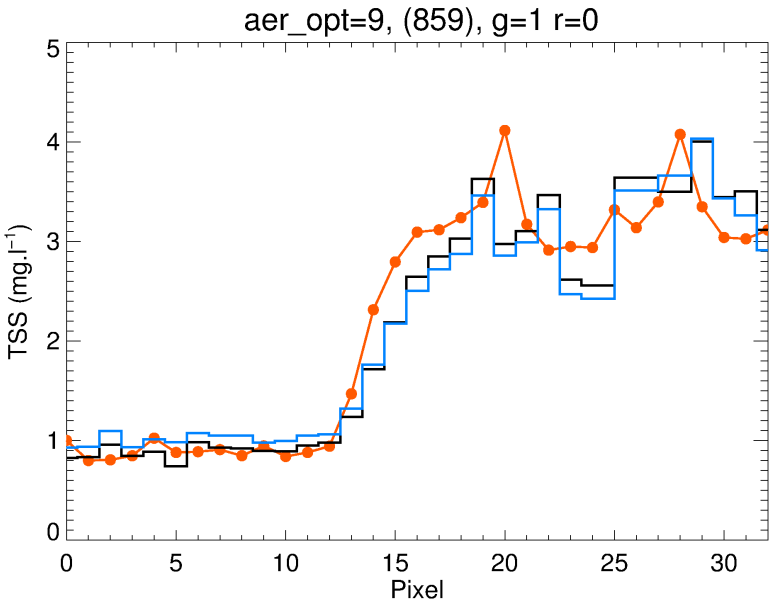

a)

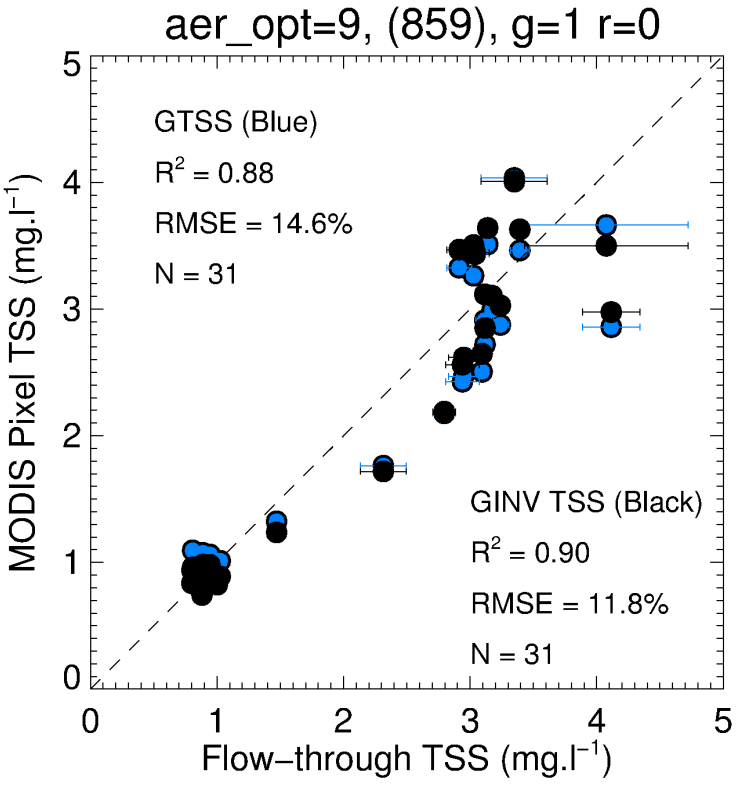

b)

Figure 5.33: The best performing MODIS-based retrieval from the matchup image a) The pixel-resolved time series, with the flow-through TSS in orange, the GINV retrieval in black bars and the purely empirical GTSS algorithm is shown in blue for comparsion. b) The comparison scatter plot. This inversion scheme used the "4-Mix" model, with $a_{NAP}(442)$ being a free inversion parameter. The GBR-specific a_{CDOM} and a_{NAP} spectral shapes were used, with the empirical b_{bp} spectral model which held γ tied to $b_{bp}(555)$. All 31 pixels yielded useful TSS information.

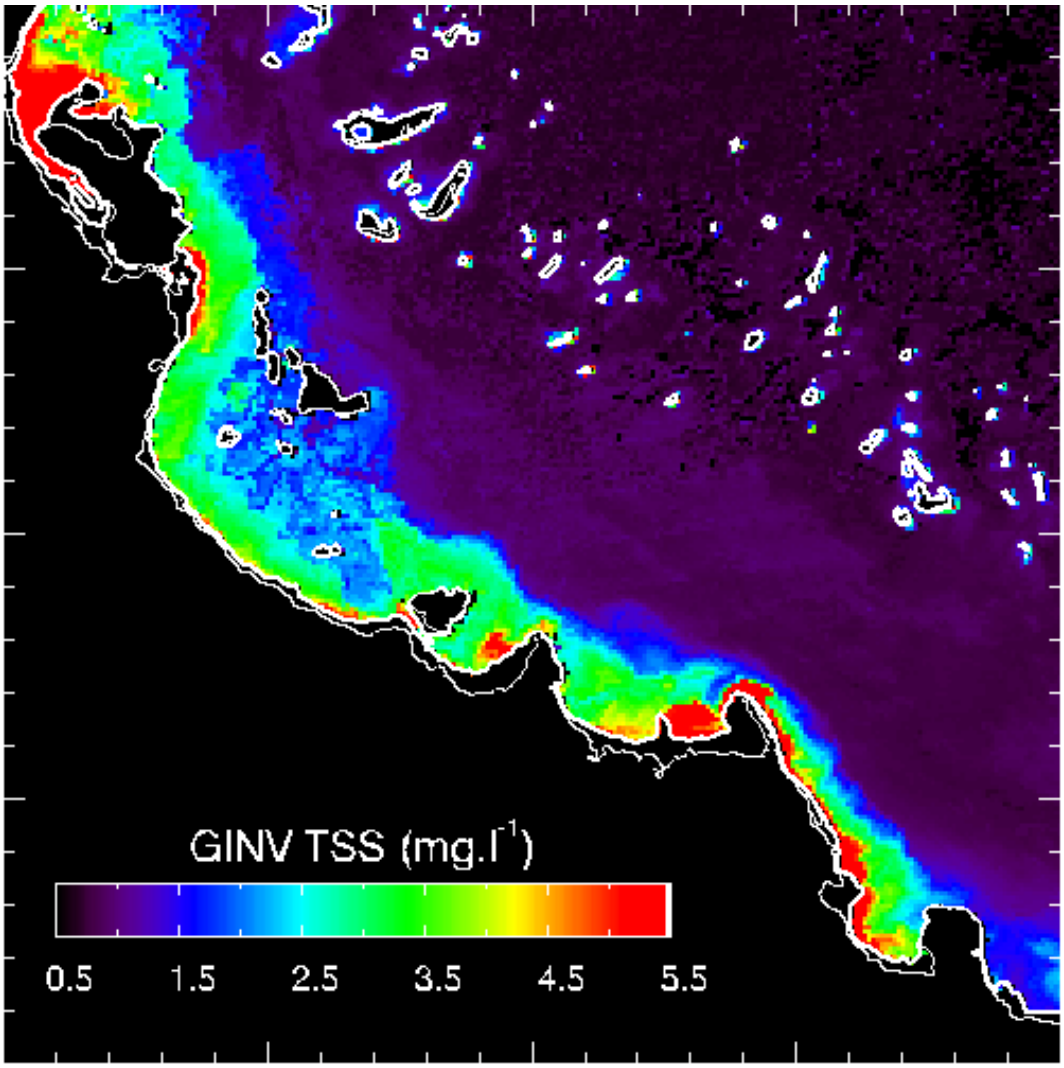

Figure 5.34: The 1km resolution GINV TSS algorithm output.

$$DOC = 2.96[a_{CDOM}(443)] + 0.64 \tag{5.1}$$

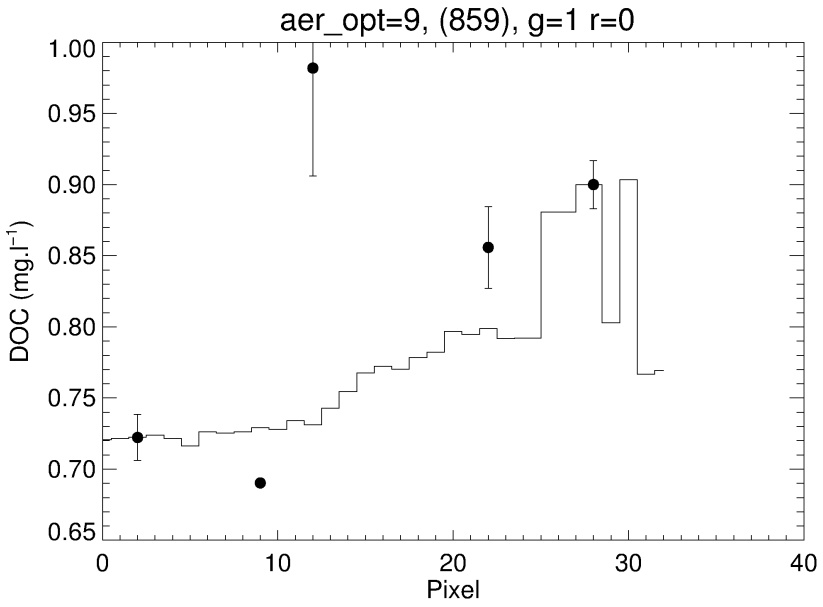

Figure 5.35: The empirically tuned pixel based GINV DOC data with *in situ* station data overplotted with circles and error bars representing the duplicate sample standard deviation. The DOC data point overplotted at pixel 12 was discarded from the regression which determined the coefficients in Eq. 5.1.

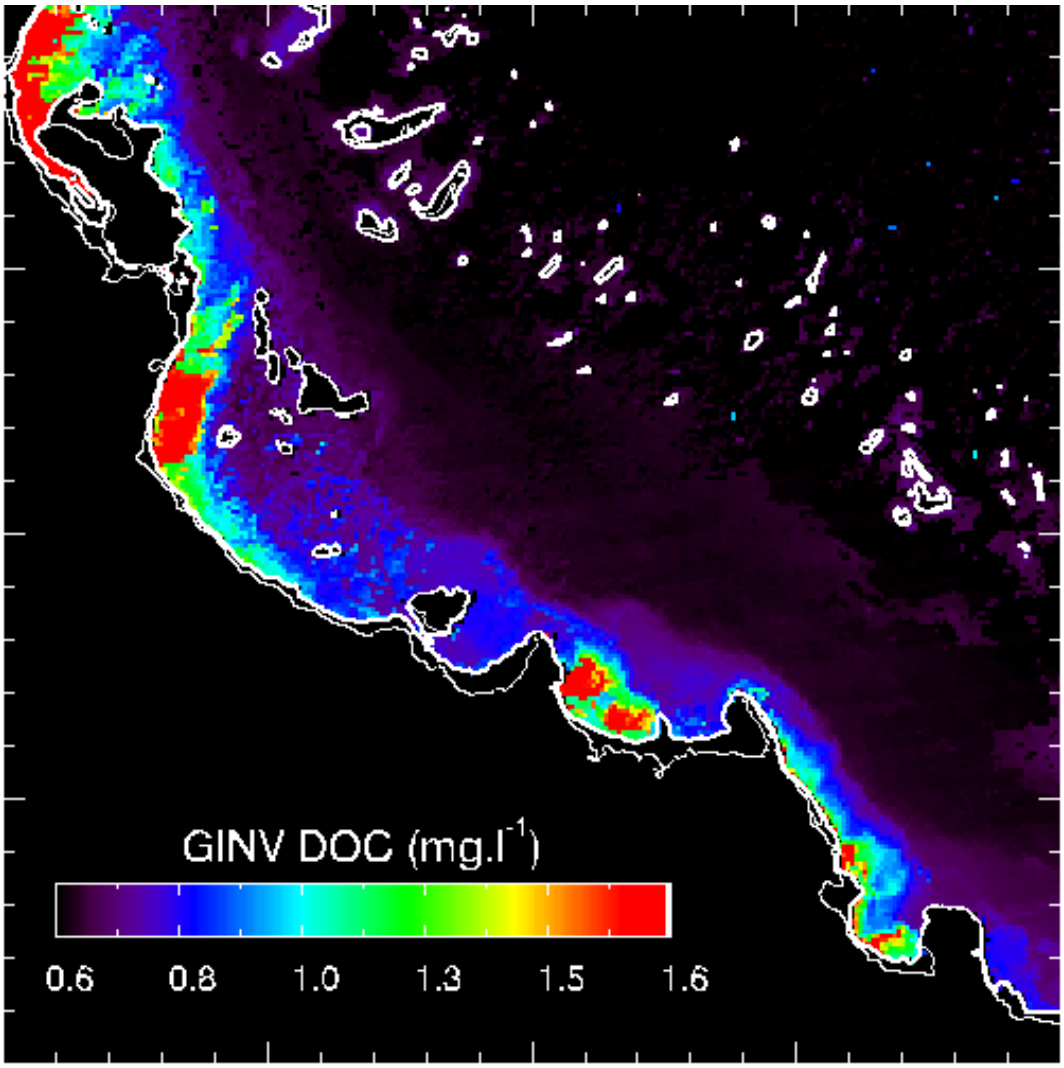

Figure 5.36: The 1km resolution GINV DOC algorithm output.

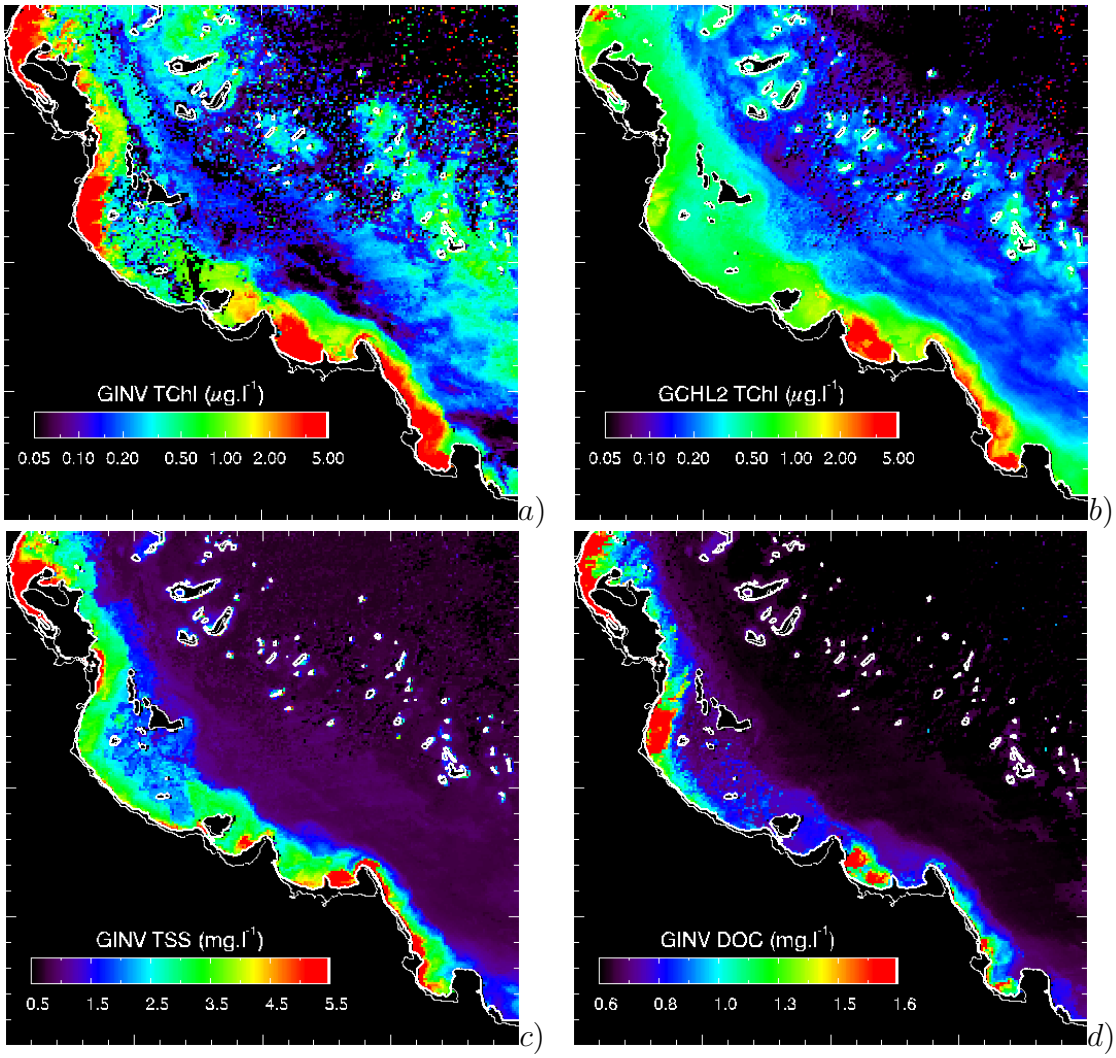

Figure 5.37: Inversion model outputs: a) GINV TChl, b) GCHL2, c) GINV TSS and d) GINV DOC.

Figure 5.37 shows four aforementioned inversion outputs side by side. The GINV TSS product highlights inshore sediment plumes that are independent of features in the GINV DOC product. This is encouraging because it is further spatial evidence that the inversion is capable of separating out different constituents. Although the 5m contour was plotted on all the images, it is possible that some un-masked pixels are influenced by light reflection from the sea floor in these scenes. This is probably not the case for the inshore waters of this MODIS scene, but further offshore in clearer waters this may be an issue. Quantifying the impact of bottom reflection is left for further work.

5.4 Summary

- The DALEC was deployed during a transect in order to collect radiometric data with which to compare with a co-incident MODIS overpass.

- Several atmospheric correction approaches were tested to determine the most accurate R_{rs} products for the match-up, whilst also yielding usable data in the sub-optimal glint-effected regions. The comparison between DALEC R_{rs} data was typically within 35% between 412 and 678nm.

- The MODIS overpass was vicariously calibrated with the DALEC R_{rs} data and a selection of water quality inversion algorithms determined in Chapter 4 were applied to the MODIS match-up data.

- All inversion outputs were then compared to the coincident *in-situ* flow-through datasets. A selection of these inversion algorithms were chosen based on their performance in the matchup scene, and their respective output parameters were empirically re-tuned to yield the most accurate water quality inversions as possible. The RMS error from the predictor-corrector GINV TChl algorithm was 26.9%. The GINV TSS algorithm RMSE was 11.9%, and the empirical GTSS RMSE was 14.6%.

- A brief sensitivity analysis was performed on the empirical TChl algorithms and the Maximum Band Ratio was shown to be adversely influenced by varying IOP concentrations and spectral shapes. The use of the empirical TChl algorithm should be avoided. Despite this, the 1km resolution re-tuned empirical GCHL2.1 TChl algorithm worked acceptably with a RMSE of 18.8% for the matchup scene.

Chapter 6

Conclusions and Suggestions for Further Work

In this thesis, regionally-specific relationships between water quality parameters, inherent optical properties and remote sensing reflectance were measured and documented. This enables the advanced interpretation of passive multispectral and hyperspectral ocean colour measurements for the GBR region. It is important to realise that the types of regression-comparison measurements used in this research are influenced by spatial uncertainties in addition to natural variability. One way to counter this is to increase the number of measurements in the area, and also to improve the spatial coherence of multi-parameter measurements in the first place. The combination of the DALEC radiometer and flow-through sampling system improved both of these aspects, and whilst these field-based relationships were determined over a short period of time, the unique sampling design and methodology allowed the collection of comparison measurements across a wide range of optical properties compared to conventional oceanographic strategies which focus more on the vertical distribution of IOPS. Given the ease of use of the DALEC and flow-through systems, there is no reason why these instruments cannot become permanent fixtures on ocean-going vessels in the future. Only with increased data density across seasons and the entire region of interest, will the true nature of concentration-specific IOPs of regions such as the Great Barrier Reef become more apparent.

In addition to the spatial variability problem, methodological uncertainty can add systematic errors on otherwise spatially coherent multi-parameter datasets. Firstly, improvements can certainly be made over measuring the absorption coefficients of marine particulates with glass fiber filters. Most of the ocean optics community now use the WETlabs ac-9 or ac-s instrument which can be adapted to the flow-through system which measures the absorption of relatively undisturbed particles whilst in suspension. Unlike the ac-9/s instruments, the filter-based absorption methodology is able to distinguish between pigmented and non-pigmented particles allowing the separation of a_{NAP} and a_{ϕ}. However, this approach is at the expense of adding potential bleach artifacts, cell disruption (pigment loss) during filtering, and spectral and magnitude uncertainties due to multiple scattering of the filter medium itself. In addition, quantifying the spectral nature of scattering losses in any transmission measurement (filter or suspension) needs improvement. Related to these methodological issues is the uncertain pathlength attenuation ('sigma') correction approach of the Hydroscat b_{bp} measurements. The sigma coefficients have changed periodically, and their use require accurate IOP inputs. The Hydrolight-based BRDF lookup table was subject to modelled phase functions, however in the future, *in situ* measured phase functions will be available, and so can be input directly into a radiative transfer forward model. This is unlikely to improve R_{rs} inversions by more than a few percent, however each methodological uncertainty through the entire chain from the water quality measurement all the way though to the satellite pixel has the ability to contribute uncertainty.

Efforts were made to quality control the DALEC data, however, as this is a new instrument, there will be improvements to the post-processing of the DALEC over time. Future improvement could include an active gymbal, which would incorporate accelerometers and a dual axis motor to compensate for any skewing of the DALEC due to strong wind or salt-effected friction damping. Ideally, in-water profile measurements to deduce $L_w(-0)$ and $E_d(-0)$ co-coincident with DALEC R_{rs} measurements will assist in the validation of the DALEC processing methodology developed in this thesis, which were based on the findings of Mobley

(1999) and Ruddick et al. (2006). To this end, further work could be inspired by the meticulous research of Stanford B. Hooker & Brown (2004) and Zibordi et al. (2004).

Additionally, further refinements of the floating Trichodesmium identification (other than simply flagging it) on both DALEC and MODIS imagery will ensure improvements in the radiative-transfer inversion process, and also allow the estimation of *Trichodesmium* concentration from Remote Sensing (McKinna et al. 2011).

As for the DALEC IOP inversions, although a wide variety of predictor-corrector inversion variant approaches were tested, other inversion approaches exist (Hedley et al. 2009, Mobley et al. 2005) which could show potential for improving the IOP yields from DALEC measurements for the situation where a_ϕ contributes minimally to R_{rs}. For the MODIS inversions, it was shown that the initial conditions provided to the Levenberg-Marquardt optimisation routine effected the output, so more work needs to be done on making sure the inversions converge on the best solution. The semi-analytical inversion model could be extended to include the fluorescence emission spectra of CDOM, Raman, Phycoerythrin and Phycocyanin, as these sources contribute to the R_{rs} spectrum between 400 and 667 nm (Spitzer & Dirks 1985, Bristow et al. 1981, French & Young 1952). Further, if red wavelength fluorescence can be either accounted for or avoided, then using spectral information from the DALEC between 667 nm and 900 nm could yield important information from shallow waters including bathymetry inversion and benthic habitat mapping (Lee et al. 1999, Hedley et al. 2009, Mobley et al. 2005).

The atmospheric correction of turbid water imagery was only briefly discussed in the last Chapter; enough to save the interested reader time in acquiring satisfactory looking images within the confines of the freely-available SEADAS software. Regionally-specific atmospheric correction needs to be studied thoroughly, and through the use of DALEC transects during satellite overpasses, researchers

may measure large amounts of sea-level validation reflectance measurements with which to spectrally quantify the effects of the atmosphere.

As for the MODIS imagery, apart from flagging or correcting for sunglint, cloud and trichodesmium, a bathymetric dataset such as the GBRDEM should be combined with a tidal model in order to estimate the water depth for a particular scene and then modify a land / bathymetry mask appropriately, otherwise shallow regions with clear water may be falsely interpreted as turbid water. This is all easily implemented, but is outside the scope of work presented here.

The DALEC-based TChl retrieval approached a RMSE of approximately 30%. Given the reported variability between a_ϕ and $TChl$, there is a question whether the focus of the ocean colour community should be shifted from providing $TChl$ to a_ϕ retrievals. Absorption is a more directly-measured parameter using remote sensing, more directly relevant to photosynthesis, and is also a consistent parameter with which to perform regional comparisons. The relative contribution of phytoplankon absorption to total non-water absorption was also found to be an important quality control parameter to ensure the successful inversion of the down-stream TChl inversion.

The matchup image shown in Chapter 5 is only one out of approximately 75,000 scenes available from MODIS Aqua and Terra over the past decade. The most significant further work will be processing and analysing this spatio-temporal information into something relevant for the sustainability of the GBR region; both in human and nature's terms.

Bibliography

Abbott, M. R. & Letelier, R. M. (1999), Chlorophyll fluorescence (modis product number 20), *in* 'Algorithm Theoretical Basis Document', NASA Goddard Space Flight Center.

Arblaster, J. M., Meehl, G. A. & Moore, A. M. (2002), 'Interdecadal modulation of Australian rainfall', *Climate Dynamics* **18**, 519–531.

Babin, M., Morel, A., Fournier-Sicre, V., Fell, F. & Stramski, D. (2003), 'Light scattering properties of marine particles in coastal and open ocean waters as related to the particle mass concentration', *Limnology and Oceanography* **48(2)**, 843–859.

Babin, M. & Stramski, D. (2002), 'Light absorption by aquatic particles in the near-infrared spectral region', *Limnology and Oceanography* **47(3)**, 911–915.

Babin, M. & Stramski, D. (2004), 'Variations in the mass-specific absorption coefficient of mineral particles suspended in water', *Limnology Oceanography* **49(3)**, 756–767.

Babin, M., Stramski, D., Ferrari, G. M., Claustre, H., Bricaud, A., Obolensky, G. & Hoepnffner, N. (2003), 'Variations in the light absorption coefficients of phytoplankton, nonalgal particles, and dissolved organic matter in coastal waters around Europe', *Journal of Geophysical Reseach* **108(C7)**, 4.1–4.20.

Bailey, S. W., Franz, B. A. & Werdell, P. J. (2010), 'Estimation of near-infrared water-leaving reflectance for satellite ocean color data processing', *Optics Express* **18(7)**, 7521–7527.

Berthon, J.-F., Shybanov, E., Lee, M. E.-G. & Zibordi, G. (2007), 'Measurements and modeling of the volume scattering function in the coastal northern Adriatic Sea', *Applied Optics* **46**, 5189 – 5203.

Bissett, W. P., Patch, J. S., Carder, K. L. & Lee, Z. P. (1997), 'Pigment packaging and Chl a-specific absorption in high-light oceanic waters', *Limnology and Oceanography* **42(5)**, 961 – 968.

Blondeau-Patissier, D., Brando, V. E., Oubelkheir, K., Dekker, A. G., Clementson, L. A. & Daniel, P. (2009), 'Bio-optical variability of the absorption and scattering properties of the Queensland inshore and reef waters, Australia', *Journal of Geophysical Research* **114**, C05003.

Bohren, C. F. & Huffman, D. R. (1983), *Absorption and Scattering of Light by Small Particles*, John Wiley & Sons, Inc.

BOM (2009), 'Average annual rainfall gridded product', WWW.
URL: *http://www.bom.gov.au/web01/ncc/www/climatology/rainfall/rainan.ZIP*

BOM (2012*a*), 'Average daily solar exposure annual', WWW.
URL: *http://www.bom.gov.au/jsp/ncc/climate_averages/solar-exposure/index.jsp*

BOM (2012*b*), 'Climate statistics for australian locations: Monthly climate statistics', WWW.
URL: *http://www.bom.gov.au/climate/averages/tables/cw_031011.shtml*

Boss, E. & Pegau, W. S. (2001), 'Relationship of light scattering at an angle in the backward direction to the backscattering coefficient', *Applied Optics* **40**(30), 5503 – 5507.

Boss, E., Pegau, W. S., Lee, M., Twardowski, M., Shybanov, E., Korotaev, G. & Baratange, F. (2004), 'Particulate backscattering ratio at leo 15 and its use to study particle composition and distribution', *Journal of Geophysical Research* **109(C0)**, 1014–1024.

Boss, E., Pegau, W. S., Zaneveld, J. R. V. & Barnard, A. H. (2001), 'Spatial and temporal variability of absorption by dissolved material at a continental shelf', *Journal of Geophysical Reseach* **106(C5)**, 9499–9507.

Boss, E., Slade, W. H., Behrenfeld, M. & Dall'Olmo, G. (2009), 'Acceptance angle effects on the beam attenuation in the ocean', *Optics Express* **17(3)**, 1535–1550.

Boto, K. G., Alongi, D. M. & Nott, A. L. J. (1989), 'Dissolved organic carbon-bacteria interactions at the sediment-water interface in a tropical mangrove system', *Marine Ecology Progress Series* **51**, 243 – 251.

Bowers, D. G. & Binding, C. E. (2006), 'The optical properties of mineral suspended particles: A review and synthesis', *Estuarine, Coastal and Shelf Science* **67**, 219 – 230.

Bricaud, A., Babin, M., Morel, A. & Claustre, H. (1995), 'Variability in the chlorophyll-specific absorption coefficients of natural phytoplankton: Analysis and parameterization', *Journal of Geophysical Research* **100**, 13,321 – 13,332.

Bricaud, A., Claustre, H., Ras, J. & Oubelkheir, K. (2004), 'Natural variability of phytoplanktonic absorption in oceanic waters: Influence of the size structure of algal populations', *Journal of Geophysical Research* **109**, C11010.

Bricaud, A., Morel, A. & Prieur, L. (1981), 'Absorption by dissolved organic matter of the sea (yellow substance) in the UV and visible domains', *Limnology and Oceanography* **26(1)**, 43–53.

Bristow, M., Nielsen, D., Bundy, D. & Furtek, R. (1981), 'Use of water Raman emission to correct airborne laser fluorosensor data for effects of water optical attenuation', *Applied Optics* **20(17)**, 2889–2906.

Brodie, J., McKergow, L. A., Prosser, I. P., Furnas, M., Hughes, A. O. & Hunter, H. (2003), Sources of sediment and nutrient exports to the Great Barrier Reef World Heritage Area, Technical report, Australian Centre for Tropical Freshwater Research.

Buiteveld, H., Hakvoort, J. H. M. & Donze, M. (1994), The optical properties of pure water, *in* 'Ocean Optics XII Proceedings', Vol. 2258, SPIE, pp. 174 – 183.

Carder, K. L., Chen, F. R. & Hawes, S. K. (2003), Instantaneous photosynthetically available radiation and absorbed radiation by phytoplankton, *in* 'Algorithm Theoretical Basis Document', NASA Goddard Space Flight Center.

Carder, K. L., Steward, R. G., Harvey, G. R. & Ortner, P. B. (1989), 'Marine humic and fulvic acids: Their effects on remote sensing of ocean chlorophyll', *Limnology and Oceanography* **34(1)**, 68–81.

Carder, K. L., Steward, R. G., Paul, J. H. & Vargo, G. A. (1986), 'Relationships between chlorophyll and ocean colour constituents as they affect remote-sensing reflectance models', *Limnology and Oceanography* **31(2)**, 403–413.

Chami, M., Shybanov, E. B., Gueorgui A, K., Lee, M. E. G., Martynov, O. V. & Korotaev, G. K. (2006), 'Spectral variation of the volume scattering function measured over the full range of scattering angles in a coastal environment', *Applied Optics* **45(15)**, 3605 – 3619.

Chavez, F. P., Buck, K. R., Bidigare, R. R., Karl, D. M., Hebel, D., Latasa, M. & Campbell, L. (1995), 'On the chlorophyll a retention properties of glass-fiber GF/F filters', *Limnology and Oceanography* **40(2)**, 428–433.

Choukroun, S., Ridd, P. V., Brinkman, R. & McKinna, L. I. (2009), 'On the surface circulation in the western Coral Sea and residence times in the Great Barrier Reef', *Journal of Geophysical Reseach* **115**, C06013.

Church, J. A. (1987), 'East Australian Current adjacent to the Great Barrier Reef', *Australian Journal of Marine and Fresh Water Research* **38(6)**, 671 – 683.

Ciotti, A. M., Lewis, M. R. & Cullen, J. J. (2002), 'Assessment of the relationships between dominant cell size in natural phytoplankton communities and the spectral shape of the absorption coefficient', *Limnology and Oceanography* **47(2)**, 404–417.

Cleveland, J. & Weidemann, A. (1993), 'Quantifying absorption by aquatic particles: A multiple scattering correction for glass-fiber filters', *Limnology and Oceanography* **38(6)**, 1321–1327.

Cooper, T. F., Uthicke, S., Humphrey, C. & Fabricius, K. E. (2007), 'Gradients in water column nutrients, sediment parameters, irradiance and coral reef development in the Whitsunday Region, central Great Barrier Reef', *Easturine, Coastal and Shelf Science* **74**, 458 – 470.

Crosbie, N. D. & Furnas, M. J. (2001), 'Abundance, distribution and flow-cytometric characterization of picophytoprokaryote populations in central (17s) and southern (20s) shelf waters of the Great Barrier Reef', *Journal of Plankton Research* **23**, 809 – 828.

D&A (2006), *OBS-3+ information sheet*, D&A Instrument Company, 24 Seton Road, Port Townsend, Washington U.S.A. 98368.

Dall'Olmo, G. & Gitelson, A. A. (2006), Absorption properties of dissolved and particulate matter in turbid productive inland lakes, *in* 'Proceedings of Ocean Optics XVIII, Montreal, Quebec, 9-13 October, 2006, pp. 1-15.', pp. 1 – 15.

De'ath, G. & Fabricius, K. (2010), 'Water quality as a regional driver of coral biodiversity and macroalgae on the Great Barrier Reef', *Ecological Applications* **20(3)**, 840 – 850.

Del-Castillo, C. E. (2005), Remote sensing of organic matter in coastal waters, *in* R. L. Miller, C. E. Del-Castillo & B. A. Mckee, eds, 'Remote Sensing of Coastal Aquatic Environments: Technologies, Techniques and Applications', Springer, chapter 7, pp. 157–180.

Del-Castillo, C. E. & Miller, R. L. (2008), 'On the use of ocean color remote sensing to measure the transport of dissolved organic carbon by the Mississippi River plume', *Remote Sensing of the Environment* **112**, 836844.

Devlin, M. J. & Brodie, J. (2005), 'Terrestrial discharge into the Great Barrier Reef lagoon: nutrient behavior in coastal waters', *Marine Pollution Bulletin* **51**, 9–22.

Devlin, M., Waterhouse, J., Taylor, J. & Brodie, J. (2001), Flood plumes in the Great Barrier Reef: Spatial and temporal patterns in composition and distribution, Technical report, Great Barrier Reef Marine Park Authority.

Doxaran, D., Babin, M. & Leymarie, E. (2007), 'Near-infrared light scattering by particles in coastal waters', *Optics Express* **15(20)**, 12834 – 12849.

Duysens, L. M. (1956), 'The flattenning of the asborption spectra of suspensions as compared to that of solutions', *Biochimica et Biophysica Acta* **19**, 1–12.

Faust, M. A. & Norris, K. H. (1985), 'In vivo spectrophotometric analysis of photosynthetic pigments in natural populations of phytoplankton', *Limnology and Oceanography* **30(6)**, 1316 – 1322.

Forand, J. L. & Fournier, G. R. (1999), Particle distributions and index of refraction estimation for Canadian waters, *in* 'Airborne and In-Water Underwater Imaging'.

Fournier, G. R. & Forand, J. L. (1994), Analytic phase function for ocean water, *in* 'Ocean Optics XII Proceedings', Vol. 2258, SPIE, pp. 194 – 201.

Franz, B. A., Wedell, P. J., Meister, G., Kwiatkowska, E. J., Bailey, S. W., Ahmad, Z. & McClain, C. R. (2006), Modis land bands for ocean remote sensing applications, *in* 'Proceedings of Ocean Optics XVIII, Montreal, Canada'.

French, C. & Young, V. K. (1952), 'The fluorescence spectra of red algae and the transfer of energy from phycoeryrthrin to phycocyanin and chlorophyll', *The Journal of General Physiology* pp. 873–890.

Furnas, M. J. (2003), *Catchments and Corals: Terrestrial Runoff to the Great Barrier Reef*, Australian Institute of Marine Science, CRC Reef.

Furnas, M. J. & Mitchell, A. W. (1986), 'Phytoplankton dynamics in the central Great Barrier Reef - i. seasonal changes in biomass and community structure and their relation to intrusive activity', *Continental Shelf Research* **6**, 363 – 384.

Furnas, M. J., Mitchell, A. W., Gilmartin, M. & Revelante, N. (1990), 'Phytoplankton biomass and primary production in semi-enclosed reef lagoons of the central Great Barrier Reef, australia', *Coral Reefs* **9**, 1–10.

Furnas, M., Mitchell, A. & Skuza, M. (1997), River inputs of nutrients and sediment to the Great Barrier Reef, *in* D. Wachenfeld, J. Oliver & K. Davis, eds, 'State of the Great Barrier Reef World Heritage Area Workshop', Great Barrier Reef Marine Park Authority.

Furnas, M., Mitchell, A., Skuza, M. & Brodie, J. (2005), 'In the other 90enhanced nutrient avaliability in the Great Barrier Reef lagoon', *Marine Pollution Bulletin* **51**, 253–265.

GA (1998), 'Drainage - topo 2.5m 1998'. ANZCW0702000026.

Garver, S. A. & Siegel, D. A. (1997), 'Inherent optical property inversion of ocean color spectra and its biogeochemical interpretation 1. time series from the sargasso sea', *Journal of Geophysical Reseach* **102(C8)**, 18,607–18,625.

Garver, S. A., Siegel, D. A. & Mitchell, B. G. (1994), 'Variability in near-surface particulate absorption spectra: What can a satellite ocean color imager see?', *Limnology and Oceanography* **39(6)**, 1394 – 1367.

GBRMPA (2007), Measuring the economic & financial value of the Great Barrier Reef Marine Park 2005-06, Technical report, Report by Access Economics Pty Limited for Great Barrier Reef Marine Park Authority.

Gomez, F. (2007), 'Gymnodinioid dinoflagellates (gymnodiniales, dinophyceae) in the open Pacific Ocean', *Algae* **22(4)**, 273–286.

Gordon, H. R., Brown, O. B., Evans, R. H., Brown, J. W., Smith, R. C., Baker, K. S. & Clark, D. K. (1988), 'A semianalytic radiance model of ocean color', *Journal of Geophysical Research* **93(D9)**, 10909–10924.

Gordon, H. R., Brown, O. B. & Jacobs, M. M. (1975), 'Computer relationships between the inherent and apparent optical properties of a flat homogeneous ocean', *Applied Optics* **14(2)**, 417–427.

Gordon, H. R. & Wang, M. (1994), 'Retrieval of water-leaving radiance and aerosol optical thickness over the oceans with seawifs: a preliminary algorithm', *Applied Optics* **33(3)**, 443–452.

Haynes, D., Bass, D., Brodie, J., Christie, C., Devlin, M., Michalek-Wagner, K., Morris, S., Ramsay, M., Storrie, J., Waterhouse, J. & Yorkston, H. (2001), Great Barrier Reef water quality: current issues, Technical report, Great Barrier Reef Marine Park Authority.

Hedley, J., Roelfsema, C. & Phinn, S. R. (2009), 'Efficient radiative transfer model inversion for remote sensing applications', *Remote Sensing of Environment* **113(11)**, 2527–2532.

Herbland, A. (1988), The deep phaeopigments maxium in the ocean: Reality or illusion?, *in* B. J. Rothschild, ed., 'Toward a Theory on Biological-Physical Interactions in the World Ocean', Kulwer Academic Publishers, pp. 157 – 172.

HOBILabs (2008), *HydroScat-6 Spectral Backscattering Sensor USERS MANUAL*, h edn, Hydro-Optics, Biology, and Instrumentation Laboratories, Inc.

Hoepnffner, N. & Sathyendranath, S. (1991), 'Effect of pigment composition on absorption properties of phytoplankton', *Marine Ecology Progress Series* **73**, 11 – 23.

Hydrosoft 2.5 Software for HOBI Labs Optical Oceanographic Instruments: User's Manual (2002).

Islam, A., Wang, L., Smith, C., Reddy, S., Lewis, A. & Smith, A. (2007), 'Evaluation of satellite remote sensing for operational monitoring of sediment plumes producted by dredging at Hay Point, Queensland, Australia', *Journal of Applied Remote Sensing* **1 (011506)**, 1–15.

Jeffrey, S. W. & Humphrey, G. (1975), 'New spectrophotometric equations for determining chlorophylls a, b, c1 and c2 in higher plants, algae and natural phytoplankton', *Biochemie und Physiologie der Pflanzen* **167**, 191 – 194.

Kirk, J. T. O. (1983), *Light and Photosynthesis in Aquatic Ecosystems*, Cambridge University Press.

Kirkup, L. (1994), *Experimental Methods: An Introduction to the Analysis and Presentation of Data*, John Wiley & Sons, Inc.

Kishino, M., Takahashi, M., Okami, N. & Ichimura, S. (1985), 'Estimation of the spectral absorption coefficients of phytoplankton in the sea', *Bulletin of Marine Science* **37(2)**, 634–642.

Knap., A., Michaels, A., Close, A., Ducklow, H. & Dickson, A. (1994), Protocols for the joint global ocean flux study (jgofs) core measurements, *in* 'Reprint of the IOC Manuals and Guides No. 29', number 19, UNESCO.

Kullenberg, G. (1974), *Observed and computed scattering functions*, Academic Press, chapter 2, pp. 25 – 49.

Kutser, T., Dekker, A. G. & Skirving, W. (2003), 'Modeling spectral discrimination of Great Barrier Reef benthic communities by remote sensing instruments', *Limnology and Oceanography* **48(1, part 2)**, 497 – 510.

Langford, V. S., McKinley, A. J. & Quickenden, T. I. (2001), 'Temperature dependence of the visible-near-infrared absorption spectrum of liquid water', *Journal of Physical Chemistry A* **105**, 8916–8921.

Larcombe, P. & Carter, R. (2004), 'Cyclone pumping, sediment partitioning and the development of the Great Barrier Reef shelf system: a review', *Quaternary Science Reviews* **23**, 107–135.

Larcombe, P., Costen, A. & Woolfe, K. J. (2001), 'The hydrodynamic and sedimentary setting of nearshore coral reefs, central Great Barrier Reef shelf, australia: Paluma Shoals, a case study', *Sedimentology* **48**, 811 – 835.

Laurion, I., Blouin, F. & Roy, S. (2003), 'The quantitative filter technique for measuring phytoplankton absorption: Interference by MAAs in the UV waveband', *Limnology and Oceanography: Methods* **1**, 1–9.

Lee, M. E. & Lewis, M. R. (2003), 'A new method for the measurement of the optical volume scattering function in the upper ocean', *Journal of Atmospheric and Oceanic Technology* **20**, 563 – 571.

Lee, Z., Carder, K. & Du, K. (2004), 'Effects of molecular and particle scatterings on the model parameter for remote-sensing reflectance', *Applied Optics* **43(25)**, 4957–4964.

Lee, Z., Carder, K. L. & Arnone, R. A. (2002), 'Deriving inherent optical properties from water color: a multiband quasi-analytical algorithm for optically deep waters', *Applied Optics* **41(27)**, 5755–5772.

Lee, Z., Carder, K. L., Mobley, C. D., Steward, R. G. & Patch, J. S. (1998), 'Hyperspectral remote sensing for shallow waters. 1. a semianalytical model', *Applied Optics* **37(27)**, 6329–6338.

Lee, Z., Carder, K. L., Mobley, C. D., Steward, R. G. & Patch, J. S. (1999), 'Hyperspectral remote sensing for shallow waters: 2. deriving bottom depths and water properties by optimization', *Applied Optics* **38(18)**, 3831–3843.

Lee, Z., Carder, K. L., Steward, R., Peacock, T. G., Davis, C. & Mueller, J. L. (1997), 'Remote sensing reflectance and inherent optical properties of oceaninc waters derived from above-water measurements', *SPIE* **2963**, 160–166.

Lewis, A. (2001), Great Barrier Reef Depth and Elevation models: GBRDEM, Technical report, Department of Tropical Environment Studies and Geography, James Cook University.

Lewis, S. E., Brodie, J. E., Bainbridge, Z. T., Rohde, K. W., Davis, A. M., Masters, B. L., Maughan, M., Devlin, M. J., Mueller, J. F. & Schaffelke, B. (2009), 'Herbicides: A new threat to the Great Barrier Reef', *Environmental Pollution* **157**, 2470 – 2484.

Loisel, H., Meriaux, X., Poteau, A., Artigas, L. F., Lubac, B., Gardel, A., Caillaud, J. & Lesourd, S. (2009), 'Analyze of the inherent optical properties of French Guiana coastal waters for remote sensing applications.', *Journal of Coastal Research* **SI56**, 1532–1536.

Loisel, H. & Morel, A. (1998), 'Light scattering and chlorophyll concentration in case 1 waters: A reexamination', *Limnology and Oceanography* **43(5)**, 847–858.

Lorenzen, C. J. & Downs, J. N. (1986), 'The specific absorption coefficients of chlorophyllide a and pheophorbide a in 90fluorometric determination of chlorophyll and pheopigments', *Limnology and Oceanography* **31(2)**, 449 – 452.

Maffione, R. A. & Dana, D. R. (1997), 'Instruments and methods for measuring the backward-scattering coefficient of ocean waters', *Applied Optics* **36**(24), 6057 – 6067.

Marken, E. (2005), A bio-optical model for Norwegian coastal waters, PhD thesis, University of Bergen.

Markwardt, C. B. (2009), Non-linear least-squares fitting in IDL with MPFIT, *in* D. A. Bohlender, D. Durand, & P. Dowler, ed., 'Astronomical Society of the Pacific Conference Series', Vol. 411 of *Astronomical Society of the Pacific Conference Series*, pp. 251–+.

Maxwell, W. G. H. (1968), *Atlas of the Great Barrier Reef*, Elsevier, Amsterdam.

McCulloch, M., Fallon, S., Wyndam, T., Lough, E. H. J. & Barnes, D. (2003), 'Coral record of increased sediment flux to the inner Great Barrier Reef since European settlement', *Nature* **421**, 727 – 730.

McKee, D. & Cunningham, A. (2005), 'Evidence for wavelength dependence of the scattering phase function and its implication for modeling radiance transfer in shelf areas', *Applied Optics* **44(1)**, 126 – 135.

McKee, D., Piskozub, J. & Brown, I. (2008), 'Scattering error corrections for in situ absorption and attenuation measurements', *Optics Express* **16**, 19480 – 19492.

McKinna, L. I. (2008), Cdom samples.

McKinna, L. I. (2010), Optical Detection and Quantification of Trichodesmium spp. within the Great Barrier Reef, PhD thesis, James Cook University.

McKinna, L. I., Furnas, M. J. & Ridd, P. V. (2011), 'A simple, binary classification algorithm for the detection of trichodesmium spp. within the Great Barrier Reef using MODIS imagery', *Limnology and Oceanography: Methods* **9**, 50–66.

Meuller, J. L. & Austin, R. (2003), Characterization of oceanographic and atmospheric radiometers, *in* 'Ocean Optics Protocols For Satellite Ocean Color

Sensor Validation, Revision 4', Vol. II, National Aeronautical and Space Administration, pp. 17 – 33.

Mitchell, B. G., Bricaud, A., Carder, K., Cleveland, J., Ferrari, G., Gould, R., Kahru, M., Kishino, M., Maske, H., Moisan, T., Moore, L., Nelson, N., Phinney, D., Reynolds, R., Sosik, H., Stramski, D., Tassan, S., Trees, C., Weidemann, A., Wieland, J. & Vodacek, A. (2000), Determination of spectral absorption coefficients of particles, dissolved material and phytoplankton for discrete water samples, *in* G. S. Fargion & J. L. Mueller, eds, 'Ocean Optics Protocols For Satellite Ocean Color Sensor Validation, Revision 2', National Aeronautical and Space Administration, pp. 125–143.

Mitchell, B. G., Kahru, M., Wieland, J. & Stramska, M. (2003), Determination of spectral absorption coefficients of particles, dissolved material and phytoplankton for discrete water samples, *in* G. S. Fargion & J. L. Mueller, eds, 'Ocean Optics Protocols For Satellite Ocean Color Sensor Validation, Revision 4', National Aeronautical and Space Administration, pp. 39–63.

Mobley, C. D. (1989), 'A numerical model for the computation of radiance distributions in natural waters with wind-roughened surfaces', *Limnology and Oceanography* **34(8)**, 1473–1483.

Mobley, C. D. (1994), *Light and Water*, Academic Press, Inc.

Mobley, C. D. (1999), 'Estimation of the remote-sensing reflectance from above-surface measurements', *Applied Optics* **38(36)**, 7442–7455.

Mobley, C. D., Sundman, L. K. & Boss, E. (2002), 'Phase function effects on oceanic light fields', *Applied Optics* **41(6)**, 1035 – 1050.

Mobley, C. D., Sundman, L. K., Davis, C. O., Bowles, J. H., Downes, T. V., Leathers, R. A., Montes, M. J., Bissett, W. P., Kohler, D. D. R., Reid, R. P., Louchard, E. M. & Gleason, A. (2005), 'Interpretation of hyperspectral remote-sensing imagery by spectrum matching and look-up tables', *Applied Optics* **44(17)**, 3576–3592.

Morel, A. (1987), 'Chlorophyll-specific scattering coefficient of phytoplankton. A simplified theoretical approach', *Deep Sea Research* **34**, 1093–1105.

Morel, A. (1991), Optics of marine particles and marine optics, *in* 'Particle analysis in Oceanography', Vol. G27 of *NATO ASI Series*, NATO, pp. 141 – 188.

Morel, A., Ahn, Y.-H., Partensky, F., Vaulot, D. & Claustre, H. (1993), 'Prochlorococcus and synechococcus: A comparative study of their optical properties in relation to their size and pigmentation', *Journal of Marine Research* **51**, 617 – 649.

Morel, A. & Bricaud, A. (1981), 'Theoretical results concerning light absorption in a discrete medium and application to specific absorption of phytoplankton', *Deep Sea Research* **28A(11)**, 1375–1393.

Morel, A. & Prieur, L. (1977), 'Analysis of variations in ocean color', *Limnology and Oceanography* **22(4)**, 709–722.

Moss, A., Brodie, J. & Furnas, M. (2005), 'Water quality guidelines for the Great Barrier Reef World Heritage Area: a basis for development and preliminary values', *Marine Pollution Bulletin* **51**, 76 – 88.

Mueller, H. & Ayukai, T. (1998), 'Concentration and molecular weight distribution of dissolved organic carbon in a mangrove creek in the Hinchinbrook area, Australia', *Mangroves and Salt Marshes* **2**, 231–235.

Nair, A., Sathyendranath, S., Platt, T., Morales, J., Stuart, V., Forget, M.-H., Devred, E. & Bouman, H. (2008), 'Remote sensing of phytoplankton functional types', *Remote Sensing of Environment* **112**, 3366 3375.

Nelson, N. B., Prezelin, B. B. & Bidigare, R. R. (1993), 'Phytoplankton light absorption and the package effect in California coastal waters', *Marine Ecology Progress Series* **94**, 217 – 227.

NOAA (1997), Veg index users guide, Technical report, National Oceanic and Atmospheric Administration. Appendix L.

Obernosterer, I. & Benner, R. (2004), 'Competition between biological and photochemical processes in the mineralization of dissolved organic carbon', *Limnology and Oceanography* **49(1)**, 117–124.

OBPG, N. G. (2011), 'SeaWiFS Data Analysis System (SEADAS)', Software program.
URL: *http://oceancolor.gsfc.nasa.gov/seadas*

O'Bree, T. (2007), Investigations of Light Scattering by Australian Natural Water for Remote Sensing Applications, PhD thesis, School of Applied Sciences, Applied Physics, RMIT University.

Ocean Optics, I. (2011*a*), 'OOINLCorrect loading non-linearity correction coefficients instructions', WWW.
URL: *http://www.oceanoptics.com/technical/OOINLCorrect Linearity Coeff Proc.pdf*

Ocean Optics, I. (2011*b*), 'USB2000-VIS-NIR Spectrometer', WWW.
URL: *http://www.oceanoptics.com/Products/usb2000visnir.asp*

Oishi, T. (1990), 'Significant relationship between the backward scattering coefficient of sea water and the scatterance at 120°', *Applied Optics* **29**(31), 4658 – 4665.

O'Reilly, J. E., Maritorena, S., O'Brien, M. C., Siegel, D. A., Toole, D., Menzies, D., Smith, R. C., Mueller, J. L., Mitchell, B. G., Kahru, M., Chavez, F. P., Strutton, P., Cota, G. F., Hooker, S. B., McClain, C. R., Carder, K. L., Muller-Karger, F., Harding, L., Magnuson, A., Phinney, D., Moore, G. F., Aiken, J., Arrigo, K. R., Letelier, R. & Culver, M. (2000), Volume 11, SeaWiFS postlaunch calibration and validation analyses, part 3, Technical memorandum, NASA.

Orpin, A. R., Ridd, P. V. & Stewart, L. K. (1999), 'Assessment of the relative importance of major sediment-transport mechanisms in the central Great Barrier Reef lagoon', *Australian Journal of Earth Sciences* **46**, 883–896.

Parsons, T. R., Maitia, Y. & Lalli, C. (1984), *A Manual of Chemical and Biological Methods for Seawater Analysis*, Pergamon Press.

Pegau, S., Zaneveld, J. V., Mitchell, B. G., Mueller, J. L., Kahru, M., Wieland, J. & Stramska, M. (2002), Inherent optical properties: Instruments, characterizations, field measurements and data analysis protocols, *in* J. L. Mueller, G. S. Fargion & C. R. McClain, eds, 'Ocean Optics Protocols For Satellite Ocean Color Sensor Validation, Revision 4', Vol. Volume IV, National Aeronautical and Space Administration.

Pegau, W. S., Gray, D. & Zaneveld, J. R. V. (1997), 'Absorption and attenuation of visible and near-infrared light in water: dependence on temperature and salinity', *Applied Optics* **36(24)**, 6035–6046.

Petzold, T. J. (1977), *Volume scattering functions for selected ocean waters*, Stroudsberg, chapter 12, pp. 150 – 174.

Pope, R. M. & Fry, E. S. (1997), 'Absorption spectrum (380–700 nm) of pure water. ii. integrating cavity measurements', *Applied Optics* **36**(33), 8710 – 8723.

Power, S., Haylock, M., Colman, R. & Wang, X. (2006), 'The predictability of inderedcadal changes in ENSO activity and ENSO teleconnections', *Journal of Climate* **19**, 4755 – 4771.

Preisendorfer, R. W. (1976), *Hydrologic Optics*, PDF Reprint by Office of Naval Research U. S. Department of Commerce National Oceanic and Atmospheric Administration Environmental Research Laboratories.

Prieur, L. & Sathyendranath, S. (1981), 'An optical classification of coastal and oceanic waters based on the specific spectral absorption curves of phytoplankton pigments, dissolved organic matter, and other particulate materials', *Limnology and Oceanography* **26(4)**, 671–689.

Qin, Y., Brando, V. E., Dekker, A. G. & Blondeau-Patissier, D. (2007), 'Validity of SeaDAS water constituents retrieval algorithms in australian tropical coastal waters', *Geophysical Reseach Letters* **34**, L21603.

Reda, I. & Andreas, A. (2008), Solar position algorithm for solar radiation applications, Technical Report NREL/TP-560-34302, National Renewable Energy Laboratory, 1617 Cole Boulevard Golden, Colorado 80401-3393.

Revelante, N., Williams, W. T. & Bunt, J. S. (1982), 'Temporal and spatial distribution of diatoms, dinoflagellates and trichodesmium in waters of the Great Barrier Reef', *Journal of Experimental Marine Biology and Ecology* **63**, 27 – 45.

Robertson, A. W., Kirshner, S., Smyth, P., Charles, S. P. & Bates, B. C. (2006), 'Subseasonal-to-interdecadal variability of the Australian monsoon over North Queensland', *Quarterly Journal of the Royal Meteorological Society* **132**, 519 – 542.

Roesler, C. S. (1998), 'Theoretical and experimental approaches to improve the accuracy of particulate absorption coefficients derived from the quantitative filter technique', *Limnology and Oceanography* **43(7)**, 1649–1660.

Roesler, C. S. & Perry, M. J. (1995), 'In situ phytoplankton absorption, fluorescence emission and particulate backscattering spectra determined from reflectance', *Journal of Geophysical Reseach* **100(C7)**, 13,279–13,294.

Roesler, C. S., Perry, M. J. & Carder, K. L. (1989), 'Modeling the in situ phytoplankton absorption from totol absorption spectra in productive inland marine waters', *Limnology and Oceanography* **34(8)**, 1510 – 1523.

Rottgers, R., Doerffer, R., McKee, D. & Schonfeld, W. (2013), The water optical properties processor (wopp): Pure water spectral absorption, scattering and real part of refractive index model, Technical report, Helmholtz-Zentrum Geesthacht Centre for Materials and Coastal Research.

Ruddick, K. G., Cauwer, V. D. & Park, Y.-J. (2006), 'Seaborne measurements of near infrared water-leaving reflectance: The similarity spectrum for turbid waters', *Limnology and Oceanography* **51(2)**, 1167 – 1179.

Ruddick, K. G., Ovidio, F. & Rijkeboer, M. (2000), 'Atmospheric correction

of seawifs imagery for turbid coastal and inland waters', *Applied Optics* **39(6)**, 897–912.

Sathyendranath, S. (2000), Remote sensing of ocean colour in coastal, and other optically-complex, waters, Technical Report 3, International Ocean-Colour Coordinating Group.
URL: *www.ioccg.org*

SBE (2003), *Sea-Bird Electronics Data Processing software help menu*, 5.29b edn, Sea-bird Electronics Inc, seabird@seabird.com. Help menu -¿ Contents -¿ Configuring the Instrument -¿ Calibration Coefficients - Voltage Sensors.

Schaffelke, B., Carleton, J., Doyle, J., Furnas, M., Gunn, K., Skuza, M., Wright, M. & Zagorskis, I. (2011), Reef rescue marine monitoring program, Final report, Great Barrier Reef Marine Park Authority.

Scott, F. & Marchant, H., eds (2005), *Antarctic Marine Protists*. ISBN 0 642 56835 9.

SEQUIOA Scientific, I. (2008), 'LISST-100X Sales Brochure April 2008', WWW.

Shi, W. & Wang, M. (2007), 'Detection of turbid waters and absorbing aerosols for the modis ocean color data processing', *Remote Sensing of Environment* **110**, 149–161.

Siegel, D. A., Maritorena, S., Nelson, N. B., Hansell, D. A. & Lorenzi-Kayser, M. (2002), 'Global distribution and dynamics of colored dissolved and detrital organic materials', *Journal of Geophysical Research* **107(C12)**, 21.1–21.14.

Siegel, D. A., Wang, W., Maritorena, S. & Robinson, W. (2000), 'Atmospheric correction of satellite ocean color imagery: the black pixel assumption', *Applied Optics* **39(21)**, 3582–3591.

Spitzer, D. & Dirks, R. W. J. (1985), 'Contamination of the reflectance of natural waters by solar-induced fluorescence of dissolved organic matter', *Applied Optics* **24(4)**, 444–445.

Stanford B. Hooker, Giuseppe Zibordi, J.-F. B. & Brown, J. W. (2004), 'Above-water radiometry in shallow coastal waters', *Applied Optics* **43(21)**, 4252–4268.

Steinberg, D. K., Nelson, N. B., Carlson, C. A. & Prusak, A. C. (2004), 'Production of chromophoric dissolved organic matter (CDOM) in the open ocean by zooplankton and the colonial cyanobacterium trichodesmium spp.', *Marine Ecology Progress Series* **267**, 45–56.

Steven, A. D. L., Pantus, F., Brooks, D. & Trott, L. (1998), Long-term chlorophyll monitoring the Great Barrier Reef lagoon: Status report 1, 1993-1995, Technical report, Great Barrier Reef Marine Park Authority.

Stramski, D., Boss, E., Bogucki, D. & Voss, K. J. (2004), 'The role of seawater constituents in light backscattering in the ocean', *Progress in Oceanography* **61**, 27–56.

Stramski, D., Bricaud, A. & Morel, A. (2001), 'Modeling the inherent optical properties of the ocean based on the detailed composition of the planktonic community', *Applied Optics* **40(18)**, 2929 – 2945.

Subramaniam, A., Carpenter, E. J., Karentz, D. & Falkowski, P. G. (1999), 'Bio-optical properties of the marine diazotrophic cyanobacteria Trichodesmium spp. i. absorption and photosynthetic action spectra', *Limnology and Oceanography* **44(3)**, 608 – 617.

Sullivan, J. M., Twardowski, M. S., Ronald, J., Zaneveld, V. & Moore, C. C. (2013), Measuring optical backscattering in water, *in* 'Light Scattering Reviews 7', Vol. 7, Springer Praxis Books, pp. 189 – 224.

Sullivan, J. M., Twardowski, M. S., Zaneveld, J. R. V., Moore, C. M., Barnard, A. H., Donaghay, P. L. & Rhoades, B. (2006), 'Hyperspectral temperature and salt dependencies of absorption by water and heavy water in the 400-750 nm spectral range', *Applied Optics* **45(21)**, 5294–5309.

Sullivan, J. & Twardowski, M. (2009), 'Angular shape of the volume scattering function in the backward direction.', *Applied Optics* .

Tabassum, A. & Saifullah, S. (2010), 'The planktonic diatom of the genus Chaetoceros Ehrenberg from northwestern Arabian Sea bordering Pakistan', *Pakistan Journal of Botany* **42(2)**, 1137 – 1151.

Tassan, S. & Ferrari, G. M. (1995), 'An alternative approach to absorption measurements of aquatic particles on filters', *Limnology and Oceanography* **40(8)**, 1358–1368.

Teanpisut, K. & Patarajinda, S. (2007), 'Species diversity of marine planktonic diatoms around Chang Islands, Trat Province', *Kasetsart Journal (Natural Science)* **41**, 114 – 124.

Twardowski, M. S., Boss, E., Macdonald, J. B., Pegau, W. S., Barnard, A. H. & Zaneveld, J. R. V. (2001), 'A model for estimating bulk refractive index from the optical backscattering ratio and the implications for understanding particle composition in case i and case ii waters', *Journal of Geophysical Research* **106(C7)**, 14,129 – 14,142.

Twardowski, M. S., Boss, E., Sullivan, J. M. & Donaghay, P. L. (2004), 'Modeling the spectral shape of absorption by chromophoric dissolved organic matter', *Marine Chemistry* **89**, 69–88.

Twardowski, M. S. & Donaghay, P. L. (2001), 'Separating in situ and terrigenous sources of absorption by dissolved materials in coastal waters', *Journal of Geophysical Research* **106(C2)**, 2545–2560.

Twardowski, M. S. & Donaghay, P. L. (2002), 'Photobleaching of aquatic dissolved materials: Absorption removal, spectral alteration, and their interrelationship', *Journal of Geophysical Research* **107(C8)**, 6.1–6.12.

Twardowski, M. S., Moore, C., Sullivan, J. M., Slivkoff, M., Freeman, S. & Zaneveld, J. R. V. (2012), Volume scattering functions for selected ocean waters: revisited. In preparation.

Udy, J., Gall, M., Longstaff, B., Moore, K., Roelfsema, C., Spooner, D. & Albert, S. (2005), 'Water quality monitoring: a combined approach to investigate

gradients of change in the Great Barrier Reef, Australia', *Marine Pollution Bulletin* **51**, 224 238.

van de Hulst, H. C. (1957), *Light Scattering by Small Particles*, John Wiley & Sons, Inc.

van de Hulst, H. C. (1981), *Light Scattering by Small Particles*, Dover Publications Inc.

Walker, T. A. (1981), 'Dependence of phytoplankton chlorophyll on bottom resuspension in cleveland bay, north queensland', *Australian Journal of Marine and Fresh Water Research* **32**, 981 – 986.

Wang, M. & Shi, W. (2007), 'The NIR-SWIR combined atmospheric correction approach for MODIS ocean color data processing', *Optics Express* **15**, 15722 – 15733.

Warnock, R. E., Gieskes, W. W. & van Laar, S. (1999), 'Regional and seasonal differences in light absorption by yellow substance in the Southern Bight of the North Sea', *Journal of Sea Research* **42**, 169–178.

WET Labs, I. (2004), *VSF3ssd.pdf - ECO VSF 3 Specification Sheet*, d edn, WET Labs, Inc., P.O. Box 518 Philomath, OR 97370 541-929-5650.

WET Labs, I. (2005), *ECO BB-3 Specifications Sheet*, revision g edn, WETLabs, Inc., P.O. Box 518 Philomath, OR 97370 541-929-5650.

Whifield, L., Oude-Egberink, K., Wecker, B., Cravigan, L., Pozza, R. D., Hernaman, V., Scott, J. & Chidzambwa, S. (2010), Climate change in Queensland: What the science is telling us, Technical report, Queensland Climate Change Centre of Excellence.

Wolanski, E., Jones, M. & Williams, W. (1981), 'Physical properties of Great Barrier Reef lagoon waters near Townsville. ii* Seasonal variations', *Australian Journal of Marine and Fresh Water Research* **32**, 321–34.

Wolanski, E., Richmond, R., McCook, L. & Sweatman, H. (2003), 'Mud, marine snow and coral reefs'.

Wooldridge, S., Brodie, J. & Furnas, M. (2006), 'Exposure of inner-shelf reefs to nutrient enriched runoff entering the Great Barrier Reef lagoon: Post-European changes and the design of water quality targets', *Marine Pollution Bulletin* **52**, 14671479.

Yacobi, Y. Z., Alberts, J. J., Takacs, M. & McElvaine, M. (2003), 'Absorption spectroscopy of colored dissolved organic carbon in Georgia (USA) rivers: the impact of molecular size distribution', *Journal of Limnology* **62(1)**, 41–46.

Yentsch, C. & Menzel, D. (1963), 'A method for the determination of phytoplankton chlorophyll and pheophytin by fluorescence', *Deep Sea Research* **10**, 221 – 231.

Yentsch, C. S. & Phinney, D. A. (1989), 'A bridge between ocean optics and microbial ecology', *Limnology and Oceanography* **34(8)**, 1694 – 1705.

Zaneveld, J. R., Kitchen, J. C. & Moore, C. (1994), The scattering error correction of reflecting-tube absorption meters, *in* 'Ocean Optics XII', Vol. 2258, SPIE.

Zaneveld, J. R. & Pegau, W. S. (2003), 'Robust underwater visibility parameter', *Optics Express* **11 (23)**, 2997 – 3009.

Zarco-Tejada, P. J., Miller, J. R., Mohammed, G. H., Noland, T. L. & Sampson, P. H. (2000), Estimation of chlorophyll fluorescence under natural illumination from hyperspectral data, *in* 'Second EARSeL Workshop on Imaging Spectroscopy'.

Zeiss, C. (1999), MMS 1 monolithic miniature-spectrometer product information, Technical report.

Zhang, X., Hu, L. & He, M.-X. (2009), 'Scattering by pure seawater: Effect of salinity', *Optics Express* **17(7)**, 5698 – 5710.

Ziauddin, A., Franz, B. A., McClain, C. R., Kwiatkowska, E. J., Wedell, J., Shettle, E. P. & Holben, B. N. (2010), 'New aerosol models for the retrival of aerosol optical thickness and normalized water-leaving radiances from the seawifs and modis sensors over coastal regions and open oceans', *Applied Optics* **49(29)**, 5545–5560.

Zibordi, G., Melin, F., Hooker, S. B., Alimonte, D. D. & Holben, B. (2004), 'An autonomous above-water system for the validation of ocean color radiance data', *IEEE Transactions on Geoscience and Remote Sensing* **42(2)**, 401–415.

Every reasonable effort has been made to acknowledge the owners of copyright material. I would be pleased to hear from any copyright owner who has been omitted or incorrectly acknowledged.